The Institute of Paper Science and Technology

Atlanta, Georgia

Doctor's Dissertation

A Fundamental Study of Boiling Heat Transfer Mechanisms Related to Impulse Drying

Gary R. Rudemiller

July, 1989

A FUNDAMENTAL STUDY OF BOILING HEAT TRANSFER MECHANISMS RELATED TO IMPULSE DRYING

A Thesis Submitted by

Gary R. Rudemiller

B.S. 1982, Miami University

M.S. 1984, Lawrence University

in partial fulfillment of the requirements
of the Institute of Paper Science and Technology
for the degree of Doctor of Philosophy,
Atlanta, Georgia

July, 1989

TABLE OF CONTENTS

ABSTRACT

To gain insight about the role of boiling heat transfer during impulse drying of a moist paper web, fundamental boiling mechanisms in porous beds composed of incompressible ceramic fibers are investigated. Experiments executed in a boiling cell apparatus are designed to identify the effects of system pressure and average pore diameter of the bed on the characteristic boiling curve. System pressure ranges from 0.10 to 0.28 MPa, and by using three different fiber diameters, average pore diameter ranges from 30 to 250 μm.

The boiling curve exhibits two regimes, with a potentially unstable point of transition. The initial regime behaves like the nucleate regime of pool boiling as heat flux is directly related to wall superheat, and thus is termed the nucleate-type regime. The second regime exhibits no dependence on wall superheat, as heat flux is constant. In this iso-heat-flux regime, maximum heat fluxes are on the order of 25 W/cm^2. The point of transition between the two regimes, called the critical heat flux, can demonstrate moderate instability, depending on pore diameter and system pressure.

Heat transfer in the nucleate-type regime appears to be controlled by nucleation characteristics of the heater surface, and physical limitations for vapor expansion posed by the rigid porous structure. The slope of this regime is directly related to pore diameter, but exhibits no dependence on pressure prior to the critical heat flux. The magnitude of heat flux in the iso-heat-flux regime is controlled by the rate at which the fibrous bed supplies water to the heater surface, and hence is directly related to both pore diameter and system pressure. The transition between the two regimes is smooth for pore diameters less than 90 μm, regardless of system pressure. However, for average pore diameters above 220 μm, the transition exhibits a peak heat flux with an associated instantaneous rise in surface temperature. Elevated pressures exacerbate this instability.

Using dimensional analysis, data for the iso-heat-flux regime is correlated to ± 35%, but

data for the nucleate-type regime is only correlated to ± 175%. Improvements in this correlation require knowledge of the nucleation characteristics of the heater surface.

INTRODUCTION

Since the early 1970's, a number of factors have motivated efforts to improve dewatering capabilities in the papermaking process. Although significant improvements have been attained, the basic mechanisms of conventional techniques limit the potential for further major improvements. Dramatic improvements can now be best achieved through novel processes involving fundamentally different mechanisms. Impulse drying is one such process that has been under development at The Institute of Paper Chemistry since the early 1980's. Although this new process for drying paper webs has some similarities to press drying, the two are controlled by different mechanisms [1].

Ahren's initial work with "high-intensity" drying demonstrated improved drying rates through pressure application to the sheet with a very hot surface [2,3]. Impulse drying is a natural extension of high-intensity drying in that it combines the wet pressing and drying operations into a brief event by pressing the moist sheet in a nip formed by a felt-covered, unheated roll or shoe and an externally-heated roll, as illustrated in Figure 1. Heat flux data for a typical impulse drying

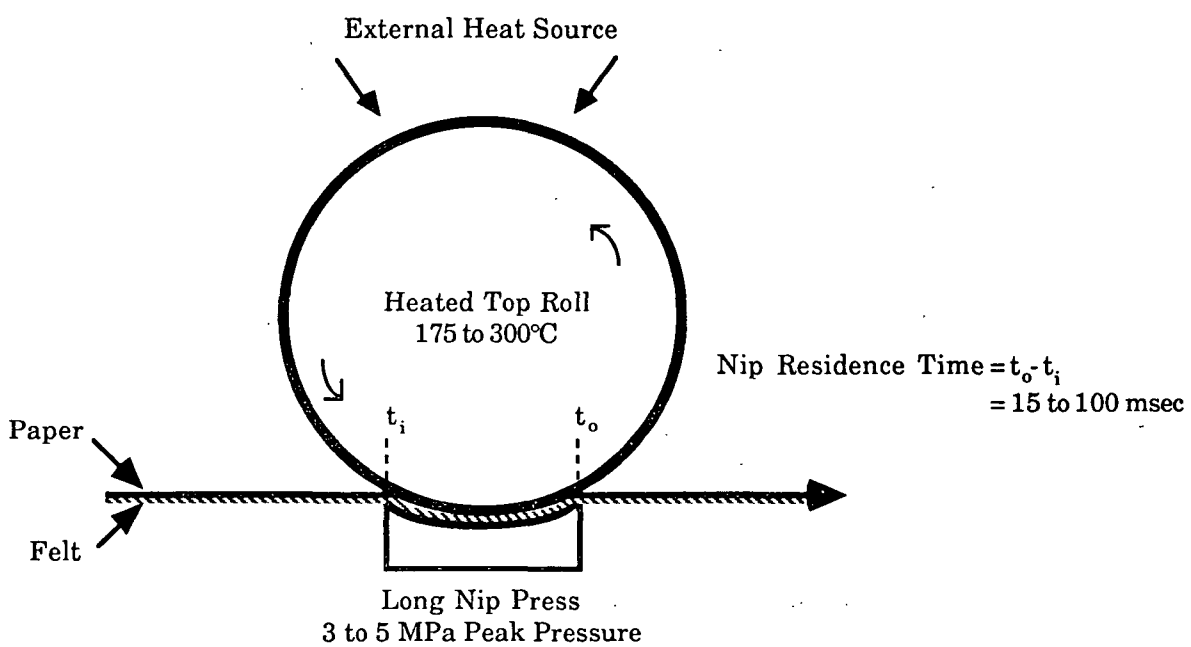

event with linerboard are illustrated in Figure 2. Heat transferred to the moist web of paper peaks at instantaneous heat fluxes on the order of 3.0 MW/m^2 as the temperature of the heated surface drops by about 25°C . By integrating the instantaneous heat flux curve, the average heat flow to the sheet is determined to be on the order of 60 kJ/m^2, which is much higher than conventional drying heat flows.

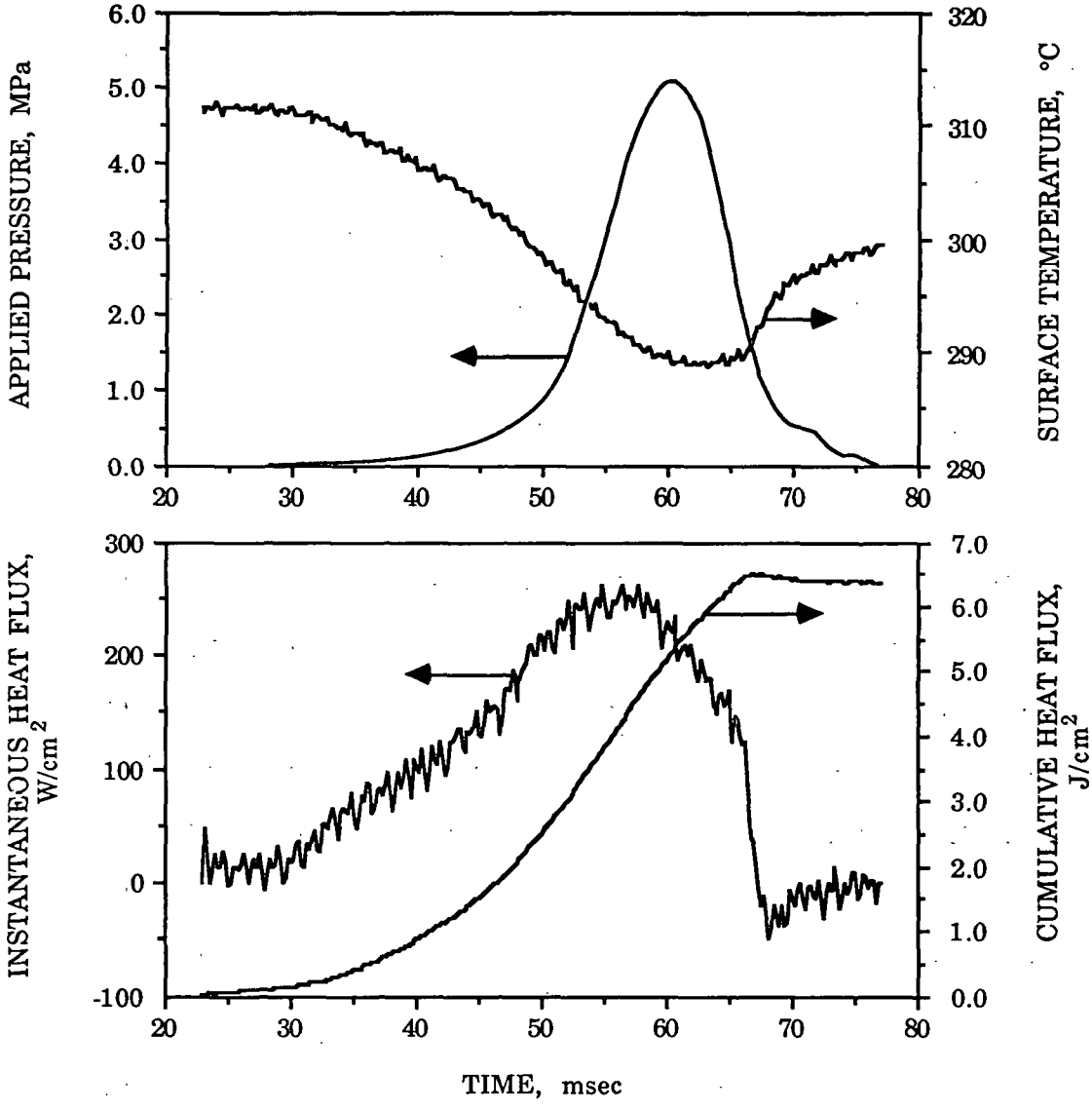

Figure 2. Data for impulse drying of 125 g/m^2 linerboard with an inlet moisture ratio of 0.87 g water/g fiber.

Initial studies of impulse drying demonstrated the ability of the process to generate drying rates on the order of 30,000 kg/(hr-m^2) [4], yielding sheet solids contents prior to the dryer section ranging from 55 to 70%. Because dewatering rates achieved with conventional pressing and drying techniques are appreciably lower, impulse drying presents opportunities to reduce energy consumption, and also to reduce the capital costs associated with conventional drying equipment.

Implementation of impulse drying will utilize a nip arrangement placed somewhere in the press section [5]. The heated roll can be placed either in the top roll position (as illustrated in Figure 1) or the bottom roll position. Based on the requirements of a particular application, nip residence times of 15 to 100 milliseconds may be required, which could be achieved with extended-nip press technology. Applied pressures of 1.0 to 5.0 MPa and roll surface temperatures of 150 to 300°C appear to be practical for the process. Because equipment necessary to achieve these operating conditions is already commercially available, no major technological developments are required for implementation of impulse drying as it is presently envisioned.

ADVANTAGES OF IMPULSE DRYING

The effects of impulse drying on paper properties have been documented for a number of grades [1,6-9]. The potential benefits in sheet quality resulting from these property changes must be interpreted in light of quality requirements for each particular grade. Sheet properties are affected by the unique sheet density profile developed during impulse drying. Although the center region of the sheet is less densified than the surface layers, the average density is higher than a conventionally-pressed and dried sheet [10]. Consequently, most of the strength properties increase with degree of impulse drying, while opacity and other optical properties decrease slightly. Impulse drying offers the potential to tailor a grade of paper for a specific end-use application.

The potential economic advantages stemming from the tremendous improvements in water removal are evident by considering a hypothetical impulse drying application for the commercial production of linerboard [8], as illustrated in Figure 3. Situating an impulse dryer in

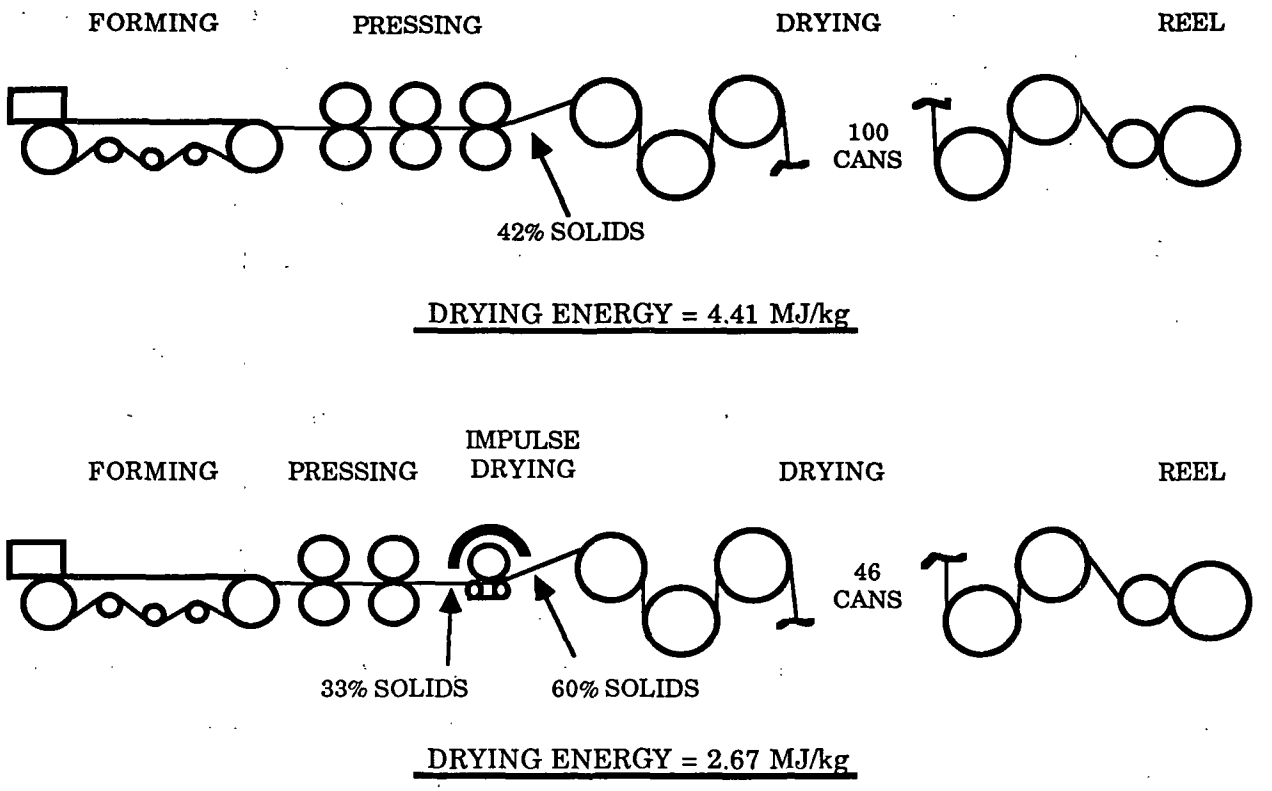

Figure 3. Comparison of energy consumption for dewatering 125 g/m^2 linerboard to a final moisture content of 5% by conventional means versus a process utilizing impulse drying [8]. Machine speed is 610 m/min, and impulse drying conditions are 315°C surface temperature, 82°C sheet temperature, 4.8 MPa peak pressure, and 30 msec nip residence time.

the third press position would dramatically increase sheet solids content entering the dryer section. The consequent reduction in energy required to achieve a final solids content of 95% represents a significant decrease in cost of producing the linerboard, although this benefit appears to be limited to sheets with pre-impulse-drying solids contents greater than 25%, as illustrated in Figure 4. Furthermore, the reduction in the number of conventional drying cylinders yields capital savings. The increase in sheet strength properties results in another potential cost-advantage of impulse drying: the quality of furnish raw materials can be compromised while maintaining strength equivalent to a conventionally-dried, virgin-fiber sheet. An economic analysis based on a MAPPS simulation of a 1000 TPD linerboard mill using impulse drying suggested possible annual savings due to a reduction in energy consumption of $1,500,000, and annual savings due to the use of a higher-yield furnish of $11,000,000 [11].

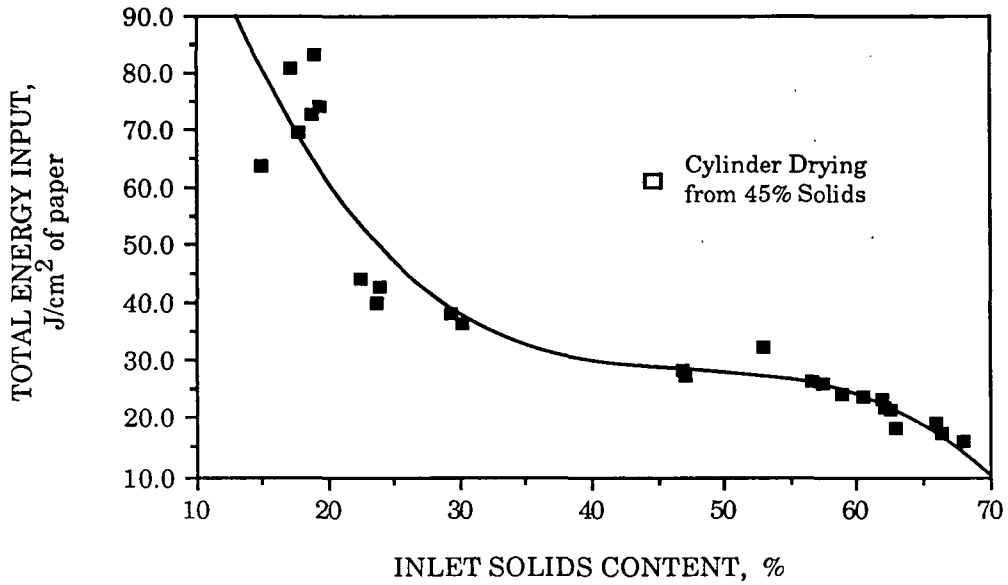

Figure 4. Energy consumption for impulse drying 125 g/m^2 linerboard at 610 m/min [8].

MECHANISMS OF IMPULSE DRYING

The dramatic increases in heat flux and water removal rate experienced with impulse drying suggest that the mechanisms that control dewatering differ significantly from those of conventional pressing and drying operations. Wet pressing water removal is limited by the compressibility of the sheet. Conventional drying is controlled by evaporation, diffusion of the vapor, and migration of the water to the plane of evaporation under the influence of capillary forces. Evidence suggests that an additional mechanism is responsible for a major portion of the water removed from the sheet during impulse drying.

A few studies have provided some information about impulse drying water removal mechanisms. Devlin has demonstrated that the high water removal rates for high-intensity drying result from the combined effects of volume reduction due to wet pressing and the bulk flow of water, presumably under the influence of a pressure gradient generated by vapor formation [12]. In high-intensity drying of a web with a moisture content of 1.33 kg water/kg fiber, 9% of the initial water content was removed by volume reduction due to wet pressing, but liquid water

removal due to "high-intensity" mechanisms amounted to 30% of the initial water in the sheet. This point is illustrated in Figure 5 for comparison of water removal rates for impulse drying and wet pressing over a range of sheet moisture contents. While exiting sheet solids content for a conventional pressing arrangement is limited to about 45% solids, impulse drying can achieve significantly higher exiting solids contents. Moreover, impulse drying also effects some degree of dewatering on sheets that are at solids contents well beyond the range of wet pressing.

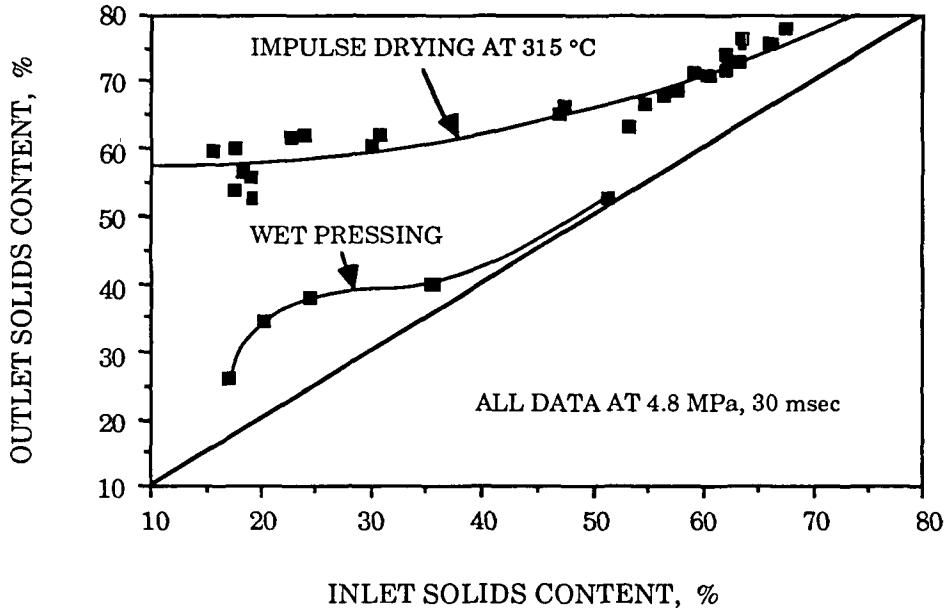

Figure 5. A comparison of dewatering capabilities of conventional wet pressing and impulse drying [8].

Further work at IPC has shown that water removal from the sheet during impulse drying occurs in both liquid and vapor forms. As illustrated in Figures 6 and 7, the relative distribution of the water phases depends on the initial moisture content of the sheet [8]. As hypothesized by researchers at the IPC, dewatering due to volume reduction is augmented by vapor generation, as the vapor pressure gradient presumably acts as a driving force for bulk liquid removal.

These pieces of evidence suggest that boiling may contribute to heat transfer during the impulse drying event. Boiling is one mode of heat transfer that generates the magnitude of heat flux demonstrated in impulse drying. Second, the generation of a vapor phase within the sheet

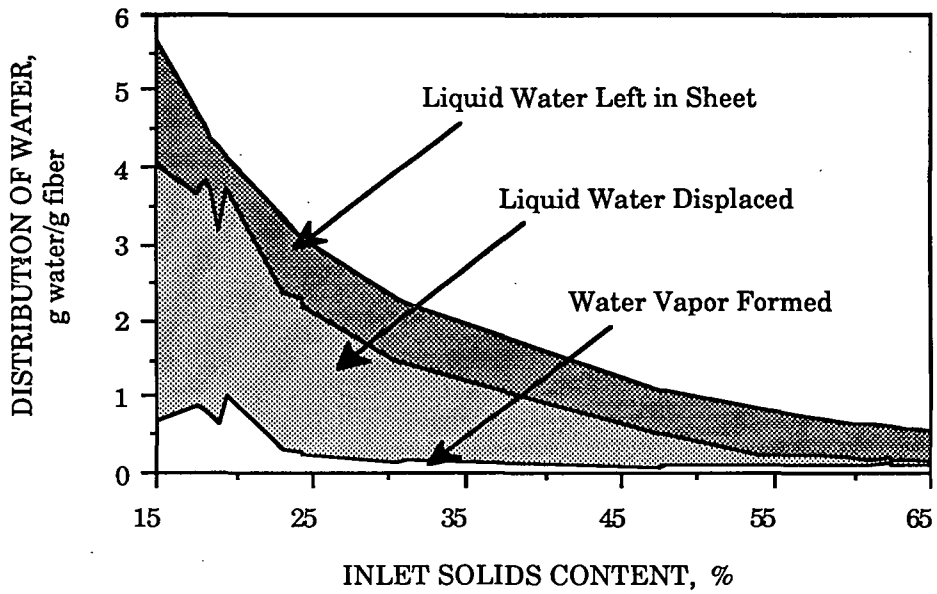

Figure 6. Redistribution of water phases during impulse drying as a function of inlet solids content [8]. Conditions for impulse drying 125 g/m^2 linerboard are 315°C surface temperature, 80°C sheet temperature, 4.8 MPa peak pressure, and 30 msec nip residence time.

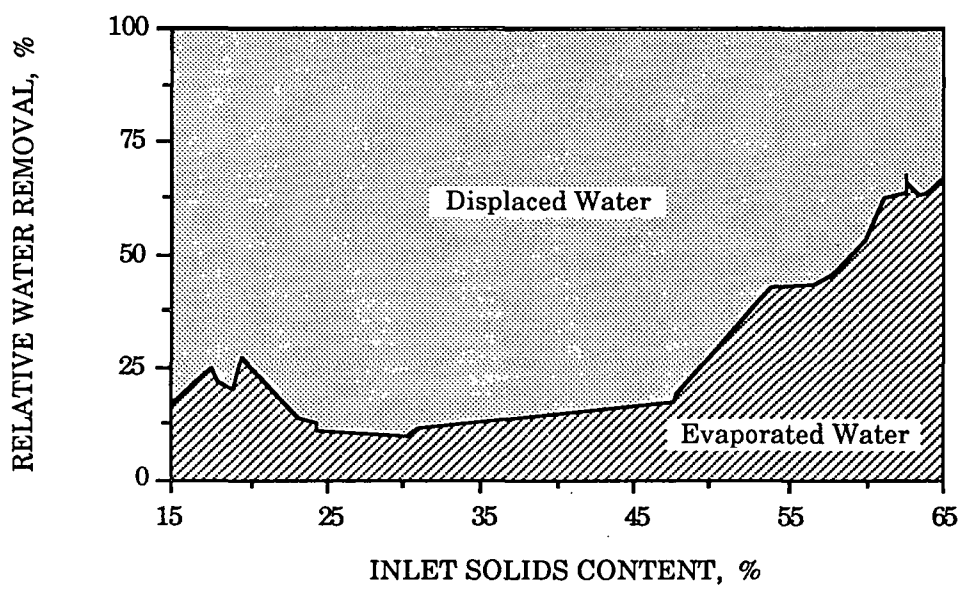

Figure 7. Distribution of water phases removed as a function of inlet solids content under conditions listed in Figure 6 [8].

requires a phase change mechanism. The final piece of evidence is the magnitude of temperature achieved by the internal structure of the sheet during an impulse drying event. The behavior of internal sheet temperature illustrated in Figure 8 supports the idea of a two-phase zone existing within the sheet.

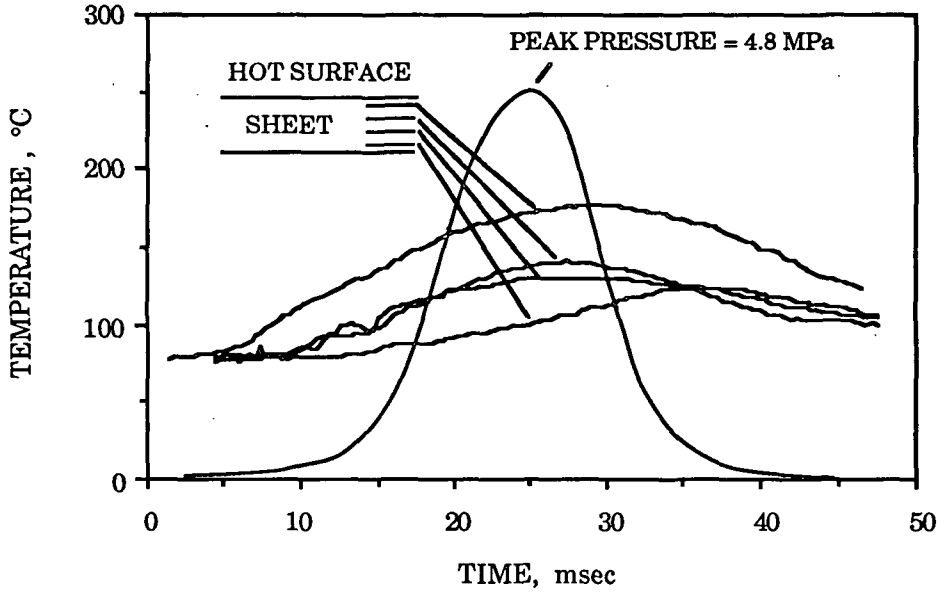

Figure 8. Internal sheet temperature profiles during impulse drying [8].

The occurrence of boiling within the cellulose fiber sheet in the short time frame of an impulse drying event presents a complex engineering problem. Interacting issues of sheet compressibility, multiphase flow through porous media, thermodynamics, and boiling heat transfer compose a problem of enormous complexity. This thesis addresses one facet of the problem by investigating fundamental principles involved with boiling in a fibrous bed. Understanding this model boiling process may provide insight regarding the impact of boiling heat transfer on the impulse drying event.

LITERATURE REVIEW

Because boiling heat transfer appears to be important to the physics of impulse drying, a review of pertinent literature is presented to familiarize the reader with the principles of boiling. General reviews of pool boiling and flow through porous media precede a discussion of boiling in the presence of porous media. The reader is assumed to be familiar with impulse drying.

The phenomena occurring within the sheet during contact of the hot roll and the sheet could be studied by following a particular point of contact through the impulse drying event. In this ideal framework, the boiling that would be observed within the sheet is more analogous to pool boiling phenomena than to convective boiling. Therefore, the following discussion focuses on classical pool boiling as a basis for understanding boiling in the presence of porous media. Qualitative descriptions, parametric effects, and correlations will be presented for each of the pool boiling regimes.

POOL BOILING HEAT TRANSFER

Pool boiling is defined as boiling from a heated surface submerged in a pool of liquid. Boiling generates extremely high heat transfer rates, but the effectiveness of heat transfer differs for the three boiling regimes. Boiling data are typically represented by a log-log plot of heat flux as a function of wall superheat (the difference between the heater surface temperature and the saturation temperature of the liquid). The characteristic boiling curve for water at atmospheric pressure is illustrated in Figure 9. An initial regime of natural convection heat transfer precedes the onset of boiling. Nucleate boiling, the initial boiling regime, is characterized by very high heat transfer coefficients and the generation of distinct bubbles. Transition boiling, the middle regime, is an unstable phenomenon consisting of a mixture of nucleate and film boiling, and is characterized by a negative slope. Film boiling, the third regime, is characterized by less effective conduction of heat across a vapor film that blankets the heater surface, with phase change occurring at the interface of the vapor and liquid phases. Figure 10 illustrates the vapor

generation phenomena occurring at the heater surface during each of these regimes.

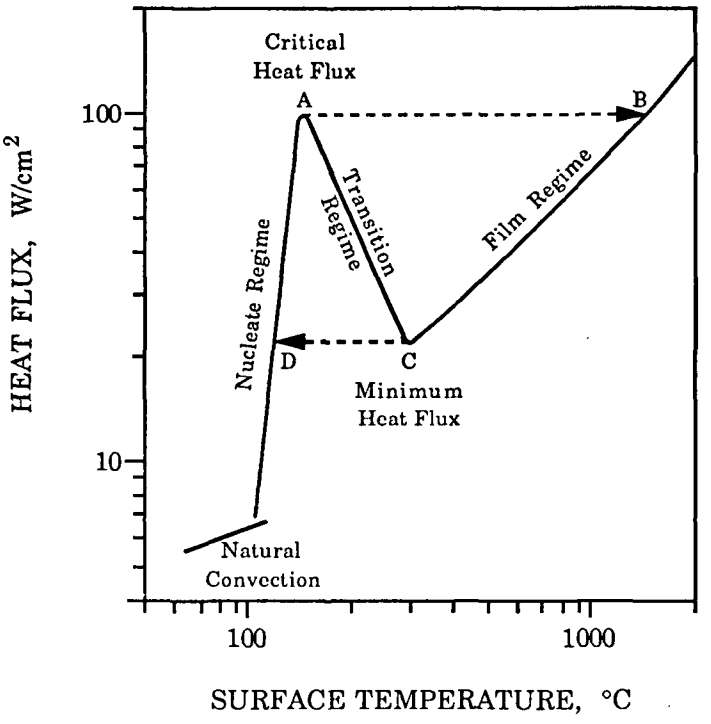

Figure 9. The characteristic curve for pool boiling of water at atmospheric pressure.

Qualitative Discussion of Pool Boiling Phenomena

The behavior of each of the pool boiling regimes and transition points results from a combination of thermal and hydrodynamic effects near the heater surface. A qualitative understanding of the phenomena that occur at the heater surface is essential to appreciate the factors that control boiling and effect transitions between the regimes. The following discussion, for which much of the general information is taken from References 13 through 17, is presented in reference to Figure 9. The boiling system consists of a pool of liquid and a submerged heater surface which initially are in thermal equilibrium at the liquid's saturation temperature. The discussion begins with a slow increase in surface temperature.

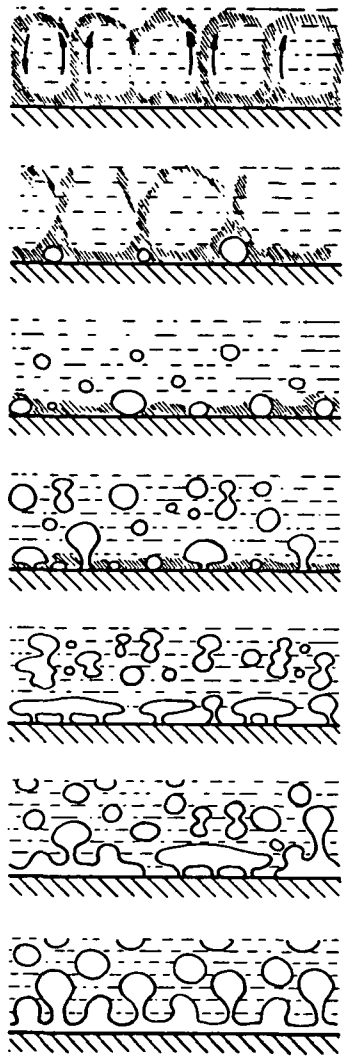

Figure 10. Vapor phase phenomena at the heater surface during pool boiling. (Reprinted from reference 15 with permission of McGraw Hill Publishing Company, New York, NY)

Natural Convection

Prior to the onset of boiling, thermal convection patterns at the hot surface prepare the liquid for active nucleate boiling. Successful completion of a bubble growth cycle requires that a developed thermal boundary exist at the surface. As the surface is heated, heat conducted to the liquid establishes a temperature gradient that promotes natural convection near the surface. The liquid in the thermal boundary layer is in a metastable, superheated state.

Onset of Nucleate Boiling

The vapor generation that results in bubble formation proceeds either by homogeneous or heterogeneous nucleation. In homogeneous nucleation, which typically occurs with organic fluids, bubbles grow from vapor embryos formed by an agglomeration of molecules with vapor-like energies. In heterogeneous nucleation, which occurs in the boiling of water, vapor or gas trapped in non-wetted voids on the heater surface is the source for nucleation. Because impulse drying appears to involve a mixture of water phases, the remaining discussion will focus on heterogeneous nucleation.

At some point during natural convection, the liquid at the heater surface attains a level of superheat capable of supporting nucleation, which occurs when a gas or vapor pocket trapped in a surface void is "activated". As the wall superheat increases to a level beyond the liquid saturation temperature, the void vapor pressure drives liquid out of the surface cavity to begin bubble growth at its entrance. Complete growth of a bubble from an active site requires that the temperature of the liquid above the infant bubble be hot enough to prevent condensation of vapor at the bubble surface. Thus, once the thermal boundary layer develops to a point where it can support bubble growth, complete nucleation cycles begin.

In addition to thermal effects, bubble stability and growth also depend on the relative magnitude of the internal vapor pressure forces that counteract the surface tension forces acting to collapse it. Neglecting the partial pressure of other gases inside the surface void, the force balance is expressed by Laplace's equation,

$$P_v - P_l = \frac{2\sigma}{r} \quad . \tag{1}$$

Thus, the pressure inside the bubble must be higher than the liquid pressure. Since a saturated condition is maintained within the bubble, the vapor must be at thermal equilibrium with the

superheated liquid in the thermal boundary layer.

The liquid superheat corresponding to the pressure difference across the bubble boundary can be determined by substituting the Clausius-Clapeyron equation and the ideal gas law into Equation 1. The minimum wall superheat for stable bubble growth is a function of liquid properties and heater surface properties. Typical wall superheats at the onset of nucleate boiling of 4 to 5°C (depending on heater surface characteristics) limit active surface voids to those with minimum entrance diameters of about 24 to 30 μm.

Nucleate Boiling Regime

Nucleate boiling is characterized by two hydrodynamic regimes - an isolated bubble regime, and a continuous vapor column regime [18]. At low wall superheats, nucleation sites are few and no interaction between adjacent sites occurs: bubble growth and departure occur as independent, cyclic events. As surface temperature increases, smaller vapor pockets are triggered into active bubble growth, which increases the density of nucleation sites on the heater surface, and also the frequency of bubble departure from a given site. The escalation in intensity of nucleation eventually results in interaction between adjacent sites, as the departing bubbles coalesce to form continuous columns of vapor ascending from the surface. Further increases in nucleation intensity increases the vapor velocity in the columns.

The effective heat transfer evident in this region results from the combination of the three heat transfer mechanisms illustrated in Figure 11 [19]. In the bubble agitation mechanism, growth and departure of a bubble causes appreciable agitation that promotes convective heat transfer in the adjacent thermal boundary layer [20]. Additionally, the Marangoni effect -- convective currents resulting from a surface tension gradient caused by the temperature gradient at the bubble surface -- contributes to this microconvection heat transfer [21]. During vapor/liquid exchange, hot liquid pumped away from the surface by a departing bubble is replaced by cooler liquid that becomes heated by transient conduction. In the evaporation mechanism, bubble growth results from

BUBBLE AGITATION

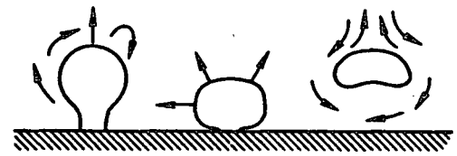

VAPOR-LIQUID EXCHANGE

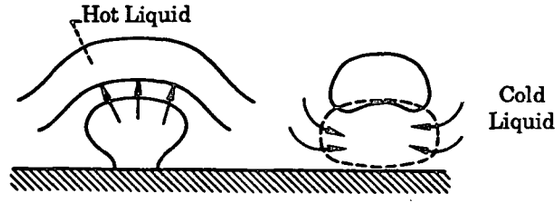

EVAPORATION

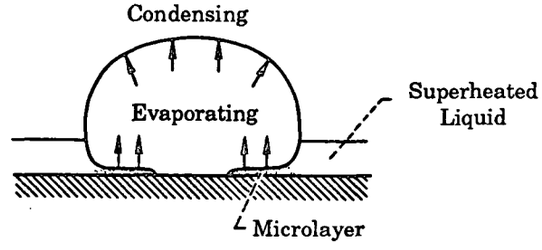

MARANGONI EFFECT

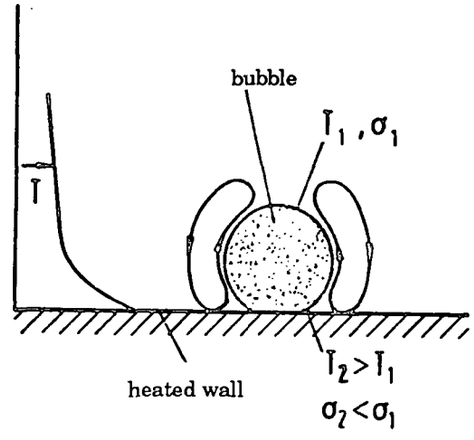

Figure 11. Schematic diagrams of the conceptual models for heat transfer in the nucleate boiling regime. (Portions of this Figure are modified with permission of Hemisphere, New York, NY, from: Stephan, K. Bubble Formation and Heat Transfer in Natural Convection Boiling. Heat Transfer in Boiling. Hahne, E. and Grigull, U. (editors), Hemisphere, Washington, 1977:3-20.)

evaporation of the thin film of liquid covering the heated surface beneath the bubble, which creates localized dry patches on the heater surface. This microlayer of liquid is typically 1000 to 4000 Å thick [19,22]. The relative contributions of each of the three mechanisms to nucleate boiling heat transfer has been debated, but current theory indicates that the evaporative mechanism becomes dominant as the critical heat flux is approached [19], as illustrated in Figure 12. The condensation of bubbles in the upper regions of the pool contributes negligibly to heat transfer [20,23].

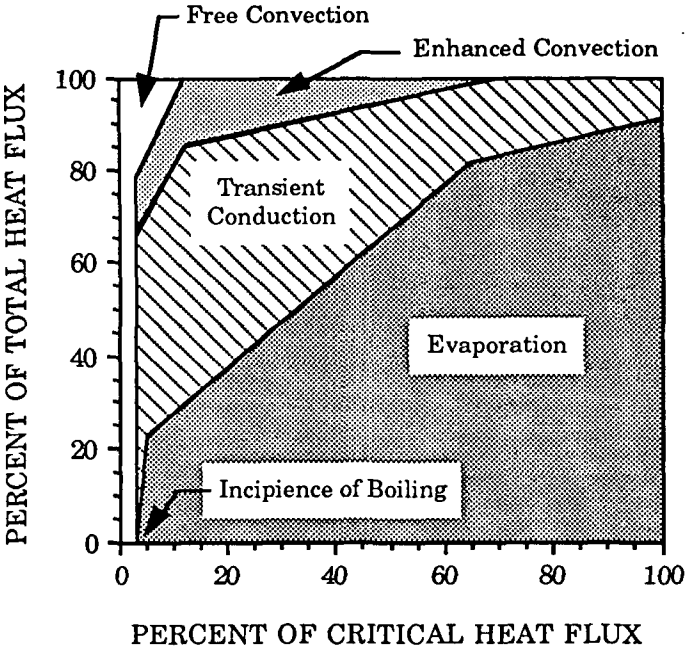

Figure 12. Relative contributions of the nucleate regime heat transfer mechanisms [19].

A number of expressions have been developed to quantify the diameter of a bubble at departure [24]. Fritz [13] initially modeled the diameter by considering a balance between buoyancy and surface tension forces at the point of departure:

$$d = 0.0208\,\beta\sqrt{\frac{\sigma}{g(\rho_l - \rho_v)}} \quad . \tag{2}$$

More complicated expressions include other factors in the bubble force balance. The importance of

the buoyant and surface tension forces to boiling heat transfer is emphasized by the recurrence of the square root term in Equation 2 in many boiling correlations.

Critical Heat Flux

The critical heat flux, which is the maximum heat flux achieved during nucleate boiling, defines the end of nucleate boiling and the beginning of transition boiling. The peak in heat flux results from a hydrodynamic transition in the thermal boundary layer that prevents the rapid flow of liquid to replenish the heater surface. The surface hydrodynamics at the critical heat flux are defined by an interaction of two hydrodynamic instability phenomena - Taylor instability and Helmholtz instability [22,25]. Taylor instability occurs with the unstable configuration of a dense fluid overlaying a less dense fluid, such as the phenomena that begins to occur during nucleate boiling as the critical heat flux is approached.

The significance of Taylor instability phenomena to boiling is understood by considering the situation illustrated in Figure 13. An interfacial wave is established as the dense fluid collapses into the less dense fluid, the nodes of which are defined by the downward motion of the heavier fluid and the upward motion of the less dense fluid. Taylor's analysis indicates that the interface is stabilized to disturbances of small wavelength by the surface tension forces that balance the potential and kinetic energies of the wave [25]. The critical interfacial wavelength above which instability occurs is analytically derived for a plane horizontal wave to be

$$\lambda_c = 2\pi \sqrt{\frac{\sigma}{g(\rho_l - \rho_v)}} \quad . \tag{3}$$

The dominant unstable wavelength, called the Taylor wavelength, is the interfacial wavelength resulting from the fastest growing disturbance,

$$\lambda_d = 2\pi \sqrt{\frac{3\sigma}{g(\rho_l - \rho_v)}} \quad . \tag{4}$$

Accordingly, the Taylor wavelength predominates during the collapse of the plane horizontal interface. Mathematical expressions for the critical and dominant wavelengths have also been determined for a horizontal cylinder boiling geometry [26].

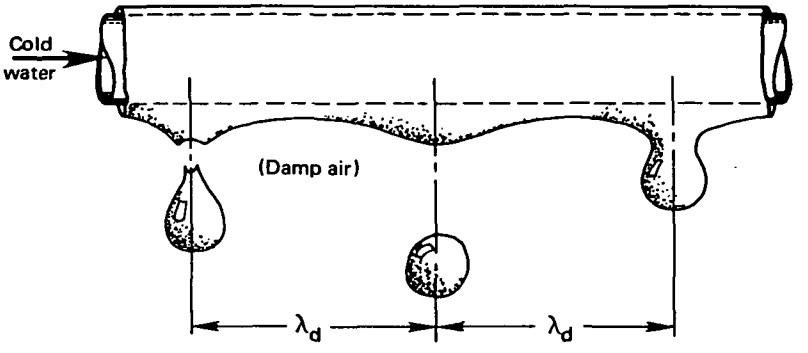

Taylor instability in the interface of the water condensing on the underside of a small cold water pipe

Figure 13. A graphic illustration of Taylor hydrodynamic instability phenomena. (Reprinted from reference 14 with permission of Prentice-Hall, Inc., Englewood Cliffs, NJ)

At higher levels of nucleate boiling heat flux, the columns of vapor become arranged on a staggered grid spaced at a distance equal to the Taylor wavelength. Near the critical heat flux, the velocity of vapor rising in the columns becomes very high. Due to the stabilizing effect of surface tension, the interface between the vapor column and the pool of liquid is stable up to some maximum relative velocity. Above this velocity, a small disturbance in the interface will amplify and grow to collapse the interface and disrupt the flow of vapor. This results in the formation of vapor domes that temporarily block liquid flow to the heater surface, as illustrated in Figure 10. Consequently, heat flux decreases. The phenomena of interface destabilization is referred to as Helmholtz instability, and is conceptually represented in Figure 14.

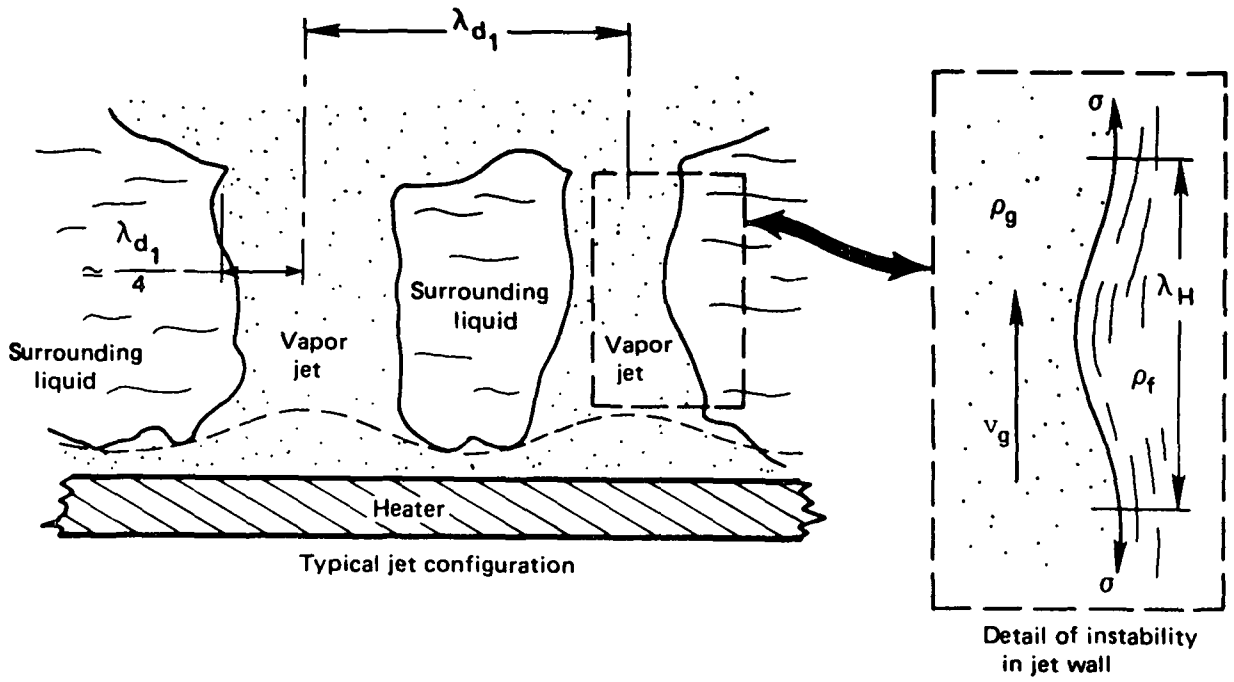

Figure 14. A graphic illustration of Helmholtz hydrodynamic instability phenomena. (Reprinted from reference 14 with permission of Prentice-Hall, Inc., Englewood Cliffs, NJ.)

Transition Boiling Regime

The transition boiling regime, which exists between the critical and minimum heat fluxes, is characterized by an inverse relationship between heat flux and wall superheat, and thus exhibits a negative slope on the characteristic boiling curve. It is a highly unstable boiling regime, which makes it of little practical interest as equipment is seldom designed to operate in this regime. However, it is a phenomenon of interest for quenching processes.

Transition boiling has been described as a combination of unstable nucleate and unstable film boiling, each of which alternately exist at a given location on the heater surface [27,28]. At wall superheats within the transition regime, the amount of vapor generated is too variable to support a stable vapor film, and too great to allow sufficient liquid to reach the heating surface in steady flow. As wall superheat increases in the transition regime, more nucleation sites are activated, resulting in further blanketing of the heater surface, and the increasing resistance to heat transfer results in a decreasing heat flux. As the process approaches the minimum heat flux, film boiling becomes more stable and nucleate boiling becomes more unstable; the reverse situation

exists as the critical heat flux is approached from the transition regime. The behavior of average heat flux with wall superheat reflects the proportion of the local boiling cycle occupied by nucleate and film boiling.

This periodic quenching of the heater surface that occurs with local oscillations between nucleate and film regimes results in large variations in surface temperature and heat flux. The largest variations in surface temperature occur in the high heat flux portions of the transition regime [29]. Near the point of minimum heat flux, the temperature variations disappear as liquid contact of the surface ceases. Once the minimum heat flux is reached, the vapor film is continuous.

Minimum Heat Flux

The point of minimum heat flux identifies the end of the transition boiling regime and the beginning of the film boiling regime. At this point, a fully developed vapor film completely covers the heater surface. The film becomes fully developed when the heat flux from the heated surface balances the minimum rate of vapor generation that will sustain a stable vapor film over the surface. The shape of the vapor film interface is determined by the hydrodynamics associated with the Taylor instability.

Film Boiling Regime

The film boiling regime is characterized by a direct relationship between the wall superheat and the heat flux. Movement from transition to film boiling represents another drastic change in the nature of the boiling process. Now, phase change occurs at the interface of the vapor film and the overlying liquid, driven by heat conducted across the stable vapor film. The large resistance of the vapor film yields a heat transfer coefficient that is much smaller than that for nucleate boiling, even though the magnitude of heat flux is similar for the two regimes. Increases in heat flux are effected by increasing the wall superheat, which is eventually limited by meltdown of the heater surface. At temperatures above 500°C, radiation across the vapor film

becomes significant.

By application of Taylor-Helmholtz instability to kinematic equations for irrotational flow, Berenson [30] has shown that the film boiling vapor/liquid interface assumes the form of a Taylor wave with a wavelength that maximizes bubble growth rate at the interface. At a node of the interfacial wave, the two-phase boundary grows until a bubble departs, which occurs when the amplitude is approximately equal to the bubble diameter. After the bubble departs, the interface snaps back toward the heater surface, providing the disturbance necessary to start growth of the neighboring antinode. Since bubbles are generated at the nodes of the interfacial wave, bubble spacing is fixed by hydrodynamic considerations.

Parametric Influences for Pool Boiling Phenomena

Though a number of factors can affect pool boiling, three of these that may impact impulse drying are system pressure, heater surface characteristics, and the degree of liquid subcooling.

System Pressure

Pool boiling phenomena are particularly sensitive to level of system pressure. An inverse relationship exists between system pressure and required liquid superheat for activation of nucleation sites during nucleate boiling. Figure 15 demonstrates this point, as superheat requirements at a particular nucleate boiling heat flux are reduced at elevated pressures. The effects on maximum heat flux are similar: the critical heat flux initially increases with pressure, and then decreases beyond a reduced pressure of about 0.3. The response of the minimum heat flux to pressure is similar to that of the critical heat flux [31], as its maximum value also occurs at a reduced pressure of about 0.3. These relationships have been documented for many different liquids [31-35]. While one study found that film boiling heat flux decreases slightly beyond reduced pressures up to 0.8 [36], another study found that the film boiling heat transfer coefficient increased steadily as pressure was increased [37].

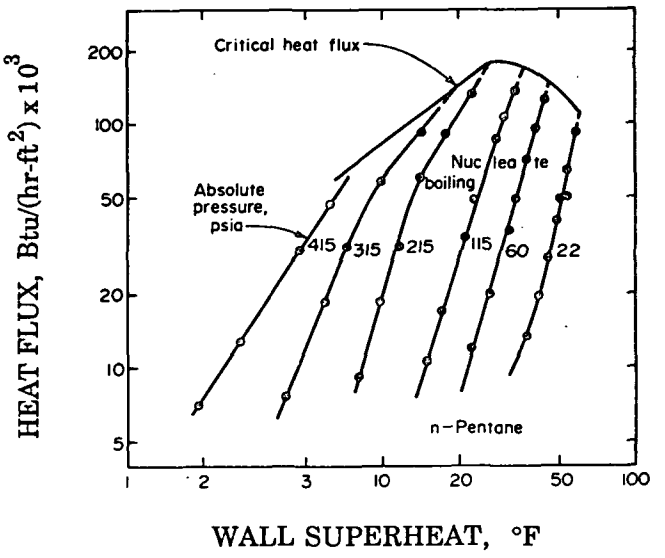

Figure 15. The effect of pressure on the nucleate regime and critical heat flux for pool boiling of *n*-pentane. (Reprinted from reference 16 with permission of McGraw Hill Publishing Company, New York, NY)

Heater Surface Characteristics

Numerous studies report significant improvements in the nucleate boiling heat transfer coefficient with surfaces that provide a higher density of nucleation sites [38]. As illustrated in Figure 16, roughening the heater surface with emery cloth reduced the wall superheat requirements for the nucleate and transition regimes, and for the critical heat flux [28]. Increasing the number of nucleation sites does not affect wall superheat requirements for the minimum heat flux or film boiling because phase change in these regions is controlled by hydrodynamics associated with the interfacial wave, and not by the characteristics of the heater surface. For the same reason, the magnitude of the critical, minimum, or film boiling heat fluxes are also unaffected. A number of surface structures have been developed to provide a high density of nucleation sites in order to take advantage of high performance boiling [38-40].

Each surface modification technique increases the number of nucleation sites, whether they be voids in the heater surface, or voids within the microstructure of a porous surface layer. However, while the mouth diameter of the cavity determines the superheat needed to initiate

subcooling, whereas the nucleate regime is unaffected. Heat flux in the film boiling regime is strongly increased near the minimum heat flux, but the difference between subcooled and saturated film boiling heat fluxes decreases as wall superheat is increased [37].

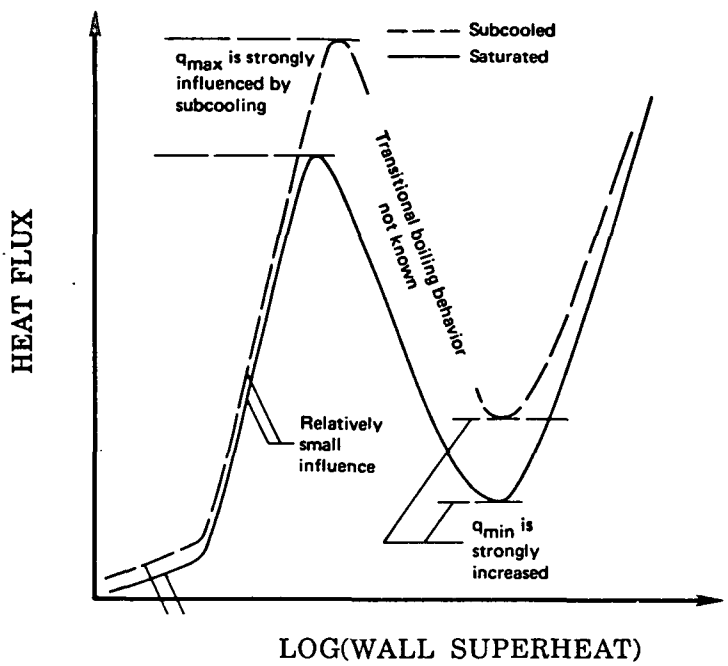

Figure 17. The effect of liquid subcooling on the characteristic curve for pool boiling. (Reprinted from reference 14 with permission of Prentice-Hall, Inc., Englewood Cliffs, NJ)

Pool Boiling Heat Transfer Correlations

Many correlations have been developed for the regimes and transition points of pool boiling to quantify the heat flux as a function of fluid and system properties. Some of the correlations are based on theory, and some are developed from dimensional analysis. Because the theoretical foundation for boiling is not well developed, the fundamentally-based correlations must be empirically corrected. Consequently, no boiling correlation enjoys universal application. The purpose of the following discussion is to give the reader an appreciation for the myriad of approaches used to model and correlate boiling data, and to familiarize the reader with the dimensionless groups significant to boiling heat transfer. A few of the significant correla-

tions for pool boiling are presented. References 14, 15, 16, 42 and 43 review a more extensive collection of correlations.

Heat transfer in the natural convection regime can be approximated according to standard correlations for natural convection heat transfer found in textbooks [15]. A correlation appropriate for the experimental heater geometry should be used.

Nucleate boiling heat transfer is obviously strongly dependent on the number of nucleation sites available on the heater surface. However, the inability to relate specific characteristics of the nucleation sites to boiling heat transfer precludes developing a correlation based on a measure of the nucleation sites. Consequently, dimensional analysis has been used for many of the nucleate boiling correlations. The first, and perhaps most widely recognized, nucleate boiling correlation was developed by Rohsenow based on an analogy between convection near the boiling surface and stream turbulence in ordinary fluid flow in a pipe [48]. Accordingly, the correlation defines a Nusselt number in terms of Reynolds and Prandtl numbers. A bubble Reynolds number is defined in terms of the mass velocity of the bubbles and their diameter as they leave the surface. Using Fritz's expression for bubble diameter (Equation 2) and Jakob's expression for departure frequency, Rohsenow defines the bubble Reynolds number as

$$Re_b = C_R \beta \left[\frac{q/A}{\mu_l \Delta h_v} \sqrt{\frac{\sigma}{g(\rho_l - \rho_v)}} \right] \tag{5}$$

where C_R is the only unknown variable. Similarly, he defines a bubble Nusselt number using the bubble diameter as the characteristic length,

$$Nu_b = C_N \beta \left[\frac{h_c}{k_l} \sqrt{\frac{\sigma}{g(\rho_l - \rho_v)}} \right] \tag{6}$$

where C_N is the only unknown variable. Including the Prandtl number because of its importance to convection heat transfer, the final correlation is rearranged to give

$$\frac{C_{p_l}\Delta T_w}{\Delta h_v} = C_{sf}\left(\frac{q/A}{\mu_l \Delta h_v}\sqrt{\frac{\sigma}{g(\rho_l - \rho_v)}}\right)^{0.33}\left(\frac{C_{p_l}\mu_l}{k_l}\right)^{s}. \qquad (7)$$

All ignorance is buried in the empirical constant, C_{sf}, which accounts for the nucleation characteristics of the particular liquid/heater combination. The value of Prandtl number exponent also depends on the liquid/heater combination [15]. Table 1 lists values of these two parameters for a few liquid/surface combinations. Though the correlation was applied to data for boiling on a flat plate and on a horizontal cylinder, it is not particularly accurate, as errors in heat flux of 100% and errors in wall superheat of 25% are typical. This correlation has been modified for boiling under vacuum by changing the exponent of 0.33 to values ranging from 0.3 to 0.377, and by decreasing the value of C_{sf} by about 40% [15]. The Rohsenow correlation was extended to include an empirical expression for nucleation site density [16].

Dimensional analysis was used in an attempt to correlate with one equation over 5000 nucleate boiling data points for various heater types and fluid types [17]. This correlation was accurate to within 22.3%. However, by segregating the fluids into one of four categories, the correlations for the individual groups were each about twice as accurate as the overall correlation, as illustrated in Table 2. This reflects the lack of a fundamental understanding of nucleate boiling phenomena, primarily due to the problem of quantifying the nucleation characteristics of the heater surface.

Since the critical heat flux is apparently influenced by the hydrodynamics associated with Taylor and Helmholtz instabilities, it is not surprising that most of the theoretically-based correlations for the critical heat flux are rooted in these two instability phenomena. Zuber developed a correlation for the critical heat flux on a horizontal flat plate [18]. An energy balance

Table 2. The dimensionless correlations developed to describe the nucleate boiling regime for four different classes of liquids.

Fluid	Correlation	Mean Absolute Error
Water	$Nu = 0.246 \times 10^{7}\ \Pi_1^{0.673}\ \Pi_2^{-1.58}\ \Pi_3^{1.26}\ \Pi_4^{5.22}$	11.3%
Hydrocarbons	$Nu = 0.0546\left[\Pi_1 \Pi_3^{1.26}\right]^{0.67}\ \Pi_2^{0.248}\ \Pi_4^{-4.33}$	12.2%
Cryogenic Fluids	$Nu = 4.82\ \Pi_1^{0.624}\ \Pi_2^{-0.329}\ \Pi_3^{0.374}\ \Pi_5^{0.257}\ \Pi_6^{0.117}$	14.3%
Refrigerants	$Nu = 207\ \Pi_1^{0.745}\ \Pi_5^{0.581}\ \Pi_7^{0.553}$	10.6%
Overall	$Nu = 0.23\ \Pi_1^{0.674}\ \Pi_2^{-0.371}\ \Pi_3^{-1.73}\ \Pi_5^{0.297}\ \Pi_8^{0.35}$	22.3%

where

$$Nu = \frac{q\,d}{k_l \Delta T_w} \qquad \Pi_1 = \frac{q\,d}{k_l T_s} \qquad \Pi_2 = \frac{\Delta h_v d^2}{\alpha_l^2}$$

$$\Pi_3 = \frac{C_{p_l} T_s d^2}{\alpha_l^2} \qquad \Pi_4 = \frac{\rho_l - \rho_v}{\rho_l} \qquad \Pi_5 = \frac{\rho_v}{\rho_l}$$

$$\Pi_6 = \frac{k_h \rho_h C_{p_h}}{k_l \rho_l C_{p_l}} \qquad \Pi_7 = \frac{\mu_l C_{p_l}}{k_l} \qquad \Pi_8 = \frac{\alpha_l^2 \rho_l}{\sigma d}$$

A lack of understanding of transition boiling precludes the development of an adequate model at this time. Typically, a log-log plot of transition boiling heat flux versus wall superheat is adequately represented by a straight line connecting the points of maximum and minimum heat fluxes [16]. Berenson correlated the data he generated in the transition regime with the following expression [50]:

$$\frac{q}{q_{crit}} = \left(\frac{T_s - T_{sat}}{T_{crit} - T_{sat}}\right)^{-1.25} \qquad (9)$$

Another approach modeled transition boiling as a periodic series of surface quenches resulting from the local oscillation between unstable states of nucleate and film boiling phenomena [51]. The liquid that periodically rushes to the heater surface was modeled as an infinite slab exposed to a step increase in temperature. This simplistic model adequately correlated Berenson's heat flux data, but has received little recognition in the boiling literature.

The point of minimum heat flux occurs when the minimum rate of vapor generation to support a stable film over the heater surface is achieved. Because the interface of the wave is influenced by Taylor hydrodynamic instability phenomena, most of the correlations are developed from Taylor instability theory. Zuber [48] developed a correlation for the minimum heat flux on a horizontal flat plate by neglecting Helmholtz instability phenomena, which essentially treated the relative velocity for destabilization of the vapor/liquid interface as negligible in comparison to the stabilizing surface tension forces. Substituting the expression for critical interfacial wavelength and corresponding frequency into the energy balance for vapor bubbles leaving the interface, the correlation takes the form

$$\frac{q_{min}}{A} = \frac{\pi}{24} \Delta h_v \rho_v \sqrt[4]{\frac{\sigma g(\rho_l - \rho_v)}{(\rho_l + \rho_v)^2}} \quad . \tag{10}$$

Because of the uncertainty in the minimum wave frequency, experimental data were used to correct the leading constant to a value of 0.09, which resulted in an accuracy of ± 1% for some organic liquids [30]. While accurate at atmospheric and sub-atmospheric pressures, the correlations based on Taylor instabilities highly overestimate the minimum heat flux as pressure is increased up to 10 MPa [37,52,53].

In the film boiling regime, the heater is covered with a stable vapor film, and vaporization occurs at the nodes of the vapor/liquid interfacial wave. Because bubble spacing is controlled by hydrodynamics, some of the correlations are based on Taylor instability theory. Because no

contact between the liquid and the surface occurs, the nuisance variable of surface nucleation characteristics that hampers modeling of nucleate boiling phenomena is avoided in correlating film boiling data. Bromley developed the first film boiling correlation by considering the conduction and radiation heat transfer across the vapor film blanketing the surface of a horizontal cylinder [54]. The film conduction heat transfer coefficient is determined by neglecting radiation effects and by incorporating proper assumptions into the differential equation for heat conduction from a horizontal cylinder:

$$h_{c,\,cond} = 0.62 \left[\frac{g \Delta h_v' C_{p_v} k_v^2 \rho_v (\rho_l - \rho_v)}{d_h \Delta T_w \left(\frac{C_{p_v} \mu_v}{k_v} \right)} \right]^{0.25} \tag{11}$$

where

$$\Delta h_v' = \Delta h_v + 0.4\, C_{p_v} \Delta T_w \tag{12}$$

The bracketed term represents the product of the vapor Rayleigh number and the ratio of the effective latent heat of vaporization to the sensible heat content of the vapor. The radiative heat transfer coefficient, calculated for parallel flat plates, was then combined with the conductive heat transfer coefficient in proportion to the relative contributions of the two heat transfer modes to yield a film boiling heat transfer coefficient that agreed well with experimental observations.

Determination of the Characteristic Boiling Curve

Typically, data from boiling studies are plotted on log-log plots of heat flux versus wall superheat, as illustrated in Figure 9. However, determination of the characteristic boiling curve is not a straightforward task. Either steady-state or transient boiling experiments using wall superheat or heat flux as the independent variable can be performed to determine the curve. Steady-state experiments allow the boiling process to stabilize at one point prior to moving to another point

on the curve. Transient experiments involve quenching a hot surface with liquid while recording the behavior of the temperature at a known location within the heater as it cools down.

Steady-State Boiling Curves

Steady-state boiling curves can be determined by either controlling the heat flux (such as boiling on an electrically heated wire), or by controlling the surface temperature (such as boiling on a tube with internal steam condensation, or other means of indirect heating). Obviously, heat-flux-controlled experiments are easier to perform, but the boiling process does not progress smoothly along the boiling curve. Starting with a saturated system, increases in heat flux result in nucleate boiling. At the critical heat flux, attempts to increase the heat flux further will cause the boiling process to undergo a rapid iso-heat-flux shift to the film boiling regime (dotted line A-B in Figure 9). Because the tremendous surface temperature increase that accompanies the move to the film regime can melt a heating wire, the critical heat flux is frequently referred to as the burnout point, or the boiling crisis. After the shift, the boiling process proceeds according to the film boiling curve: increases in heat flux will shift the process to higher wall superheats, and decreases in heat flux will shift the process to lower wall superheats. Attempts to decrease heat flux below the point of minimum heat flux will cause a rapid iso-heat-flux shift to the nucleate boiling regime (dotted line C-D in Figure 9), accompanied by a large decrease in heater surface temperature. After this shift, changes in heat flux will move the process along the nucleate portion of the curve. The transition regime is typically inaccessible with direct heating systems.

Complete steady-state characterization of the boiling curve is usually accomplished with a surface-temperature-controlled experiment through the aid of a process control system. However, the existence of transition points where the slope of the curve changes sign, and the inherent instability of the transition regime, complicate this task tremendously. Process control systems must be equipped with special features that allow sensitivity to slope of the boiling curve in order to successfully access the transition regime. Because this thesis requires determination of boiling curves, some aspects of process control systems for boiling experiments will be discussed.

Prior to discussing process control systems, it is instructive to point out that stable operation within the transition regime is possible without the aid of a process control system as long as Stephan's stability criterion is satisfied [29]. Simply stated, if the thermal conductance of the heater is larger than the magnitude of the slope of the boiling curve in the transition regime, stable operating points can be attained in the transition regime during steady-state boiling experiments. A number of curves obtained for boiling of refrigerants from the surface of a tube heated indirectly with an internal flow of hot fluid were measured without the aid of a process control system [29]. This suggests that a heater can be designed for stable operation within the transition regime if the nature of the characteristic boiling curve is known.

Process Control Systems for Steady-State Boiling Curve Determination

A few process control systems have been designed that allow complete characterization of the boiling curve with steady-state boiling experiments using heater surface temperature as the control variable. Because transition boiling is inherently unstable, positive feedback is needed to transform the unstable process into a stable one. The control system must also be capable of manipulating heat flux in direct proportion to wall superheat in the nucleate and film regimes, while during the transition regime it must be capable of manipulating heat flux in inverse proportion to wall superheat. For most of the developed control systems, specific electronic components have been designed to combat the problem of transition regime instability.

The first reported control system was developed for the geometry of pool boiling on a horizontal wire [55,56]. The main feature of the feedback control system is a comparator bridge circuit designed to sense the heater wire temperature based on the its coefficient of thermal resistance [57]. The four arms of the comparator bridge consist of the wire resistance, a fixed resistance, and the two sides of a potentiometer. The first output signal of the bridge establishes the heater power level, and the second output signal represents the difference between the desired temperature and the actual wire temperature. This output is demodulated, amplified, and fed back negatively through a compensation network to produce the first bridge output signal. First-order

transfer functions are developed from the heat conduction equation for each of the three pool boiling regimes by assuming linear response of the boiling phenomena for small increments in temperature or heat flux [58]. Stable operation in the transition regime is accomplished by adding a compensation function to the system transfer function [55]. This control system has also been extended to flow-boiling processes [59].

A similar concept was used to design a control system for temperature-controlled boiling on a platinum rod [27]. The voltage signals from a resistance bridge are forwarded to an analog computer, which calculates the rod surface temperature and compares it to the setpoint. The offset is forwarded to a power amplifier to manipulate electrical current to the rod. First-order transfer functions are developed for the three regimes.

A control system developed for flow boiling experiments utilizes a proportional controller, which precludes the need for regime transfer functions [60,61]. An inconel tube centered along the axis of a large copper block serves as the flow channel. Two banks of cartridge heaters positioned concentrically within the copper block about the axis of the tube provides the heat. An ON-OFF temperature controller meters electric current to the outer bank of heaters, and a proportional controller meters electric current to the inner bank of heaters. Thermocouple signals of the flow channel wall temperature are fed as input to the controllers. Each steady-state data point is collected by heating the flow section to a temperature well into the film regime prior to introducing liquid flow. This technique is repeated until a full characteristic curve is determined.

Another system uses electronic feedback of the flow section wall temperature to control intensity of the electric heating current [62]. Amplified surface thermocouple signals are compared to the setpoint surface temperature and are filtered prior to input to a power amplifier. The electric current from the power supply is actuated in response to this signal according to the heating cell transfer function. Simplifying the energy conservation equation, a second-order transfer function incorporating the slope of the boiling curve is developed for the flow section. A corrective filter insures stable operation in the transition regime. The time constants of the system transfer

function and gain of the corrective filter are determined iteratively based on the slope of the boiling curve and Stephan's stability criterion.

Obviously, measuring the complete boiling curve using the steady-state approach with heater surface temperature as the control variable is no simple task. Sophisticated process control systems are required to handle the complicated and variable process dynamics associated with pool boiling phenomena. Conversely, transient boiling experiments do not require control systems, as a hot heater is allowed to cool in a pool of liquid at a rate governed only by process dynamics.

Transient Boiling Curves

Boiling curves can also be determined by heating the heater prior to the introduction of liquid. During a quench test, heat addition ceases once liquid is introduced, as the enthalpy of the heater drives the boiling process. Dynamic tests deviate from steady-state tests in that the process commences in the film regime and passes through the transition and nucleate regimes as the heater cools. As illustrated in Figure 18, large amounts of time are spent in the nucleate and film regimes, but the quenching process passes rapidly through the transition regime. Total quenching times of up to 7 hours have been reported for heaters with large thermal storage capabilities [63].

The temperature at a particular point within the heater is monitored during the transient cooling of the heater. The resulting curve (Figure 18) is analyzed to determine the surface temperature and instantaneous heat flux at any point in time. For heaters with Biot numbers ($Bi = h_c L/k$) less than 0.1 [64], a lumped parameter model can be used to determine heat flux [63,65]. For heaters with large Biot numbers, more complicated models based on transient conduction in a finite slab are utilized to calculate heat flux [63,66,67]. The resulting data is used to generate the characteristic boiling curve.

At the expense of more involved data analysis, quenching tests are much easier to perform than steady-state tests. However, if precautions to insure that the quench test is done in a quasi-

Macroscopic Properties of a Porous Medium

The unique internal structure of a porous medium limits the effectiveness of first-principles approaches for studying fluid flow phenomena. Scientists resort to characterizing the pore structure and transport properties of the medium with macroscopic parameters which can be determined experimentally.

Some of the more common macroscopic parameters for describing the structure of a porous medium will be defined here. Porosity describes the fraction of the medium's volume that is occupied by void space. The sum of porosity and solid fraction, therefore, must equal one. All of the void space in the medium may not contribute to transport of a fluid, however, as some void volume may be isolated or non-interconnected. Permeability describes the ability of a medium to conduct flow of a Newtonian fluid, and hence is inversely related to flow resistance. Tortuosity is defined as the path length that a fluid particle will travel in passing through a medium relative to the thickness of the medium, but is typically neglected because the actual path length is very difficult to determine. One final characteristic of the medium is some measure of the average pore diameter, which, for determination, usually requires an assumption of the pore structure. These factors are all related, but except for simple geometric arrangements, can not be modeled or predicted accurately.

Many interesting applications of flow through porous media involve two-phases (such as drying processes), which presents a major complication to the already empirical science of single-phase flow in porous media. The flow networks of the two phases are segregated for the most part, as the wetting phase occupies the narrower pores, and the nonwetting phase occupies the wider pores. The issue of two phases flowing simultaneously introduces additional properties which are of significance to this thesis. First, saturation describes the fraction of available void volume that is occupied by the wetting phase, and typically has a spatially-dependent profile associated with it. Second, the presence of the nonwetting phase flowing in tandem with the wetting phase changes the medium's conductivity to either phase. Hence, the permeability of each phase, as measured in

accordance with Darcy's law under single-phase flow conditions, must be modified with a fractional term called the relative permeability. Typically, the relative permeability of the wetting phase increases with saturation, and that of the nonwetting phase decreases with saturation, in a non-linear fashion.

Pertinent Issues of Fluid Flow

Three issues of porous media flow that are pertinent to this thesis are capillary pressure, Washburn's equation, and Darcy's law. Capillary pressure is a measure of the discontinuity in pressure at the interface between two immiscible fluids, and its magnitude is defined by LaPlace's equation,

$$P_v - P_l = \frac{2\sigma\cos\beta}{r} \quad , \tag{13}$$

where r is the mean radius of curvature of the interface. Since it is related to the curvature of the interface, the capillary pressure within the small pores of a porous medium can be large. A wetting fluid will flow into a nonwetted pore to displace the nonwetting fluid under the influence of capillary pressure. Hence, capillary forces are responsible for absorption of water by a sponge or a sheet of paper.

Whereas the height to which a wetting fluid will rise in a capillary depends largely on the capillary pressure, the rate at which it rises can be modeled simplistically by Washburn's equation:

$$v = \frac{dh}{dt} = \frac{r^2}{8\mu h}\left[\frac{2\sigma\cos\beta}{r} - \rho g h\right] \tag{14}$$

Hence, a wetting fluid will penetrate into capillaries of larger diameter faster than into ones of

smaller diameter. This model is usually considered to be rigorous for the case of quasi-steady-state capillary penetration into a uniform capillary tube or bundle of uniform capillary tubes [72]. It assumes that one end of the capillary is submerged in a pool of fluid with a flat surface; the height, h, defines the height of the meniscus above the surface of the liquid pool. When applying the Washburn equation to fluid penetration into a porous medium, a constant equivalent mean square capillary radius is assumed, which implies a sharp interface between the penetrating wetting phase and the nonwetting phase.

The transport of a fluid through a porous medium under an imposed pressure gradient was first studied by Darcy [75], who investigated the flow of water in sand filters in reference to the fountains of Dijon, France. This work resulted in an empirical expression relating flow rate to the driving force,

$$Q = \frac{KA}{\mu}\frac{\Delta P}{L} \quad . \tag{15}$$

This equation provides the classical definition for permeability as the proportionality constant between the superficial velocity (defined as the total flow rate, Q, divided by the cross-sectional area, A) of a Newtonian fluid and the driving force under viscous flow conditions. Though widely used in porous media studies, Darcy's law is limited in scope to viscous flow regimes, as deviations from linearity are experienced when inertial effects become important. The transition from a viscous to inertial flow regime occurs at a Reynolds number (typically defined in terms of particle diameter) ranging from 0.1 to 75. Though empirical in nature, Darcy's law can be derived from the equation of motion for flow of an incompressible, Newtonian fluid through a porous medium by neglecting the inertial terms [76].

In multiphase flow systems, Darcy's law applies only as long as the relative permeabilities at a fixed saturation are independent of the pressure gradients [72], which is usually the

case. Darcy's law is applied to each phase by multiplying the single-phase permeabilities by the relative permeabilities. The pressures of the wetting and nonwetting phases are assumed to be related at any point in the porous medium by the capillary pressure, and consequently, the two pressure gradients are related by the gradient of the capillary pressure.

First-principles approaches to modeling flow through porous media on a microscopic level are not successful due to an inability to accurately model the pore structure of a medium. Volume-averaging is a useful technique which generates a set of macroscopically-applicable conservation equations by averaging the system properties over an arbitrarily-defined relative elementary volume [77,78]. (This concept is introduced in Appendix I.) Similarly, the difficulty in accounting for the pore structure has led to the development of a group of modeling approaches that express the flow resistance of a porous medium in terms of a friction factor [72,73], typically resulting in an expression describing permeability as a function of porosity and/or particle diameter. First, phenomenalogical models are empirical in nature, and yield correlations for permeability that are based on particle properties and medium packing structure. Second, conduit flow models assume some knowledge of the medium structure. The simplest geometric model (a subset of the conduit models) treats the medium as a bundle of capillary tubes, and the Carmen-Kozeny model is similar, but less restrictive in its assumption of pore structure. Statistical models (another subset of the conduit models) utilize probability laws to represent the pore structure, and hence are typically complicated. Finally, models based on flow around submerged objects are variants, extensions, or generalizations of Stokes's law.

The Capillary Pressure Function

The capillary pressure function, represented by the curve of capillary pressure at different levels of saturation, is a source of much information about the medium. The function, illustrated in Figure 19, is determined by displacing one fluid from the medium with another. An imbibition curve is determined by displacing a nonwetting fluid from an initially nonwetted medium with a wetting fluid, and a drainage curve is determined by displacing a wetting fluid from an initially

wetted medium with a nonwetting fluid. The capillary pressure function displays hysterisis, as the imbibition and drainage curves do not coincide for a given medium. In determining either curve, the final equilibrium state will involve a mixture of the two fluids in the medium. For the drainage curve, the final value of saturation of the wetting phase is termed the irreducible saturation (S_{wo}), while for the imbibition curve, the final value of saturation of the nonwetting phase is termed the residual saturation (S_{nwo}). In measuring the drainage curve, a minimum pressure, termed the threshold pressure, must be exceeded in order to displace wetting fluid from the medium.

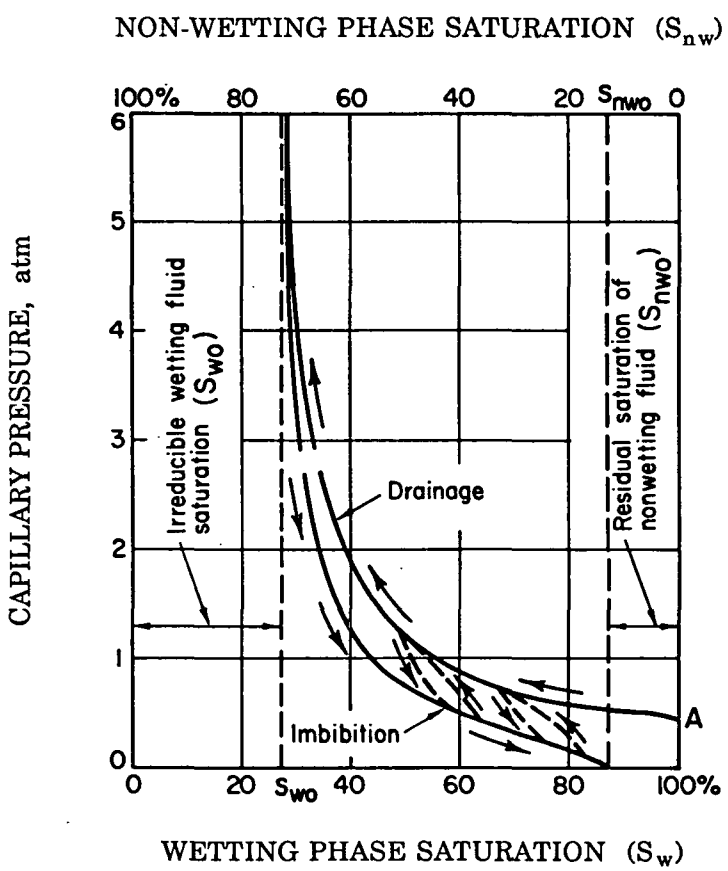

Figure 19. The capillary pressure function for a hypothetical porous medium illustrating hysteresis between the imbibition and drainage curves. (Reprinted from reference 70 with permission of the author)

Several empirical expressions are available in the literature which attempt to relate the

hydrothermal systems.

Many studies in the generic area of boiling in porous media actually address the convective patterns within the porous bed induced by phase change, while fewer studies have addressed the heat transfer and phase change phenomena occurring at the heater surface. Accordingly, the following discussion will be divided into two sections. First, a qualitative discussion of two-phase flow phenomena in porous media will be presented, followed by a discussion of models describing the heat transfer in the two-phase region. Second, studies that investigate the surface heat transfer phenomena associated with boiling in the presence of porous media will be discussed.

Phase Change and Two-Phase Convection in Porous Media

In this section, flow phenomena in the two-phase region during low-heat-flux phase change will be discussed. Typically, the studies addressing two-phase flow phenomena resulting from boiling, or phase change, in porous media involve heat fluxes less than 5 W/cm^2. At low heat fluxes, phase change at the heater surface probably occurs as a very low-intensity boiling process, which is necessary to generate a somewhat quiescent, rather than chaotic, flow of the vapor and water phase. Reference 80 presents a comprehensive review of phase change and two-phase flow phenomena in porous media.

A number of studies have investigated two-phase flow phenomena during boiling in porous media at low heat fluxes with heat application from below [81-87]. The porous beds are typically composed of glass beads or silica sand with average diameters ranging from 0.1 to 1.1 mm, have permeabilities ranging from 1 x 10^{-11} to 140 x 10^{-11} m^2 and porosities ranging from 0.33 to 0.42, and are from 10 to 20 cm in height. Despite the differences between the bed properties, certain phenomena are consistent among all of the studies. Starting from a cold, quiescent state, heat is conducted through the liquid-saturated porous bed to create a linear temperature profile. Natural convection in the liquid-saturated region occurs only if the critical single-phase Rayleigh number

(defined in Equation 17) is exceeded:

$$Ra = \frac{gHK\gamma_l(T_{bot} - T_{top})}{\upsilon_l\left(\frac{k_{eff}}{\rho_l C_{p_l}}\right)} \quad , \qquad (17)$$

where T_{bot} is the temperature at the bottom of the bed, T_{top} is the temperature at the top of the bed, and k_{eff} is an effective thermal conductivity based on a parallel model of the liquid and solid phases of the media [a]. In the majority of the studies where the Rayleigh number exceeded the critical value, the natural convection cells that develop transport hot liquid up away from the surface and cold liquid down to the surface. This flow pattern transforms the linear temperature profile into an S-shaped profile, as illustrated in Figure 20.

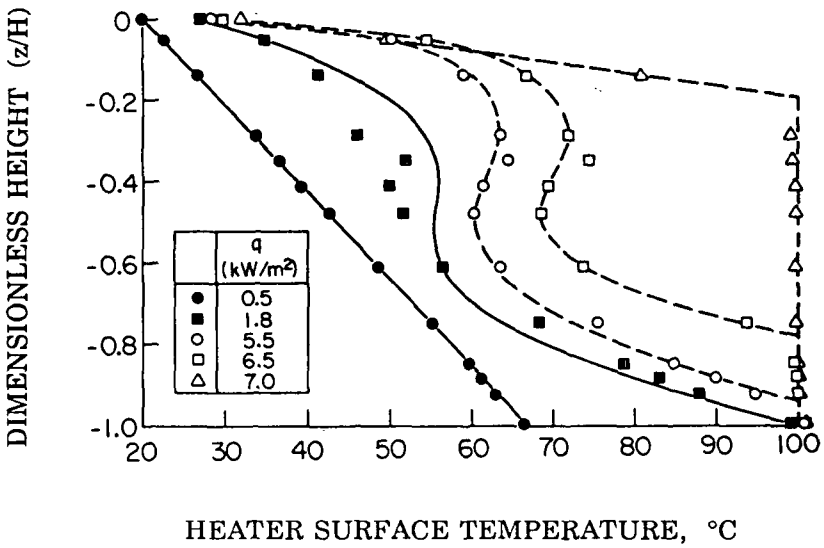

Figure 20. Axial temperature profiles in a liquid-saturated porous medium resulting from thermally-induced convection. (Reprinted from reference 86 with permission of Pergamon Press plc. and the principal author)

[a] This critical value of the single-phase Rayleigh number is 27.1 for a permeable upper boundary and an isothermal lower boundary [80]. However, if the permeability of the bed is sufficiently low, no natural convection will occur below the critical value [85].

After the temperature of the liquid near the heaters reaches 100°C, boiling commences. The superheat at this point is typically less than 1°C [86], which is much lower than that for the onset of nucleation during pool boiling. The vapor rises due to buoyant forces and a vapor pressure gradient, and liquid is pulled down to the heater surface by capillary forces and gravity. This two-phase zone that develops is very nearly isothermal, and its height is directly proportional to the heat flux, as illustrated in Figure 20. Heat transfer that occurs with the counterpercolation of the vapor and water phases is best described as an evaporation/convection/condensation (ECC) mechanism. As the vapor convects to the top surface of the two-phase zone, it condenses and releases its latent heat to the overlying liquid-saturated zone. The enthalpy of the cooler liquid pulled down to the heater surface increases as it undergoes phase change. In this respect, this heat transfer mechanism is very similar to the heat pipe effect.

Initial vapor generation at the onset of phase change results in the formation of local two-phase fingers extending into the porous bed [82]. The fingers spread both laterally and vertically until they coalesce with adjacent ones. The shape of this continuous two-phase zone is initially influenced by the flow patterns of the natural convection cells, but at higher heat fluxes, a horizontal interface between the two-phase zone and the overlying liquid-saturated region develops. At very high heat fluxes, a vapor layer can form below the two-phase zone if the heat flux exceeds a system-dependent critical value [87]. Figure 21 illustrates the stratification of the three zones in the porous medium.

With heat application from above, Udell observed that the porous bed segregated into three zones [88]. The top zone at the heater surface was filled with vapor, and heat transfer through this zone was dominated by conduction, evident as a linear temperature gradient. Beneath this vapor zone was a counterpercolating, nearly-isothermal two-phase zone, which overlaid a water-saturated zone. In the two-phase zone, vapor generated at the interface with the vapor zone convected downward under the influence of a slight pressure gradient, and liquid flowed up to the interface under the influence of capillary forces. To maintain the three zones in an equilibrium,

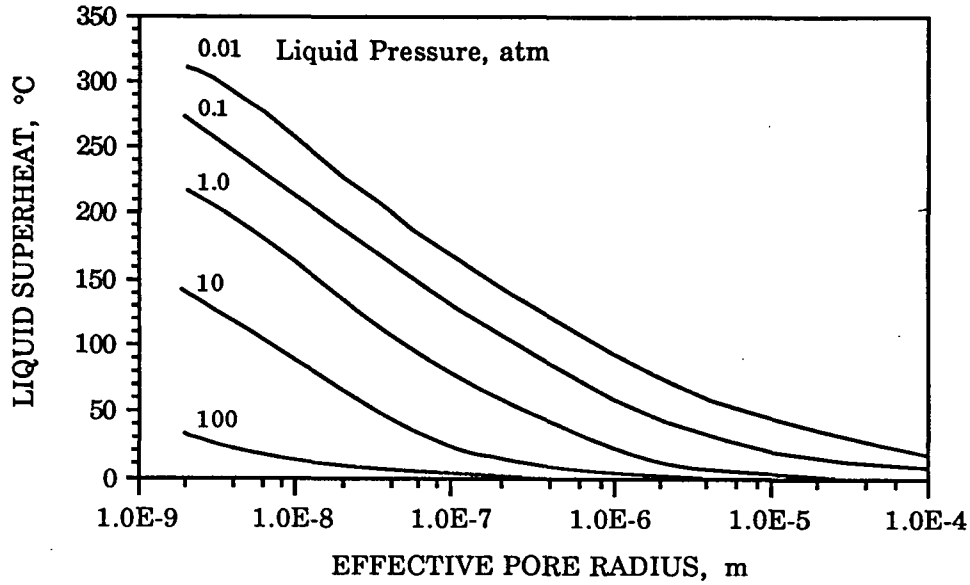

Figure 22. Degree of liquid superheat in the pores of á porous medium as a function of liquid pressure. (Data taken from reference 89 with permission of the Society of Petroleum Engineers)

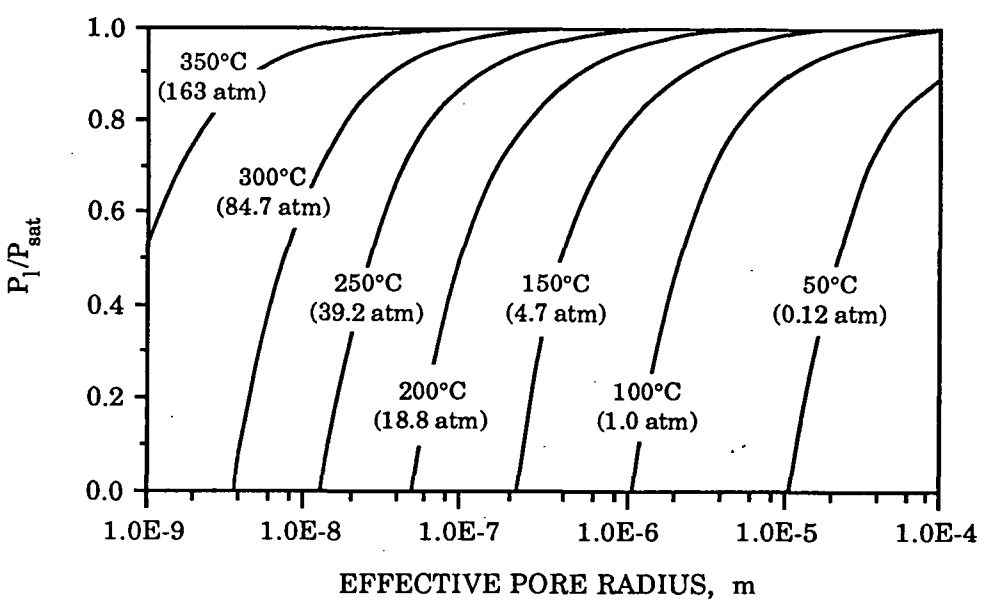

Figure 23. Liquid pressure lowering in the pores of a porous medium as a function of saturation temperature. (Data taken from reference 89 with permission of the Society of Petroleum Engineers)

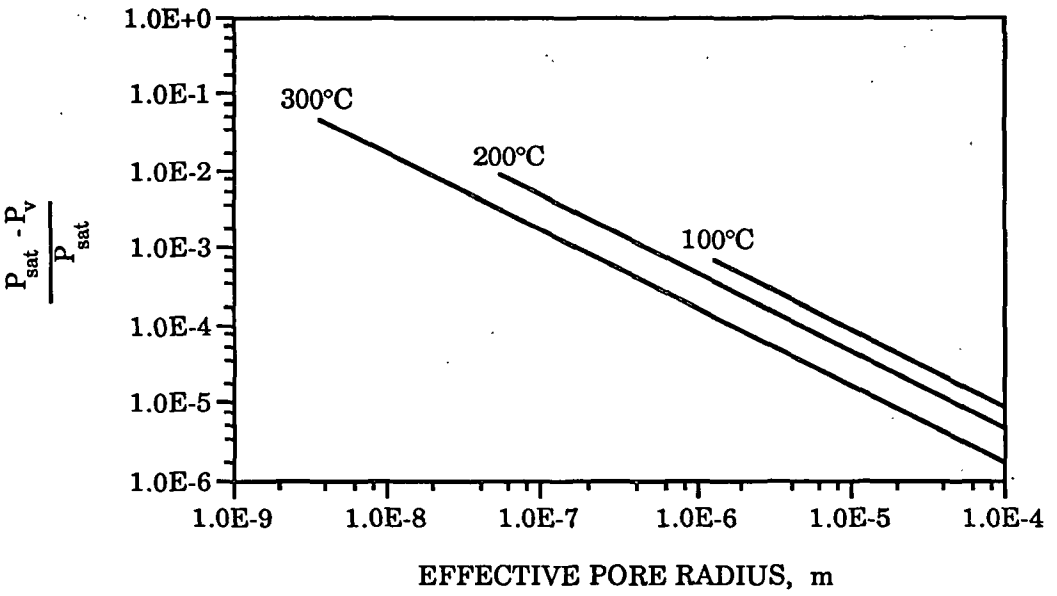

Figure 24. Vapor pressure lowering in the pores of a porous medium as a function of temperature. (Data taken from reference 89 with permission of the Society of Petroleum Engineers)

The volume-averaged equations for mass, momentum, and energy conservation are simplified with some of the following assumptions. All of the models neglect inertial effects to reduce the equation of motion for both phases to Darcy's law. The relative permeabilities in the Darcy expressions are commonly modeled as a parallel arrangement of the two phases (i.e. the relative permeability of liquid is equal to the saturation, and the relative permeability of vapor is equal to the difference between 1 and the saturation), although the cubic of these expressions are also used [87,88]. As a further simplification, some of the models neglect capillary pressure [80-83]. The models that retain capillary pressure utilize the Leverett function to express it as a function of saturation. The energy conservation equation is typically reduced to simply a latent heat term accounting for phase change by neglecting spatial temperature gradients, which is justified by the isothermal nature of this zone.

There are a number of varied objectives of the two-phase zone heat transfer models. One model develops a complicated expression for saturation as a function of heat flux [81,82], which can be simplified to the following form for saturations not too close to zero:

$$S = 1 - \frac{q\mu_v}{\Delta h_v K \rho_v g (\rho_l - \rho_v)} \quad . \tag{18}$$

Another study derives the second term on the right hand side of Equation 18 as a non-dimensional heat flux by combining the simplified conservation equations [85]. This is alternatively expressed as a function of saturation:

$$\Gamma = \frac{q\mu_v}{\Delta h_v K \rho_v g (\rho_l - \rho_v)} = \frac{S(1-S)}{(1-S)\frac{\upsilon_l}{\upsilon_v} + S} \quad . \tag{19}$$

This relationship, illustrated in Figure 25, exhibits a maximum heat flux at a low level of saturation, which, by differentiating Equation 19, is determined to be

$$q_{max} = \frac{\Delta h_v K g (\rho_l - \rho_v)}{\left(\sqrt{\upsilon_l} + \sqrt{\upsilon_v}\right)^2} \quad . \tag{20}$$

When the heat flux exceeds this maximum, a vapor layer will replace the two-phase zone. A criterion for the development of a two-phase zone is developed by limiting the heat flux to a value less than this maximum through the two-phase zone [85]. The resulting Rayleigh number for the onset of boiling is

$$Ra_b > \frac{\left(1 + \sqrt{\frac{\upsilon_v}{\upsilon_l}}\right)^2 \gamma_l C_{p_l} (T_{sat} - T_{top})^2}{\Delta h_v \left(1 - \frac{\rho_v}{\rho_l}\right)} \quad . \tag{21}$$

This critical Rayleigh number depends only on fluid physical properties and bed temperatures. For water at atmospheric pressure, Ra_b must be greater than 0.3 for a two-phase zone to develop.

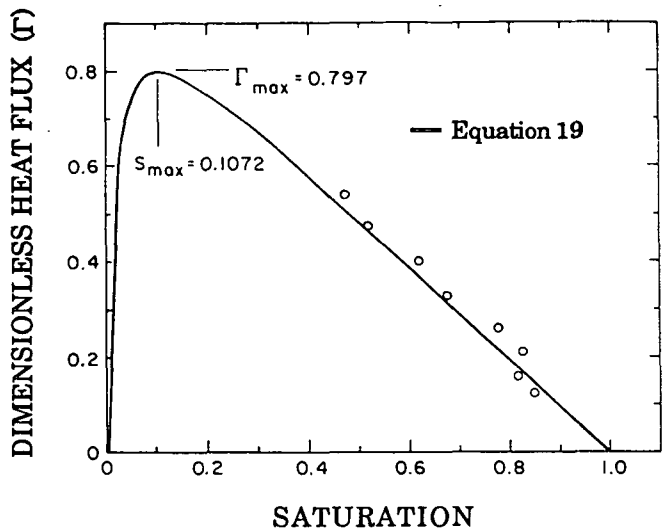

Figure 25. Dimensionless heat flux as a function of saturation for two-phase heat transfer in porous media. (Reprinted from reference 85 with permission of Pergamon Press plc. and the principal author)

One approach taken to derive an expression for height of the two-phase zone involves using Fourier's law of heat conduction to determine the height of the water-saturated zone above the two-phase zone, and then subtracting this height from the overall height of the bed [85]. Another model develops a differential equation expressing two-phase zone height as a function of saturation and heat flux, which is then numerically integrated [87,88].

In all of the above models, media porosity is assumed to be constant. Chuah and Carey extended the Darcy approach with capillary pressure to a medium with nonuniform porosity [90]. In this model, the porosity difference between the top and bottom of the bed diminishes exponentially with height, which is somewhat analogous to the porosity profile that develops in the cellulose fiber sheet during impulse drying. Numerical solutions of the governing equations for a steam/water system indicates that variation of the porosity profile strongly affects the height of the two-phase zone and the temperature difference across the two-phase layer. The exact effects depend on whether the maximum porosity is at the top or bottom of the bed.

Boiling Heat Transfer Phenomena in Porous Media

The effects of porous media on boiling phenomena have been investigated for a number of different media/surface configurations. The changes effected in the characteristic boiling curve appear to depend on some measure of the pore size in the media, which is easily manipulated by adjusting media particle size. Typically, the porous medium is composed of small spheres of various materials, or of fibrous wicking materials, particularly for studies of heat pipes. The discussion below will concentrate on studies that specifically address the mechanism of boiling heat transfer in porous media.

The conceptual understanding of the role of hydrodynamics in classical pool boiling becomes less certain when the boiling occurs in the presence of a porous medium. Because the physical structure of the porous medium interferes with fluid flow, the controlling hydrodynamics probably differ significantly from those of pool boiling . Due to an inability to adequately characterize the unique nature of a porous medium, most studies of the boiling curve use a dimensional analysis approach to quantify the heat flux.

Costello and Redeker investigated the ability of wicking material to continuously supply coolant to a surface in order to sustain boiling [91]. A vertical, electrically-heated stainless steel tube was surrounded by unbonded glass fiber batt in a chamber of water. The total measured heat flux during the boiling experiments was only about 10% of that expected to result from the wicking action of the fibrous batt. This inefficiency was attributed to an inhibition of liquid flow to the heater surface due to vapor blockage of the pores in the wick. Modifying the medium by adding channels through which vapor could easily escape from the surface significantly improved the wicking ability of the batt, and consequently, the heat transfer performance of the system improved significantly. Thus, proper venting of vapor from the boiling surface is necessary to fully utilize capillary wicking as a means to supply coolant to a boiling surface.

Using a vertically-oriented boiling tube, Baum and Greaney investigated the effects of

evaporator tube particulate accumulations on heat transfer [92]. The particulate matter was approximated with metal alloy spheres of various compositions that gave average bed pore sizes of 0.02 to 0.40 mm. Boiling tests were performed at pressures between 5.5 and 7.6 MPa and heat fluxes between 9.5 and 47.3 W/cm^2. The temperature profile of the tube wall strongly suggests that the lower portion of the wall is actively engaged in nucleate boiling, while a stable vapor film blankets the surface near the top of the tube. This evidence indicates that formation of a vapor film perhaps inhibits water flow to the tube surface.

Cornwell, et.al. visualized the behavior of water and vapor on the boiling surface beneath a 6 mm thick layer of porous polyurethane foam [93]. Boiling occurred on a pyrex plate heated by radiation, and the surface phenomena were observed from below. At any point during boiling, the surface is covered by pockets of vapor and water. The heat flux is observed to vary in direct proportion to the fraction of surface area covered with vapor. Photographs of the interface activity reveal large variations in the size of the vapor pockets.

In a study by Abramenko, et.al., convective boiling on a surface coated with sintered bronze exhibited all three pool boiling regimes, but the location and magnitude of the transition points differed from those in pool boiling [94]. The porous layer had an average pore size of 0.12 mm, and its thickness was varied from 0.85 to 4 mm. A counterpercolation of water and vapor is surmised, with vapor occupying the larger pores and the capillarity of the smaller pores wicking liquid to the heater surface. As heat flux increases, an increasing number of pores are filled by vapor until excessive rates of vapor generation starve the surface of water, which defines the point of maximum heat flux. Increasing surface temperature in the transition regime decreases the contact angle of the fluid. The resulting decrease in the bubble diameter to a level equal to the pore size of the layer improves vapor extraction. Consequently, some pores resume wicking water to the surface, and heat flux increases again. For the range of porous layer thicknesses, the maximum heat flux ranged from 7 to 11 W/cm^2 at temperatures of 22 to 30°C, and the minimum heat flux ranged from 5 to 10 W/cm^2 at surface temperatures of 40 to 60 °C. The effect of the porous layer on

the boiling phenomena is obviously dramatic, as the values for the two transition points are much lower than those for pool boiling.

Rannenberg and Beer studied the boiling of refrigerants in layered wire mesh structures up to the point of maximum heat flux [95]. The stainless steel or phosphor bronze wire mesh, with mesh sizes of 38 mesh to 198 mesh, was placed over the heater surface up to 9 layers deep. Maximum heat fluxes of about 70 W/cm^2 occur at wall superheats of about 20°C. Regardless of mesh size, heat transfer at wall superheats below 15°C is enhanced compared to pool boiling data, but the degree of enhancement does not appear to depend on the number of mesh layers. However, layers of fine mesh structures appear to inhibit bubble formation, which increases the wall superheat requirements for incipience of boiling. By non-dimensionalizing the conservation equations for this system, the resulting similarity variables were used to formulate the following correlation:

$$\frac{h_c D_H}{k_l} = 3.8\left(\left[\frac{q D_H}{\Delta h_v \mu_l \varepsilon}\right]\left[\frac{C_{p_l} \mu_l}{k_l}\right]\right)^{0.59}\left(\frac{\varepsilon D_H^2}{K}\right)^{0.16}\left(\frac{k_{eff}}{k_l}\right)^{0.28} ¥^{-1.0} \qquad (22)$$

where the hydraulic diameter of the structure is

$$D_H = d\left(\frac{\varepsilon}{1-\varepsilon}\right) . \qquad (23)$$

The first square-bracketed term in Equation 22 is the Reynolds number, normalized to a characteristic velocity defined as the evaporation rate divided by the medium porosity. The second term on the right-hand side is a product of the Reynolds and Euler numbers, and represents a collection of the important bed properties. The effective thermal conductivity includes only the liquid and solid conductivities apportioned according to porosity in a complicated manner, and the last term (¥) is a geometrical shape factor determined as the ratio of the thickness of one wire mesh to the mesh aperture. The correlation fits the boiling data to within 15%.

To determine the effects of corrosion products or contaminants on saturated pool boiling

heat transfer from a horizontal surface, Chuah and Carey studied boiling in an unconfined layer of small spheres on a chrome-plated copper boiling surface [96]. Both copper and glass spheres with diameters ranging from 0.10 to 0.475 mm were layered at various depths up to 20 mm. The experiments only investigated heat fluxes up to 10 W/cm^2 and wall superheats up to 15°C. The effect of the particles on heat flux depends on the characteristics of the particles: glass beads inhibit pool boiling heat transfer, while copper beads improve it. The improvements in microconvection near the surface once the layer becomes fluidized probably act to increase heat transfer, but this effect appears to be dominated by the thermal conductivity of the bead material, at least in the region of low heat fluxes investigated here. The degree of difference between the pool boiling data and boiling with the bead layer is directly proportional to the diameter of the beads. For depths greater than 5 mm, the depth of the bead layer does not affect the heat transfer.

Fukusako, et.al. studied boiling from a wire embedded in a porous bed composed of glass beads ranging in diameter from 2.0 to 16.3 mm to determine the effects of bead diameter and bed height on heat flux [97]. Wall superheats up to 100°C generated heat fluxes up to 60 W/cm^2 for the beds ranging in porosity from 0.37 to 0.44 and in permeability (determined from the Blake-Kozeny formula) from 0.28×10^{-10} to 40.1×10^{-10} m^2. An interaction between bed height and particle diameter is evident. For bed depths of 5 mm, heat flux in the bed of 2.0 mm diameter beads increases significantly over that for pool boiling, while the 16.3 mm diameter beads have little or no effect on heat flux, as illustrated in Figure 26. However, at bed depths of 60 mm, the presence of the beads actually decreases heat flux significantly in inverse proportion to bead diameter. Because the only force preventing fluidization of the bed is the weight of the particles, the likelihood of fluidization at smaller bed depths probably accounts for some of the dependence of heat flux on bed depth. At large bed depths, the smaller pore sizes associated with the smaller beads in the rigid layer near the surface may restrict escape of vapor and water flow to the surface, whereas fluidization of small beads at lower bed depths may assist heat transfer by increasing microconvection near the surface.

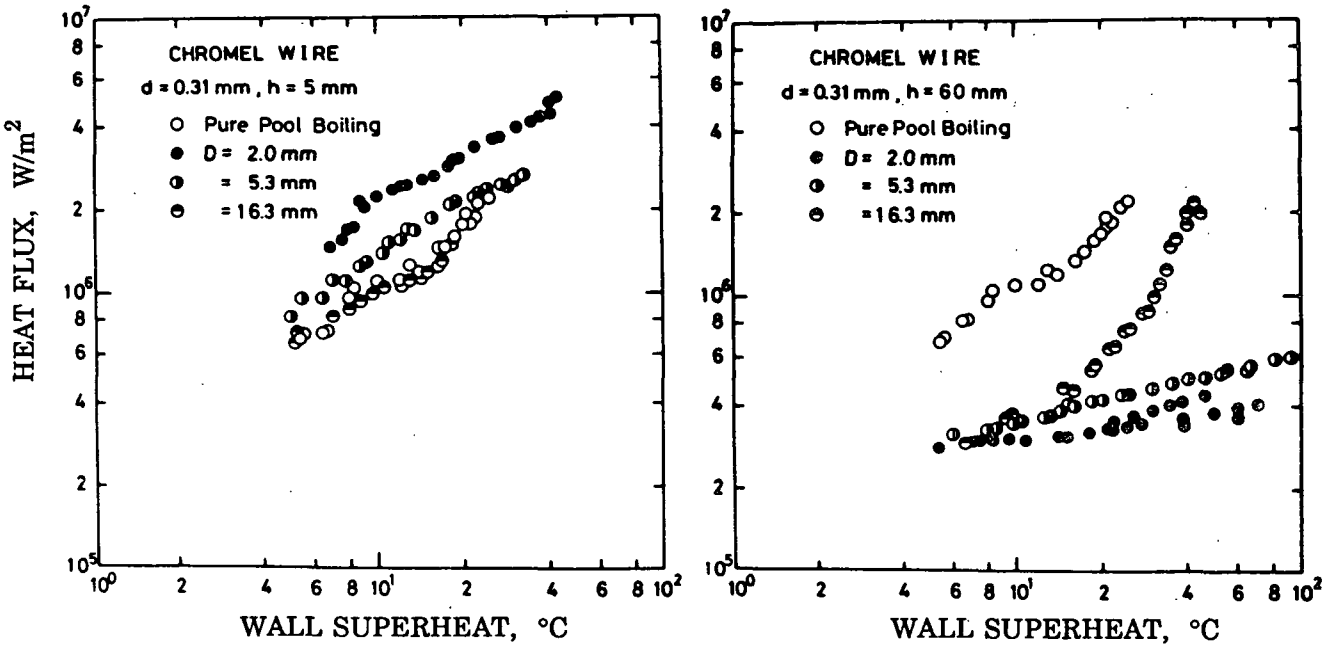

Figure 26. Effect of bead diameter and bed height for boiling from a chromel wire in a porous bed. (Reprinted from reference 97 with permission of the American Society of Mechanical Engineers)

Fukusako's Porous Medium Boiling Study

Fukusako, et.al. modified the previous experiment to investigate boiling in a rigid bed of packed spheres on a flat plate heater [98]. Characteristic boiling curves were determined as a function of bead diameter, bead material, and bed depth. Packed beds composed of glass or steel spheres with diameters ranging from 1.1 to 16.3 mm were formed on a horizontal copper boiling surface to depths ranging from 10 to 300 mm. Bed porosities ranged from 0.39 to 0.50, and bed permeabilities (as determined from the Kozeny-Carman formula) ranged from 1×10^{-11} to 700×10^{-11} m^2. As illustrated in Figure 27, the presence of the porous bed drastically changes the behavior of the boiling curve. The required wall superheat for incipience of boiling is reduced. The degree to which the beds exhibit a nucleate-type regime with a slope similar to that of classical pool boiling depends in a complex manner on the bead diameter. In this regime, the heat flux throughout most of the regime is enhanced compared to pool boiling, which agrees with the observation of Rannenberg and Beer. Deviation from nucleate-type boiling behavior also depends

on the diameter of the beads. For large beads, three regimes of boiling are still evident, but the magnitude of the critical heat flux is reduced. However, for smaller beads, the transition from the traditional nucleate regime to the film regime is characterized only by a change in slope of the boiling curve, not by a change in sign of the slope: a point of critical heat flux and the subsequent transition regime cease to exist. Similar results are found for the steel spheres.

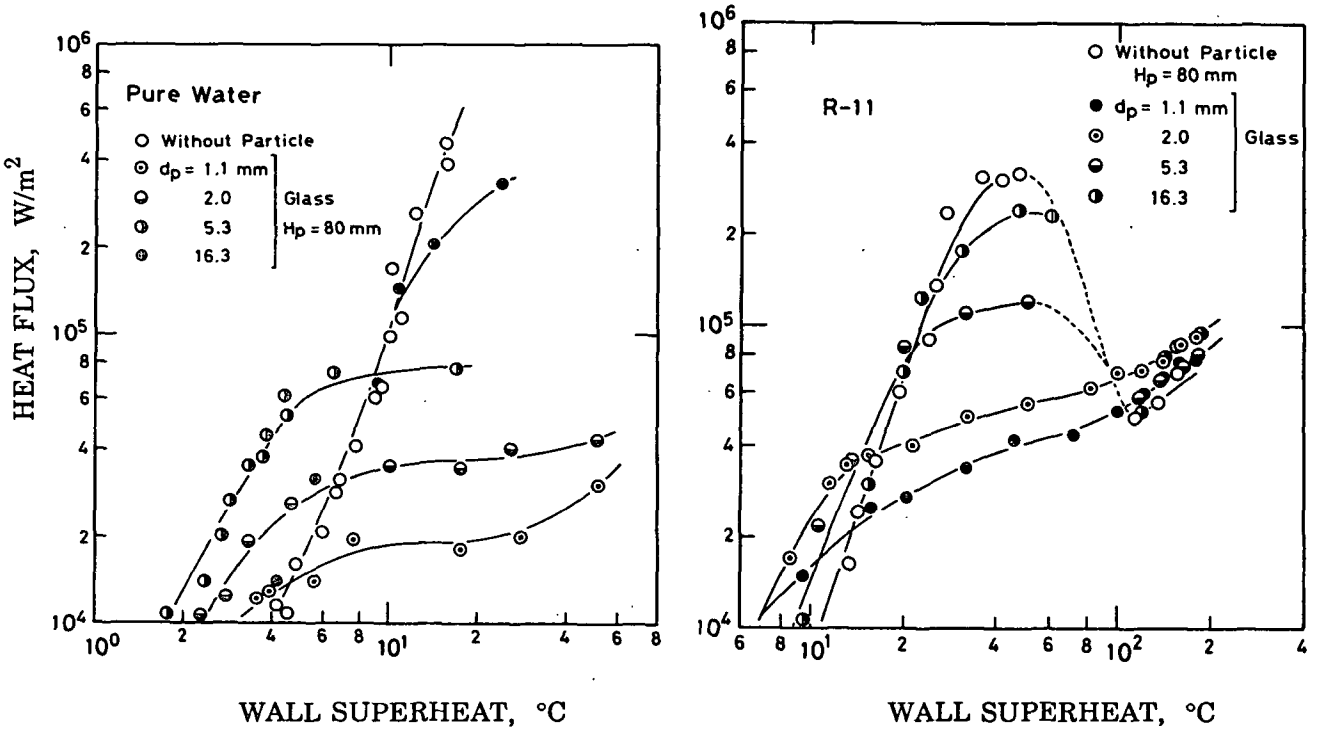

Figure 27. The effect of bead diameter on the boiling curve for a porous medium on a flat plate heater. (Reprinted from reference 99 with permission of the American Society of Mechanical Engineers)

The behavior of the boiling curves indicates a change in the phenomena controlling heat transfer at a bead diameter between 2 and 5 mm. This change is attributed to inhibition of water flow to the surface as increasing surface nucleation generates vapor at a rate large enough to block the small channels in the beds composed of small-diameter spheres. For a given particle diameter, boiling curve behavior is not affected by bed height, which suggests that the effect of the porous bed on boiling phenomena is confined to a layer near the surface. The thermal boundary layer at the heater surface increased with wall superheat to thicknesses of about 20 mm.

Dimensional analysis was used to correlate data in the transition and film boiling regimes. The transition regime correlation applies only to the data for the monotonically increasing boiling curves. The specific heat and thermal conductivity of the bed are modeled as a parallel combination of liquid and solid weighted according to porosity. The following correlation fits the data to ± 30%:

$$\frac{q\,d_p}{k_{l,eff}\,\Delta T_w} = 7.50 \times 10^{-2}\left[d_p\sqrt{\frac{g(\rho_l-\rho_v)}{\sigma}}\right]^{0.9}\left[\frac{C_{p_{L,eff}}\,\Delta T_w}{\Delta h_v}\right]^{-m}\left[\frac{k_{l,eff}}{k_l}\right]^{n} Pr_l^{2.37} \tag{24}$$

where

$$m = 1.30\left[d_p\sqrt{\frac{g(\rho_l-\rho_v)}{\sigma}}\right]^{0.6} Pr_l^{-0.8} \tag{25}$$

and

$$n = -0.59\ Pr_l^{0.3} \quad . \tag{26}$$

The dependent group in Equation 24 is the Nusselt number, the first square-bracketed term is the Bond number, and the second square-bracketed term is the Jakob number.

The film boiling correlation is based on Bromley's correlation for the pool boiling film regime (Equation 11), and applies to all of the film boiling data generated in this study. The specific heat and thermal conductivity of the bed are modeled as a parallel combination of vapor and solid weighted according to porosity. The following correlation fits the data to ± 30%:

$$\frac{q\,d_p}{k_{v,eff}\,\Delta T_w} = 4.10\left[\frac{d_p^3 g\rho_v(\rho_l-\rho_v)}{\mu_v^2}\right]^{0.25}\left[\frac{C_{p_{v,eff}}\,\Delta T_w}{\Delta h_v}\right]^{-0.04}\left[\frac{k_{v,eff}}{k_v}\right]^{-0.95}\left[\frac{d_p}{H}\right]^{0.15} Pr_v^{0.25} \tag{27}$$

where the first square-bracketed group is the Grashof number. For the data sets that do exhibit a critical and minimum heat flux, a correlation for the minimum heat flux fits the data to ± 30%:

$$\frac{q_{min}^2 d_p}{\rho_v \sigma \Delta h_v^2} = 9.21 \times 10^3 \left[d_p \sqrt{\frac{g(\rho_l - \rho_v)}{\sigma}} \right]^{0.65} \left[\frac{k_{v,eff}}{k_v} \right]^{0.1} \left[\frac{\rho_v}{\rho_l} \right]^{0.5} \quad (28)$$

where the dependent group is the Weber number.

SUMMARY OF BOILING RESEARCH

Widely-accepted theories regarding boiling phenomena have been developed into conceptual models that explain the phenomena associated with the various pool boiling regimes. However, little success with first-principles approaches for modeling has been experienced due to nuisance variables, especially for nucleate boiling. Consequently, models are either completely empirical, or are based on fundamental theory and are empirically corrected.

Controlling phenomena for boiling in a porous medium appear to depend on the properties of the medium. For media that do not possess significant capillary forces, the hydrodynamic instability responsible for the critical heat flux in classical pool boiling are suppressed to an extent dependent on pore size, and are inhibited below some critical pore size. Evidence also suggests that though nucleation still occurs, the presence of the bed modifies the surface phenomena. It is interesting, though, that data for beds of differing particle sizes merge to the classical film boiling curve.

Much of the research into boiling in porous media possessing significant capillary forces has focused on understanding the two-phase counterpercolation mechanism for heat transfer within the bed. Some studies have investigated the effects of the media on heat flux for wall superheats representative of the classical nucleate boiling regime, typically for very specific geometries, and found that generally heat flux is lower than what is achieved in classical pool boiling.

Little of the present information provides insight into boiling phenomena that may impact

impulse drying. Available information for boiling in porous media spans only a limited range of surface temperature, most often for media composed of spherical particles. An interesting concept that must be considered is the difference in boiling behavior between a pore structure composed of fibers and one composed of spherical particles. Research is needed to obtain information about the characteristic boiling curve over a broad range of surface temperature for a fibrous medium possessing significant capillary forces.

ANALYSIS OF THE PROBLEM

The difficulty in studying impulse drying heat transfer mechanisms stems from the complicated interaction of phenomena during the very short time frame of the event. Present knowledge indicates that a vapor-phase displacement mechanism drives water from the sheet due to volume expansion upon phase change. Thus, boiling heat transfer and internal sheet thermodynamics must play important roles, but their contributions are intertwined with sheet structural changes resulting from compression that occurs with pressure application. Obviously, the impulse drying event is characterized by the simultaneous occurrence of many phenomena in a short time frame.

The different impulse drying regimes (Figure 2) likely reflect changes in these interactions during the event. The rapid escalation in heat flux suggests that boiling could initiate abruptly and vigorously [b], which probably depends on the availability of water at the hot roll surface. The peak heat flux may signal the end of a saturated sheet surface, and may be defined for a particular sheet pore structure by an optimum combination of roll surface temperature and applied pressure pulse. The subsequent decline in heat flux indicates a transition in the mechanisms that control heat transfer to the sheet. Although it is likely that surface water is quickly depleted, the magnitude of heat flux indicates that boiling is active to some degree throughout practically the entire event.

Internal sheet thermodynamics undoubtedly play a major role in influencing heat transfer to the sheet. However, accurate identification of the thermodynamic state within the sheet is difficult because a detailed knowledge of the sheet pore structure is required, as previously discussed [89]. The dynamic compression-induced change in sheet structure further complicates the role of sheet thermodynamics. Once surface boiling initiates, the magnitude of the vapor pressure

[b] Conduction heat transfer from the hot roll to the moist sheet of paper may also account for this rapid rise in heat flux.

that develops is governed by the backpressure to fluid flow provided by the pore structure of the sheet. Associated with this vapor pressure is an equilibrium temperature that defines the local thermodynamic state in the sheet. However, continued compression of the sheet during the first half of the event, coupled with a changing rate of vapor generation, changes the backpressure posed by the sheet structure as the event progresses. Because these interactions effect a continuous change in vapor pressure, it is difficult to define the thermodynamic state within the sheet at any point during the event.

The contribution of boiling heat transfer is obscured by the dynamic behavior of the heat transfer driving force. Two factors cause the wall superheat to continuously decrease during the impulse drying event. First, the surface temperature of the heated roll decreases as heat is transferred to the sheet. Secondly, the vapor pressure build-up within the sheet increases the local equilibrium temperature as the event proceeds. The continuous decrease in wall superheat through at least the first half of the event represents a decrease in the heat transfer driving force.

Another factor to consider is the availability of liquid water at the hot surface. The rapid increase in heat flux early in the event may indicate that the transition from a subcooled sheet surface to a vigorous boiling process is nearly instantaneous, which may deplete the hot surface of the initially available water. The vapor film that develops probably behaves as a front that pushes liquid water away from the hot surface (although there will be some residual saturation which must evaporate). However, the high heat fluxes throughout the event indicate that boiling is maintained to some degree, probably fueled by some type of resupply mechanism to replenish the plane of evaporation with liquid water. Previously-discussed studies of phase change in porous media report the existence of a two-phase, counterpercolation zone of steam and liquid water, which may occur in impulse drying to supply the liquid water necessary to sustain boiling.

Consideration of these complex interactions illustrates the need to study individual components of the impulse drying event to achieve an understanding of their roles. The dominant mechanism of heat transfer at the sheet/roll interface throughout much of the event has been

assumed to be analogous to the nucleate regime of pool boiling [1]. However, contacting the moist sheet to the surface of the extremely hot roll is somewhat analogous to the Leidenfrost phenomena: a water droplet placed on a very hot surface sizzles due to the instantaneous formation of a vapor film. Similarly, a vapor film is likely to develop instantaneously at the interface of the sheet and the hot surface, indicating that film boiling is also a possible heat transfer mechanism during impulse drying. Research into the boiling phenomena in a fibrous porous medium is needed to resolve these possibilities.

IMPLICATIONS OF PREVIOUS POROUS MEDIA BOILING STUDIES

The previously-discussed studies of boiling in the presence of porous media report conflicting data. Some studies document improvements in heat flux compared to standard pool boiling, while other studies suggest that the porous medium inhibits boiling heat transfer. Although some small portion of the heat transfer discrepancies can be attributed to the thermal conductivity of the particles composing the porous bed, the cause most frequently cited is the propensity of the bed to assist or inhibit vapor flow from the hot surface. This is certainly related to the characteristic pore structure of the bed.

The possibility that classical pool boiling phenomena apply to boiling in a porous medium must also be considered. Classical pool boiling regimes are either controlled by heater surface characteristics or by hydrodynamic instabilities, with transitions between regimes resulting from a shift between controlling mechanisms. The data of Fukusako, et.al. (Figure 27) provide some interesting insights regarding boiling in a porous medium [98]. Three distinct regimes are evident for each size of bed particle. The occurrence of transitions reminiscent of those in classical pool boiling for media composed of "larger" particles suggests that hydrodynamic instabilities influence the boiling activity to some degree. Conversely, the distinct absence of the classical negative-slope transition regime for media composed of "smaller" particles suggests that the hydrodynamic instabilities are suppressed. These observations indicate some critical particle size that dictates a change in controlling phenomena in the transition region.

Regardless of the size of the medium particles, surface nucleation characteristics are expected to be affected little by the presence of a porous bed. However, the interaction between the developing vapor bubbles and the pores of the medium are expected to change the significance of surface nucleation characteristics to heat transfer. Physical constraints may prevent the growth of distinct, spherical bubbles, so it is likely that bubbles will grow into pore openings. The resultant frictional forces acting on the vapor bubble would tend to retard vapor flow away from the surface, thus assisting the growth of a vapor layer at the surface. The extent that this mechanism may operate is likely to be inversely related to the size of the pores, and may explain the decrease in effectiveness of nucleate-type boiling heat transfer as particle diameter decreases, as illustrated in Figure 27.

While the nature of the porous media boiling curve in the nucleate-type region is similar to classical pool boiling, the onset of nucleate boiling occurs at a much lower wall superheat, which also suggests some modification of the role of surface nucleation. During the film regime, the surface nucleation characteristics become unimportant, and the differences in boiling behavior for the beds of different size particles diminish. It appears as if the porous medium does little to inhibit the growth of a vapor layer at the heater surface at higher wall superheats.

Although Fukusako's data indicate that the porous bed affects the extent to which hydrodynamic instabilities influence boiling behavior, an additional factor likely to have major significance to this proposed study was not considered -- the effect of capillary forces. None of the porous beds used in Fukusako's study have pore diameters small enough to possess appreciable capillary forces. To investigate boiling mechanisms that may occur in impulse drying, the effects of capillary forces must be considered by using porous media possessing pores diameters representative of those occurring in paper. Since capillary forces are known to be of prime importance in heat pipe phenomena, one might expect the occurrence of the heat pipe effect during impulse drying, which is likely to have a dramatic effect on boiling phenomena.

DIRECTIVES OF THIS THESIS

This thesis focuses on the impact of fibrous porous media on pool boiling heat transfer, which hopefully will provide insight into the role of boiling heat transfer phenomena in impulse drying. Using incompressible fibers to form the bed eliminates compression-induced complexities of transient thermodynamics. Dimensional analysis is used to identify dimensionless groups of importance, and to develop correlations to mathematically represent the data.

Modeling the dynamic event of boiling during impulse drying with a static experiment of pool boiling in a fibrous bed represents significant contradictions regarding the time scale of each event. Whereas impulse drying involves a wide spectrum of phenomena in a matter of milliseconds, static boiling occurs on a time frame of hours. It is recognized that the static boiling study pursued here can not adequately reproduce the dynamics of impulse drying, but the dynamics of the event are compromised for the purpose of identifying some of the fundamental principles and variables that may control boiling during impulse drying. Additionally, the results of this thesis will contribute to the fundamental understanding of boiling in porous media.

Thesis Goals

The major goal of the thesis is to identify boiling heat transfer mechanisms that control phase-change within fibrous bed. This will be accomplished through a fundamental study of boiling in the presence of a fiber bed aimed at identifying and quantifying important phenomena and variables that occur during boiling in a porous fibrous bed. Identification of controlling variables in the simplified model system will be a major step towards understanding the factors that control boiling heat transfer during an impulse drying event. Completion of the following goals will allow realization of this main objective:

1. to develop the characteristic curves for pool boiling in the presence of beds of incompressible fibers, and
2. to quantify the impact of important parameters on the boiling heat transfer through a

dimensionless correlation.

Characteristic curves for pool boiling in the presence of porous fibrous structures will be determined for different fiber diameters and system pressures. Understanding the impact of a porous medium on boiling phenomena will provide insight into the boiling heat transfer mechanisms that are hypothesized to occur in impulse drying. Dimensionless correlations will quantify the impact of important system parameters on the heat flux during boiling in the presence of the fibrous bed.

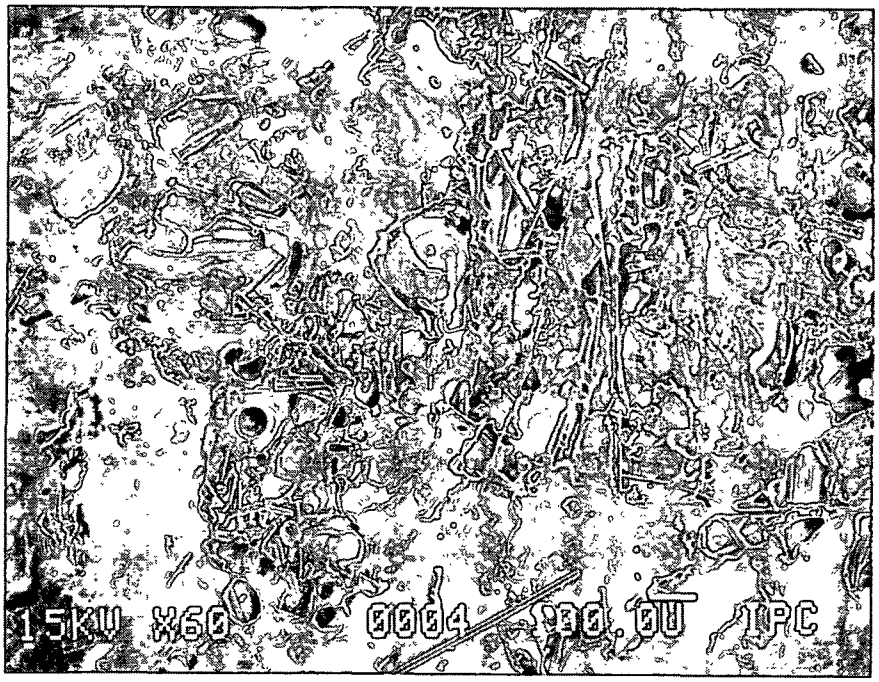

Figure 28. Microphotograph of the "water glass" precipitate that formed on the heater surface during boiling in a bed of glass fibers. Magnification is 60X.

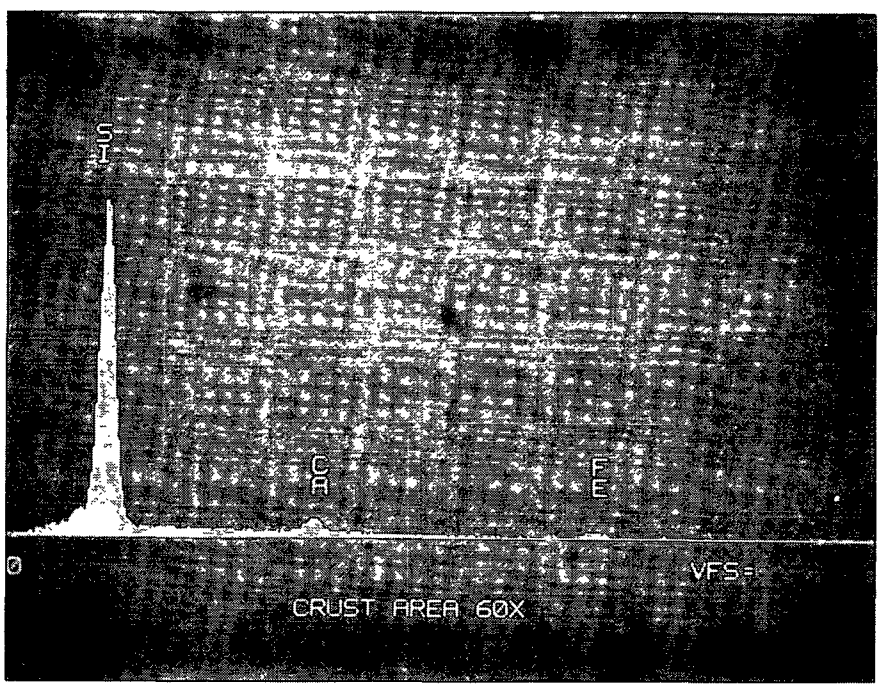

Figure 29. Elemental analysis spectra of the "water glass".

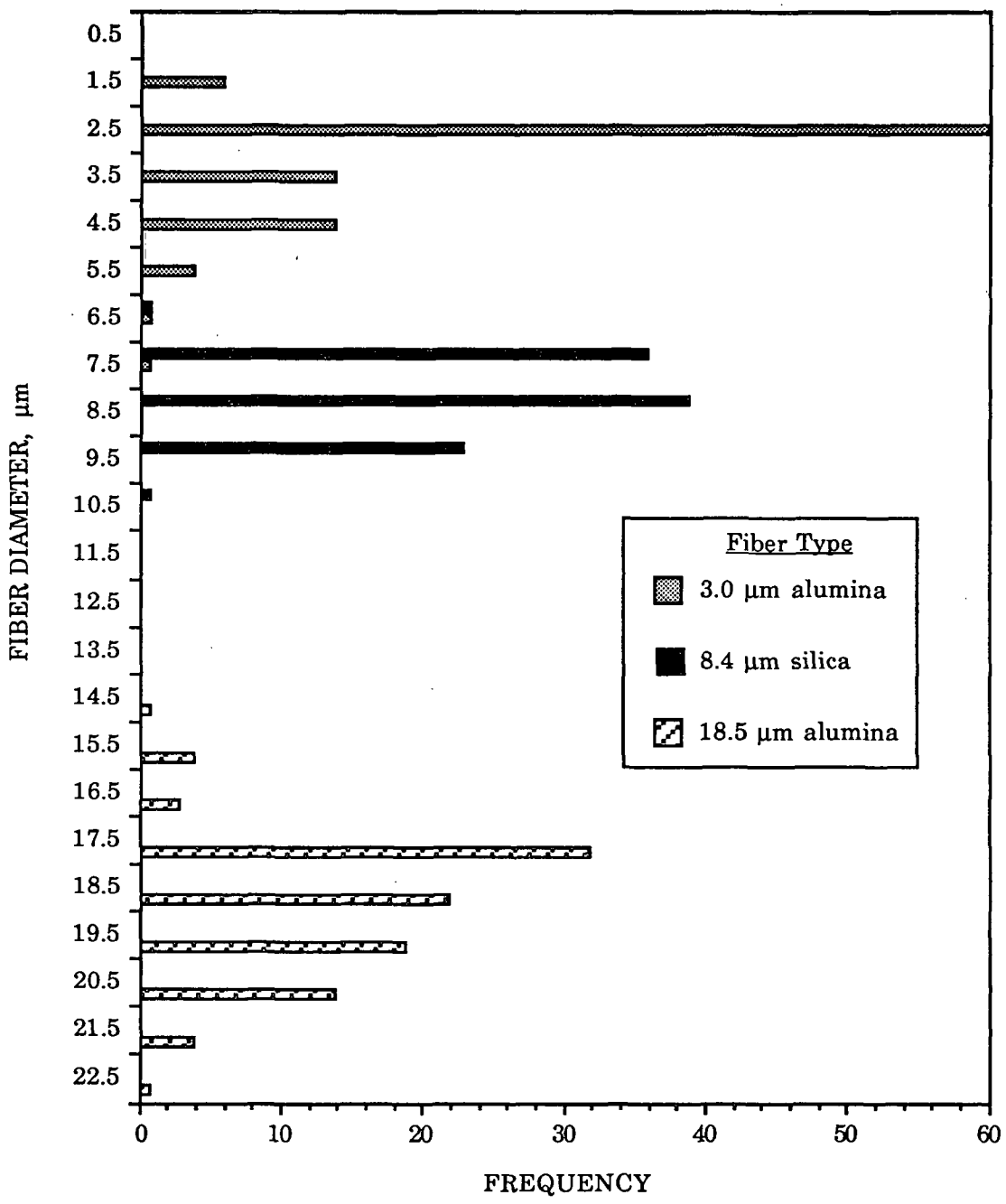

Figure 30. Diameter distributions for the ceramic fibers.

diameters for the glass fibers was 13.1 µm to 37.0 µm, and these are replaced with ceramic fibers with a diameter range of 3.0 µm to 18.5 µm. The ceramic fibers collected here represent the only three diameters commercially available in round cross-sectional form at this time. Pertinent information about these fibers is listed in Table 3, and microphotographs and elemental analysis

spectra are shown in Figures 31, 32 and 33. No precipitation problems have been encountered for these three fiber types during boiling experiments.

Table 3. Thermal and physical properties of the ceramic fibers.

Fiber Type	Chemical Composition	Fiber Diameter (μm) Average	Fiber Diameter (μm) Standard Deviation	Density (g/cm^3)	Thermal Conductivity (W/(cm-°C)) [a]	Heat Capacity (J/(g-°C)) [a]
Alumina	99.5% Al_2O_3	18.5	1.51	3.95	0.292	840
Silica	99.99% SiO_2	8.4	0.75	2.20	0.125	1320
Alumina	96% Al_2O_3 4% SiO_2	3.0	1.09	3.60	0.292	840

a - Reported values are for bulk material.

Special techniques are needed during the bed formation process to insure appropriate fiber length because neither of the alumina fiber lots was supplied cut to length. Additionally, for all of the fibers, adequate dispersion is difficult to achieve in an environment void of high shear. Therefore, a five-liter Waring blender is used to disperse the fibers. Agitation time is controlled to achieve an average fiber length of 1 to 1.5 mm, as illustrated in Figure 34 [d]. The silica fiber, which was delivered in lengths of about 3 to 7 mm, and the 3.0-μm diameter alumina fiber, which was obtained in staple form, are added directly to the blender for agitation. The 18.5-μm diameter alumina fiber, which was delivered in lengths of about one foot, are cut with a paper cutter to a length of about one inch prior to agitation. Each dispersed batch is then added to the slurry (at about 0.1% to 0.2% consistency) in a mixing tank which is located on a mezzanine above the boiling cell apparatus.

The silica fiber and the 18.5-μm diameter alumina fiber are coated with an organic binder during manufacture to improve handling capability for winding operations. This is removed by

[d] Fiber length was measured with the Institute of Paper Chemistry's fiber length recorder, which has a resolution of 0.2 mm. The reported length is an average of 600 individual fibers.

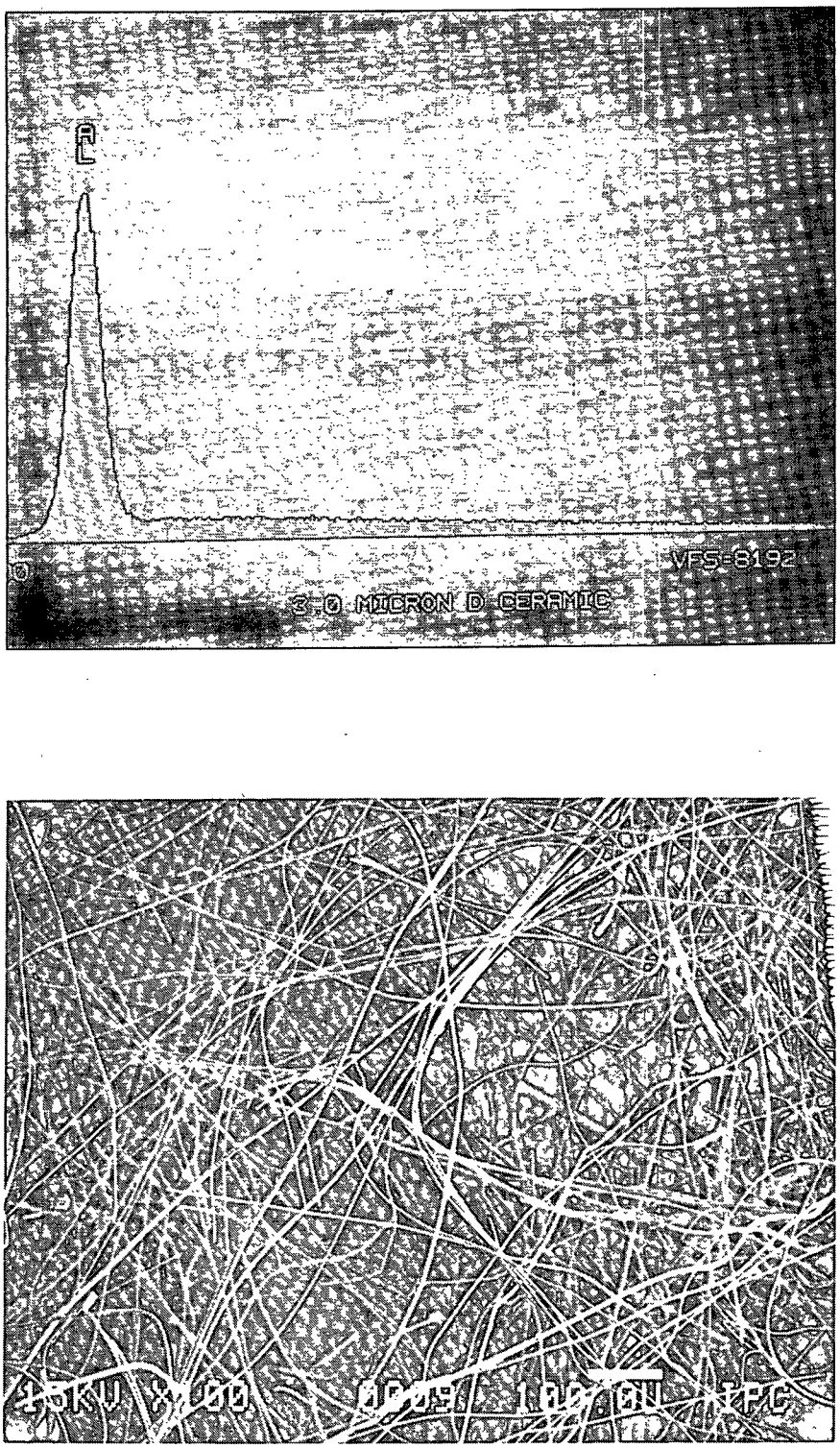

Figure 31. Elemental analysis spectra and microphotograph (magnification is 100X) for the 3.0 μm diameter alumina fiber.

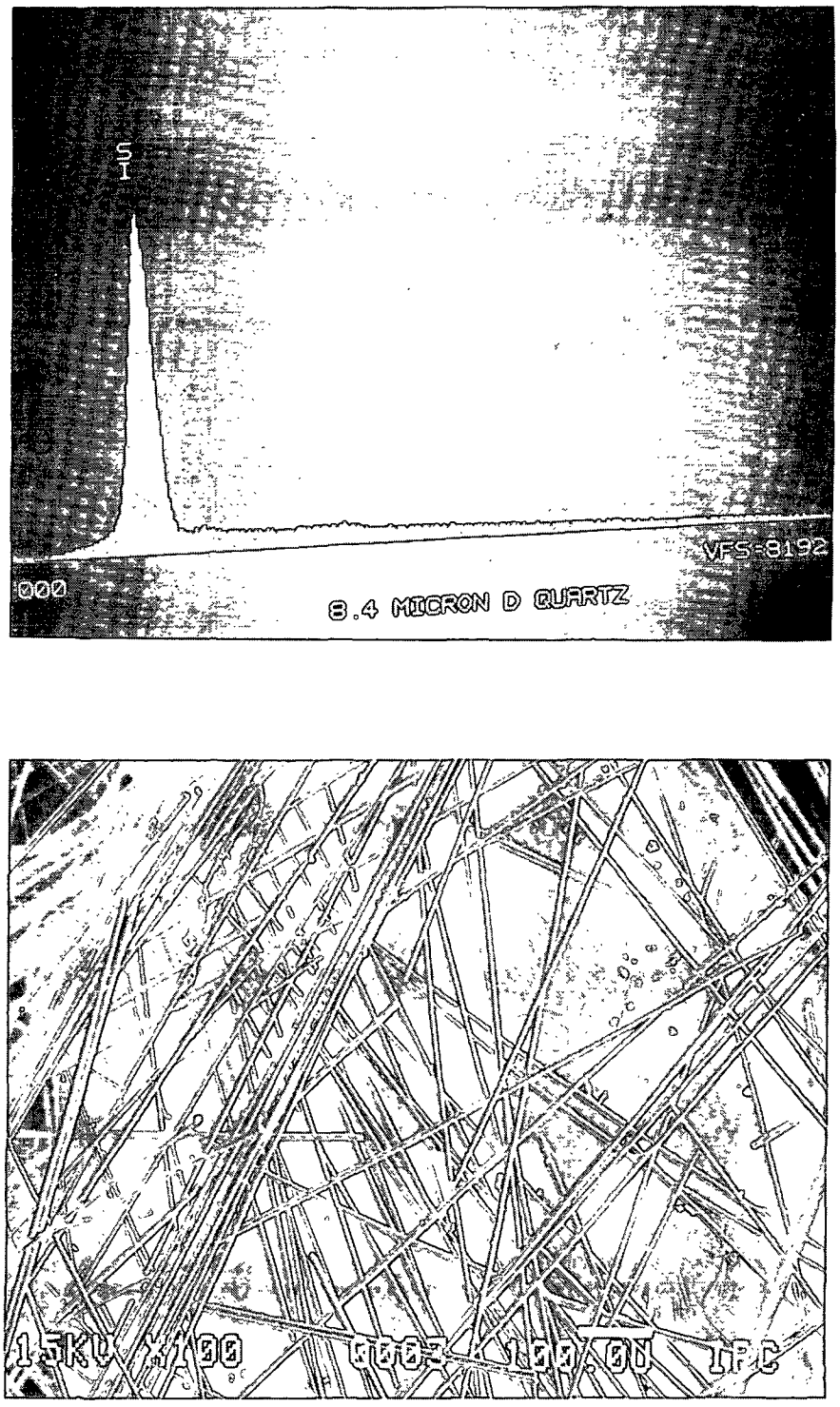

Figure 32. Elemental analysis spectra and microphotograph (magnification is 100X) for the 8.4 μm diameter silica fiber.

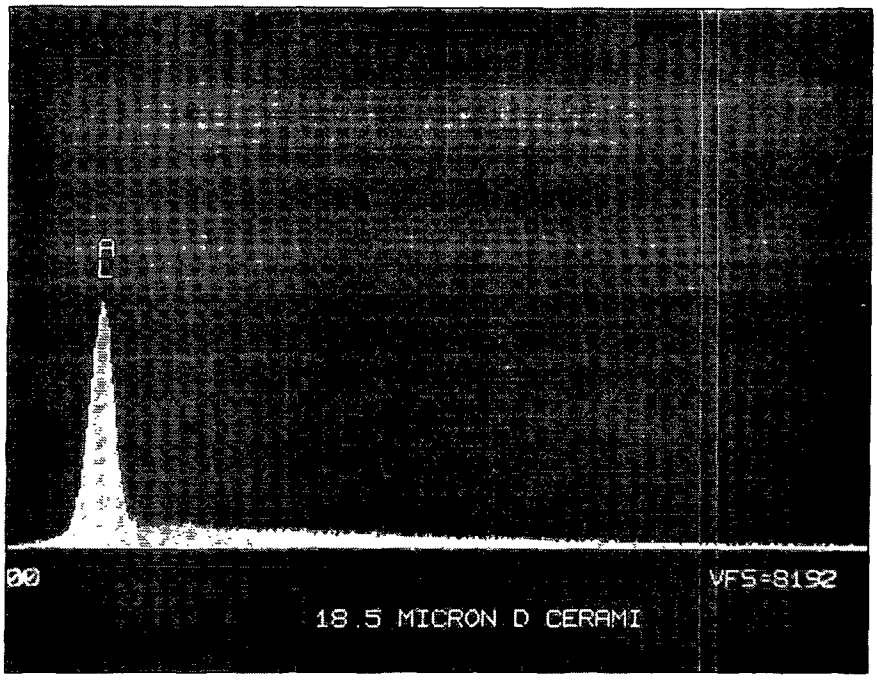

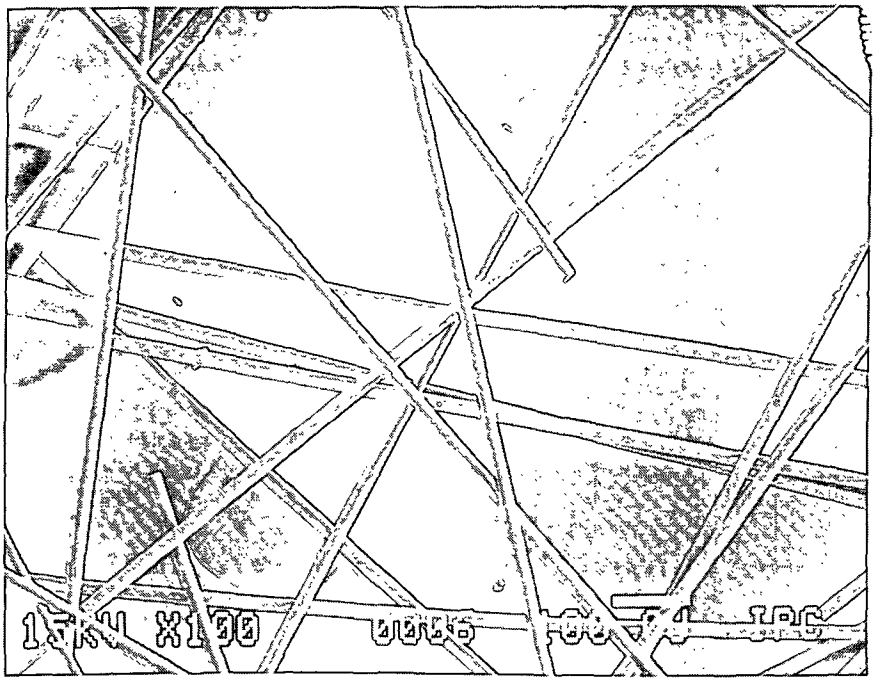

Figure 33. Elemental analysis spectra and microphotograph (magnification is 100X) for the 18.5 μm diameter alumina fiber.

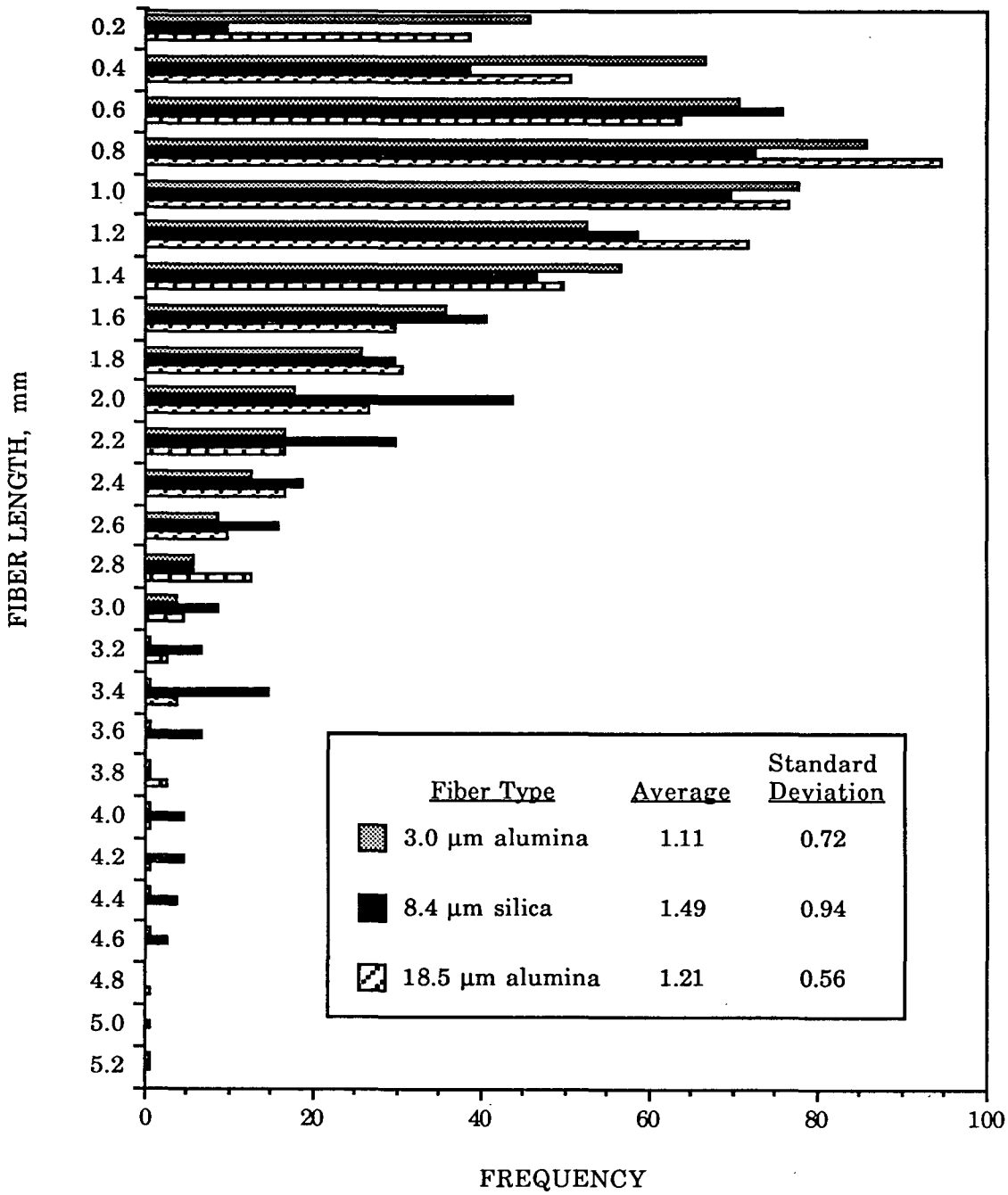

Figure 34. Length distributions for the ceramic fibers after agitation.

heating in a muffle furnace under prescribed conditions. Prior to use, the silica fiber is heated at 540°C for four hours, and the alumina fiber is heated at 700°C for one hour.

THE APPARATUS FOR THE BOILING EXPERIMENTS

The apparatus designed for the boiling experiments is comprised of four systems -- the boiling cell, the heat supply system, the process control system, and the data acquisition system. These systems are discussed in reference to the schematic of the apparatus, illustrated in Figure 35. A photograph of the boiling cell apparatus appears in Figure 36. Details of the fabricated and purchased components of the apparatus are listed in Table 4.

The Boiling Cell

The boiling cell is designed to house the fibrous bed within which boiling and two-phase flow occur. A fused-quartz cylinder with dimensions of 90-mm ID x 5-mm wall thickness x 110-cm length was selected as the raw material for the boiling cell based on the following requirements: 1) the raw material must have a low thermal conductivity to prevent excessive heat conduction from the fiber bed; 2) the material should be transparent to allow visualization of the phenomena; 3) the material must possess sufficient structural integrity at moderate temperatures to allow boiling at pressures on the order of 50 psig, and 4) the material must be machinable. The axial-compression fracture stress of this quartz cylinder was calculated to be 550 psi [100], and during pressurization experiments, a 60 cm length of cylinder axially compressed to a torque of 80 in-lb_f successfully withstood a static pressure of 200 psi. Table 5 lists pertinent physical properties of fused quartz.

The boiling cell is designed to provide the capability to measure temperatures within the fiber bed. A number of half-inch OD quartz nipples are welded onto the quartz cylinder at various locations in the region of the fiber bed. Swagelok® fittings affixed to most of the nipples allow insertion of type-K, ungrounded, open-junction thermocouples into the bed. The two nipples closest to the heating block surface are angled to allow positioning of the thermocouple junction close to the surface. Thermocouples are positioned at distances of approximately 0.2, 1.2, 3.8, 6.4, 9.5, and 13.3 cm from the block surface.

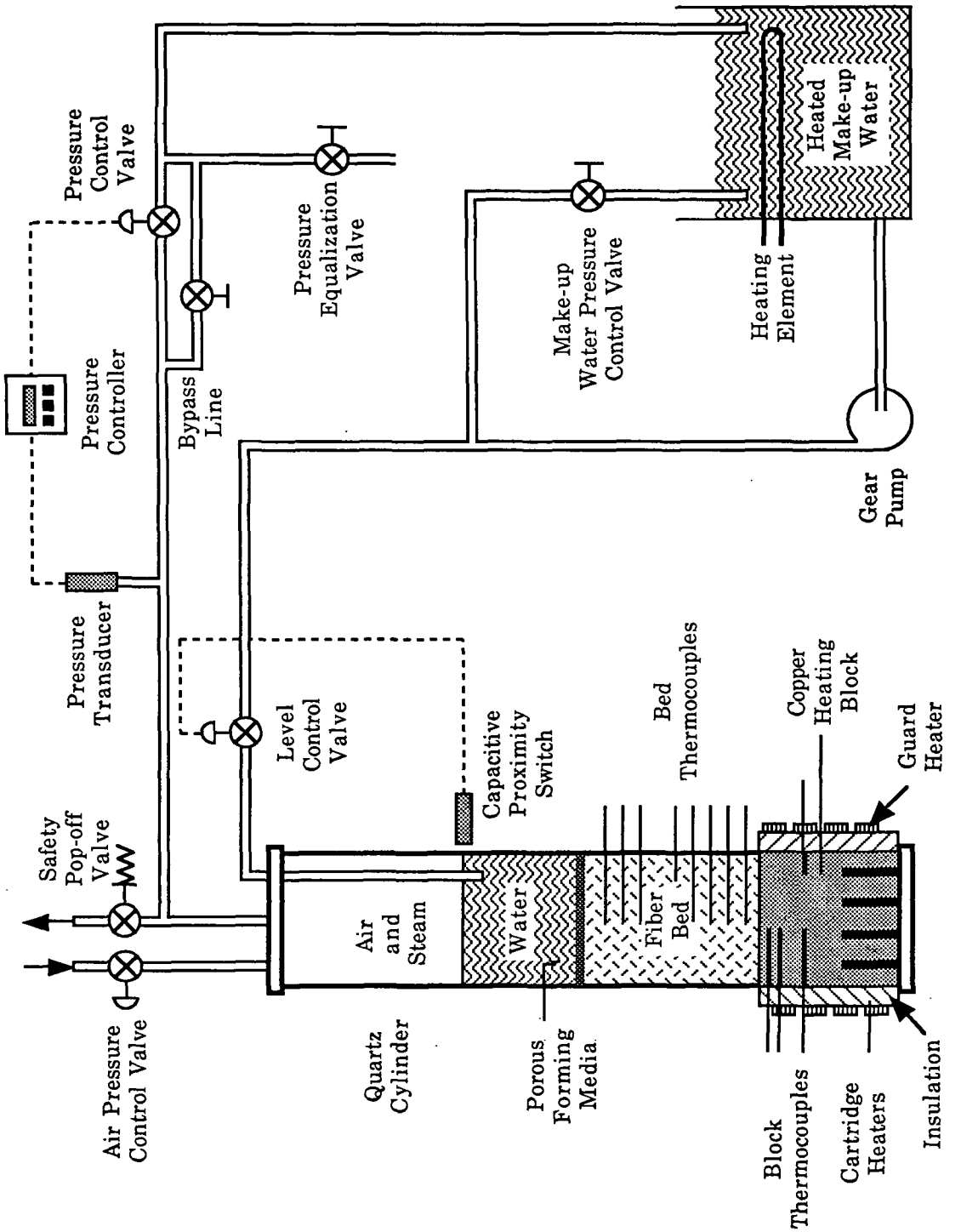

Figure 35. Schematic of the boiling cell apparatus.

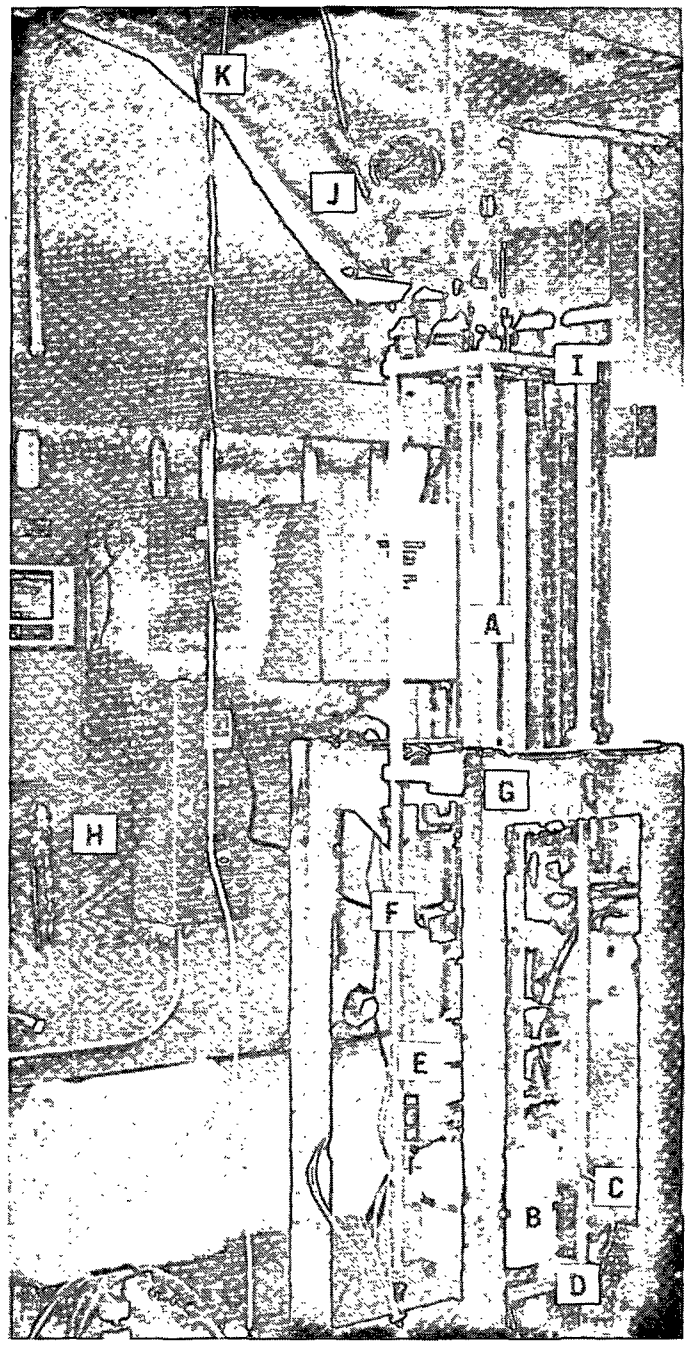

A - quartz boiling cell
B - insulated heating block
C - block thermocouple
D - bottom mounting plate
E - bed thermocouple and Swagelok® fitting
F - 5/8-inch diameter support rod
G - supporting framework
H - electrical supply system panel
I - top mounting plate
J - pressure transducer (to the left of the pressure gage)
K - air supply and vapor vent piping

Figure 36. A photograph of the boiling cell apparatus.

TABLE 4. List of component materials and vendors for the boiling cell apparatus.

APPARATUS COMPONENT	DESCRIPTION OF COMPONENT	VENDOR
BOILING CELL		
Supporting Framework		
Metal pieces	IPC drawing no.'s A490-1-A-3, A490-1-A-6, A490-1-C-7, A490-1-C-10, A490-1-A-10, A490-1-A-11, A490-1-A-12, A490-1-C-13, A490-1-A-14	Fox Valley Tool and Die Kaukauna, WI (414)-766-9455
Ceramic piece	Corning Macor® machinable glass ceramic, per IPC drawing no. A490-1-A-4	Technical Products, Inc. Germantown, WI (414)-255-7355
Wood piece	Rock maple, per IPC drawing no. A490-1-A-8	IPC's machine shop
Insulating board piece	Babcock and Wilcox Kaowool® ceramic fiber board, per IPC drawing no. A490-1-A-18	IPC's machine shop
Boiling Cell		
Quartz tube	GE Quartz part no. CFG-214-HV, per IPC drawing no. A490-3-C-1	Quality Products, Inc. Mentor, OH (216)-255-4481
Porous forming screen	IPC drawing no. A490-1-A-9	Fox Valley Tool and Die
Bed thermocouples	0.0625" sheathed type-K, ungrounded junction, unsheathed bead	Nanmac Corp. Framingham, MA (508)-872-4811
Thermocouple fittings	Swagelok fitting no. SS-810-6-1-ZV, 1/2" tube to 1/16" tube reducing union	Neenah Valve and Fitting Corp. Neenah, WI (414)-722-8736
Permeability test fittings	Swagelok fitting no. SS-810-6-4, 1/2" tube to 1/4" female pipe thread reducing union	Neenah Valve and Fitting Corp.
Silica fiber	8.4 μm diameter; Astroquartz® I	JPS Industrial Fabrics Corp. Slater, SC (803)-836-8011
Alumina fiber	3.0 μm diameter; Saffil®	Thermal Ceramics Augusta, GA (404)-796-4200
	18.5 μm diameter; Fiber FP®	E.I. DuPont de Nemours & Co. Wilmington, DL (302)-695-3764
Gasket material	1/8" thick Graph-Lock®, flexible graphite gasketing; stable to at least 500°C	Appleton Packing and Gasket Appleton, WI (414)-731-4487

TABLE 4. (continued)

APPARATUS COMPONENT	DESCRIPTION OF COMPONENT	VENDOR
HEAT SUPPLY SYSTEM		
Copper heating block	ASTM B301 (Tellurium 145), per IPC drawing no.'s A490-3-D-16, A490-1-A-20	Central Steel and Wire Co. Chicago, IL (312)-471-3800 built by Fox Valley Tool and Die
Cartridge heaters	Watlow part no. J4A262A with 4" long ceramic bead leads; 1000 W, 240 V; 4" long x 0.5" OD	Ash Equipment Co. Milwaukee, WI (414)-352-3060
Silicon-controlled rectifier	Halmar model no. LZF1-2440, 240 V, 40 A, 4-20 mA input	Halmar Electronics Columbus, OH (614)-275-0530
Watt transducer	F.W. Bell model PX-2222BL; 220 V, rated at 20 A, 4000 W; ± 55 mV output at rated load	F.W. Bell Orlando, FL (407)-678-6900
Guard heater	Fibrox heavily-insulated fiberglass heating tape; 1 inch wide, 96 inches long; heat to 482°C	Cole-Parmer Instrument Co. Chicago, IL (312)-647-7600
Guard heater temperature controller	Omega model no. 6102 time-proportional controller; type-K thermocouple input, 10 A output; 0-1000°F	Omega Engineering, Inc. Stamford, CT (203)-359-1660
PROCESS CONTROL SYSTEMS		
Surface Temperature Control System		
Block thermocouples	all type-K grounded-junction wall design with 1/4" OD copper thermowell; (4) part no. E-12-9-K, (1) part no. E6-40-K-1/2	Nanmac Corp.
PID controller	LFE model 2012, part no. B5-50RZA3XX with isolated RS232 communications option, 0-5 V input, 4-20 mA output	CMI Meter Master Itasco, IL (312)-351-4554
Pressure Control System		
Pressure transducer	Sensotec model no. BP531PR, 100 psia, 0-5 V output, 10 V excitation voltage; temperature compensation to 400°F	Comtel Midwest New Berlin, WI (414)-544-6042
Amplifier/signal conditioner	Sensotec model no. 450D, single channel	Comtel Midwest
PID controller	Partlow MIC 6000, part no. 6230001-NI-304002, 0-5 V input, 4-20 mA output	Simone Engineering, Inc. Appleton, WI (414)-731-4111
Pneumatic control valve	1/2" Baumann globe, part no. 32-24102S/768, fail open	Simone Engineering

TABLE 4. (continued)

APPARATUS COMPONENT	DESCRIPTION OF COMPONENT	VENDOR
Pressure Control System (cont'd)		
Air supply regulator valve	Wilkerson model P10, part no. R16-02-000; 0-125 psi; 1/4" fittings	Neff Engineering Appleton, WI (414)-739-0181
Safety pop-off valve	1/2" Consolidated, part no. 1543D, set at 75 psi	Simone Engineering
Level Control System		
Capacitive proximity switch	Effector part no. 8057BC20NL2AAXX, 20 mm OD, 2 wire AC	A-A Electric Green Bay, WI (414)-499-6000
Solenoid valve	1/8" Asco 2-way direct acting, part no. 8262C35, AC, normally open	Simone Engineering
Gear pump	Viking model FH 32, bronze construction; mounted on base w/ 1/2 hP TEFC motor, 3 gpm at 1750 rpm	Crane Engineering Sales, Inc. Appleton, WI (414)-733-4425
DATA ACQUISITION SYSTEM		
Computer	AMT286 AT compatible w/ 40 M hard drive, 12 MHz clock speed	American Micro Technology Tustin, CA (714)-731-5914
Data acquisition hardware	(1) DAS16F high speed A/D I/O expansion board, (2) EXP16 universal analog-input expansion sub-multiplexer, (1) STA-U universal terminal board	Metrabyte Corp. Taunton, MA (508)-880-3000

Table 5. Pertinent properties of fused quartz, which is the raw material for the boiling cell.

Physical Property	
Thermal Conductivity	0.014 W/(cm-°C) @ 20°C
Heat Capacity	670 J/(kg-°C) @ 20°C
Density	2.2 g/cm^3
Coefficient of Thermal Expansion	5.5 x 10^{-7} °C^{-1}, average for 20°C to 320°C

The design of the supporting framework exposes the quartz boiling cell only to axial compression, thus minimizing stresses on it. A center support bracket houses a wood sleeve that fits around a shoulder welded on the perimeter of the quartz tube. This sleeve bracket is mounted on the framework via bearings to allow for rotation of the boiling cell. Four threaded support rods (5/8-inch diameter) slightly longer than the tube are fastened to this sleeve, and extend parallel to the axis of the tube. The support rods fit through the bored holes in the end mounting plates. Nuts with Belleville washers are tightened on the threaded ends of the support rods to compress the boiling cell between the mounting plates.

One end of the tube is sealed against a junction plate that connects the air pressure supply line, the steam vent line, and the water resupply line to the boiling environment. A ceramic spacer used between this junction plate and the mounting plate insulates against heat loss. The end of the tube with the welded nipples is mounted against the copper heating block. A fiberboard spacer used between the heating block and the mounting plate minimizes conduction heat losses. At both ends, Graph-Lock®, a high temperature gasket material, is used to seal the tube.

Fiber Bed Formation in the Boiling Cell

A formation tube attaches to the end of the boiling cell that houses the fibrous bed to allow formation of the bed. The 8.89-cm ID, 38-cm long plexiglass section is mounted on the inverted boiling cell with a mounting plate, and a rubber gasket seals between the forming tube and the boiling cell. From the 50-gallon mixing tank located on the mezzanine above the boiling cell apparatus, the fiber slurry flows by gravity to the forming section, where the fibers settle to form a

mat on the porous forming screen in the cell as the water drains from the bottom of the cell. The turbulence of the flowing suspension maintains good fiber dispersion in the forming section.

The Heat Supply System

The heat supply system supplies enough heat for atmospheric pool boiling of water. Referring to Figure 9, a 90-mm diameter heating surface requires about 6300 W at the critical heat flux. Building in a safety factor, this system is designed to supply 9000 W of thermal energy. The system components are the copper heating block, the cartridge heaters, and the electrical supply circuit. Five Type-K thermocouples with 4-inch long, 1/4-inch diameter copper thermowells are mounted within the block. One is mounted in the bottom near the cartridge heaters to monitor the temperature in the hottest region of the block. The other four measure temperatures in the block near the surface, and are discussed later in the section of heating block surface temperature control. A small disk of 1-μm thick copper foil is inserted into each thermocouple hole to insure good thermal contact. The thermocouples are mounted such that the thermal junction is perpendicular to the axis of the heater.

To aid in design, heat transfer in the heating block was studied with the aid of the three-dimensional computational fluid dynamics code, FLUENT. Cases based on pool boiling of water were run to determine the size of the heating block, as detailed in Appendix II. The design of the heating block, illustrated in Figure 37, represents a compromise between thermal mass and unidirectional heat flow. To rapidly conduct heat and rapidly dissipate temperature variations, the heating block was machined out of ASTM B301 (Tellurium 145), which is an alloy containing 99.5% copper and 0.5% tellurium. The nine 1000-W cartridge heaters are positioned symmetrically in a vertical orientation within the bottom region of the block. A distance of 3 cm between the cartridge heater region and the thermocouple region dampens temperature non-uniformities to insure one-dimensional heat flow. Due to the length of the cartridge heaters and the spacing requirement for the block thermocouples, a large thermal mass must be tolerated. The non-uniformity in heater surface temperature caused by the shoulder is mostly confined to the

perimeter. High-temperature gasket material seals between the quartz boiling cell and the shoulder of the heating block.

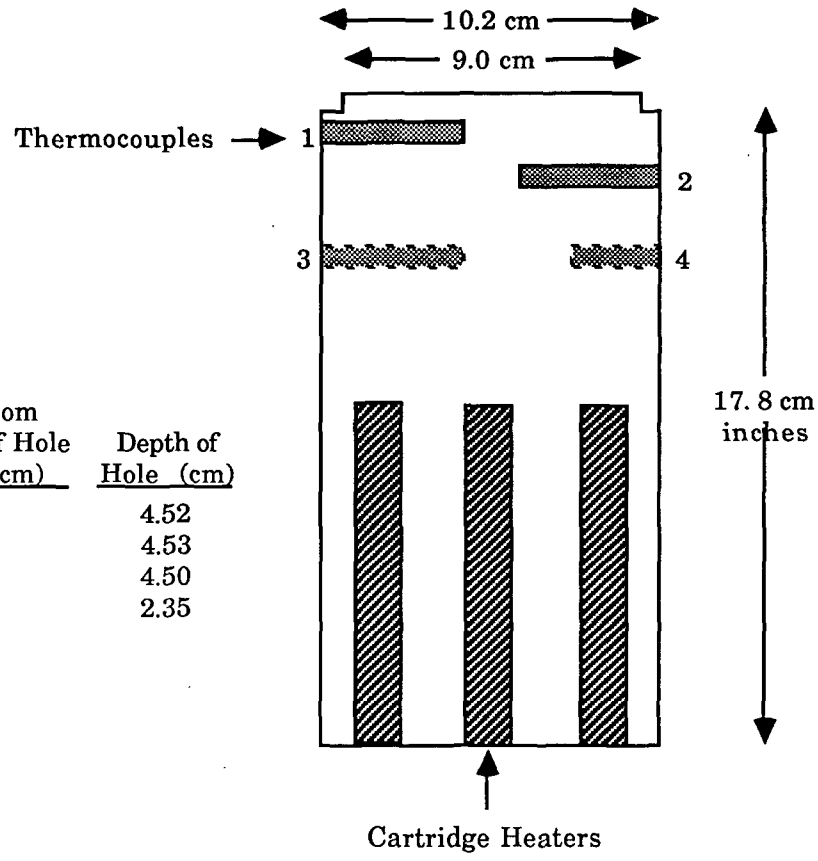

Thermocouple	Distance from Center Line of Hole to Surface (cm)	Depth of Hole (cm)
1	1.165	4.52
2	2.286	4.53
3	3.809	4.50
4	3.805	2.35

Figure 37. Schematic of the copper heating block illustrating the position of the block thermocouples. Thermocouples 3 and 4 are positioned into the plane of the paper, 90° from thermocouples 1 and 2. The fifth thermocouple, located in the bottom of the block near the cartridge heaters, is not shown.

The high thermal conductivity of the copper insures rapid dissipation of thermal gradients to quickly establish one-dimensional flow of heat in the block. However, as illustrated in Appendix III, the potential for convective heat losses to the ambient threatens the uniformity of heat flow to the surface. Even with the block insulated with 4.45-cm thick $CaSiO_4$ pipe insulation, radial heat losses at the higher block temperatures can be as large the heat flow to the fibrous bed. To insure unidirectional heat flow, steps must be taken to minimize these losses. A heating tape wrapped around the perimeter of the block insulation is used as a guard heater. A type-K, open

junction thermocouple is placed between the heating tape and the insulation to provide the input to a time-proportional controller. The setpoint of this controller is matched to the average of the block thermocouples near the boiling surface. The output of this controller supplies up to 10 A at 120 V to the heating tape. The control band of the guard heater temperature is typically ± 5°C.

During initial runs, the boiling surface of the copper heating block became heavily oxidized, creating two problems. First, the boiling surface was changing throughout the experiment, which is an important effect that can not be quantified. Second, extensive polishing was required to remove the oxidation products and create a fresh surface for boiling. To eliminate these problems, the surface was wet-lapped with 600-grit sandpaper, and plated with a 12.7-μm thick chrome layer.

The schematic for the electrical supply circuit is illustrated in Figure 38. The circuit provides a 40-A, 240-V, 60-Hz, single-phase supply for the cartridge heaters. Two features of the circuit interact with the surface temperature control system. First, the silicon-controlled rectifier (SCR) operates as a rheostat to meter electrical current to the cartridge heaters according to a 4 to 20-mA signal from the temperature controller. This SCR is a zero-crossing firing device which passes a sinusoidal current waveform composed of a number of half-cycles in an on-off fashion, with each pulse of current beginning at zero voltage. As the input signal approaches 20 mA, the output current waveform approaches a continuous sinusoidal waveform. (A phase-angle firing SCR chops the sinusoidal waveform and transmits only a portion of each current half-cycle. Figure 39 graphically illustrates the difference between these two SCRs.) Second, a 50-A relay prior to the SCR breaks the circuit if a high-surface-temperature condition is detected by the temperature controller.

As needed for pool boiling of water, maximum power is achieved by running the nine cartridge heaters in parallel. Since porous media boiling requires only a portion of full power, the parallel arrangement of cartridge heaters is oversized for this type of operation. Operating the apparatus in the full-power mode while boiling in a porous medium makes control of surface

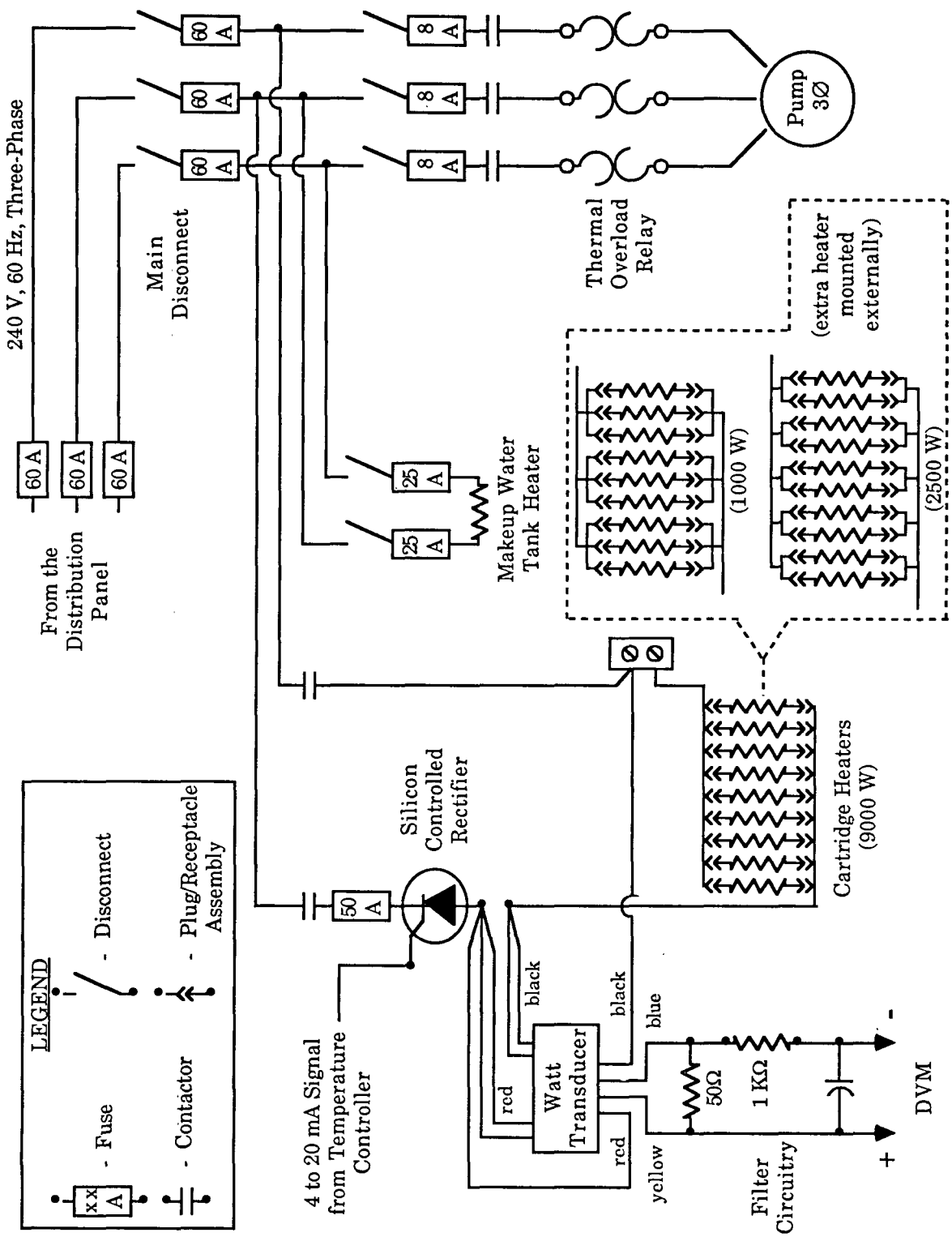

Figure 38. The 240-V electrical supply system.

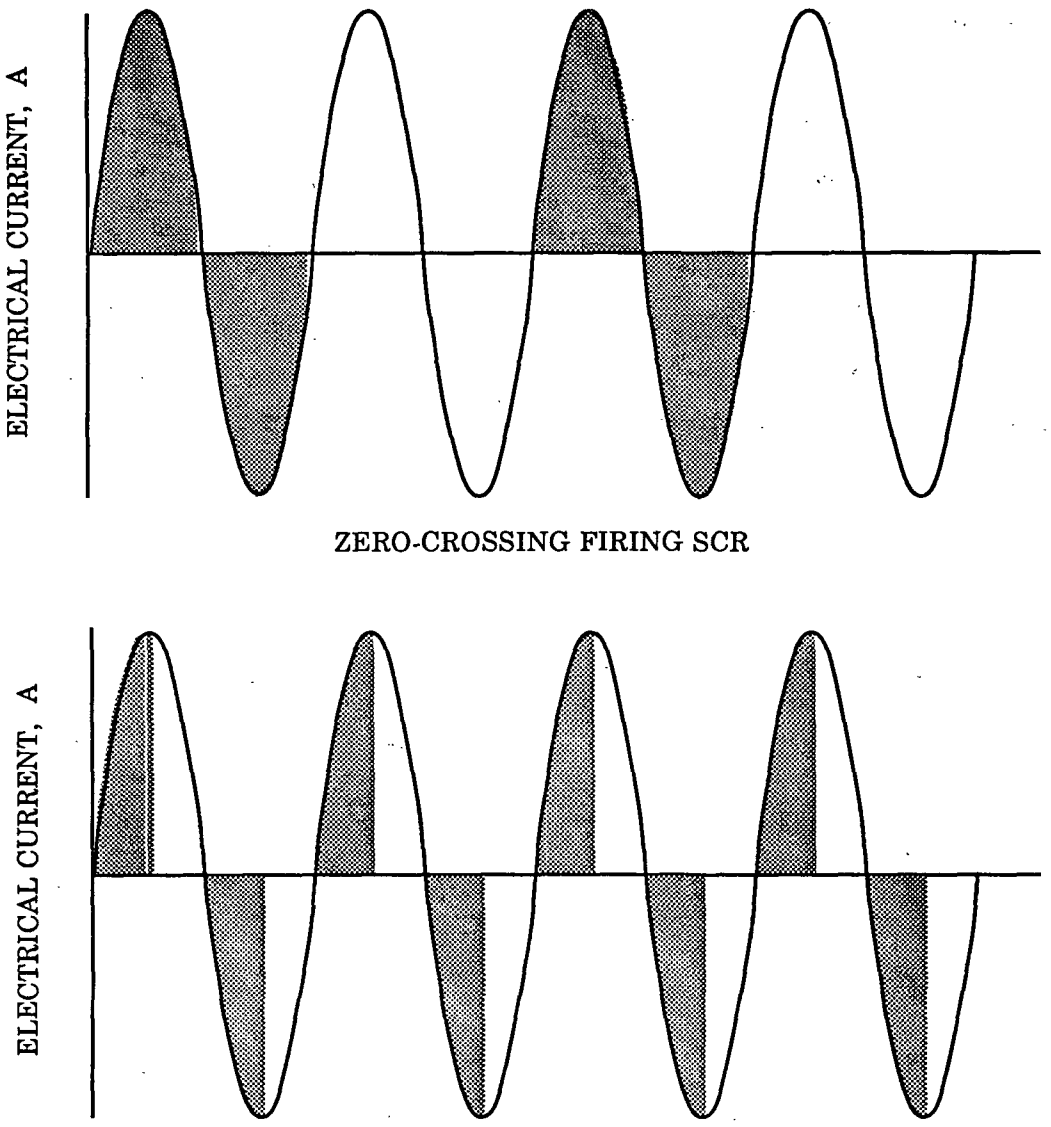

Figure 39. Illustration of the waveform generated by the two types of silicon-controlled rectifiers.

temperature difficult; the need for small adjustments of power often results in overshoot and oscillation. This situation is rectified by connecting the cartridge heaters in a manner depending on the boiling situation. Referring to Figure 38, the cartridge heaters can be configured to supply a maximum of 9000 W (for pool boiling of water), 2500 W (which is sufficient for beds of larger pore diameter), or 1000 W (which is sufficient for beds of very small pore diameter). The different techniques for connecting the heaters improves sensitivity of the temperature controller for the

respective boiling situation.

A final feature of the electrical supply circuit is the use of an analog watt transducer to independently monitor power input to the cartridge heaters. This device, which operates by the Hall effect, generates a continuous dc voltage output that is proportional to an exact, real-time multiplication of SCR current and line voltage. Because the output voltage signal mirrors the waveform from the SCR current, a filter used to integrate the a-c component smooths the transducer output. The filter circuitry illustrated in the electrical schematic reduces the ripple to less than 1%. The conversion factor for the transducer's output is 72.73 W per mV.

The Process Control System

Execution of a boiling experiment requires control of heating block surface temperature, pressure within the boiling cell, and water level in the boiling cell. A process control loop is dedicated to each of these parameters. The surface temperature and pressure control systems are tied into the data acquisition system, as illustrated in Figure 40.

The Surface Temperature Control System

Control of the heating block surface temperature is accomplished with readings from three of the thermocouples mounted in the block, control software, a PID controller, and the SCR of the electrical supply circuit. A unique feature of this control loop is that the process variable, the surface temperature, is not directly measured, but is calculated. The sensitivity of nucleation phenomena to surface roughness precludes the use of a surface thermocouple. Furthermore, a surface thermocouple would provide a measure of instantaneous, fluctuating temperature, as opposed to the desired bulk average. The bulk average surface temperature is calculated based on the readings of the three block thermocouples that are mounted in similar radial positions, but different axial positions. The fourth block thermocouple is mounted in the same axial position, but different radial position as the third one, to determine the degree of one-dimensional heat flow.

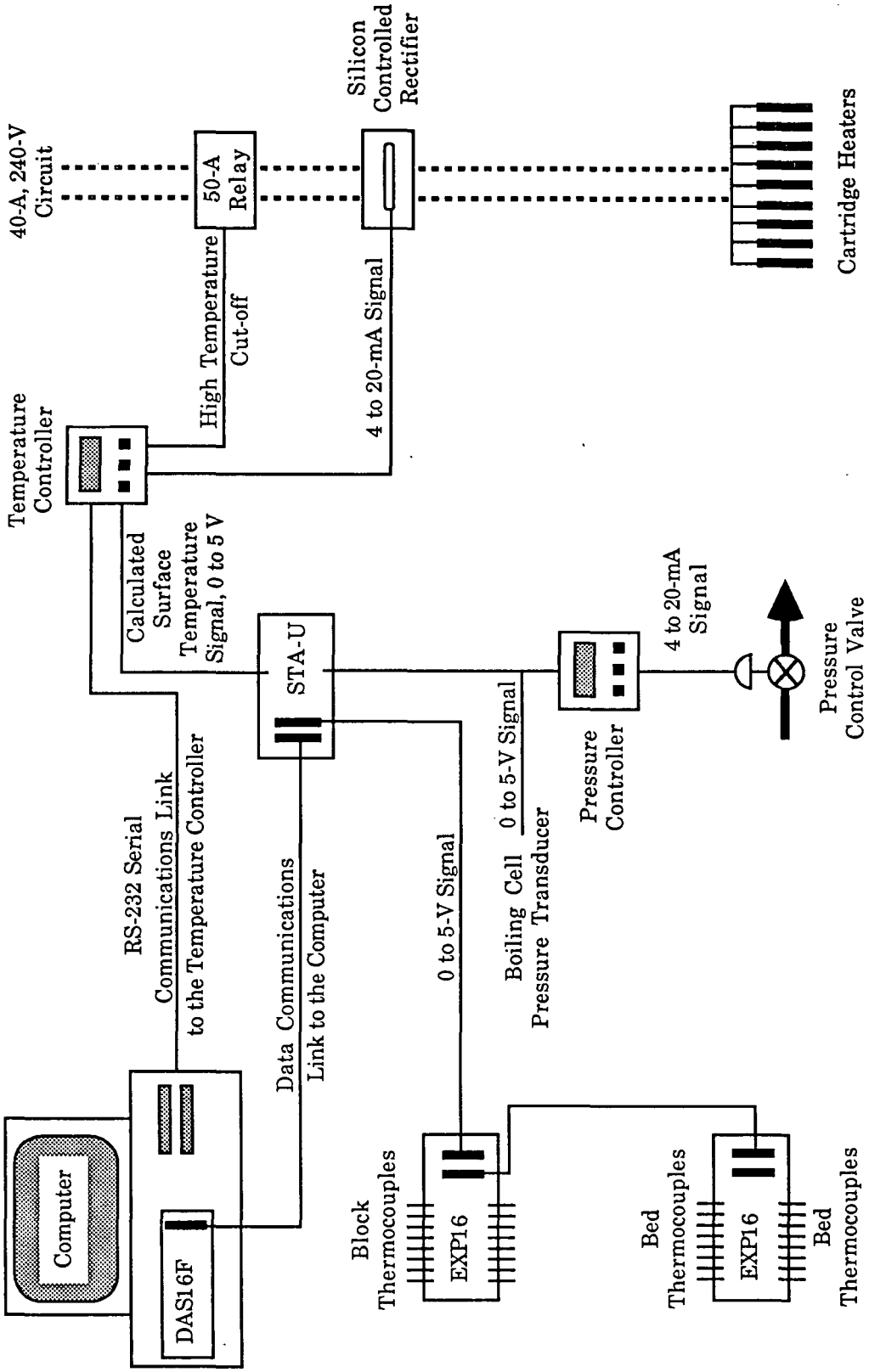

Figure 40. The electronic control system hardware.

A computer program was written to indirectly determine the surface temperature by interfacing with the data acquisition system. The main function of the program, which will be discussed in detail in subsequent sections, is to continuously read the data acquisition channels corresponding to the three block thermocouples, calculate the surface temperature, and download this value to the temperature controller as a 0 to 5-V signal via one of the D/A channels of the main data acquisition board, the DAS16F (manufactured by Metrabyte Corporation). In response, the controller generates a 4 to 20-mA output that actuates the SCR to meter current to the cartridge heaters. It is estimated that the software updates the controller at a rate on the order of one time per second.

Due to the complex nature of the boiling phenomena, temperature setpoints are approached in a slow, orderly fashion by utilizing the ramp/soak capabilities of the temperature controller. Although it would be convenient to program the ramp/soak profiles for the entire experiment prior to starting, the need for definition in the characteristic boiling curve requires that the subsequent temperature setpoint be identified only after the present setpoint is achieved. The new setpoint and the corresponding ramp rate are selected via specially-defined function keys, and are downloaded from the control software to the controller via the computer's RS232 serial communications link. The magnitudes of the temperature setpoint increment and the ramp rate are based on the sensitivity of the region of the boiling curve being approached. Due to the potential for process instabilities and the thermal lag in the heating block, the setpoints are approached slowly, generally on the order of 1.5°C per minute.

Tuning the PID temperature controller is difficult due to the time lag in response of the system resulting from the large thermal mass of the heater block, and due to the relatively low heat flux for boiling in a porous medium. The control range is set to desired operating range of 50°C to 450°C to maximize sensitivity of the controller. To achieve acceptable control, the span of the controller is set to two to three times the control range. Within this operating window, acceptable control is best obtained by frequently adjusting the proportional band (proportional action) in

accordance with the changing process dynamics. A reset time (integral action) of 0.15 repeats/minutes, and a rate (derivative action) of 1.11 minutes^{-1} are suitable for all of the boiling regimes.

The Boiling Cell Pressure Control System

Pressure control is accomplished by regulating an air pressure supply line and a vapor vent line. Referring to Figure 35, the air pressure supply line is simply regulated with a manual regulator valve. Regulating flow in the vent line involves the use of automatic process control equipment. A 100-psia pressure transducer mounted on the vent line supplies a 0 to 5-V output signal to the data acquisition system, and to a PID controller as the process variable. The controller feeds a 4 to 20-mA output signal to the I/D converter of the pneumatic control valve, which then adjusts air pressure to actuate the control valve.

Tuning the PID pressure controller is a simple task because of the rapid dynamics of the system. Excellent control to both load and setpoint changes is achieved with a proportional band of 12.5% and an automatic reset time (integral action) of 5.0 repeats/min No derivative action is used because even a small amount of it rapidly induces process instability.

The Level Control System

The flow of make-up water into the boiling cell is regulated by the level control system. The make-up water heater is manually operated to maintain a water temperature of about 75°C, and the make-up water pump runs continuously. The pressure in this loop is manually set at 5 psi above boiling cell pressure by adjusting the valve on the bypass line of the makeup water loop.

The control of water level in the boiling cell is accomplished by a very simple technique. A capacitive proximity switch mounted about 2.2 cm from the exterior of the boiling tube senses the level of water, which interrupts the capacitive field. This generates a current that keeps the normally-open solenoid valve on the water supply line closed. When the water level drops, the

contact in the switch is broken, and the valve opens, allowing water to flow into the boiling cell. This system controls water level to ± 2 cm.

The Data Acquisition System

The data acquisition hardware and the computer software written to control the boiling experiment are discussed together because they operate in conjunction for the data acquisition.

The Data Acquisition Hardware

The data acquisition hardware consists of a host computer and electronic circuitry boards, with details given in Table 6. The host computer is an AT-compatible AMT 286, and the electronic boards are manufactured by Metrabyte. The DAS16F high speed A/D I/O board, mounted on the computer's motherboard, is connected to two external, daisy-chained EXP16 universal expansion sub-multiplexer boards via an STA-U universal terminal board. The EXP16 boards read the analog millivolt signals from the thermocouples and amplify them to 0 to 5 V for input to the DAS16F, where the amplified signals are converted to digital signals. The EXP16 boards are equipped with cold junction compensation circuitry to zero-point reference the thermocouple voltages. As illustrated in Figure 40, one EXP16 board is dedicated to the heater block thermocouples, and the other is dedicated to the fibrous bed thermocouples. The 0 to 5 V output of the pressure transducer is fed to the DAS16F via terminals on the STA-U board.

Instrumentation is calibrated on an as-needed basis. The pressure transducer, which requires infrequent calibration, is calibrated with a National Bureau of Standards dead weight tester. Thermocouples are typically calibrated once per month to insure continued accuracy. The two EXP16 boards are calibrated immersing the appropriate thermocouples in two standards - boiling water (about 99.5°C after correcting for barometric pressure) and hot mineral oil (about 190°C as measured with a National Bureau of Standards calibrated thermometer). Both of these temperatures are cross-checked with a digital thermometer using a type-E thermocouple. Calibration involves adjusting the potentiometer for the cold junction compensation device, the

Table 6. Pertinent information about the electronic components of the experimental apparatus.

Instrumentation	
Block thermocouples	Type K; grounded wall design with copper thermowell.
Bed thermocouples	Type K; ungrounded, unsheathed, fine-gage.
Pressure transducer	Strain-gage type; complete 4 arm, 350 ohm strain-gage bridges, 0-100 psia, 0-5 V output, 10 V excitation voltage; temperature compensation to 400°F.
Data Acquisition Equipment	
Metrabyte DAS16F	High speed A/D I/O expansion board; 0-5 V input, 8 differential or 16 single-ended, multiplexed channels with 12 bit resolution; 2 independent A/D channels with 12 bit resolution, 0-5 V output; 100 kHz maximum throughput rate.
Metrabyte EXP16	Universal analog-input expansion sub-multiplexer; 5 V DC/DC converter amplifies thermocouple signals to 0-5 V for input to DAS16F; adjustable gains, cold junction sensing and compensation circuitry.
Metrabyte STA-U	Universal terminal board.
Computer System	
AMT286	AT-compatible; 80286 microprocessor with 12 MHz clock speed; 40 M Priam hard disk with 24 msec access time.
PID Controllers	
LFE Model 2012 (temperature)	1/4 DIN, single loop, setpoint programmable, with ramp/soak capabilities; 0-5 V input, 4-20 mA reverse output to SCR, high-deviation alarm (non-latching), high-process alarm (latching) solid-state relay (rated for 1 A at 240 V) to a 50 A relay; isolated RS232 communications requires 12 V power supply.
Partlow MIC 6000 (pressure)	1/4 DIN, single loop, setpoint programmable, with ramp/soak capabilities; 0-5 V input, 4-20 mA direct output to control valve; no alarms.

zero potentiometer, and the gain potentiometer, in sequence.

The Computer Control Software

Though the main purpose of the computer control software is the calculation of heater block surface temperature for the surface temperature control loop, other specialized functions are incorporated to allow the operator to run the experiment with relative ease. The basic flowsheet of the program illustrated in Figure 41 shows a few of the auxiliary functions, programmed as subroutines; a detailed explanation of the entire program is found in Appendix IV. The main section of the program is a continuous loop that reads the appropriate block thermocouple channels,

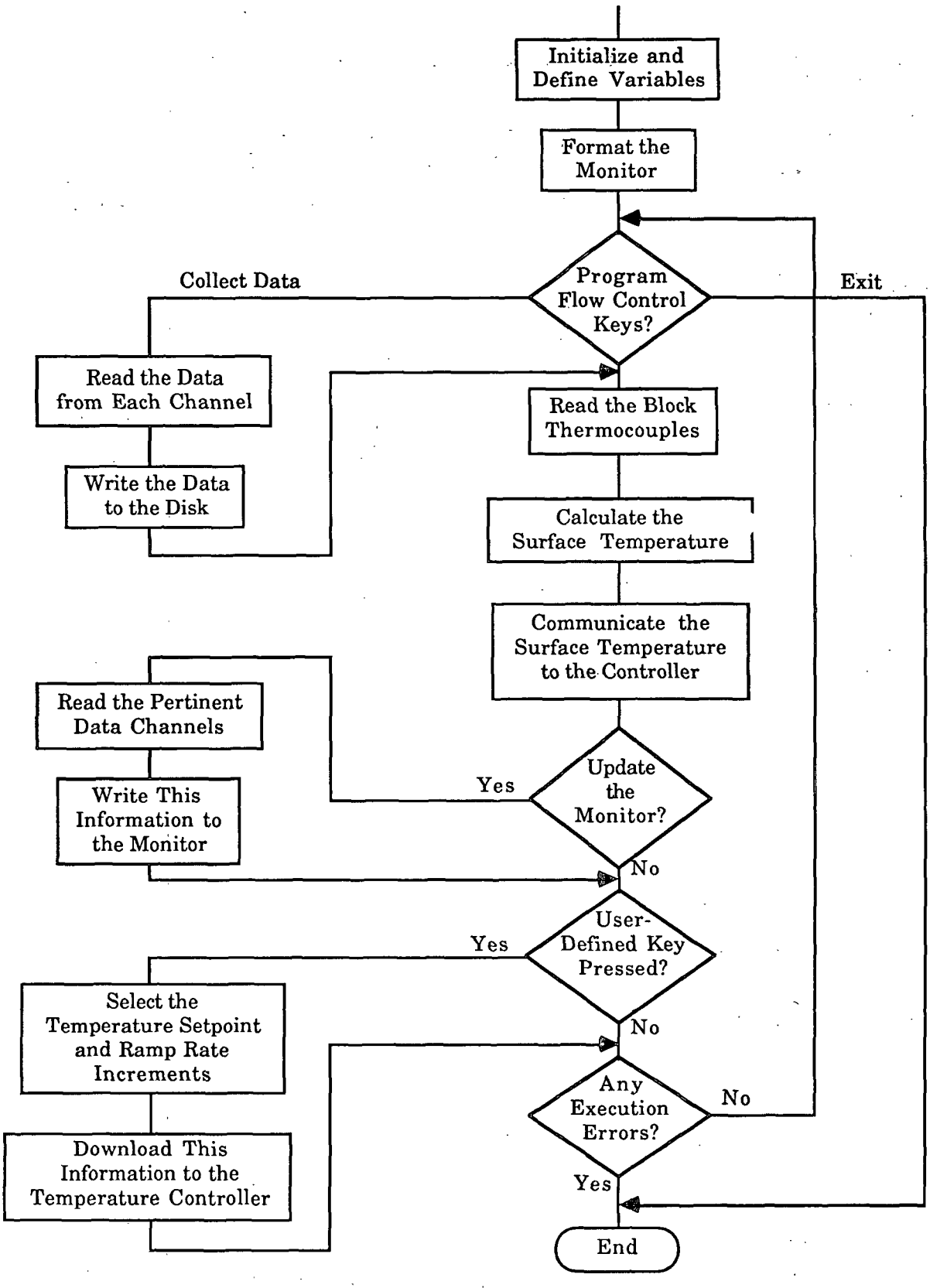

Figure 41. Flowsheet of the computer control software for the boiling experiments.

automatically interrupted after five cycles to collect recent process data for updating the faceplate of the monitor, which occurs approximately every five seconds. Through the use of specifically defined keys, the operator can interrupt the main program to accomplish other tasks. The most time-consuming task is acquisition of a complete data set, but at no time is the main program interrupted for more than two seconds.

The computer program was written in TBASIC, which is actually a hybrid of interpretive and compilable BASIC. Its attractive features are acceptable computational speed and an interactive editor mode that automatically detects improper command syntax. Metrabyte provides software drivers for data acquisition that are compatible with many computer languages. However, to utilize TBASIC as the programming language, Transera agreed to write a TBASIC version of Metrabyte's DAS16F driver.

The faceplate of the monitor is designed to allow user-friendly execution of a boiling experiment by supplying the user with pertinent information. It is continuously updated with recent values of important process variables, it reminds the operator of the functions of specially-defined keys, and it provides the operator with an interactive interface to the software. This last feature allows the operator to collect data, to download setpoint information to the temperature controller, or to end the experiment, when desired.

Data acquisition is an integral part of the control software. Block thermocouple data are collected continuously, bed thermocouple and boiling cell pressure data are collected every monitor-update cycle, and all data acquisition channels are read when the operator prompts the computer to collect a group of experimental data. A complete set of data consisting of tens groups is collected once steady-state conditions have been achieved at a given setpoint. Then, new setpoint information is downloaded to the temperature controller, and the process is brought to the new setpoint.

While it is necessary to maximize accuracy of the data, it is also imperative that the main

loop of the control software not be interrupted for more than a few seconds at a time. In light of the information gained through uncertainty analysis (Appendix V), the following technique was adopted to minimize precision error of the data without unduly interrupting the control software. Each time data is collected, the computer reads the data acquisition channels in succession, repeating the cycle fifteen times before averaging the data. The averages of fifteen readings for each channel are stored in a data array. Rather than consume precious processor time by manipulating the data during the experiment, the averaged readings are written to a data file on the hard disk immediately after they are collected. Control is immediately returned to the main program.

Ten data sets are collected for each surface temperature setpoint. Thus, any data point represents the average of 150 readings. For post-experiment, statistical data analysis, the population mean is calculated for each process variable, and the appropriate population standard deviation is determined by pooling the standard deviation from each of the ten data groups.

THE CAPILLARY PRESSURE / SATURATION APPARATUS

The capillary pressure function is measured for pads of each fiber diameter to determine the average pore diameter as a function of porosity. The data required for this experiment are pressure difference across the bed, the volume of displaced water, and the porosity of the bed. Because equilibration time is lengthy, these experiments take four to seven days to complete, making it impractical to determine for the fiber bed in the boiling cell. Thus, an apparatus has been assembled to measure the capillary pressure function for small pads of fibers over a range of porosities for each of the three fiber diameters. The ultimate objective is to convert these data into characteristic curves of average pore diameter versus porosity. By knowing the porosity of the fiber bed in the boiling cell, its average pore diameter can be determined graphically from these curves.

Due to the long periods of equilibration, the capillary pressure/saturation apparatus

illustrated in Figure 42 is designed to gather data for two fiber pads during one experiment. This apparatus, photographed in Figure 43, is based on the porous plate technique used by other researchers [101,102]. The main component of the apparatus is a 300-ml fritted-disk Buchner funnel, which houses the fiber pad. The cavity of the funnel is sealed with an air-tight lid and pressurized to provide the pressure drop across the pad. The fritted ceramic disk has a pore size distribution of 4.0 to 5.5 μm, which allows a maximum applied pressure of 39.3 cm Hg. Shims are placed around the perimeter of the pad, and a sintered bronze disk with a pore diameter of 100 μm is laid on top of the pad. Springs placed on top of the bronze disk compress the pad to shim height when the air-tight lid is positioned. Shim height is 1.552 cm for one funnel, and 1.545 cm for the other. The other key components are the 25-ml buret, which measures the volume of water displaced from the pad, and the Validyne® differential pressure transducer, which measures the pressure difference across the pad. The pressure transducer is calibrated with a Hg or CCl_4 manometer. Depending on pressure range of the capillary pressure/saturation experiment, the transducer is outfitted with a one psi or 100-cm of water diaphragm.

The funnel assemblies are supported from ring stands with ring clamps and universal clamps. Tygon tubing and polyethylene tubing connect the burets and the water supply flask to the funnels. Distilled, de-ionized water from the supply flask fills the system tubing prior to an experiment. The tops of the burets are sealed with rubber stoppers and Tygon tubing into Erlenmeyer flasks filled with water. The flasks are capped with drying tubes containing wetted glass wool to minimize evaporation from the buret.

A number of data points of pressure difference across the fiber pad and the corresponding volume of water displaced from the pad is required to determine the capillary pressure/saturation curve. Water is displaced from the pad as the cavity of the funnel is pressurized by introducing compressed nitrogen. Increments in applied pressure are controlled with a precision regulator valve that is designed for an operating range of 0 to 10 psi. The reading of the differential pressure transducer must be corrected for the constant head of water on the low-pressure port of the

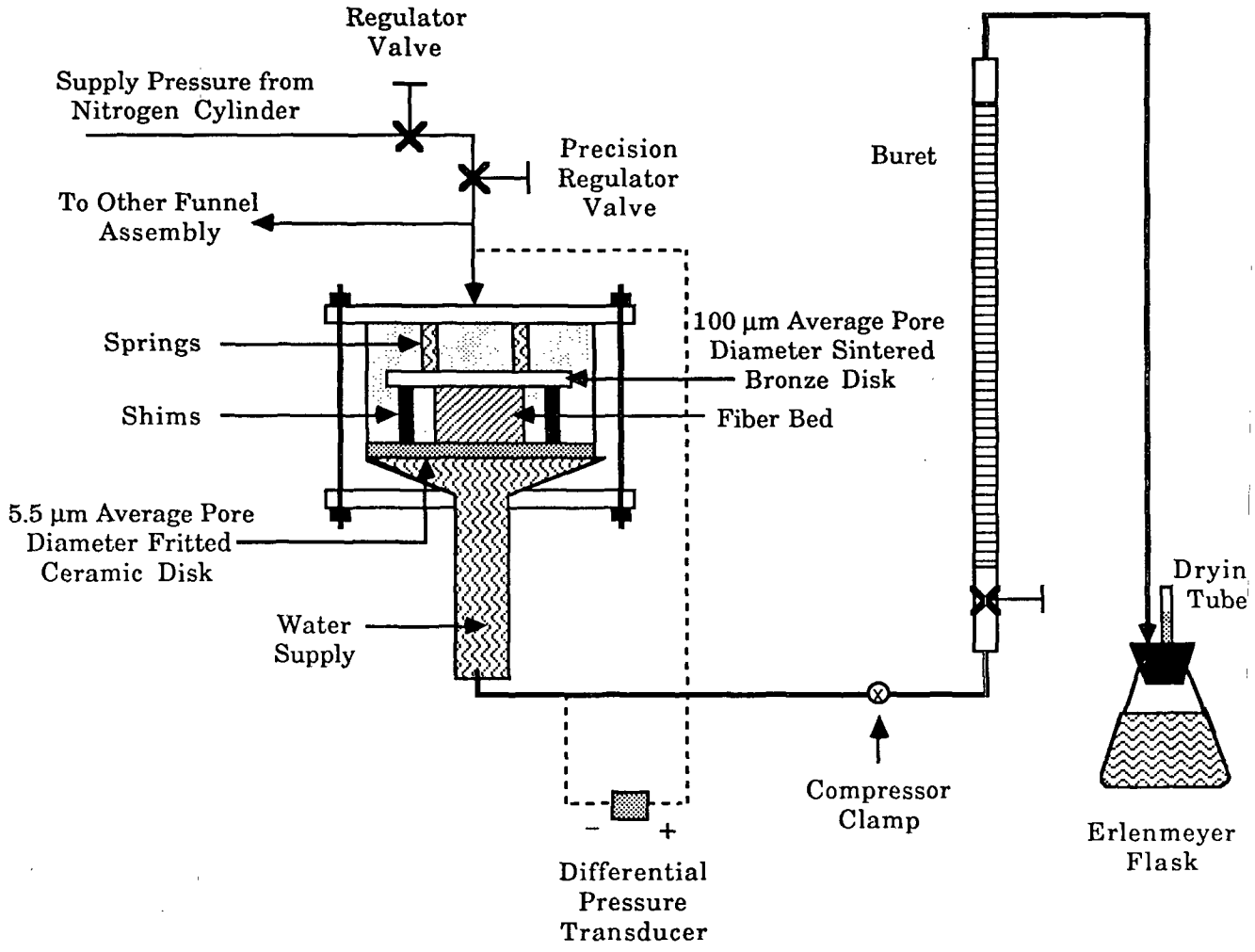

Figure 42. Schematic of the capillary pressure/saturation apparatus.

transducer. Upon completion of the experiment, the dewatered bed is weighed, dried, and re-weighed for determination of porosity and irreducible saturation.

The apparatus for forming the fiber pads for this test is illustrated in Figure 44, and the technique developed for forming is detailed in Appendix I. The inside diameter of the forming tube is 5.08 cm, but capillary-force-induced shrinkage yields a drained pad diameter slightly smaller. The pads formed in this apparatus have a drained porosity of 0.96 to 0.97.

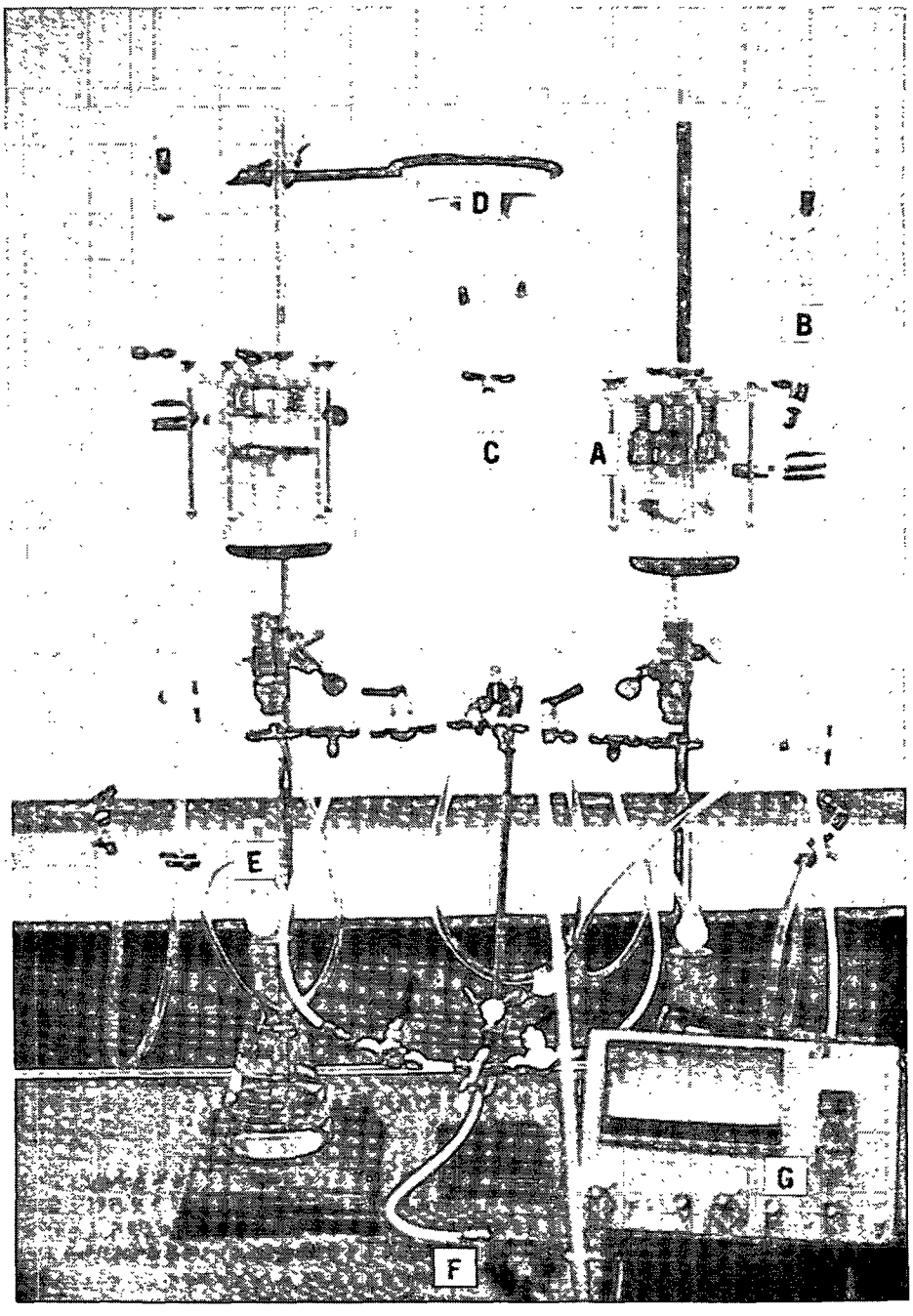

A - 300 ml fritted-disk Buchner funnel
B - 25 ml buret
C - compressed nitrogen pressure supply
D - water supply flask
E - drying tube
F - Validyne pressure transducer
G - signal conditioner for the pressure transducer

Figure 43. A photograph of the capillary pressure/saturation apparatus.

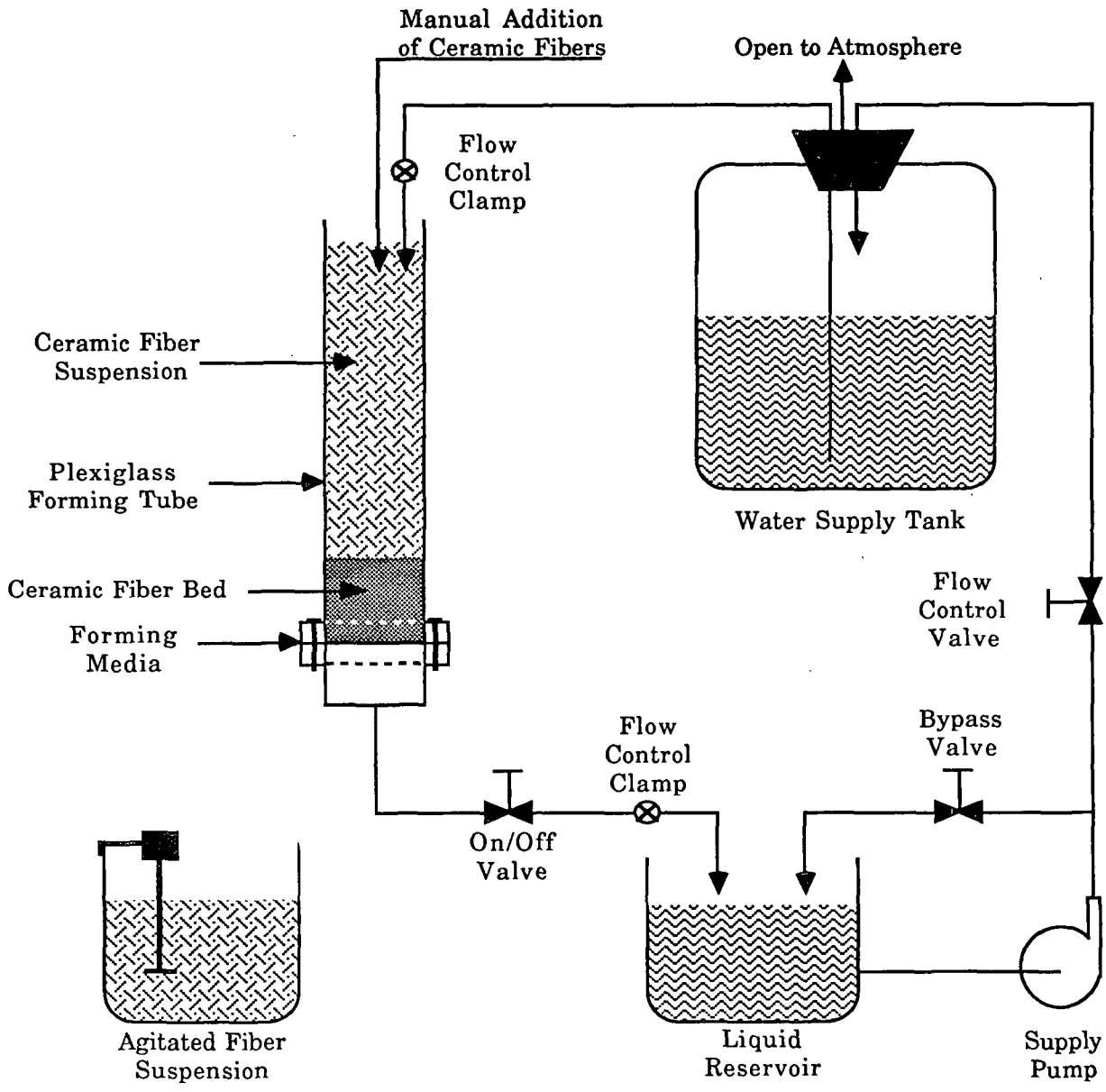

Figure 44. Schematic of the fiber pad formation apparatus.

PERMEABILITY MEASUREMENT APPARATUS

Permeability is determined for pads of each fiber diameter by measuring the flow rate as a function of pressure drop across the pad. The formation tube used to make fiber pads for the capillary pressure/saturation experiment is modified to perform the entire permeability measurement in the tube, as illustrated in Figure 45. Two pressure taps are positioned a distance

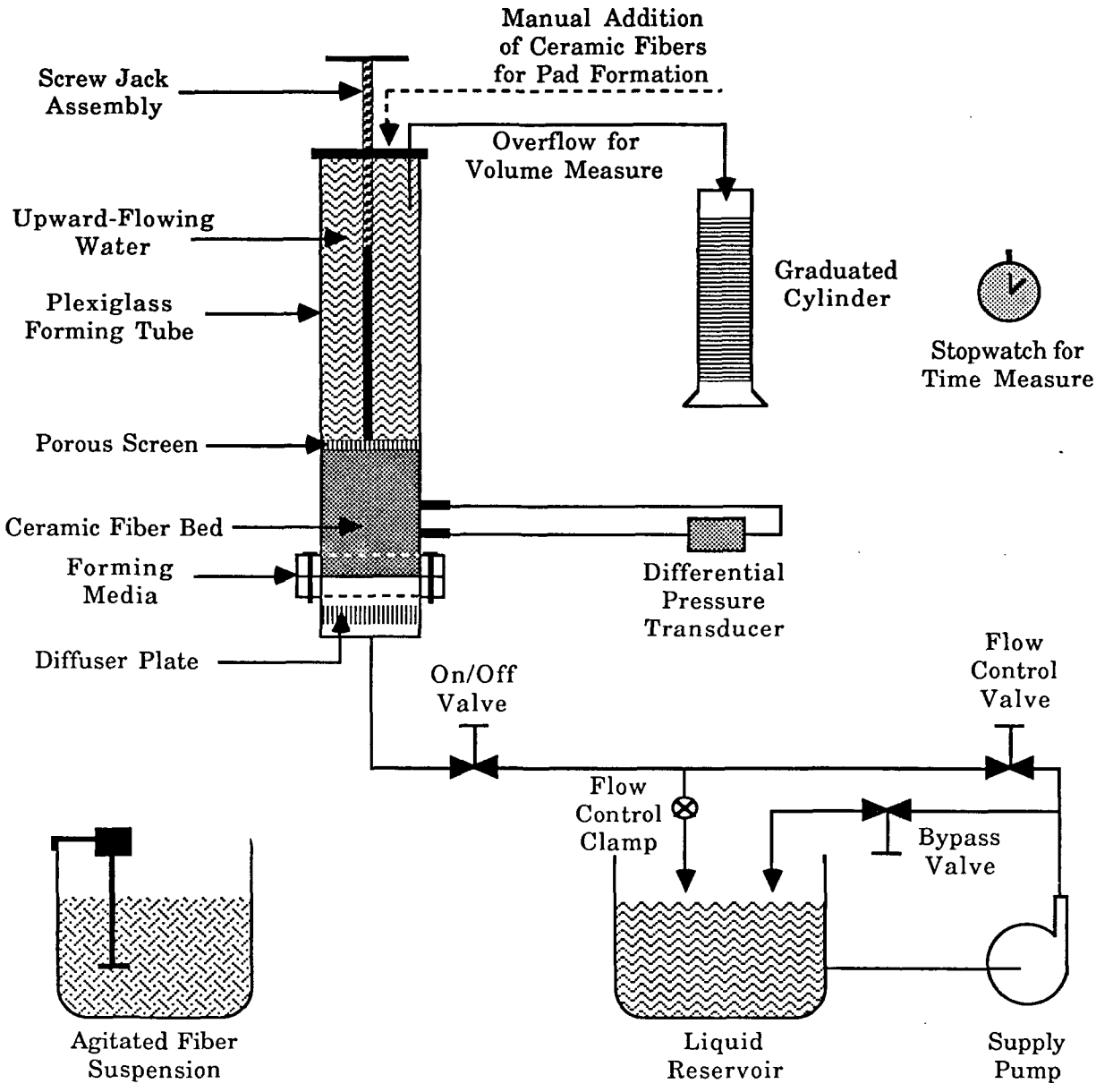

Figure 45. Schematic of the permeability measurement apparatus.

of 2.47 cm apart along the axis of the tube, and a drilled metal plate is placed beneath the forming media in the bottom piece of the tube to act as a diffuser. A screw jack assembly mounted on top of the tube is rotated to compress the formed pad to the desired porosity. The shaft of this assembly is composed of two pieces so that the porous screen that rests on the surface of the pad remains stationary as the shaft is rotated. The apparatus is photographed in Figure 46.

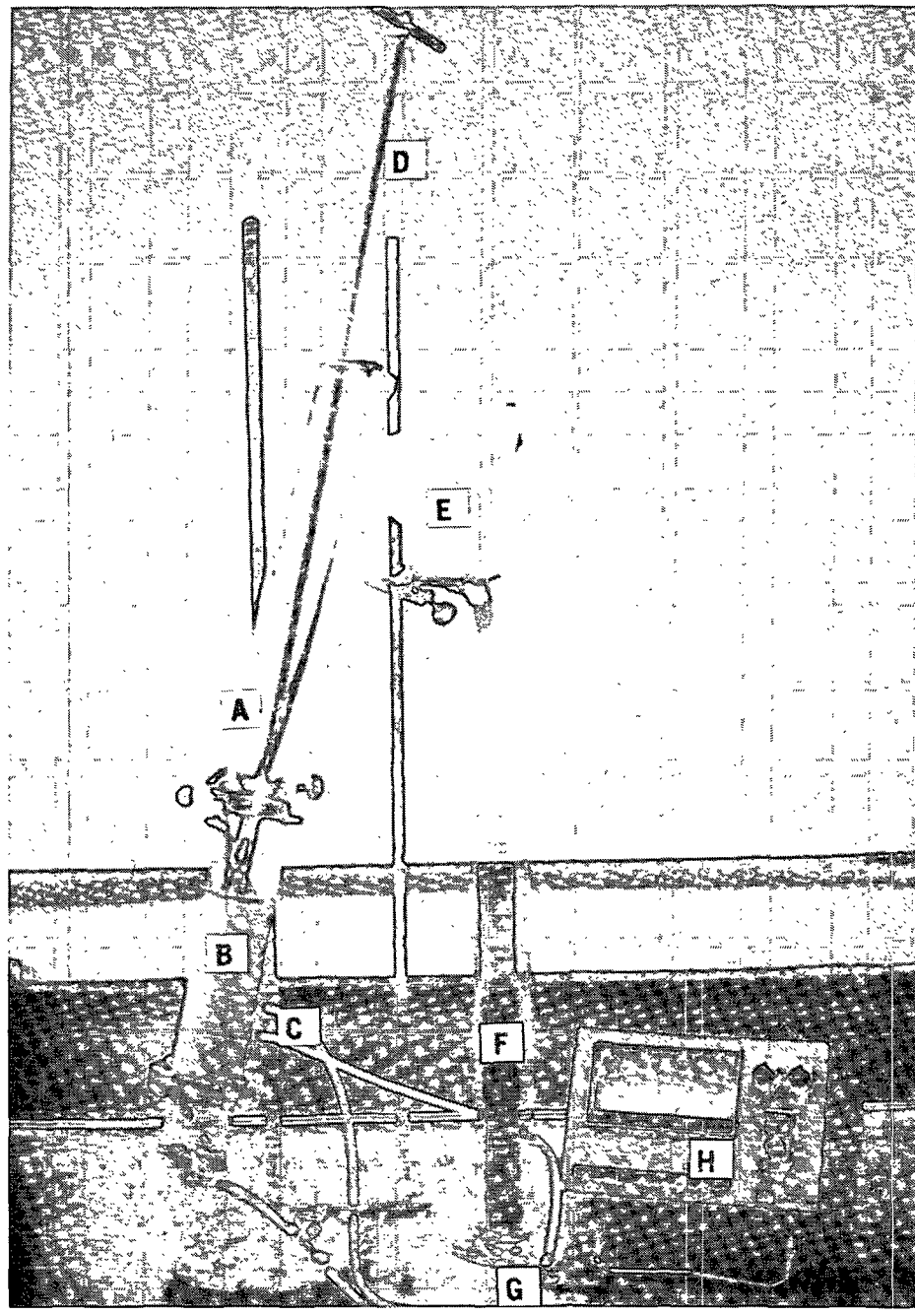

A - formation tube
B - ceramic fiber pad
C - the two pressure taps
D - screw jack assembly
E - funnel
F - graduated cylinder
G - Validyne pressure transducer
H - signal conditioner for the pressure transducer

Figure 46. A photograph of the permeability measurement apparatus.

Water flow introduced through the bottom piece of the tube passes through the diffuser to smooth any flow non-uniformities. The Validyne® pressure transducer measures the pressure drop across the pressure taps, and a graduated cylinder and a stopwatch are used to measure the flow rate as water overflows from the top of the tube. Six different flow rate/pressure drop data points are collected at each level of compression, and six different levels of bed compression are tested.

EXPERIMENTAL DESIGN

The objective of this thesis is to investigate the factors that control boiling in fibrous porous media as a means to gain insight into possible controlling mechanisms during impulse drying. Two of the factors that undoubtedly influence the impulse drying event are the level of thermodynamic pressure attained in the sheet, and the pore structure of the sheet. Therefore, in this fundamental boiling study, two primary variables to be investigated are the system pressure within the cell, and the pore size of the bed.

The characteristic boiling curves are determined for different conditions of pressure and average pore diameter of the fibrous beds. Because it is difficult to target an average pore diameter of the bed, the fiber diameter is used as the bed characteristic for the purpose of an experimental design. Table 7 illustrates the conditions for nine experiments necessary to test three levels of each variable. However, as will be discussed, many more boiling experiments have been executed. The pressure range listed here is moderate, and probably does not reflect levels attained in impulse drying. The original maximum desired pressure of 0.44 MPa was based on structural concerns for the boiling cell, but catastrophic failure during a boiling run at 0.28 MPa precludes boiling at higher pressures. The experimental design shown here reflects the adjustment to lower pressures necessitated by this failure.

Table 7. The basic design of the fibrous media boiling experiments.

	SYSTEM PRESSURE, MPa			FIBER DIAMETER, μm		
RUN	0.10	0.19	0.28	3.0	8.4	18.5
1	X			X		
2		X		X		
3			X	X		
4	X				X	
5		X			X	
6			X		X	
7	X					X
8		X				X
9			X			X

MATHEMATICAL ANALYSIS OF THE DATA

This section details the mathematical techniques used to analyze the data collected in this thesis. Because the main focus of this thesis is characterizing the effect of a fibrous porous medium on the boiling curve, analysis of data from the boiling experiments will be discussed first. Then, analysis techniques for data to supplement the boiling experiments will be presented.

DIMENSIONAL ANALYSIS OF THE BOILING SYSTEM

Dimensional analysis based on the Buckingham Pi Theorem [103] is used to develop correlations to mathematically represent the relationship between heat flux and wall superheat for boiling in the presence of fibrous beds. Mathematical expressions with applicability to similar phenomena can be developed from a first-principles approach where an appropriate set of conservation equations, based on well-developed theory, are non-dimensionalized. Unfortunately, boiling theory is not sufficiently developed to allow a first principles approach. Consequently, dimensional analysis is often resorted to for mathematical analysis of boiling data. Many of the correlations previously discussed are of this type, although some represent a semi-empirical approach where the dimensionless groups are derived from theoretical considerations. The limitations in both accuracy and scope of application of these correlations are the main disadvantages of the dimensional analysis approach.

Using inspectional analysis, conservation equations appropriate for multiphase flow through a porous medium with heat transfer were non-dimensionalized, as presented in Appendix VI, but this approach was abandoned in favor of dimensional analysis for two reasons. First, the goal of this thesis is to define the heat flux boundary condition at the hot surface, and not to define fluid flow within the porous medium. Second, the dimensionless groups developed from inspectional analysis involve a number of parameters that are difficult to quantify for this system.

Dimensional analysis involves identification of important physical properties of the

experimental system, which are combined to yield a set of appropriate dimensionless groups. Some insight into the physics of the process is necessary to select appropriate physical parameters, and to rearrange the derived dimensionless groups to yield a final set that have physical significance for the system. In this sense, dimensional analysis is somewhat arbitrary: many different dimensionless groups can be derived for a particular physical system based on selection and combination of the important parameters.

The Buckingham Pi Theorem was applied to the important parameters of the boiling system collected in Table 8. The comprehensive list of parameters has been classified according to level of significance based on consideration of the physics of the system. For the purpose of dimensional analysis, the dimensions of each parameter are reduced to the four fundamental units of mass (M), length (L), temperature (T), and time (t).

Table 8. Classification of variables for dimensional analysis of the boiling cell system.

High Level of Significance			Low Level of Significance		
		FLUID PROPERTIES			
ρ_v	(g/cm^3)	[ML^{-3}]	ρ_l	(g/cm^3)	[ML^{-3}]
μ_l	(Pa-sec)	[ML^{-1}t^{-1}]	μ_v	(Pa-sec)	[ML^{-1}t^{-1}]
C_{p_l}	(J/(g-°K))	[L^{2}t^{-2}T^{-1}]	C_{p_v}	(J/(g-°K))	[L^{2}t^{-2}T^{-1}]
Δh_v	(J/g)	[L^{2}t^{-2}]			
k_l	(W/(cm-°K))	[MLt^{-3}T^{-1}]			
k_v	(W/(cm-°K)	[MLt^{-3}T^{-1}]			
σ	(N/cm)	[Mt^{-2}]			
$g(\rho_l - \rho_v)$	(g/(m^2-sec^2))	[ML^{-2}t^{-2}]			
		FIBER BED PROPERTIES			
K	(m^2)	[L^2]	ρ_f	(g/cm^3)	[ML^{-3}]
$\overline{D}$	(μm)	[L]	C_{p_f}	(J/(g-°K))	[L^{2}t^{-2}T^{-1}]
k_f	(W/(cm-°K))	[MLt^{-3}T^{-1}]			
H	(cm)	[L]			
		SYSTEM PROPERTIES			
ΔT_w	(°K)	[T]	T_{sat}	(°K)	[T]
$\mathcal{R}$	(μm)	[L]	ρ_h	(g/cm^3)	[ML^{-3}]
P	(Pa)	[ML^{-1}t^{-2}]	C_{p_h}	(J/(g-°K))	[L^{2}t^{-2}T^{-1}]
q	(W/cm^2)	[Mt^{-3}]	k_h	(W/(cm-°K))	[MLt^{-3}T^{-1}]

Some discussion of a few of the variables in Table 8 is warranted. The average pore diameter of the fibrous bed is used as the characteristic length of the system. The density of vapor is chosen as a parameter of primary importance, whereas the density of liquid water is not, because the former is affected by moderate levels of pressure and the latter is not. The product of the gravitational constant and the density difference is a measure of buoyancy force, which is of prime importance in boiling, especially for correlations of bubble departure diameter. Because boiling correlations that account for pressure effects through the physical properties of the vapor are not accurate, system pressure is included as a primary parameter. Because system pressure defines saturation temperature, the saturation temperature is not considered significant. Finally, bed porosity, which is found in one of the dimensionless groups, is not included in the parameter list because it is a dimensionless quantity.

The sixteen primary dimensional variables are reduced by three by eliminating surface roughness and by combining the thermal conductivities. The roughness of the heating surface strongly affects boiling, as illustrated in Figure 16. However, the exact characteristic of surface roughness that affects boiling is not well understood, so an accurate measure to quantify roughness for inclusion in the physical property list is not possible; therefore, surface roughness is eliminated from the list of primary parameters. Due to the multiphase nature of flow in the porous medium, use of an effective thermal conductivity simplifies accounting for conduction heat transfer in the bed. A parallel model of the three phases defines an effective thermal conductivity as a function of saturation and porosity:

$$k_{eff} = S\varepsilon k_l + (1-S)\varepsilon k_v + (1-\varepsilon)k_f \quad . \tag{29}$$

This expression is usually simplified by neglecting vapor phase conduction. While bed porosity is easily quantified, saturation is a function of heat flux and is difficult to accurately determine. Consequently, the effective thermal conductivity is typically defined in terms of a saturated bed

(e.g., S = 1) [98], which reduces the parallel model to account for only liquid and fiber:

$$k_{eff} = \varepsilon k_l + (1-\varepsilon)k_f \quad (30)$$

The thirteen parameters in four dimensions can be described by nine dimensionless groups. Expressing the system functional equation with heat flux as the dependent variable results in the following relationship:

$$q = fn\left(\mu_l, \Delta h_v, C_{p_l}, k_{eff}, \sigma, \rho_v, g(\rho_l - \rho_v), K, \overline{D}, H, \Delta T_w, P\right) \quad (31)$$

In dimensionless form, this equation becomes

$$\Pi_1 = fn\left(\Pi_2, \Pi_3, \Pi_4, \Pi_5, \Pi_6, \Pi_7, \Pi_8, \Pi_9\right) \quad (32)$$

The nine dimensionless groups derived for this boiling system are listed in Table 9.

Comparison to Dimensionless Groups in Boiling Correlations

Many of the dimensionless groups developed for this system are commonly used for analysis of pool boiling data. The Prandtl number and various forms of the Nusselt number are frequently used in boiling heat transfer correlations. The Bond number is typically found in bubble diameter correlations, but the buoyancy force term and the surface tension appear in many boiling correlations, especially those for nucleate boiling. The Jakob and Grashof numbers frequently appear in film boiling correlations. Each of these five groups also appear in one or more of the correlations presented for boiling in porous media. The group relating viscous and capillary forces is similar to the capillary number, but among boiling systems, appears to be unique to this system.

Table 9. The dimensionless groups developed with the Buckingham Pi Theorem.

GROUP	KNOWN NAME	PHYSICAL INTERPRETATION
$\frac{q\overline{D}}{k_{eff}\Delta T_w}$	Nusselt Number	Total heat flux -vs- Conductive heat flux
$\frac{C_{p_l}\Delta T_w}{\Delta h_v}$	Jakob Number	Sensible heat consumption -vs- Latent heat consumption
$\frac{\overline{D}^2 g(\rho_l-\rho_v)}{\sigma}$	Bond Number	Buoyancy forces -vs- Capillary forces
$\frac{\rho_l \overline{D}^3 g(\rho_l-\rho_v)}{\mu_l^2}$	Grashof Number	Buoyancy forces -vs- Viscous forces
$\frac{C_{p_l}\mu_l}{k_l}$	Prandtl Number	Momentum diffusivity -vs- Thermal diffusivity
$\frac{\mu_l^2 \Delta h_v}{\sigma^2}$	- -	Viscous forces -vs- Capillary forces
$\frac{P\overline{D}}{\sigma}$	- -	Ratio of bubble force to system pressure force
$\frac{K}{\varepsilon \overline{D}^2}$	Darcy Number	Flow resistance -vs- Area available for flow
$\frac{\overline{D}}{H}$	Geometric Scale Factor	Ratio of physical dimensions of the fibrous beds

The remaining three groups are defined in terms of macroscopic properties of the porous medium. The Darcy number represents a dimensionless permeability, and conveniently combines all of the properties that characterize the porous bed. The next group can be interpreted as an expression of LaPlace's equation for a bubble force balance. Finally, the last group is a geometric scale factor that accounts for the height of the bed.

The Nusselt, Bond, and Grashof numbers are typically defined in terms of a characteristic length appropriate for the particular system. In pool boiling correlations, the Bond number is usually based on the bubble diameter at departure, the Grashof number is usually based on a characteristic length of the heater, and the Nusselt number has been based on both. For porous medium boiling, the Bond and the Grashof numbers have been based on the diameter of the particles composing the bed (Equations 24 and 27, respectively), and the Nusselt number has been based on a hydraulic diameter of the medium (Equation 22), and on the diameter of the particles composing the bed (Equations 24 and 27). In this study, the average pore diameter of the fibrous bed is used as the characteristic length for the Nusselt, Bond, and Grashof numbers.

One noticeably absent dimensionless group is the Reynolds number. The classical definition of the Reynolds number is inapplicable for this system due to the difficulty in defining a characteristic velocity for flow within the fibrous bed. However, an appropriate expression results from defining the velocity in terms of evaporation rate to yield the following expression [95]:

$$Re = \frac{q\,\overline{D}}{\Delta h_v \mu_l \varepsilon} \quad . \tag{33}$$

In order to maintain a mutually exclusive list of dimensionless groups, use of this Reynolds number must exclude the Bond, Jakob, Nusselt, or Darcy number.

The Method for Correlating the Data

Statistical techniques are used to correlate the data from the boiling experiments [104]. After reducing the raw data to dimensionless groups, the data is correlated with multiple linear regression techniques utilizing the log form of the dimensionless groups, as follows:

$$\log \Pi_1 = \log C + \alpha_2 \log \Pi_2 + \alpha_3 \log \Pi_3 + \alpha_4 \log \Pi_4 + \ldots \alpha_9 \log \Pi_9 \quad . \tag{34}$$

The dependent variable is some group that contains the heat flux. The statistically-significant dimensionless groups in the correlation are identified through use of the F-test to yield a final correlation of the form (assuming three statistically-significant independent variables in this illustration)

$$\Pi_1 = C' \Pi_2^{\alpha_2} \Pi_3^{\alpha_3} \Pi_4^{\alpha_4} \quad . \tag{35}$$

Finally, a lack of fit F-test is performed to determine the adequacy of the model in representing the data.

QUANTIFICATION OF SYSTEM PARAMETERS

Each of the thirteen important parameters must be quantified for each experiment to determine the value of the dimensionless groups. Block thermocouple data are used to determine heat flux and heater surface temperature, and the pressure transducer measures system pressure. The porosity of the bed in the boiling cell is measured, and the average pore diameter and permeability of the bed are determined based on correlations for small pads of fibers. Finally, the physical properties of the fluids are based data for a flat vapor/liquid water interface in thermodynamic equilibrium. i.e. the effects of the curved interface in the pore on thermodynamics is neglected. The curve-fitted physical property data are presented in Appendix VII.

For meaningful interpretation of data, it is necessary to know the degree of certainty that a piece of data is accurate. Directly-measured data inherently contain some degree of error, and the extent to which the accuracy of information calculated from these data are affected by propagation of measurement errors must be quantified. In Appendix V, uncertainty analysis for the experimental data of this thesis is performed to account for the effects of both bias and precision errors on accuracy.

Technique for Calculating Heat Flux

The three thermocouples positioned near the surface of the copper heating block are used to calculate heat flux based on one-dimensional heat conduction. The temperature-dependence of the thermal conductivity of the copper precludes direct application of Fourier's law. As detailed in Appendix III the thermal conductivity is mathematically expressed as a function of temperature over the range of 25 to 400°C:

$$k_h = 3.967 - 0.001345\,T + 2.560\times10^{-7}\,T^2 + 2.118\times10^{-9}\,T^3 \quad . \tag{36}$$

This function must be incorporated in the heat diffusion equation to develop the appropriate equation for heat conduction:

$$q = \frac{3.967(T_3 - T_1) - 6.725\times10^{-4}\left(T_3^2 - T_1^2\right) + 8.533\times10^{-8}\left(T_3^3 - T_1^3\right) + 5.295\times10^{-10}\left(T_3^4 - T_1^4\right)}{x_3 - x_1} \quad . \tag{37}$$

As written, this equation expresses the heat flux based on block temperatures measured closest to and furthest from the surface because uncertainty analysis identifies maximum accuracy in calculated heat flux using these two block thermocouple readings. The uncertainty associated with heat flux is 0.9 W/cm^2, which represents between 2 and 20% error for most of the boiling data, but can be as high as 50% in the region of natural convection, incipience of boiling, and boiling in the smallest pore size beds, where the magnitude of heat flux is small. The calculated heat flux can be checked with that measured independently with the watt transducer.

Technique for Calculating Surface Temperature

For simplicity during control of the experiment, the surface temperature of the heating block is simply determined as the intercept of the regression line determined by the temperatures

of the three block thermocouples and their respective positions relative to a surface position of zero. From linear regression analysis, the surface temperature is determined as

$$T_s = \frac{\left(\sum_{i=1}^{3} T_i\right)\left(\sum_{i=1}^{3} x_i^2\right) - \left(\sum_{i=1}^{3} x_i\right)\left(\sum_{i=1}^{3} x_i T_i\right)}{3\left(\sum_{i=1}^{3} x_i^2\right) - \left(\sum_{i=1}^{3} x_i\right)^2} \quad . \tag{38}$$

This method is not correct in a strict sense because the temperature dependence of the thermal conductivity makes the conduction process non-linear. Therefore, after completion of the experiment, the correct surface temperature is determined by iteration using Equation 37 with the heat flux calculated from the first and third thermocouples, and the temperature reading and position of the third thermocouple. The iterated surface temperature differs no more than 0.5°C from the temperature calculated from Equation 38 in any case examined. Uncertainty analysis reveals that the surface temperature is accurate to 0.6°C.

Calculation of Average Pore Diameter

The average pore diameter of the fibrous bed in the boiling cell is based on data from the capillary pressure/saturation experiments using pads made from the three sets of ceramic fibers used in this study. An inherent assumption associated with a pore size distribution determined from the capillary pressure function is that the capillaries are straight channels that extend through the height of the bed. On this basis, each set of data is converted to an average pore diameter which is plotted as a function of porosity. By knowing the porosity of the bed in the boiling cell, an average pore diameter can be graphically interpolated. This approach, of course, assumes that the formation characteristics of the bed in the boiling cell are comparable to those of the small pads used in the capillary pressure/saturation apparatus.

To determine the average pore diameter of the fiber pads used, the capillary pressure function is converted to a curve relating pore diameter to bed water volume, as illustrated in

Figure 47. Each value of pressure difference across the fiber pad is converted to pore diameter with the LaPlace Equation, which requires the contact angle of water on ceramic. Previous studies have used a contact angle of zero for liquid water in glass fiber beds [105,106]. Although a bead of water on a dry glass surface will have a contact angle of about 135° [107], a saturated glass surface

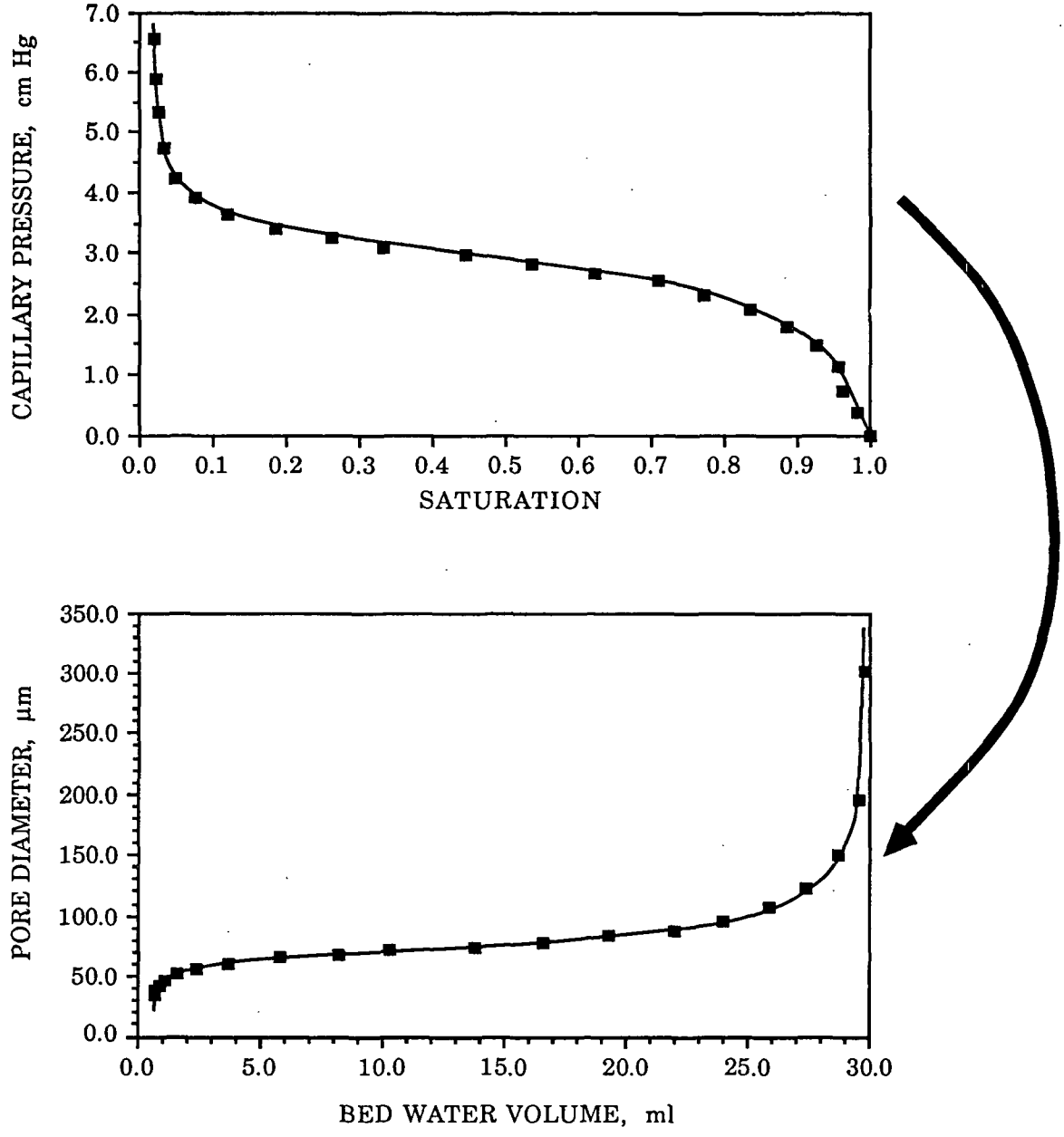

Figure 47. Conversion of a capillary pressure function into a graph relating pore diameter to water volume. These particular data are for a pad composed of 8.4 µm diameter silica fibers with a porosity of 0.933 and a number average pore diameter of 74.0 µm.

will have a contact angle of zero [108]. Because drainage from an initially saturated fiber pad is occurring here, a contact angle of zero degrees is assumed [e], and the LaPlace Equation reduces to

$$\Delta P_c = \frac{4\sigma}{D} \quad . \tag{39}$$

Bed water volume is determined as the difference between saturated bed water volume and displaced water volume. From this graph, the change in bed water volume (displaced water volume) corresponding to equal increments in pore diameter (for example, equal increments of 10 μm) is determined. As illustrated in Table 10, this information is used to generate a pore diameter distribution. The frequency is determined as the number of straight-through capillaries having a volume equivalent to the change in water volume for a given increment in diameter. The number average diameter, determined as

$$\overline{D} = \frac{\sum\left(\text{Local Average Diameter x Frequency}\right)}{\sum \text{Frequency}} \quad , \tag{40}$$

is used as the average pore diameter of the bed. With this definition, the small pores affect the average to a greater degree than do the large pores. Uncertainty analysis reveals an uncertainty of 2.3% for the average pore diameter.

As is evident in Figure 47, pore diameter approaches infinity at very small capillary pressures. A small volume of water occupies these largest pores that are dewatered in going from a saturated state to the first data point (the largest pore diameter detected in the experiment). To account for this volume during graphical analysis of the pore diameter/bed water volume curve,

[e] If the true contact angle is not zero, then the calculated average pore diameter will overestimate the true average by a factor equivalent to the cosine of the true contact angle.

Table 10. Mathematical reduction of the capillary pressure function to an average pore diameter.

Pore Diameter (μm)	Bed Water Volume (ml)	Average Pore Diameter [$\bar{d}$ (μm)]	Change in Bed Water Volume [ΔV (ml)]	Frequency $\left[\frac{\Delta V}{(\pi/4)\bar{d}^2 L}\right]$	Frequency x Average Pore Diameter
...	...	...	...	...	...
250	19.2	255	2.3	1773	452115
260	21.5	265	1.6	1142	302630
270	23.1	275	1.6	1061	291651
280	24.7	...	...	...	...
...	...				

the pore diameter is incremented beyond the largest measured one, and the volume of water initially removed is distributed among these larger pore diameters in a decreasing fashion. Typically, eight to ten additional diameter increments are needed to distribute this initially-displaced volume of water. Because this volume is such a small portion of the total displaced water volume (each increment is typically assigned volumes of 0.1 to 0.3 ml), this subjective assignment affects the number average pore diameter by less than one percent.

Permeability Measurement

Due to geometric constraints, accuracy of permeability measurement of the fibrous bed in the boiling cell is limited. Therefore, permeability of small-diameter pads of fibers is measured as a function of porosity, and from this relationship, the permeability of the fibrous bed in the boiling cell is determined as a function of porosity. As a flow of water is passed through the bed, a graduated cylinder and a stopwatch measure the flow rate, and a Validyne differential pressure transducer measures the pressure drop across a distance of 2.47 cm. For each fiber diameter, a data set is collected at each of six different levels of pad porosity, and each data set is composed of six pairs of pressure drop/water flow rate data. The raw data for this experiment is illustrated in Figure 48 for the 3.0 μm diameter fiber. To insure that the measurements are made in the viscous

flow regime where Darcy's law applies, very low water flow rates are used. The linearity of the data in Figure 48 is evidence of the Darcy flow regime. Accordingly, the permeability is determined as

$$K = \frac{V \mu_l L}{A t \Delta P} \quad . \tag{41}$$

Uncertainty analysis shows that the calculated permeability is accurate to within 2.9%.

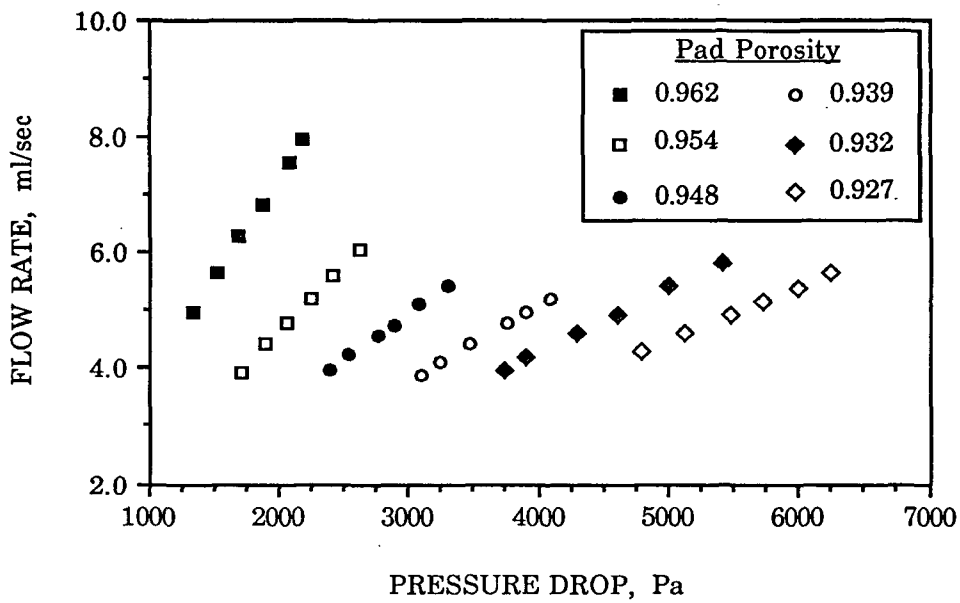

Figure 48. Raw data for determination of permeability for the pad made from 3.0 μm diameter alumina fibers.

Porosity Determination

Porosity is determined for the fiber pad in the capillary pressure/saturation apparatus, and for the fibrous bed in the boiling cell. Porosity of the fiber pad is determined from total pad volume, as determined by the sum of displaced water volume, residual water volume, and ceramic fiber volume:

$$\varepsilon = \frac{V_R + V_D}{V_R + V_D + \frac{W_f}{\rho_f}} \quad . \tag{42}$$

Residual water volume is determined after completion of the capillary pressure/saturation experiment as the difference in weight between the moist pad and pad weight after drying. Uncertainty analysis reveals an accuracy for pad porosity of 0.2%.

Boiling cell porosity is determined from the dimensions of the bed and from the weight of fiber in the bed, as determined gravimetrically by drying after the boiling experiment:

$$\varepsilon = \frac{\frac{\pi}{4} H\, d_{bc}^2 - \frac{W_f}{\rho_f}}{\frac{\pi}{4} H\, d_{bc}^2} = 1 - \frac{W_f}{\frac{\pi}{4} \rho_f H\, d_{bc}^2} \quad . \tag{43}$$

Uncertainty analysis reveals an accuracy for boiling cell porosity of 0.5%.

RESULTS AND DISCUSSION

The experiments performed in this thesis are segregated into two groups. The main thesis experiments focus on boiling in the fibrous beds, while supplementary experiments provide data to macroscopically characterize the fibrous beds. Results of the supplementary experiments will be discussed prior to the main experiments. All data utilized in this thesis are collected in Appendix VIII in either raw or reduced form.

The dimensionless correlations presented in this discussion are formulated from stepwise regression analysis, and the lack of fit F-test [104] is used to determine if the correlation does statistically fit the data. Because there are no genuine repeated runs as required by strict application of the lack of fit test, the data has been classified according to values of the statistically-significant independent dimensionless groups to approximate repeat runs. Briefly, testing for lack of fit involves segregating the residual sum of squares into its two components - pure error and lack of fit. Then, the ratio of lack of fit mean square to pure error mean square defines the F-statistic for the correlation, which upon comparison to tabulated values reveals the significance of fit. Reference 104 provides a detailed discussion of the procedure.

EXPERIMENTS TO CHARACTERIZE THE FIBROUS BEDS

As previously discussed, it is essential to characterize macroscopic parameters of the fibrous beds used in the boiling studies to adequately quantify their impact on the boiling process. The porosity of the bed is measured in the boiling cell, but practical considerations necessitate that bed permeability and average pore diameter be measured for small pads of fibers with supplemental apparatuses. By curve-fitting the data collected for these properties against porosity, appropriate values of permeability and average pore diameter are determined for the fiber bed in the boiling cell apparatus.

Average Pore Diameter Data

The data for average pore diameter as determined from the capillary pressure functions are illustrated in Figure 49. Each data point is reduced from one capillary pressure function. The porosities of the fiber pads are very high, indicating a large pore volume, which is typical of porous media composed of incompressible fibers [109,110]. As expected, the average pore diameter decreases as the pad is compressed to lower porosities. The curvature of the data for the 18.5 μm diameter fibers is much more pronounced than either of the small diameter fibers, and, as discussed below, appears to be a reflection of the packing structure of the fibrous beds.

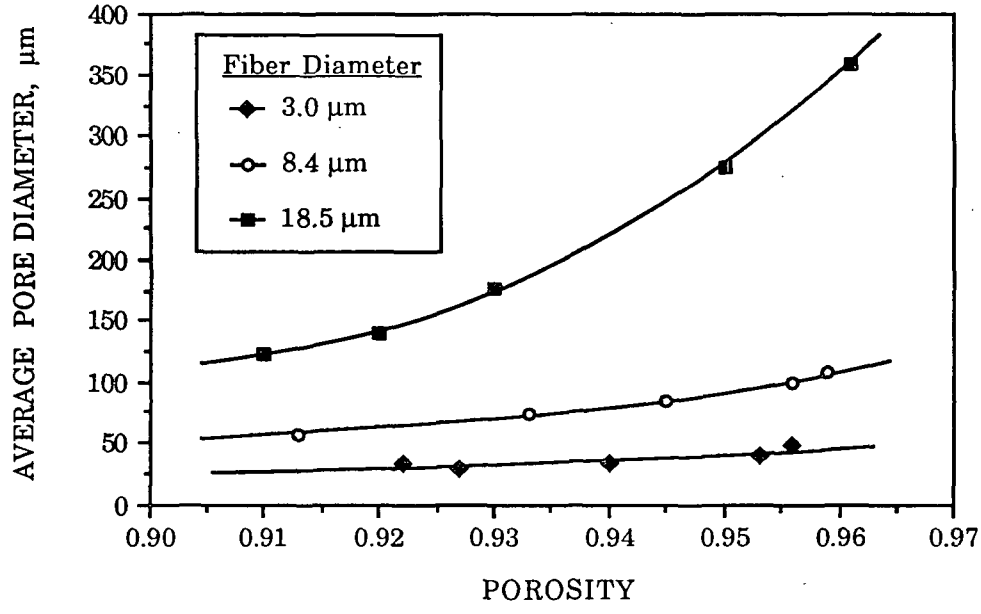

Figure 49. The average pore diameter data determined from the capillary pressure functions.

The magnitude of the average pore diameter intuitively seems to be large in comparison to the diameter of the fibers themselves. Rather than truly representing the actual pore size of the pad, the assumption of straight-through capillaries inherent in deducing the average pore diameter from a capillary pressure function tends to overestimate the actual pore diameter. Considering the practicality of other measurement techniques, this approach is justified because it does provide a relative ranking of the fibrous beds.

The three sets of data are curve-fitted with the following equations:

3.0 μm diameter: $$\overline{D} = \frac{1}{(0.5068 - 0.4944\sqrt{\varepsilon})} \quad , \qquad r^2 = 0.87 \qquad (44)$$

8.4 μm diameter: $$\overline{D} = \frac{1}{(0.3343 - 0.3317\sqrt{\varepsilon})} \quad , \qquad r^2 = 0.99 \qquad (45)$$

18.5 μm diameter: $$\overline{D} = -173{,}112.0 + 609{,}855.2\,\varepsilon - 714{,}424.2\,\varepsilon^2 + 278{,}525.9\,\varepsilon^3 \quad , \qquad r^2 = 0.99 \qquad (46)$$

These equations are used to determine the average pore diameter of the fibrous bed in the boiling cell from knowledge of the bed porosity. The range of porosity achievable in the boiling cell appears to be about 0.94 to 0.95 for beds made from the ceramic fibers studied here, which limits the average pore diameter range for the boiling experiments to about 30 to 275 μm.

By applying dimensional analysis, the average pore diameter data can be correlated with one equation. The following functional equation is developed from considerations of the packing structure of the fibrous medium:

$$\overline{D} = fn(d_f, L_f, \zeta) \quad , \qquad (47)$$

where ζ is the total fiber length per unit volume. Then, the solid fraction is determined to be

$$1 - \varepsilon = \frac{\pi}{4} d_f^2 \, \zeta \quad , \qquad (48)$$

from which the definition of zeta is found to be

$$\zeta = \frac{1 - \varepsilon}{\frac{\pi}{4} d_f^2} \quad . \qquad (49)$$

By application of the Buckingham Pi Theorem, four variables in one dimension yield three dimensionless groups, which transforms the functional equation into the following dimensionless form:

$$\frac{\overline{D}}{L_f} = fn\left(\left[\frac{1-\varepsilon}{\frac{\pi}{4}d_f^2}\right]L_f^2, \frac{d_f}{L_f}\right) \quad . \tag{50}$$

By inspection, the following equation is found to correlate the data very well:

$$\frac{\overline{D}}{L_f} = 0.0200 + \frac{1.664}{\left(\left[\frac{1-\varepsilon}{\frac{\pi}{4}d_f^2}\right]L_f^2\right)^{1.5}\left(\frac{d_f}{L_f}\right)^{1.5}} \quad . \tag{51}$$

This correlation, which fits the data to ± 12.5%, is illustrated in Figure 50, the normalized residuals (defined as the difference between actual and predicted values divided by the actual value) are illustrated in Figure 51, and the regression statistics are listed in Table 11. The lack of fit test indicates that the correlation cannot be rejected with more than 95% certainty.

The dimensionless groups of this correlation indicate that the average pore diameter depends on the diameter and length of the fibers, and the solid fraction of the medium. These three factors determine how the fibers are distributed in the medium, which essentially defines pore size. The significance of the exponent of 1.5 is not apparent.

Permeability Data

The data for permeability as determined under Darcy flow conditions is illustrated in Figure 52. Each data point represents the average of six readings that are measured for a particular level of pad compression under different conditions in the Darcy flow regime. As

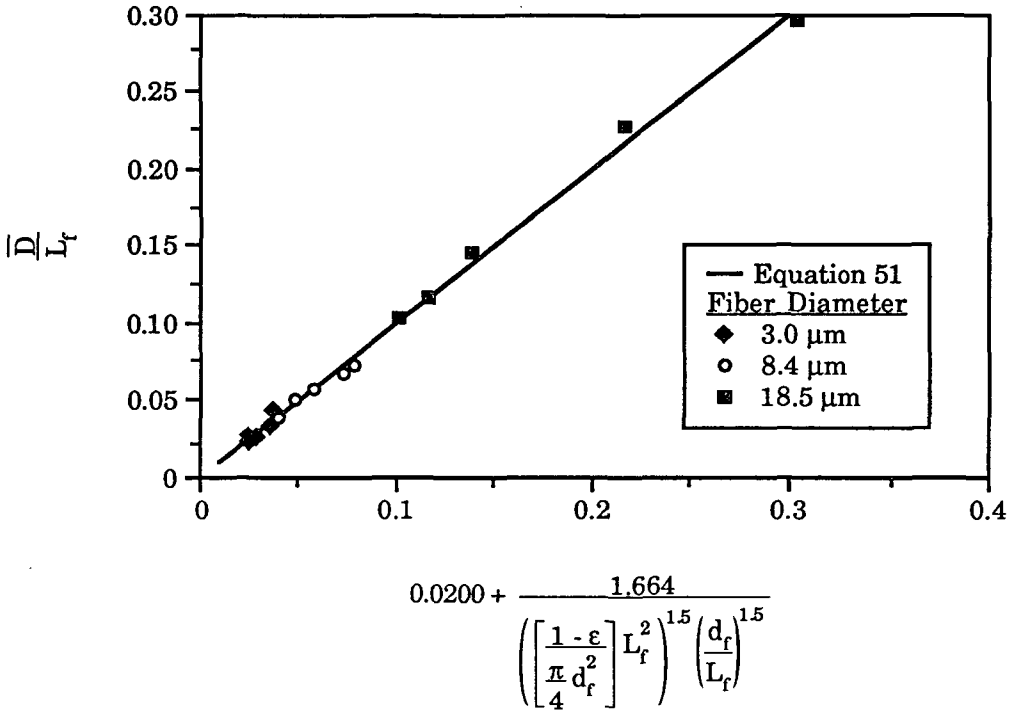

Figure 50. Dimensionless correlation for the average pore diameter data.

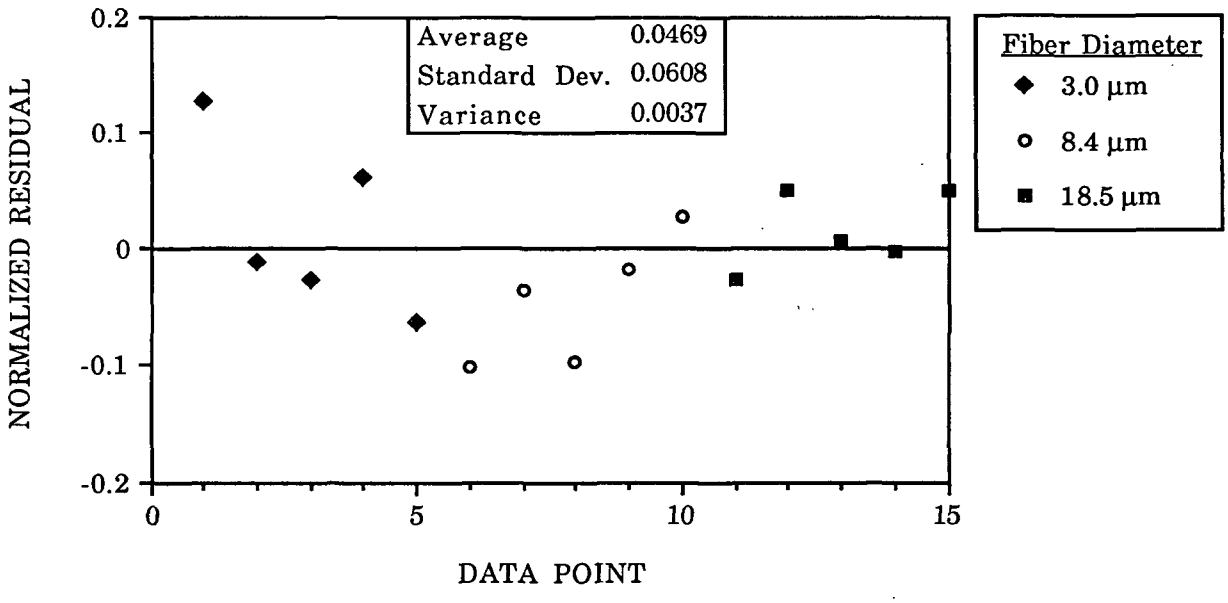

Figure 51. Normalized residuals for the average pore diameter correlation.

Table 11. Statistics for the stepwise regression and lack of fit F-test for the average pore diameter correlation (Equation 51).

Stepwise Regression

Adjusted coefficient of determination (r^2_{adj}) = 0.995

Critical F-statistic = F(15,15,0.99) = 3.52

Analysis of Variance

Source	Degrees of Freedom	Sum of Squares	Mean Square	F-statistic for Correlation
Regression	1	0.088	0.088	2953.18
Residual	13	0.0003853	0.0000296	
Total	14	0.088		

F-statistic for $\left(\left[\frac{1-\varepsilon}{\frac{\pi}{4}d_f^2}\right]L_f^2\right)^{-1.5}\left(\frac{d_f}{L_f}\right)^{-1.5}$ = 2953.18, and standard error = 0.031.

Lack of Fit Test

Source of Residual Sum of Squares	Degrees of Freedom	Sum of Squares	Mean Square	F-statistic for Lack of Fit
Pure Error	5	0.002843	0.000569	0.072
Lack of Fit	7	0.000286	0.000041	

F(7,5,0.99) = 10.5
F(7,5,0.95) = 4.9

Because the F-statistic for lack of fit is less than either of the critical values, the correlation cannot be rejected with more than 95% certainty.

expected, the permeability of the fibrous pad decreases as it is compressed to lower porosities. Though the data appear to be linear on the log ordinate axis, the data for all three of the fiber diameters are fitted with cubic polynomials:

3.0 μm diameter: $K = \left(-0.9652 + 3.096\,\varepsilon - 3.310\,\varepsilon^2 + 1.180\,\varepsilon^3\right) x 10^{-6}$, $r^2 = 0.99$ (52)

8.4 μm diameter: $K = \left(-2.759 + 8.888\,\varepsilon - 9.543\,\varepsilon^2 + 3.416\,\varepsilon^3\right) x 10^{-6}$, $r^2 = 0.99$ (53)

18.5 μm diameter: $K = \left(-3.315 + 10.97\,\varepsilon - 11.86\,\varepsilon^2 + 4.278\,\varepsilon^3\right) x 10^{-6}$, $r^2 = 0.99$ (54)

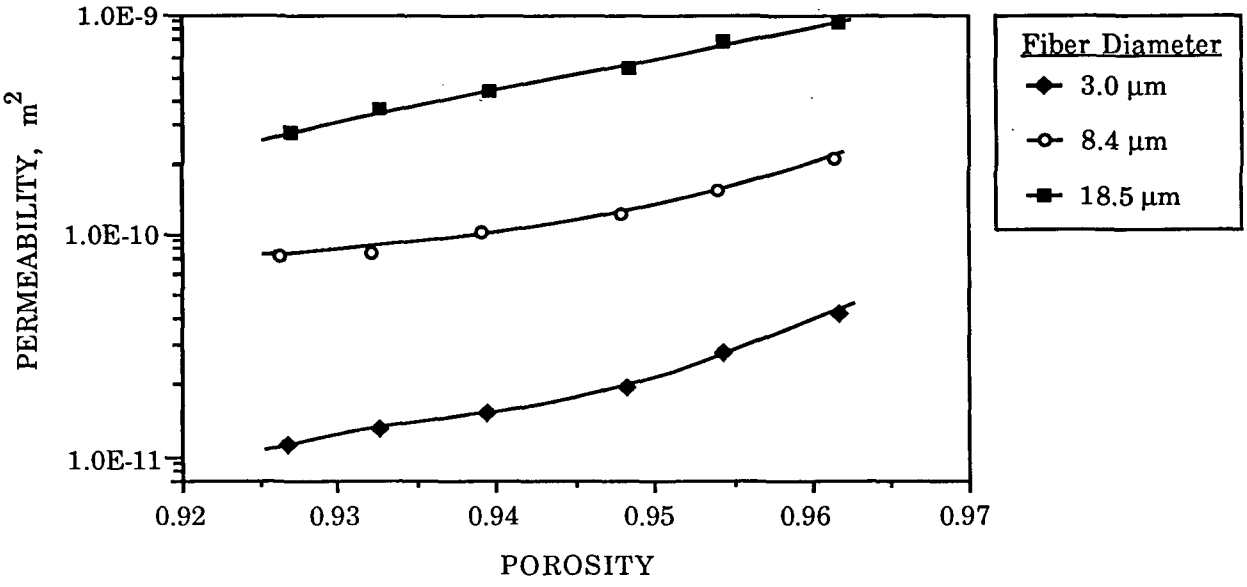

Figure 52. Permeability data determined for small pads of ceramic fibers.

These equations are used to determine the permeability of the fibrous bed in the boiling cell from knowledge of the bed porosity. In the range of achievable porosity, the bed permeability is limited to a range of 2×10^{-11} to 6×10^{-10} m^2 for the boiling experiments.

DATA FOR BOILING IN A FIBROUS BED

As illustrated in Figure 53, boiling in a porous medium generates exciting phenomena, as vigorous vapor flow occurs through a bed height of even 25 cm! To investigate this phenomena, twenty-one fibrous media boiling experiments have been completed, for which pertinent information is listed in Table 12. In comparison to the experimental design in Table 7, many additional experimental conditions have been afforded by compressing the fiber beds to different average pore diameters. Most of the experiments have been performed with beds composed of 18.5 μm diameter alumina fiber because this is the easiest and cleanest fiber to work with. However, enough data for beds made from each type of fiber have been collected to draw some interesting conclusions. The reduced data for heat flux and wall superheat are listed for each experiment in Table 13, and the corresponding graphs are located in Appendix VIII.

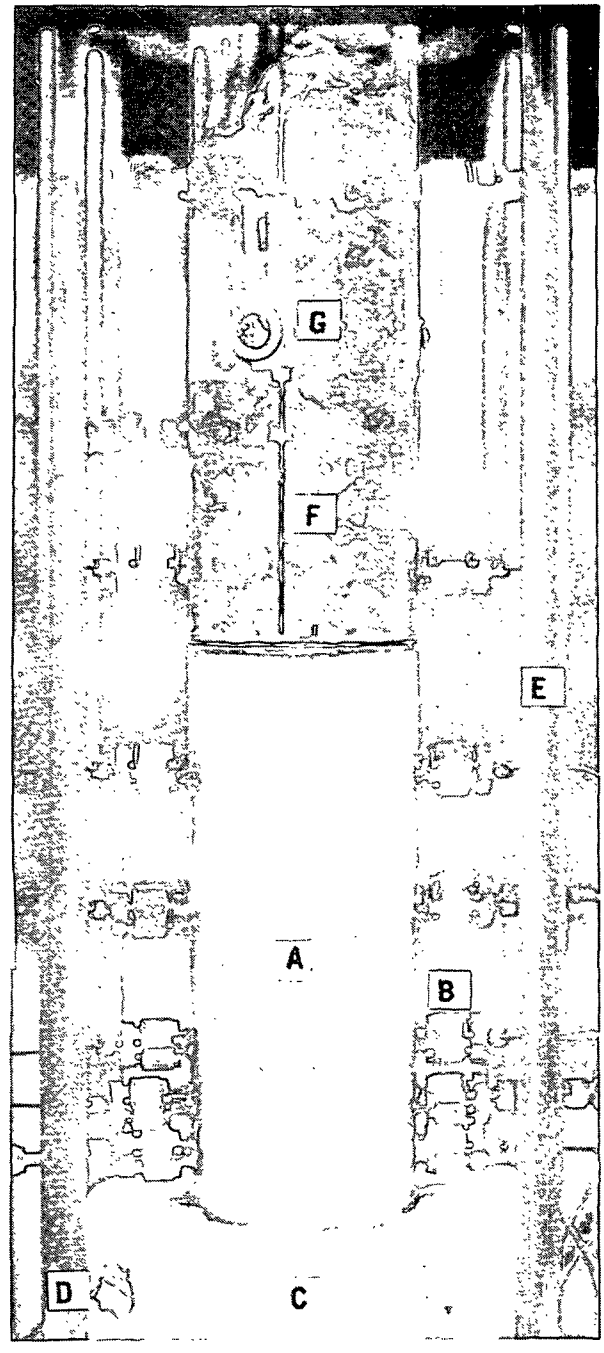

A - ceramic fiber bed
B - bed thermocouple and Swagelok® fitting
C - insulated heating block
D - block thermocouple
E - 5/8-inch diameter support rod
F - overlying liquid pool
G - teflon forming media support

Figure 53. A photograph of boiling in a 25-cm high bed composed of 18.5 μm diameter fibers.

Table 12. Information about the fibrous beds and experimental conditions for the boiling experiments. The designation "CBE" for the data sets is an acronym for "Critical Boiling Experiment".

Data Set	Fiber Diameter (μm)	Porosity	Average Pore Diameter (μm)	Permeability (m^2)	Bed Height (cm)	System Pressure (MPa)	Initial Saturation	Iso-Heat Flux Value (W/cm^2)
CBE13	18.5	0.946	250.8	5.48E-10	12.38	0.28	0.90	25.6
CBE14	18.5	0.946	250.8	5.48E-10	12.38	0.19	0.78	19.8
CBE15	18.5	0.947	256.8	5.66E-10	12.38	0.14	0.68	17.8
CBE17	18.5	0.946	250.8	5.48E-10	12.22	0.14	0.53	21.4
CBE18	18.5	0.943	233.6	4.98E-10	11.43	0.10	0.72	17.3
CBE21	18.5	0.943	233.6	4.98E-10	15.56	0.10	0.58	15.5
CBE22	18.5	0.945	244.9	5.31E-10	11.76	0.10	0.61	16.1
CBE23	18.5	0.943	233.6	4.98E-10	7.95	0.10	0.66	21.3
CBE24	18.5	0.946	250.8	5.48E-10	15.56	0.10	0.61	16.9
CBE25	18.5	0.946	250.8	5.48E-10	15.57	0.10	0.59	16.4
CBE26	18.5	0.944	239.2	5.14E-10	7.95	0.10	0.58	16.0
CBE29	18.5	0.942	228.2	4.82E-10	9.21	0.10	0.58	16.0
CBE30	18.5	0.943	233.6	4.98E-10	9.21	0.19	0.60	23.5
CBE8	8.4	0.946	85.9	1.13E-10	16.51	0.10	0.47[a]	4.5
CBE9	8.4	0.934	73.0	8.72E-11	13.02	0.10	0.43[a]	4.0
CBE16	8.4	0.945	84.7	1.10E-10	10.95	0.19	0.63[a]	6.4
CBE10	3.0	0.957	43.4	3.19E-11	15.56	0.10	0.32[a]	2.2
CBE12	3.0	0.949	39.9	2.05E-11	12.70	0.10	0.38[a]	1.5
CBE27	3.0	0.955	42.4	2.83E-11	10.48	0.10	0.43[a]	1.8
CBE28	3.0	0.951	40.7	2.26E-11	9.53	0.19	0.47[a]	4.4
CBE31	3.0	0.956	42.9	3.00E-11	10.48	0.28	0.43[a]	4.4

a - The bed did not become fully engulfed in two-phase flow.

Table 13. The reduced data for the boiling experiments. The data below lists the heat flux and wall superheat for each boiling curve determined from the raw temperature data measured by the block thermocouples. The designation "1->3" indicates the two block thermocouples used to calculate the heat flux (Equation 37). Thermocouple 1 is closest to the boiling surface, thermocouple 3 is furthest from the surface, and thermocouple 2 is inbetween. Experiments CBE19 and CBE20 are for pool boiling of water, and the rest are for boiling in fibrous beds.

	CBE13		CBE14		CBE15		CBE17		CBE18	
Data Point	Wall Superheat (°C)	Heat Flux 1->3 (W/cm^2)	Wall Superheat (°C)	Heat Flux 1->3 (W/cm^2)	Wall Superheat (°C)	Heat Flux 1->3 (W/cm^2)	Wall Superheat (°C)	Heat Flux 1->3 (W/cm^2)	Wall Superheat (°C)	Heat Flux 1->3 (W/cm^2)
1	1.30	1.06	1.35	0.81	1.00	1.65	1.41	1.13	3.81	1.43
2	3.90	1.89	3.58	1.86	3.28	3.63	4.85	2.77	6.40	3.96
3	8.33	4.16	5.65	2.98	7.08	3.84	7.75	3.63	8.58	5.33
4	11.54	9.22	9.05	3.23	10.98	6.55	10.61	4.10	15.34	7.36
5	9.55	17.87	12.91	4.10	13.70	9.04	14.52	3.88	19.93	9.74
6	11.26	27.35	15.23	8.47	16.55	10.80	20.41	6.75	22.25	10.64
7	12.90	24.74	13.29	17.26	20.05	11.74	21.70	9.38	23.72	11.58
8	17.29	25.53	13.28	23.19	22.13	15.34	21.82	12.49	26.17	14.86
9	23.31	26.31	20.78	21.10	25.01	17.20	21.85	15.86	31.96	17.09
10	35.92	26.31	23.46	18.74	26.81	17.00	24.71	21.25	35.48	17.59
11	52.31	26.51	32.73	17.90	30.38	16.83	30.06	19.13	42.73	18.35
12	76.46	25.28	40.91	18.41	37.58	18.47	35.00	20.75	57.59	17.93
13	100.74	25.22	56.77	19.08	50.46	17.86	43.50	22.07	79.15	17.26
14	130.38	25.33	76.46	20.17	66.34	18.78	60.15	21.74	104.37	17.12
15	163.86	25.19	96.36	19.96	90.96	17.99	81.17	21.39	135.10	15.97
16	203.40	25.18	120.81	19.53	114.27	17.54	103.46	22.09	168.25	15.60
17			159.94	20.15	138.68	18.09	133.50	21.53	202.79	18.50
18					162.96	17.78	161.21	22.19		
19					187.28	17.83	189.89	21.74		

Table 13. (continued)

Data Point	CBE21 Wall Superheat (°C)	CBE21 Heat Flux 2->3 (W/cm^2)	CBE22 Wall Superheat (°C)	CBE22 Heat Flux 1->3 (W/cm^2)	CBE23 Wall Superheat (°C)	CBE23 Heat Flux 1->3 (W/cm^2)	CBE24 Wall Superheat (°C)	CBE24 Heat Flux 1->3 (W/cm^2)	CBE25 Wall Superheat (°C)	CBE25 Heat Flux 1->3 (W/cm^2)
1	2.01	1.64	2.33	1.17	1.11	1.35	0.25	2.42	1.18	1.84
2	3.78	3.37	4.80	3.28	4.37	2.86	1.22	2.82	4.72	4.15
3	7.01	4.95	8.72	5.69	8.98	3.44	5.03	3.90	10.20	7.46
4	11.27	7.17	12.10	7.28	13.03	4.97	8.54	5.99	14.51	10.64
5	17.01	6.80	17.16	10.60	19.59	6.82	14.90	7.69	19.38	17.51
6	19.93	9.09	26.71	16.23	19.92	8.12	20.29	9.17	20.13	21.39
7	25.31	8.06	33.31	16.57	19.26	8.53	20.80	20.26	28.99	15.93
8	29.34	10.51	40.88	16.26	24.83	10.92	28.21	16.18	34.85	15.89
9	31.91	14.64	48.73	16.19	29.19	17.36	34.68	16.94	46.65	16.27
10	37.90	14.09	63.07	15.15	38.40	20.18	46.27	16.67	63.66	16.98
11	45.08	14.29	77.07	15.53	44.85	21.26	60.25	17.01	83.73	16.38
12	54.82	14.84	94.35	16.04	51.85	21.26	80.67	16.92	109.76	16.65
13	71.23	15.23	118.91	15.81	63.86	20.82	108.93	17.39	143.07	16.49
14	93.47	15.82	151.85	16.32	77.54	20.94	153.17	16.87	176.04	16.36
15	121.76	16.17	199.54	17.32	96.54	20.64	202.10	17.13	209.53	16.24
16	156.29	16.12			114.47	21.44				
17	199.43	17.76			139.39	21.69				
18					169.41	21.49				
19					204.38	21.89				

Table 13. (continued)

Data Point	CBE26 Wall Superheat (°C)	CBE26 Heat Flux 2->3 (W/cm^2)	CBE29 Wall Superheat (°C)	CBE29 Heat Flux 2->3 (W/cm^2)	CBE30 Wall Superheat (°C)	CBE30 Heat Flux 1->3 (W/cm^2)	CBE8 Wall Superheat (°C)	CBE8 Heat Flux 1->3 (W/cm^2)	CBE9 Wall Superheat (°C)	CBE9 Heat Flux 1->3 (W/cm^2)
1	2.11	0.91	1.65	2.62	2.27	1.93	1.12	1.49	1.25	0.97
2	5.26	3.29	4.44	3.97	5.58	3.36	3.74	1.53	3.28	1.87
3	10.94	5.77	10.48	6.77	10.61	6.35	6.77	2.30	6.91	2.02
4	16.15	9.53	16.59	7.65	12.82	10.08	9.79	3.31	9.91	2.97
5	20.11	12.88	20.41	10.31	14.64	12.90	12.77	3.94	13.69	2.64
6	21.68	16.13	20.40	13.20	14.48	16.98	15.75	5.85	16.75	3.11
7	27.78	15.03	21.73	15.63	14.11	22.38	21.28	3.88	21.66	3.45
8	34.61	15.86	25.37	19.28	12.90	28.64	26.08	4.58	27.28	3.88
9	47.06	15.78	32.83	15.97	19.06	25.06	31.58	4.47	37.27	3.49
10	63.02	17.11	36.42	16.57	26.55	23.87	40.44	4.37	48.34	3.67
11	87.18	15.53	46.10	16.60	35.26	24.80	51.80	4.27	62.26	4.13
12	118.34	15.36	65.01	15.04	52.77	23.62	62.48	4.86	77.63	3.73
13	152.70	16.90	84.27	15.28	74.80	23.06	76.67	4.31	102.06	3.81
14	203.49	16.58	107.14	15.26	97.77	23.10	91.64	4.52	127.59	4.38
15			139.95	16.22	126.45	23.32	114.70	5.21	155.94	4.04
16			173.17	16.95	161.06	23.06	142.45	4.37	198.15	4.11
17			205.77	18.24			176.40	4.53	237.11	3.99
18							221.14	4.51	285.09	4.52
19							260.58	4.93		

Table 13. (continued)

Data Point	CBE16 Wall Superheat (°C)	CBE16 Heat Flux 1->3 (W/cm^2)	CBE10 Wall Superheat (°C)	CBE10 Heat Flux 1->3 (W/cm^2)	CBE12 Wall Superheat (°C)	CBE12 Heat Flux 1->3 (W/cm^2)	CBE27 Wall Superheat (°C)	CBE27 Heat Flux 1->3 (W/cm^2)	CBE28 Wall Superheat (°C)	CBE28 Heat Flux 1->3 (W/cm^2)
1	3.12	0.82	1.98	0.61	1.65	0.48	1.96	0.54	1.75	1.55
2	4.48	1.63	4.71	1.04	3.35	1.39	4.68	0.65	4.83	2.85
3	7.99	2.41	7.28	1.00	7.28	2.10	8.52	0.87	8.15	4.85
4	11.78	3.26	11.40	1.07	14.36	0.98	12.43	1.52	14.80	4.38
5	17.73	4.91	14.14	1.37	18.89	1.64	16.57	1.25	20.58	3.96
6	23.87	6.33	17.82	1.34	23.42	1.51	20.79	1.67	26.39	4.63
7	30.63	6.78	22.66	2.03	29.52	1.85	27.65	1.51	36.06	4.31
8	45.00	5.66	33.25	2.39	38.44	1.52	32.95	1.51	50.45	4.59
9	53.17	6.50	43.69	2.09	55.50	1.61	45.19	1.46	71.10	4.76
10	67.05	6.02	57.97	1.92	69.43	1.01	59.58	1.83	96.08	4.48
11	82.01	6.38	73.87	2.12	87.58	1.50	78.86	2.39	121.04	4.98
12	101.37	7.02	94.04	1.96	113.12	1.42	104.91	1.43	151.20	4.30
13	125.31	6.35	119.45	1.93	137.76	1.81	134.18	1.80	181.65	4.19
14	150.70	6.36	145.59	2.46	175.98	1.44	167.61	2.56	211.56	4.26
15	174.52	6.21	181.08	2.44	202.69	1.14	212.05	2.29		
16	204.57	6.39	219.50	2.50	241.97	1.29				
17			270.37	2.45	287.32	1.34				

Table 13. (continued)

Data Point	CBE31 Wall Superheat (°C)	CBE31 Heat Flux 1->3 (W/cm^2)	CBE19 Wall Superheat (°C)	CBE19 Heat Flux 1->3 (W/cm^2)	CBE20 Wall Superheat (°C)	CBE20 Heat Flux 1->3 (W/cm^2)
1	2.83	2.11	2.14	3.26	1.47	4.08
2	6.93	2.72	2.99	4.89	3.89	6.35
3	12.72	4.20	7.03	8.82	6.44	9.91
4	18.47	4.19	10.33	18.81	7.88	18.02
5	22.36	4.60	12.49	32.04	10.15	26.41
6	27.08	4.47	13.88	41.53	12.24	39.37
7	35.21	4.43	14.58	49.84	14.01	47.13
8	45.90	4.22	15.72	61.87	15.56	57.86
9	61.58	4.62	15.70	74.79	17.56	69.88
10	80.23	4.50	16.66	91.65		
11	104.67	4.47				
12	130.85	4.17				
13	154.71	4.47				
14	180.68	4.20				

The discussion of the boiling data will be segregated into four sections. First, visual observations of the boiling experiment will be presented, followed by a discussion of the postulated mechanisms. Third, the effects of parametric influences studied here will be presented. Finally, correlation of the boiling data will be discussed.

The reader is cautioned that the data comparisons to be presented are only intended to illustrate trends effected by experimental parameters. Because data to be compared are from experiments with similar, but not identical, average pore diameters and bed heights, the data should not be interpreted for absolute magnitudes of parametric effects.

Visual Observations of the Boiling Phenomena

After forming the fiber bed in the boiling cell, the apparatus is assembled and prepared for a boiling experiment. The experiment is initiated from a room temperature, quiescent state by slowly heating to a surface temperature about 7°C above the system saturation temperature, where the process is held in a boiling state for about one hour. Then, the initial desired surface temperature setpoint and its associated ramp rate are selected and downloaded to the temperature controller, and the data acquisition portion of the experiment begins. Completion of a boiling experiment requires approximately five hours.

As the system is heating up, thermal changes occur within the bed. At surface temperatures below the system saturation temperature, no activity is visually observed in the system. The temperature measured by the bed thermocouple near the heater surface rises slowly due to conduction of heat from the heater surface. At a surface temperature about 1 to 2°C above saturation, boiling begins. The temperature near the heater surface rapidly increases to a value near the system saturation temperature as a two-phase zone begins to develop. As heat flux increases, the height of the two-phase zone increases, and a faint line of demarcation between the two-phase zone and the liquid-saturated portion of the bed is observed to rise. Concurrently, the liquid water displaced from the bed raises the height of the overlying column of water. As the

rising interface between the two-phase and liquid-saturated zones contacts a bed thermocouple, the temperature reading rapidly escalates to near the system saturation temperature. For the beds with a large average pore diameter, the height of this isothermal, two-phase zone increases until the entire bed is engulfed in two-phase flow, which typically occurs before a wall superheat of 5°C is reached. However, for beds with a small average pore diameter, the maximum height of the two-phase zone is about 8 to 10 cm, so depending on bed height, the entire bed may not be engulfed in two-phase flow. Temperature measurements at various locations within the bed indicate that the entire height of the two-phase zone is isothermal.

Description of the phenomena in the overlying liquid layer can be illustrated by referring to Figure 54, which includes four photographs representing the activity at various stages of an experiment for boiling in a bed composed of 18.5 μm diameter fibers. As the two-phase zone begins to develop, the quiescent liquid layer rises in the boiling cell (Figure 54a). At some point, the two-phase zone engulfs the entire bed, and the small bubbles that begin to protrude from the top of the bed condense to warm the liquid. As this occurs, the height of the liquid is observed to surge up and down as much as ± 0.5 cm. As the level surges up, strong thermal currents protruding from the bed are visually apparent. When the overlying liquid layer reaches saturation temperature, the vapor bubbles no longer condense, but rather, agitate the pool of liquid. Figure 54b depicts this situation at low heat flux. As heat flux increases, churning of liquid becomes more vigorous (Figure 54c), and finally achieves a turbulent state (Figure 54d). This turbulent condition is achieved early during the experiment and is maintained throughout the boiling run. Agitation of the pool is not observed for beds with small average pore diameters because two-phase flow does not engulf the entire bed height. Rather, most of the vapor condenses within the bed.

A Qualitative Description of the Postulated Phenomena

Typical boiling curves measured with the experimental system are compared in Figure 55. Only the nucleate regime of the pool boiling curve for water was measured. The curve for the fibrous bed exhibits two boiling regimes and a point of transition between them that represents the

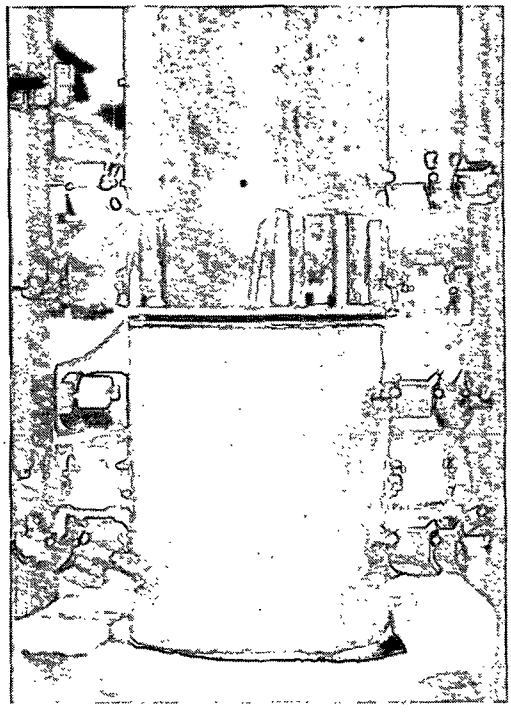

a. Stagnant, rising pool as vapor is contained in the bed.

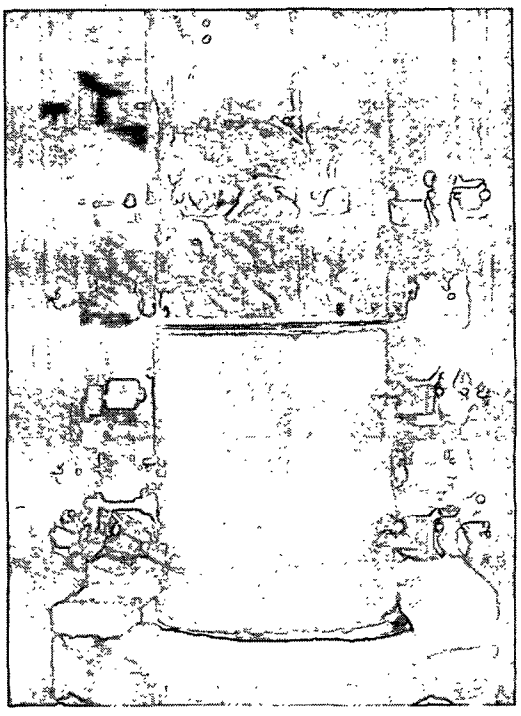

b. Distinct bubbles emanating from the bed at low heat fluxes.

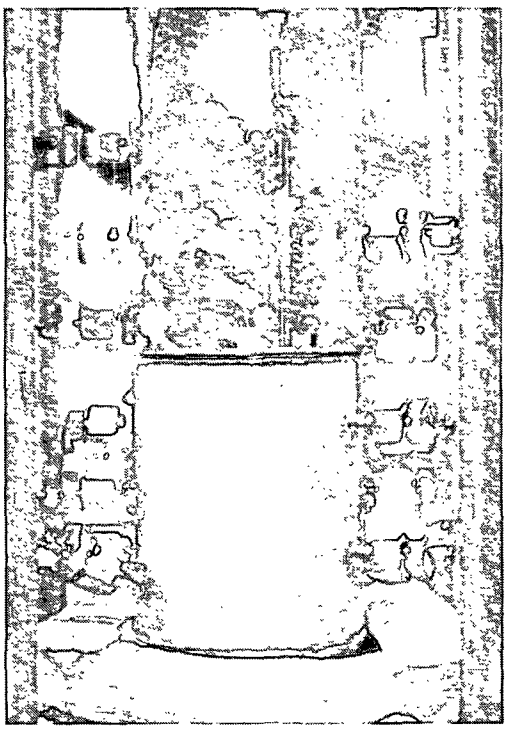

c. Vigorous agitation of pool by vapor.

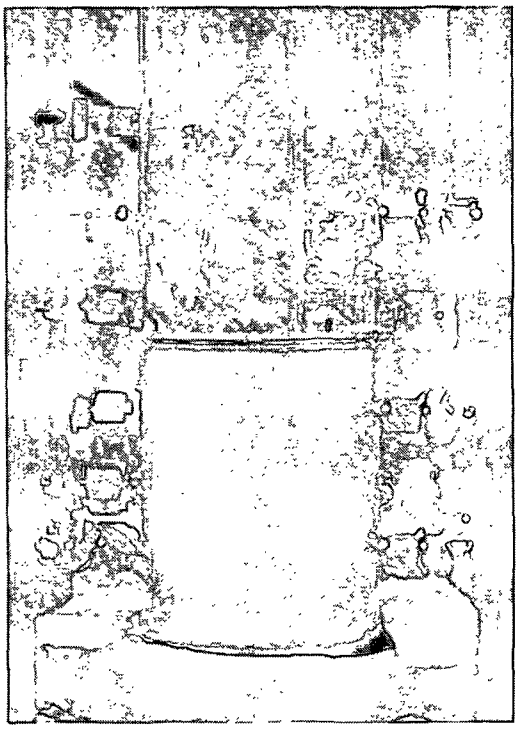

d. Turbulence in the pool of water.

Figure 54. A sequence of photographs illustrating behavior in the overlying pool of water as heat flux is increased.

peak heat flux attained during the experiment. The direct dependence of heat flux on wall superheat in the initial regime is similar to the nucleate pool boiling regime. Heat transfer apparently is limited by the ability of the heater to supply heat to the boiling surface, which is related to nucleation characteristics of the heater surface. Apparently, some form of active nucleation is occurring at voids on the heater surface. While completion of a full bubble growth cycle is unlikely, the initiation of bubble growth is certain to proceed within limits posed by physical constraints of the pore structure. Physical inhibition of nucleation may account for the reduced nucleate boiling effectiveness demonstrated by the fibrous medium. During this nucleate-type regime, vapor generated at the heater surface flows upward under the influence of a partial pressure gradient and buoyant forces, and liquid flows down to the heater surface under the influence of capillary forces and gravity.

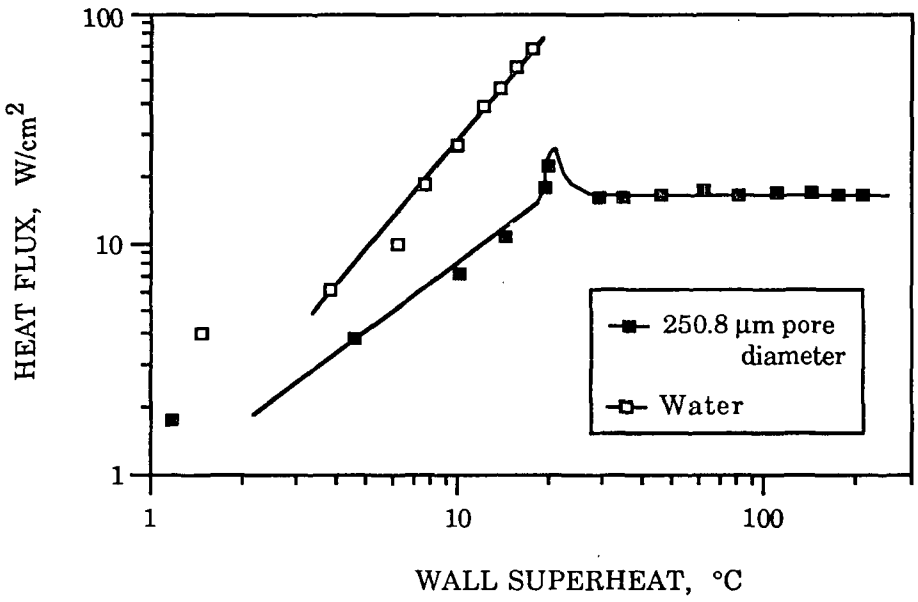

Figure 55. Typical boiling curves measured at atmospheric pressure with the boiling cell apparatus. Only the nucleate regime of the pool boiling curve for water is shown.

In the second regime, the heat flux is totally independent of wall superheat, and is controlled by the rate of liquid flow to the heater surface under the influence of capillary forces of the bed. The flow rate depends on the saturation characteristics and pore size distribution of the

bed. The development of a vapor film on the heater surface in this regime is unlikely because the inertial force of the liquid flowing to the surface would break through the film, which would have a maximum thickness on the order of a couple hundred microns. Consequently, some degree of liquid/surface contact is likely to occur throughout this regime, which means that phase change may occur by nucleation throughout the entire boiling curve.

The point of transition between the two regimes, called the critical heat flux (CHF), is a potentially unstable condition that requires prompt action by the surface temperature control system. The beds with average pore diameters greater than 220 μm exhibit a peak heat flux with a magnitude greater than that of the iso-heat flux regime. The phenomena associated with this peak are experimentally observed to be very sensitive: more scatter is apparent in the thermocouple readings as the process approaches the CHF. At the CHF, these beds experience a dramatic change in the fluid flow phenomena that reduces the heat-absorbing capacity of the bed. Attempts to increase surface temperature beyond the CHF yield an instantaneous, rapid rise in surface temperature (typically, an increase of 10 to 15°C in a period of 10 to 15 seconds) until the control system arrests the rise. Frequently, the process must be returned to a lower temperature, as the rise often overshoots the controller's setpoint.

Saturation is undoubtedly a major factor in controlling heat flux, particularly in the iso-heat-flux regime. The saturation profile, and not necessarily the overall magnitude of saturation, is important because the supply of liquid at the heater surface will depend on the quantity available in the bed very near to the surface. The profile is likely to exhibit a maximum saturation near the top of the bed and a minimum saturation near the surface, with an exponential increase from bottom to top.

The observation of a peak heat flux and subsequent decline to the iso-heat-flux regime for beds of large average pore diameter may be related to the saturation profile. This occurrence is postulated to be caused by a reduction in the ability of the bed to supply water to the heater surface. Since the pore structure of the rigid bed is unchanged, something must happen at the CHF to change

the saturation profile in the bed. Due to volume expansion upon phase-change, the velocity of vapor in the flow channels is likely to be much higher than that of liquid. In a manner analogous to the Helmholtz instability at the interface of two immiscible fluids, the vapor velocity in the flow channels may reach a critical level that effects a change in the relative distribution of water and vapor phases within the bed.

The Effect of Average Pore Diameter

The behavior of the characteristic curve for boiling in a fibrous bed depends on the average pore diameter of the bed, as illustrated in Figure 56. The slope of the nucleate-type regime decreases in direct proportion to pore diameter, most probably because of the effects on the hydrodynamics of the vapor phase. First, vapor generation involved with nucleation is probably inhibited in direct proportion to the average pore diameter, which defines the physical space that the vapor phase can grow into. Second, the resistance to vapor flow away from the heater surface will increase as the diameters of the flow channels decrease. Any accumulation of vapor at the surface will increase the resistance to heat transfer at the surface, thus reducing the heat transfer coefficient in the nucleate regime.

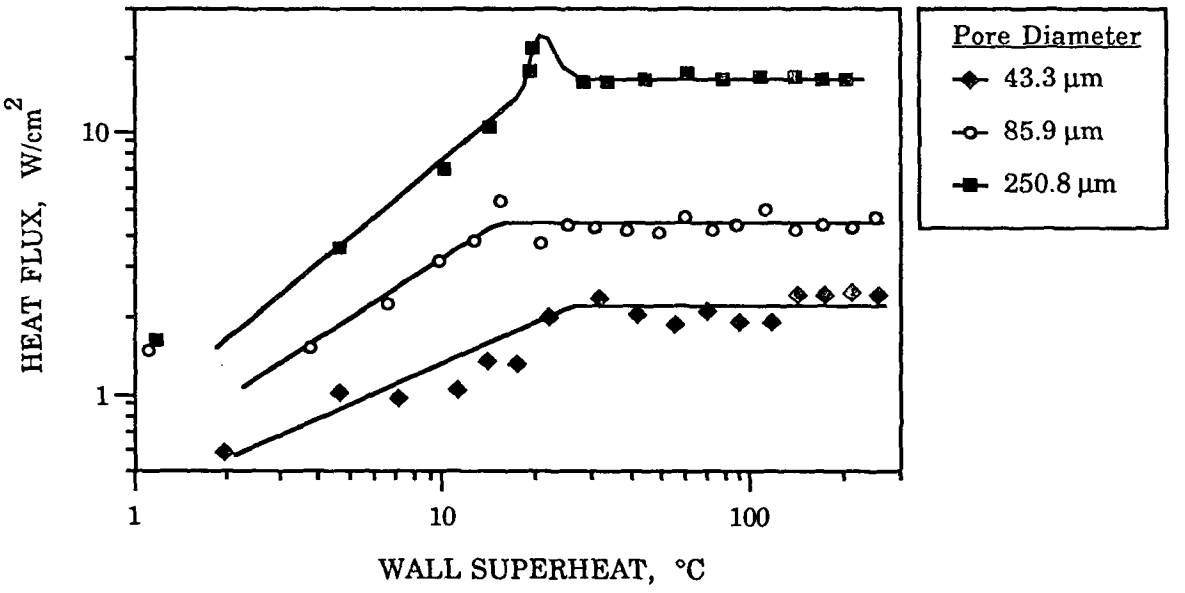

Figure 56. The effect of average pore diameter on the boiling curve at atmospheric pressure.

Behavior at the CHF is affected by the average pore diameter of the bed, as well. Each of the boiling curves for the large average-pore-diameter beds (220 to 260 μm) exhibits a distinct peak in heat flux between the two regimes, and an associated rapid escalation in surface temperature. However, none of the small average-pore-diameter beds (35 to 90 μm) exhibits either of these phenomena. Rather, the transition from the nucleate-type regime to the iso-heat-flux regime is smooth. This difference in behavior at the CHF may be related to the curvature of the saturation profile in the bed, which is certainly related to the geometric scale factor defined in Table 9. A critical scale factor that determines the occurrence of a peak heat flux and associated surface temperature rise may exist. Regardless of transition phenomena, all experiments at 0.10 MPa exhibit transition at a wall superheat of about 20°C.

The magnitude of heat flux in the iso-heat-flux regime is directly related to average pore diameter. As indicated by Washburn's equation (Equation 14), the rate of liquid supply to the heater surface depends on the diameter of the pores. Accordingly, as the pore diameter decreases, the rate of water supply, and hence, the heat flux, decreases. Of course, use of Washburn's equation in this analysis does not mean to imply direct applicability, because assumptions in its derivation limit its scope. However, for illustrative purposes, the role of pore diameter can be inferred from it.

The data for the smallest average pore diameter in Figure 56 exhibits a fair amount of scatter for two reasons. First, utilizing a log ordinate axis amplifies the scatter of this data because of broadening of the scale in the 0.8 to 2.0 W/cm^2 range. Second, the temperature difference between the two thermocouples used to calculate heat flux is approaching the same order of magnitude as the precision in thermocouple readings. Consequently, the uncertainty for this set of data is higher than that for larger average pore diameters.

The Effect of System Pressure

Figure 57 illustrates the effect of system pressure on the boiling curves for fibrous beds with

average pore diameters of approximately 250 μm [f]. Prior to the region of transition, the nucleate-type regime is insensitive to pressure in the studied range. Because classical pool boiling studies with water indicate significant changes in the nucleate regime at pressures of 0.34 MPa [32,35], this observation suggests that geometric constraints of the pore structure dominate pressure effects in controlling phase change, and consequently heat transfer. It is interesting to note that although bed saturation is higher due to the increased vapor phase density at elevated pressures, heat flux in the nucleate-type regime below wall superheats of about 20°C does not increase. This also suggests that geometric constraints dominate pressure effects in controlling nucleation. The nucleate-type regimes for beds with average pore diameters of 80 μm also do not appear to be affected by pressure, but for beds with average pore diameters of 40 μm, the nucleate-type regime appears to be shifted to lower wall superheats while retaining the same slope. This difference may be related to a critical value of geometric scale factor.

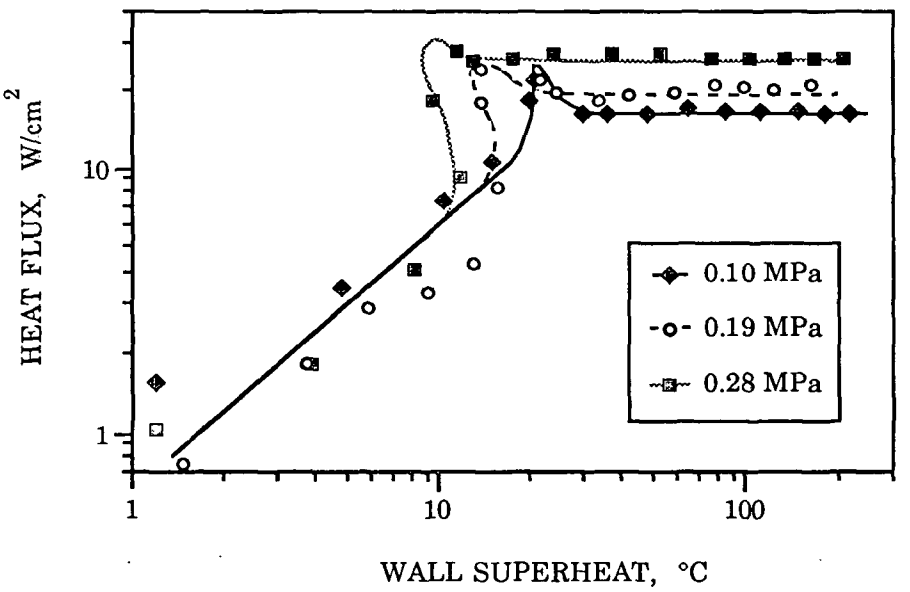

Figure 57. The effect of system pressure on the boiling curve for a fibrous bed with an average pore diameter of approximately 250 μm.

[f] The pressure range investigated in this research was limited based on a catastrophic failure of the boiling cell during an experiment at an applied pressure of 0.28 MPa.

For beds with large average pore diameters, process instability at the CHF is exacerbated as the system pressure increases. Under pressure, system stability as the process nears the CHF is attained with increasing difficulty. At some point, the heretofore-experienced direct relationship between wall superheat and heat flux reverses, as the wall superheat actually decreases as higher heat fluxes are approached. This is exhibited as a backward bend in the boiling curve, until finally, the heat flux peaks and the surface temperature rapidly escalates. Experimentally, these points are observed as the surface temperature control system increases power to the heater block in an attempt to increase surface temperature. However, the surface temperature decreases as heat flux increases, and once the process stabilizes at the lower temperature, a data set is collected. The behavior of decreasing wall superheat at increased levels of heat flux just prior to the critical is reproduced in all of the pressurized boiling runs for beds with average pore diameters above about 220 μm. The wall superheat at the CHF is inversely proportional to pressure, which agrees with the trend observed in classical pool boiling. For beds with small average pore diameters, the smooth transition between the regimes is not affected by pressure.

The effect of pressure on the magnitude of heat flux in the iso-heat-flux regime is in part due to the increased density of the vapor phase. The consequent increase in bed saturation results in greater liquid water supply to the heater surface, which increases the heat-absorbing capacity of the bed. For all average pore diameters, the magnitude of the iso-heat-flux regime under pressure is greater than that for atmospheric conditions.

Comments on the Significance of Bed Saturation

Bed saturation profile undoubtedly plays an important role in controlling heat flux during boiling in a fibrous medium through its impact on water supply to the heater surface. Though it is difficult to monitor saturation profile throughout the event, a gross measure of "initial" saturation was made for each experiment. The height rise of the overlying liquid layer due to growth of the two-phase zone was measured just after bubbles began to protrude from the top of the bed (prior to agitation of the liquid pool), which corresponds to a condition of two-phase flow throughout the

entire bed height. Assuming an initially-saturated bed, the corresponding displaced water volume is converted to an average initial saturation by dividing the difference between the bed void volume (which is equal to the saturated water volume) and the displaced water volume by the void volume. The data must be interpreted cautiously because beds made from the 3.0 and 8.4 μm diameter fibers were not completely engulfed in two-phase flow, and consequently the upper portions of the bed remained nearly saturated with water. Accordingly, the initial saturation is actually lower than measured. Secondly, the beds were not completely saturated initially, as air pockets were evident around the perimeter of the bed. Being mindful of these sources of error, some conclusions can be deduced from the data in Table 12. First, initial saturation is directly related to pore diameter, which is congruent with the observed direct relationship between heat flux and pore diameter. It is interesting to note that beds of small average pore diameter have lower levels of saturation than beds of large average pore diameter. Second, initial saturation appears to be directly related to pressure, which is congruent with the observed direct relationship between heat flux and system pressure in the iso-heat-flux regime. Though this gross measure of average saturation in the bed during the initial portions of the boiling experiment does not necessarily provide information regarding the profile or indicate subsequent behavior of the profile as boiling proceeds, it does appear to indicate the significance of saturation to the phenomena.

Additional Issues for the Boiling Experiments

A few issues and observations of apparatus behavior noted during the experiments are worth noting. First, the proportional band of the temperature controller must be frequently adjusted during the experiment to match the process dynamics to insure prompt response of the surface temperature control system. Process dynamics range from heat fluxes less than 1 W/cm^2 prior to boiling to heat fluxes of 25 to 30 W/cm^2 at the CHF. A single value of proportional band may control adequately in one range of heat flux, while at higher heat fluxes, no control action is evident. This explains the process stabilizing at surface temperatures less than the setpoint near the CHF during the pressurized experiments. The dramatic increase in heat flux experienced just

prior to the CHF apparently moves beyond the range of control for the particular level of proportional band. Achieving the temperature setpoint requires decreasing the proportional band.

Oxidation of the thermal junction of the block thermocouples can reduce the accuracy of the temperature reading. When the resistance across the leads of the thermocouple exceeds 5 Ω, the thermocouples are removed from the block to renew the junctions by lightly sanding the surface of the thermowell with coarse emery cloth. To insure perpendicularity of the junction surface, the thermowell is placed in a jig having a hole drilled precisely to 0.2496 inches during sanding.

The potential effects of an oxidized junction on accuracy of the data can be determined by comparing the calculated heat flux with that measured by the wattmeter. As previously mentioned, heat flux is calculated based on temperature readings from the thermocouples closest to and furthest from the heater surface. If these values differ significantly from those measured by the wattmeter, the heat fluxes calculated from the other two combinations of block thermocouples are examined, and the combination affording the best agreement with the wattmeter readings is selected. As illustrated in Appendix VIII, judicious selection of heat flux data was required for three boiling experiments due to the effects of an oxidized thermocouple junction.

Comparison of temperature readings for block thermocouples 3 and 4 (see Figure 37) reveals that radial heat flow is non-existent at low wall superheats, and is very small at elevated wall superheats, typically on the order of 1 to 2°C. Therefore, one-dimensional heat flow in the region of the block thermocouples is achieved with the use of the guard heater.

Sensitivity of the nucleate-type boiling regime to height of the overlying liquid layer was experimentally observed. Infusion of makeup water during the regime resulted in a decrease in wall superheat of 1 to 2°C for beds with large pore diameters, presumably due to its effect on bed saturation profile. Infusion typically is not needed until the heat flux exceeds about 10 W/cm^2, and then it may occur two or three times prior to the CHF. Because minimal vapor flow from the boiling cell at the low heat fluxes does not require makeup water, beds of small pore diameter do

not experience makeup-water infusion. Although this behavior was not studied extensively, lateral movement of data on the boiling curve may account for some of the scatter in the nucleate-type data for the large-pore-diameter beds. No sensitivity was observed for the iso-heat flux regime, but because heat flux is independent of wall superheat here, changes in wall superheat would not be detected because data would move along the boiling curve. If further boiling research is pursued, more precise level control is recommended.

Since contact between the liquid and the heater surface is likely to occur throughout the entire boiling experiment, heater surface roughness and wettability are important factors to consider. As previously discussed, a lack of understanding about the exact aspects of surface roughness important to nucleation precludes inclusion of roughness in the correlation. To insure a uniform boiling surface experimentally, the heater surface was prepared in exactly the same manner prior to each experiment: it was cleaned in sequence with concentrated sulfamic acid solution (to remove inorganic precipitates), dimethylformamide (to remove organic precipitates), and acetone. This sequence is effective in removing the small deposits that typically foul the surface during a boiling experiment. However, following experiments CBE12, CBE18, and CBE28, tenacious inorganic deposits sparsely distributed on the surface could not be removed by the surface cleaning solutions. Thus, the surface was either polished with a buffing wheel, or the chrome plating was removed and the surface was replated. These actions probably changed the nucleation characteristics of the heater surface, but were deemed less dramatic than boiling on the fouled surface.

Repeatability of the experimental technique is illustrated in Figure 58 for duplicate experimental runs. Two sets of data were collected at atmospheric pressure for a fibrous bed with an average pore diameter of 250.8 μm and a height of 15.6 cm. Repeatability is very good in the iso-heat-flux regime, as the average heat flux values for the two sets are 17.1 and 16.4 W/cm^2, which is within the range of uncertainty of 0.9 W/cm^2. Some deviation is apparent in the nucleate-type regime, especially as the CHF is approached, and probably results from process dependence on

heater surface characteristics, infusion of makeup water, and instability near the CHF. Because the heater surface is capable of providing adequate heat beyond the point of transition, the iso-heat-flux regime is affected little by surface nucleation characteristics, and consequently, exhibits little variation. Considering the sources of error, repeatability is surprisingly good.

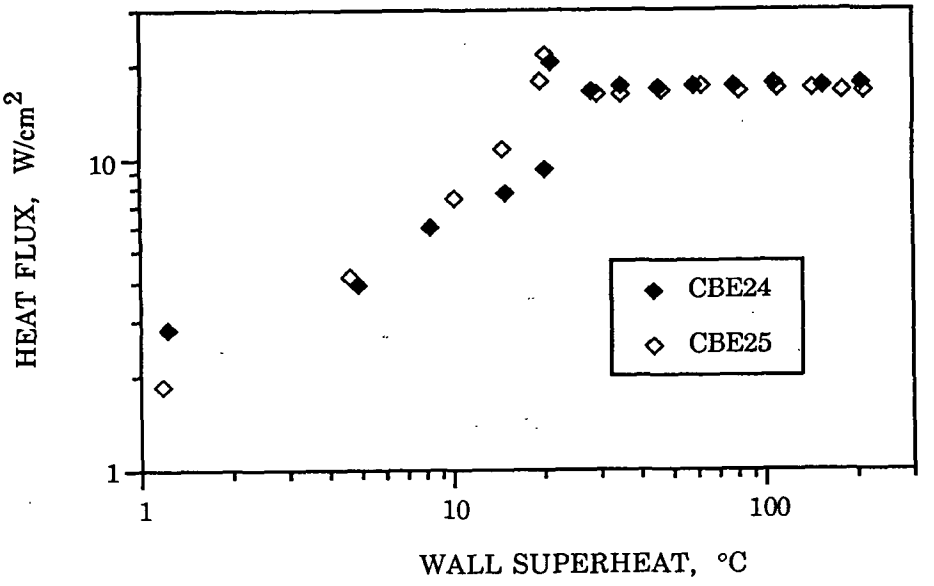

Figure 58. Repeatability of the boiling experiment. Data are for beds with average pore diameters of 250 μm at atmospheric pressure.

CORRELATION OF THE BOILING DATA

The values of the dimensionless groups that remain constant throughout a given boiling experiment are listed in Table 14. The ranges for the Reynolds, Nusselt, and Jakob numbers for the nucleate-type regime are 2.105×10^{-4} to 0.1606, 9.326×10^{-3} to 12.57, and 4.715×10^{-4} to 7.171×10^{-2}, respectively, and for the iso-heat-flux regime are 8.911×10^{-4} to 0.1501, 1.042×10^{-3} to 1.004, and 0.187 to 0.589, respectively. The effective thermal conductivity in the Nusselt number is defined according to Equation 29 using a saturation of 0.5. For correlation purposes, the data has been segregated into two groups according to boiling regime. Each correlation is developed from a stepwise regression according to Equation 34 with appropriate F-statistics using Stat View™ 512+ software for the Apple Macintosh computer, and each correlation is tested for lack of fit. No attempt

Table 14. Values of the dimensionless groups that are constant for a given experiment. All groups are defined in Table 9 except the iso-heat-flux number, which is defined in Equation 55.

Data Set[a]	Bond	Grashof	Prandtl	Group 6	Group 7	Darcy	Geometric Scale Factor	Iso-heat-flux
CBE13 (6)	1.091E-2	3108.7	1.289	33.81	1334.3	0.0092	2.025E-3	3.508E-6
CBE14 (8)	1.051E-2	2546.9	1.435	38.99	849.2	0.0092	2.025E-3	4.128E-6
CBE15 (9)	1.079E-2	2384.5	1.547	43.27	652.8	0.0091	2.074E-3	4.526E-6
CBE17 (10)	1.029E-2	2220.9	1.547	43.27	637.5	0.0092	2.051E-3	4.634E-6
CBE18 (9)	8.702E-3	1476.9	1.724	50.54	401.6	0.0097	2.044E-3	5.892E-6
CBE21 (9)	8.702E-3	1476.9	1.724	50.54	401.6	0.0097	1.502E-3	5.892E-6
CBE22 (6)	9.562E-3	1701.1	1.724	50.54	421.0	0.0094	2.082E-3	5.621E-6
CBE23 (10)	8.702E-3	1476.9	1.724	50.54	401.6	0.0097	2.939E-3	5.892E-6
CBE24 (7)	1.003E-2	1826.2	1.724	50.54	431.0	0.0092	1.612E-3	5.490E-6
CBE25 (6)	1.003E-2	1826.2	1.724	50.54	431.0	0.0092	1.611E-3	5.490E-6
CBE26 (6)	9.122E-3	1584.9	1.724	50.54	411.1	0.0095	3.009E-3	5.755E-6
CBE29 (8)	8.304E-3	1376.6	1.724	50.54	392.3	0.0098	2.479E-3	6.032E-6
CBE30 (8)	9.125E-3	2059.7	1.435	38.99	791.2	0.0097	2.537E-3	4.430E-6
CBE8 (5)	1.177E-3	73.5	1.724	50.54	147.7	0.0162	5.205E-4	1.602E-5
CBE9 (8)	8.507E-4	45.1	1.724	50.54	125.6	0.0175	5.611E-4	1.885E-5
CBE16 (6)	1.199E-3	98.1	1.435	38.99	286.8	0.0162	7.732E-4	1.222E-5
CBE10 (7)	2.997E-4	9.4	1.724	50.54	74.5	0.0177	2.787E-4	3.175E-5
CBE12 (3)	2.533E-4	7.3	1.724	50.54	68.5	0.0136	3.138E-4	3.454E-5
CBE27 (4)	2.932E-4	9.1	1.724	50.54	73.7	0.0171	4.093E-4	3.210E-5
CBE28 (4)	2.824E-4	11.2	1.435	38.99	139.2	0.0148	4.315E-4	2.518E-5
CBE31 (5)	3.190E-4	15.6	1.289	33.81	228.2	0.0171	4.093E-4	2.051E-5

a - The number in parentheses following the name of the data set indicates the number of data points used in correlating data for the nucleate-type regime.

is made to correlate the CHF due to an insufficient amount of data; a regimented study of the phenomena controlling the transition between the two boiling regimes is recommended for development of a correlation.

The Iso-Heat-Flux Regime

Because heat flux is completely independent of wall superheat, the average value of heat flux in the iso-heat-flux regime of each boiling curve is used in the correlation. This reduces the number of data points from approximately 200 to 21. Additionally, the lack of dependence of heat flux on wall superheat diminishes the significance of the Nusselt number. Consequently, the Reynolds number defined in Equation 33 is used as the dependent dimensionless group rather than the Nusselt number, and is based on the average heat flux of the regime for each data set.

Correlation of log(Re) against the logs of the independent dimensionless groups shows a strong dependence on the Bond and Grashof numbers with an adjusted coefficient of determination of 0.99 and F-statistic for the correlation of 677. However, by dividing the Bond number by the Grashof number, another dimensionless group is developed,

$$\Pi_{10} = \frac{\mu_l^2}{\overline{D}\,\rho_l \sigma} \quad , \tag{55}$$

which replaces either the Bond or Grashof number in the stepwise regression. Though the adjusted coefficient of determination is unchanged, use of this group improves the F-statistic for the correlation to 1166. The correlation for the iso-heat-flux regime is

$$\frac{q\,\overline{D}}{\Delta h_v\,\mu_l\,\varepsilon} = 7.161 \times 10^{-11} \left(\frac{\mu_l^2}{\overline{D}\,\rho_l \sigma}\right)^{-1.861} \left(\frac{\overline{D}}{H}\right)^{0.296} \tag{56}$$

The correlation, which fits the data to ± 11.5% on average and ± 35% peak-to-peak, is illustrated in Figure 59, and normalized residuals are illustrated in Figure 60. The statistics for the stepwise regression and lack of fit test are listed in Table 15. The lack of fit test indicates that the correlation cannot be rejected with more than 95% certainty.

Previously, the ability of the bed to supply water to the heating surface was suggested as the controlling mechanism for the iso-heat-flux regime. This correlation provides additional insight, as the dominant independent dimensionless group involves viscous, inertial, and capillary forces. All three of these factors impact the flow of water to the boiling surface. The capillary forces essentially drive the flow of water, and are opposed by viscous forces, which also oppose inertial forces. It is interesting to note that the buoyancy force does not appear to be significant in this regime. The appearance of the average pore diameter in each dimensionless group of the correlation highlights the significance of physical space limitations for nucleation to the phenomena in the iso-heat-flux regime. This dominant dimensionless group is new and unique, and is termed the iso-heat-flux number throughout the remainder of this text.

The statistical significance of the geometric scale factor reflects the importance of the thickness of the medium on the phenomena, which is why the boiling curves illustrated earlier must only be interpreted for trends, and not absolute effects. A critical value for the geometric scale factor may determine whether a medium experiences an elevated CHF. All of the mediums that exhibited a sharp surface temperature rise at the transition to the iso-heat-flux regime have scale factors greater than 0.0015, and all of the mediums that exhibited a smooth transition to the iso-heat-flux regime have scale factors less than 0.0008. The existence of a critical value between 0.0008 and 0.0015 could be investigated by adjusting bed height.

It is interesting that the significant impact of pressure on boiling in fibrous media is not explicitly obvious in the correlation. To verify that the pressure effects are accounted for in the physical properties of the liquid, the data was correlated with the geometric scale factor and the iso-heat-flux number defined with fluid properties at atmospheric pressure. The resulting adjusted

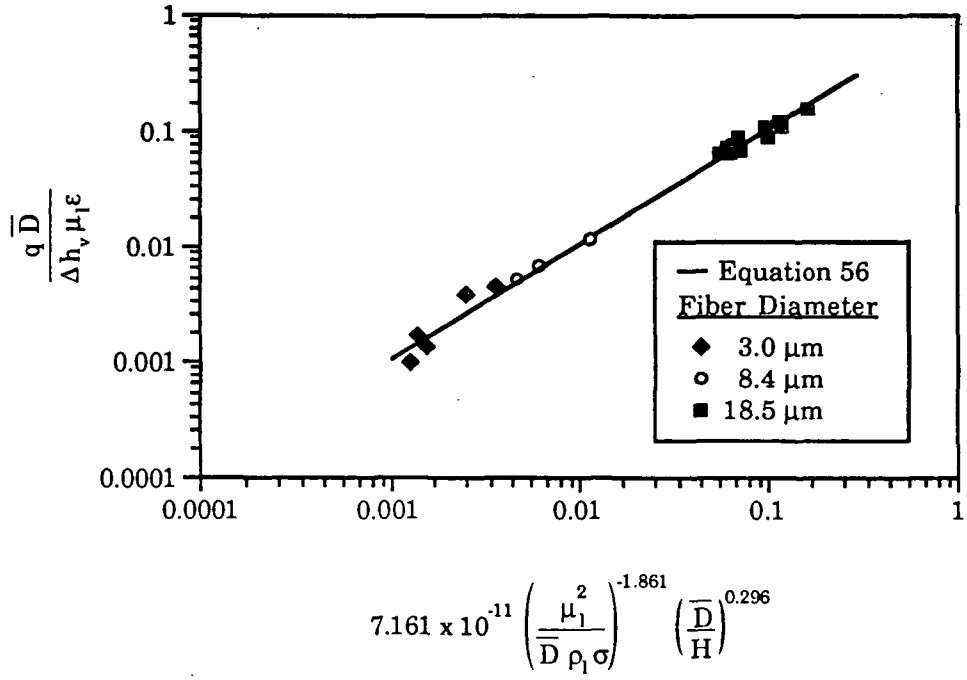

Figure 59. Dimensionless correlation for the iso-heat-flux regime.

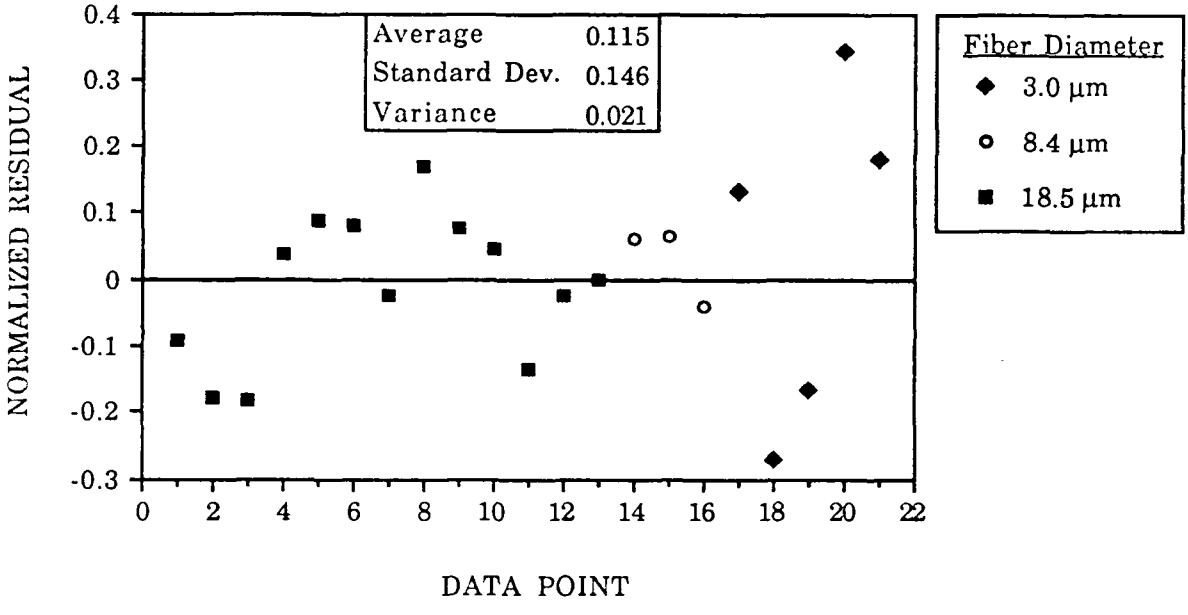

Figure 60. Normalized residuals for the iso-heat-flux regime correlation.

Table 15. Statistics for the stepwise regression and lack of fit F-test for the iso-heat-flux regime correlation (Equation 56).

Stepwise Regression

Adjusted coefficient of determination (r^2_{adj}) = 0.991

Critical F-statistic = F(21,21,0.99) = 2.8

Analysis of Variance

Source	Degrees of Freedom	Sum of Squares	Mean Square	F-statistic for Correlation
Regression	2	10.765	5.382	1166.08
Residual	18	0.083	0.005	
Total	20	10.848		

F-statistic for $\log\left(\frac{\mu_l^2}{\overline{D}\,\rho_l\,\sigma}\right)$ = 151.30, and standard error = 0.151.

F-statistic for $\log\left(\frac{\overline{D}}{H}\right)$ = 4.19, and standard error = 0.145.

Lack-of-Fit Test

Source of Residual Sum of Squares	Degrees of Freedom	Sum of Squares	Mean Square	F-statistic for Lack-of-Fit
Pure Error	8	0.001444	0.000181	0.301
Lack of Fit	10	0.000543	0.000054	

F(10,8,0.99) = 5.81
F(10,8,0.95) = 3.35

Because the F-statistic for lack-of-fit is less than either of the critical values, the correlation cannot be rejected with more than 95% certainty.

coefficient of determination was 0.956, and the average normalized residual was 25.7 ± 15.4% (95% confidence limits), which indicates that pressure dependency is accounted for with the fluid properties. In an attempt to incorporate a more explicit dependence of heat flux on pressure, two additional correlations using the geometric scale factor and the iso-heat-flux number defined in terms of vapor density rather than liquid density were attempted. In the first case, the iso-heat-flux number was defined completely in terms of vapor properties, yielding a correlation with an

adjusted coefficient of determination of 0.990, and an average normalized residual of 14.8 ± 7.69%. In the second case, the density of liquid was used in the iso-heat-flux number, yielding a correlation with an adjusted coefficient of determination of 0.969, and an average normalized residual of 23.8 ± 12.9%. However, none of these attempts yielded an improved fit compared to quation 56, which has a coefficient of determination of 0.99, and an average normalized residual of 11.5 ± 6.6%.

The Nucleate-type Regime

Because all data in the nucleate-type regime demonstrate a direct dependence on wall superheat, each of the 144 data points is retained for the correlation [g]. More than 40 attempts to correlate the Nusselt number with various combinations of dimensionless groups yielded maximum values of the adjusted coefficient of determination and the F-statistic of 0.87 and 242, respectively. More than 30 additional attempts to correlate the Reynolds number yielded noticeable improvements in both statistical values. Thus, the correlation to be presented utilizes the Reynolds number as the independent parameter rather than the Nusselt number.

It can not be overemphasized that at least ten correlations, each with different statistically-significant independent dimensionless groups, yielded equally good (or bad) correlations for both the Reynolds and Nusselt numbers. In an effort to identify one correlation that fit the data better than any others, the dimensionless groups in Table 9, the iso-heat-flux number, the following group,

$$\Pi_{11} = \frac{\rho_l g \sigma}{P^2} \quad , \tag{57}$$

various products and quotients of these groups, and even combinations of the log of one group

[g] The following data points from Table 13 are not included in the nucleate-type regime correlation: point 1 in data set CBE8, points 2,3, and 4 in data set CBE12, and point 1 in data set CBE27.

raised to the power of another, were used in the stepwise regression. These efforts proved fruitless, as no correlation was identified as being exceptional.

Stepwise regression of log(Re) against the logs of the independent dimensionless groups yielded the following correlation as being slightly better than any other:

$$\frac{q\,\overline{D}}{\Delta h_v\,\mu_l\,\varepsilon} = 2.838 \times 10^{-10} \left(\frac{C_{p_l}\,\Delta T_w}{\Delta h_v}\right)^{0.703} \left(\frac{\mu_l^2}{\overline{D}\,\rho_l\,\sigma}\right)^{-1.744} \quad . \tag{58}$$

The correlation, which fits the data to ± 37.0% on average and ± 175% peak-to-peak, is illustrated in Figure 61, and normalized residuals are illustrated in Figure 62. The statistics for the stepwise regression and lack of fit test are listed in Table 16. The lack of fit test indicates that the correlation cannot be rejected with more than 95% certainty. Though this correlation statistically represents the data, its accuracy as a tool for predicting nucleate-type regime heat flux is severely limited. Normalized residuals as high as 175% indicate that the correlation can at best be used to predict trends. Attempts to segregate goodness of fit based on average pore diameter or system pressure proved fruitless.

The inaccuracy of this correlation probably stems from the inability to incorporate surface nucleation characteristics into the correlation. Heat flux in the nucleate-type regime depends on the occurrence of nucleation phenomena to dissipate heat delivered to the heater surface. The Jakob number indirectly accounts for nucleation phenomena, as both the Jakob number and nucleation intensity increase with wall superheat. The appearance of the iso-heat-flux number underscores the importance of the fibrous medium's ability to transport liquid to the surface. However, neither of these dimensionless parameters directly accounts for nucleation characteristics of the heater surface. Improvement of correlation accuracy without incorporating surface nucleation characteristics may be impossible.

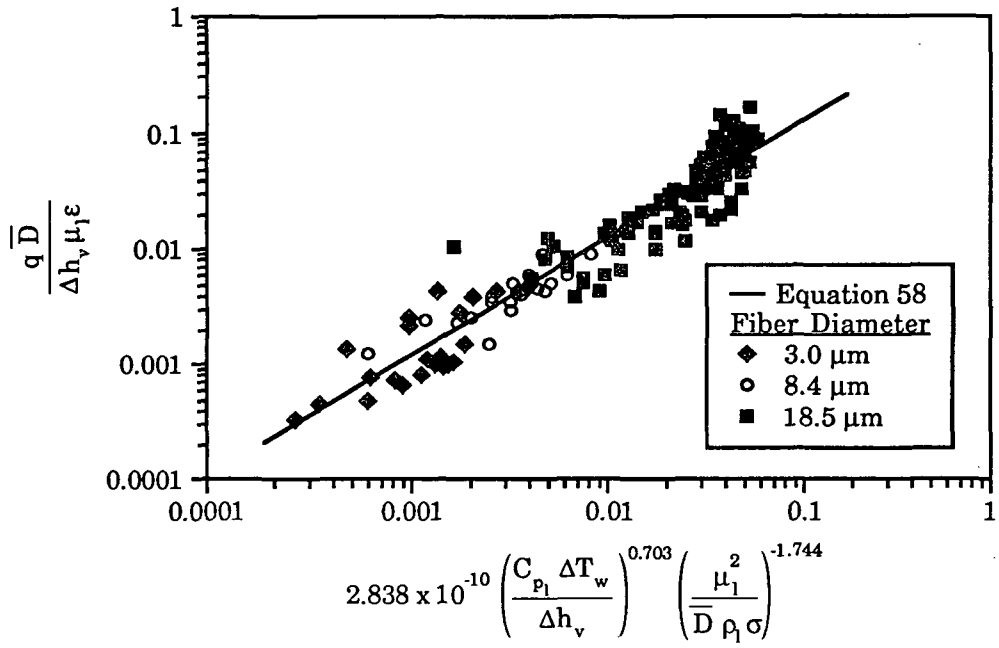

Figure 61. Dimensionless correlation for the nucleate-type regime.

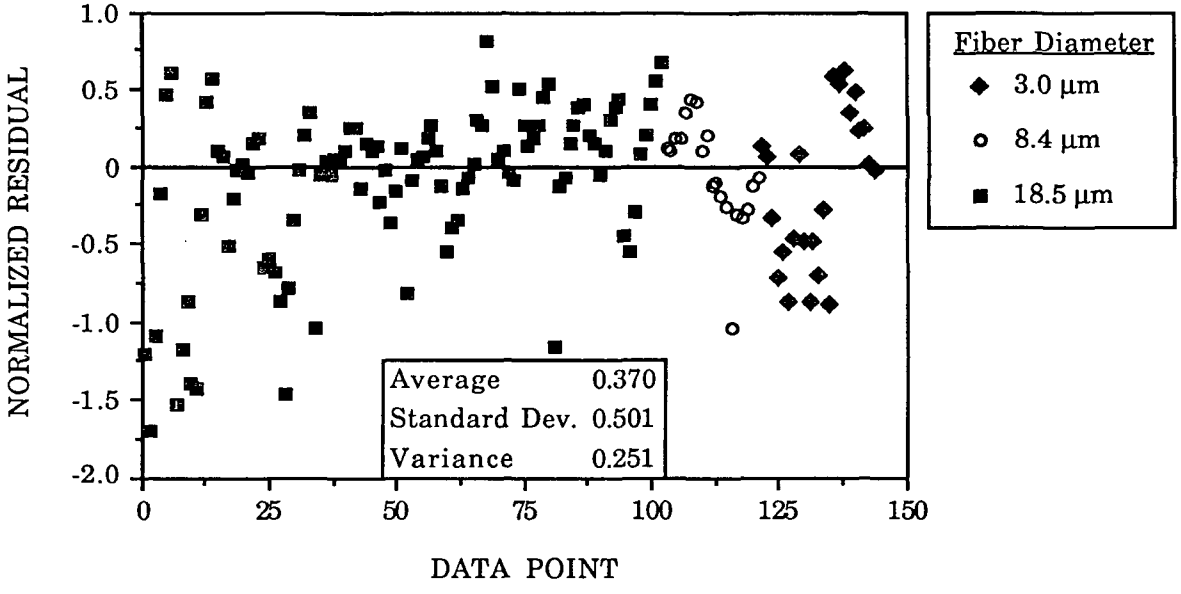

Figure 62. Normalized residuals for the nucleate-type regime correlation.

Table 16. Statistics for the stepwise regression and lack of fit F-test for the nucleate-type regime correlation (Equation 58).

Stepwise Regression

Adjusted coefficient of determination (r^2_{adj}) = 0.902

Critical F-statistic = F(144,144,0.99) = 1.5

Analysis of Variance

Source	Degrees of Freedom	Sum of Squares	Mean Square	F-statistic for Correlation
Regression	2	52.39	26.195	1166.08
Residual	141	5.619	0.04	
Total	143	58.009		

F-statistic for $\log\left(\frac{C_{p_l}\,\Delta T_w}{\Delta h_v}\right)$ = 287.74, and standard error = 0.041.

F-statistic for $\log\left(\frac{\mu_l^2}{\overline{D}\,\rho_l\,\sigma}\right)$ = 994.49, and standard error = 0.055.

Lack-of-Fit Test

Source of Residual Sum of Squares	Degrees of Freedom	Sum of Squares	Mean Square	F-statistic for Lack-of-Fit
Pure Error	71	0.0289	0.000408	0.745
Lack of Fit	70	0.02131	0.000304	

F(70,71,0.99) = 1.8
F(70,71,0.95) = 1.5

Because the F-statistic for lack-of-fit is less than either of the critical values, the correlation cannot be rejected with more than 95% certainty.

Comments on Accuracy of the Correlations

For physical processes involving only one fluid and a restricted range of physical dimensions, one might expect a correlation to fit the data better than ± 35% peak-to-peak. However, the correlation for the iso-heat-flux regime neglects the role of bed saturation level or profile because of the difficulty in quantifying these properties. Additionally, the method of

determining average pore diameter based on a pore structure modeled as straight capillaries of equivalent pore volume, while providing a relative rank of the fibrous beds, probably overestimates the actual average pore diameter because it fails to account for tortuosity and interconnection of pores. Considering the significance of these two issues to boiling in porous media, agreement between actual and predicted values of ± 35% is certainly acceptable.

The correlation for the nucleate-type regime suffers from the inability to account for heater surface nucleation characteristics. Inaccuracies of ± 175% are unacceptable for predictive purposes. However, the correlation does predict the trend of heat flux.

IMPLICATIONS FOR IMPULSE DRYING

The results of this boiling research provide insight into the contribution of sheet pore size and internal pressure in controlling heat transfer to the sheet during impulse drying. Data collected by Lavery [8] indicate some interesting phenomena as the impulse drying event is extended. As illustrated in Figure 63, three superimposed events of different nip residence times track each other very closely throughout the event. After the rapid initial rise to the peak heat flux, the heat flux decays to a lower value. In the case of a short event, the decay is rapid, but in the case of an extended event, the heat flux decays exponentially, and nearly asymptotes at about 75 W/cm^2 until nip pressure is relieved. During this latter portion of the extended event, the phenomena within the sheet approach a quasi-steady state.

Based on the results of this investigation, this latter portion of the extended impulse drying event may be controlled by an interaction of sheet pore size, pressure buildup within the sheet, and counterpercolation of steam and liquid water within the sheet. In the iso-heat-flux regime for boiling in fibrous media, the characteristic curves demonstrate that heat flux is independent of thermal driving force, and depends on the pore size of the media and its ability to deliver liquid to the heater surface, and also on the system pressure. By the time the quasi-steady regime in the impulse drying event occurs, free water at the heater surface is likely to be depleted, and the plane

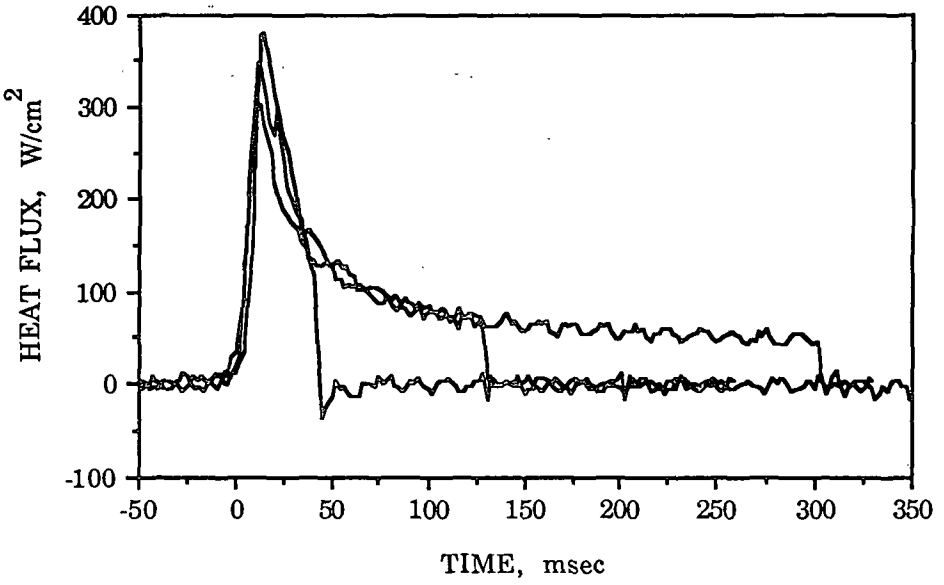

Figure 63. Impulse drying events of varying duration. The data are for 125 g/m^2 linerboard sheets initially at 40% solids presteamed to 80°C. Nip conditions are a peak pressure of 3.4 MPa and a hot surface temperature of 315°C.

of evaporation probably is located within the sheet structure. At this point, heat flux will be controlled by the rate at which the pore structure of the sheet can supply liquid water to the plane of evaporation for phase change. As with the model fibrous bed, a nearly isothermal zone, however thin, exhibiting counterpercolation of steam and liquid water, delivers liquid to, and vents vapor from, the plane of evaporation. Thus, the heat flux will depend to a large degree on the pore structure of the sheet in this regime. The slight decrease in this regime's heat flux evident in Figure 63 may be an indication of continued sheet compression and resultant decrease in pore size of the sheet, leading to a decrease in liquid flow rate.

The difference in magnitudes of heat flux between the iso-heat-flux regime of steady-state boiling in fibrous media and the quasi-steady regime of an extended impulse drying event may be bridged by the role of pressure. The highest heat flux in fibrous media boiling of about 25 W/cm^2 is obtained at 0.28 MPa. Sheet temperatures experienced during impulse drying (see Figure 8) indicate that internal pressures could be on the order of 1.25 MPa. If the trend of increasing magnitude of heat flux in the iso-heat-flux regime with pressure could be extrapolated to 1.25 MPa, values in the neighborhood of 75 W/cm^2 may be attainable.

These results also suggest that papermaking operations that reduce the average pore diameter of the sheet may be detrimental to impulse drying water removal. In general, impulse drying water removal rates are directly related to heat flux, which is the driving force for water removal by displacement due to growth of a vapor phase. Based on this research, heat flux may be directly related to pore diameter in the portion of the event where heat flux is limited by sheet structure. Thus, by reducing the sheet pore diameter, mechanical refining of the furnish reduces the driving force for water removal in the latter portion of the impulse drying event. Additionally, the structural changes in the fiber induced by refining increases its water-holding capability. The additive effects of increased difficulty of water removal and decreased driving force for water removal indicates that refining may reduce the potential for water removal in impulse drying.

CONCLUSIONS

Boiling in the presence of a fibrous porous medium possessing significant capillary forces exhibits interesting phenomena that differ significantly from classical pool boiling phenomena. The characteristic curves for boiling in a fibrous bed exhibit two regimes. The first regime is similar to the nucleate regime of classical pool boiling in that heat flux is directly proportional to wall superheat. Heat transfer in this nucleate-type regime appears to be controlled by nucleation characteristics of the heater surface. The heat flux of the second regime is constant and is, therefore, independent of wall superheat. Heat transfer in this iso-heat-flux regime appears to be controlled by the rate at which the pores of the fibrous bed supply water to the heater surface.

The average pore diameter of the bed is an important factor for boiling in a fibrous medium. The slope of the nucleate-type regime, and the magnitude of heat flux in the iso-heat-flux regime, are directly proportional to the average pore diameter. The behavior at the point of transition between the two regimes appears to depend on a critical value of average pore diameter. Beds with average pore diameters above 220 μm exhibit a peak heat flux with an associated rapid rise in surface temperature, while beds with average pore diameters below 90 μm exhibit a smooth transition between the nucleate-type and iso-heat-flux regimes.

System pressure apparently has no effect on the portion of the nucleate regime prior to the transition region. However, at elevated pressures, an interaction between system pressure and pore diameter is apparent in the process behavior near the critical heat flux. For beds with average pore diameters above 220 μm, wall superheat actually decreases for increases in heat flux as the CHF is approached, evident as a backward bend in the boiling curve near the CHF. However, for beds with average pore diameters below 90 μm, the nucleate-type curve is extended to a higher wall superheat where a smooth transition to the iso-heat-flux regime occurs. The magnitude of heat flux in the iso-heat-flux regime increases with pressure as the decrease in density of the vapor phase yields higher levels of bed saturation.

Correlations based on dimensional analysis are statistically proven to fit the data. The iso-

heat-flux regime data are fitted to ± 35% peak-to-peak, but the nucleate-type regime data is fitted to only ± 175% peak-to-peak.

SUGGESTIONS FOR FUTURE WORK

In addition to providing insight regarding mechanisms of boiling heat transfer in impulse drying, this thesis has opened many avenues for research of boiling in fibrous porous media. First and foremost, saturation and its distribution in the bed must be studied to identify its role in controlling heat flux throughout the boiling curve. The concept of a bottleneck in liquid flow corresponding to a minimum value of saturation within the bed must be experimentally verified.

Another area fertile for research is the phenomena associated with the critical heat flux. A critical value of average pore diameter, or perhaps geometric scale factor, may exist that determines the occurrence of a peak heat flux and subsequent rapid rise in surface temperature, or a smooth transition between the two boiling regimes. Additionally, for beds that exhibit a peak, the CHF phenomena appears to be very sensitive to pressure, as reductions of wall superheat are experienced for increases in heat flux near the CHF. Further research is needed to clarify these phenomena.

An interesting issue for further research is the interaction between the heater surface and the water phases. It has been postulated that contact between the liquid and heater surface occurs throughout the entire boiling curve, as inertial forces of the liquid flowing to the heater surface are likely to break through any vapor film that may begin to establish. Consequently, nucleation would occur throughout the entire boiling curve. Research is needed to conclusively address this issue of heater surface nucleation phenomena.

This study did not involve a regimented investigation of the effects of bed height or the height of the overlying liquid layer on boiling. Bed height is incorporated in dimensional analysis, but the height of the overlying liquid layer, though controlled during the experiments, is basically ignored. Considering the Washburn equation (for illustrative purposes only, being mindful of its limitations in application), the velocity of the liquid in the pores depends on bed height, which could be interpreted to indicate that beds of smaller height will exhibit a higher heat

flux in the iso-heat-flux regime. This appeared to be observed experimentally. Additionally, the concept of a critical geometric scale factor regarding CHF phenomena introduces the significance of bed height. A final thought on bed height is the inverse relationship it has to curvature of the saturation profile, and the implications this presents for the boiling curve. Regarding the overlying liquid layer, experimental observations indicate that rapid changes in the height of this pool do shift the nucleate-type curve, but have no effect on the iso-heat-flux curve. The effects on the nucleate-type regime are probably a reflection of the changes effected in the saturation profile due to the height change of the pool. This area needs to be fully researched.

Finally, the importance of the iso-heat-flux number to impulse drying must be investigated. Its applicability for describing heat flux in the quasi-steady portion of an extended event may parallel its importance to the iso-heat-flux regime for boiling in a fibrous medium.

NOMENCLATURE

Symbol

- A - area
- C_p - heat capacity
- d - bubble or pipe diameter
- $\overline{d}$ - local average pore diameter
- D - pore diameter
- $\overline{D}$ - average pore diameter
- D_H - hydraulic diameter
- g - gravitational acceleration
- h - height
- h_c - heat transfer coefficient
- Δh_v - latent heat of vaporization
- H - height of porous bed
- k - thermal conductivity
- K - permeability
- L - length or distance
- $\dot{m}$ - mass flow rate
- M - mass
- P - pressure
- $\mathcal{P}$ - piezometric head
- ΔP - pressure difference
- ΔP_c - capillary pressure
- q - heat flux
- Q - flow rate
- r - radius
- $\mathcal{R}$ - surface roughness
- S - saturation
- t - time
- T - temperature
- ΔT_w - wall superheat
- v - velocity
- V - volume
- W - weight
- x - local coordinate position
- z - local coordinate for height

Dimensionless Groups

- Bi - Biot number
- Nu - Nusselt number
- Pr - Prandtl number
- Ra - Rayleigh number
- Re - Reynolds number
- Γ - dimensionless heat flux
- Θ - dimensionless temperature

Greek Symbols

- α - thermal diffusivity
- β - contact angle
- γ - coefficient of thermal expansion
- ε - porosity
- λ_c - critical wavelength
- λ_d - dominant unstable wavelength
- μ - viscosity
- ν - kinematic viscosity
- ρ - density
- σ - surface tension
- Ψ - arbitrary property
- ζ - fiber length/unit volume

Subscripts

- b - onset of boiling, or, bubble
- bc - boiling cell
- bot - bottom of porous bed
- $crit$ - critical
- D - displaced
- eff - effective
- f - fiber
- h - heater
- l - liquid
- max - maximum
- min - minimum
- nw - nonwetted
- p - particle
- R - residual
- s - surface
- sat - saturation
- top - top of porous bed
- v - vapor
- w - wetted
- ∞ - condition at infinity
- o - initial condition, or surface condition

ACKNOWLEDGMENTS

The success I have enjoyed in completing this thesis over the last two years has resulted from the coordinated efforts of many people. I would like to acknowledge those who made significant contributions to this end. First, I thank my advisor, Jeff Lindsay, whose constant encouragement, concern, and insight contributed greatly to the direction and success of my work. I would like to thank my committee members, Hugh Lavery (my original advisor), Dave Orloff, Cyrus Aidun, and especially Clyde Sprague, whose favorite expression must be "sweat the details". His insistence that I do just that has contributed greatly to the quality of this work.

A handful of Institute staff contributed immeasurably to constructing the boiling cell apparatus. First , I would like to thank Kurt Lorenz, who meticulously designed the apparatus and helped assemble it. Second, I would like to thank Rich Mirabello, who designed and installed the electrical systems for the apparatus. Third, I would like to thank Doug Wheeler, who assisted in identifying the data acquisition system and in optimization of the TBASIC source code for the control software. Finally, I would like to thank Glenn Winkler and Paul Van Rossum, whose prompt and courteous machine work was indispensible for adjustments to the apparatus.

A number of Institute staff helped in other areas that necessitate acknowledgment. I would like to thank Jerry Kloth, for his assistance in mechanical design issues; Bruce Andrews, for his guidance in addressing "problems" with Validyne pressure transducers, his willingness to share his accumulated knowledge, and contribution of odds and ends; Orlie Kuehl and Russ Tyler, for providing numerous odds and ends to supplement my apparatus; Lyle Vandenberg, for his assistance in troubleshooting electrical problems; Milo Godschalx, Keith Hardacker, and Leon Straub, for their help in addressing electrical and electronic design issues; Jud Conkey, for his generous contribution of conditioned lab space used to perform capillary pressure/saturation experiments and permeability experiments; Marianne Fiscus, for performing numerous computerized literature searches; Mary Cronmiller, for locating many of the literature references identified by Marianne; Sara Spielvogel, for expert assistance with microphotography and

elemental analysis with the EDS system; and finally, Don Beyer and Bill Summer, whose assistance in preparing photographs and slides is priceless.

I would like to thank The Institute of Paper Chemistry and its member companies for allowing me to pursue the Doctorate degree. I would like to thank the United States Department of Energy for providing funds for this research (Contract No. DE-FGO2-85CE407238). I would like to thank Mr. Atul Shah at The E.I. DuPont de Nemuors and Company and Mr. Alan Jackson at Thermal Ceramics for providing the alumina ceramic fibers used in this thesis at no cost, and Dr. Ralph Brandon at Owens-Corning Fiberglass for providing glass fibers at no cost.

Finally, and most importantly, I thank my lovely wife, Doris, and my terrific sons, Kyle and Nathan, upon whose shoulders has fallen the burden of sacrifice these last two years. The love, encouragement, support, and interest of my family has truly been instrumental in my thesis program.

BIBLIOGRAPHY

1. Sprague, C.H. Impulse Drying and Press Drying: A Critical Comparison. Proceedings of the Tappi Papermakers Conference. Atlanta, GA, April 6-7,1987:35-41.

2. Ahrens, F.W. Heat Transfer Aspects of Hot-Surface Drying at High Temperature and and Mechanical Loading. Journal of Pulp and Paper Science 9(3):TR79-TR83(July 1983).

3. Ahrens, F.; Kartsounes, G.; Ruff., D. A Laboratory Study of Hot-Surface Drying at High Temperature and Mechanical Loading. Pulp and Paper Canada 85(3):93-98(1984).

4. Arenander, S.; Wahren, D. Impulse Drying Adds New Dimension to Water Removal. Tappi Journal 66(9):123-126(September 1983).

5. Sprague, C. H.; Lavery, H. P. Impulse Drying: How Mills Can Take Advantage of it. Preprints of the CPPA Annual Meeting, Book B. Montreal, January 28-29, 1987:215-221.

6. Lavery, H.P.; Impulse Drying of Linerboard. Technical Paper Series Number 214, The Institute of Paper Chemistry, Appleton, WI. November, 1986: 6 p.

7. Lavery, H.P.; Impulse Drying of Newsprint. Proceedings of the Tappi Papermakers Conference. Atlanta, GA, April 6-7,1987:43-49.

8. Lavery, H.P. High-Intensity Drying Processes - Impulse Drying. Report Three. U.S. Department of Energy Contract No. FG02-85CE40738. February 1988. 80 p.

9. Lavery, H.P.; Sprague, C.H. Impulse Drying: A Status Review. Technical Paper Series Number 275, The Institute of Paper Chemistry, Appleton, WI. February, 1988: 12 p.

10. Burton, S. W. An Investigation of Z-Direction Density Profile Development During Impulse Drying. Doctoral Dissertation. Appleton, WI, The Institute of Paper Chemistry, 1987. 124 p.

11. Bartz, W. J. An Evaluation of Impulse Drying in a Simulated Linerboard Mill. A-190 Project. Appleton, WI, The Institute of Paper Chemistry, 1988. 84 p.

12. Devlin, C. P. An Investigation of the Mechanism of High-Intensity Drying. Doctoral Dissertation. Appleton, WI, The Institute of Paper Chemistry, 1987. 122 p.

13. Collier, J.G. Convective Boiling and Condensation. McGraw Hill Book Company (UK) Limited, London, 1972.

14. Lienhard, J.H. A Heat Transfer Textbook. Prentice-Hall, Engelwood Cliffs, NJ, 1981.

15. Collier, J.G. Boiling and Evaporation. Chapter 2.7 in Heat Exchanger Design Handbook. Hemisphere Publishing Co., 1983.

16. Rohsenow, W.M.; Hartnett, J.P. Boiling. Section 13 in The Handbook of Heat Transfer. McGraw Hill, New York, 1973.

17. Rohsenow, W.M. Heat Transfer in Boiling. Modern Developments in Heat Transfer, W. Ibele (editor). Academic Press, New York, 1963:85-158.

18. Moissis, R.; Berenson, P.J. On the Hydrodynamic Transitions in Nucleate Boiling. Journal of Heat Transfer 85:221-229(August 1963).

19. Graham, R.W.; Hendricks, R.C. Assessment of Convection, Conduction, and Evaporation in Nucleate Boiling. NASA Technical Note D-3943, May 1967. 42 pgs.

20. Rohsenow, W.M.; Clark, J.A. A Study of the Mechanism of Boiling Heat Transfer. Transactions of the ASME 73:609-620(July 1951).

21. Stephan, K. Bubble Formation and Heat Transfer in Natural Convection Boiling. Heat Transfer in Boiling. Hahne, E. and Grigull, U. (editors), Hemisphere, Washington, 1977:3-20.

22. Pasamehmetoglu, K.O.; Nelson, R. A. The Effect of Helmholtz Instability on the Macrolayer Thickness in Vapor Mushroom Region of Nucleate Pool Boiling. International Communications in Heat and Mass Transfer 14:709-720(1987).

23. Forster, H.K.; Grief, R. Heat Transfer to a Boiling Liquid - Mechanism and Correlations. Journal of Heat Transfer 81:43-53(February 1959).

24. Jensen, M.K.; Memmel, G.J. Evaluation of Bubble Departure Diameter Correlations. Proceedings of the 8th International Heat Transfer Conference, Volume 4. San Francisco, CA, August 17-22,1986:1907-1912.

25. Tong, L.S. Boiling Heat Transfer and Two-Phase Flow. John Wiley and Sons, New York, 1965.

26. Lienhard, J.H.; Wong, P.T.Y. The Dominant Unstable Wavelength and Minimum Heat Flux During Film Boiling on a Horizontal Cylinder. Journal of Heat Transfer 86:220-226(May 1964).

27. Sakurai, A.; Shiotsu, M. Temperature-Controlled Pool-Boiling Heat Transfer. Proceedings of the Fifth International Heat Transfer Conference, Tokyo, Japan (1974). Paper B3-1:81-85.

28. Berenson, P.J. Experiments on Pool Boiling Heat Transfer. International Journal of Heat and Mass Transfer 5:985-999(1962).

29. Hesse, G. Heat Transfer in Nucleate Boiling, Maximum Heat Flux and Transition Boiling. International Journal of Heat and Mass Transfer 16:1611-1627(1973).

30. Berenson, P.J. Film-Boiling Heat Transfer from a Horizontal Surface. Journal of Heat Transfer 83:351-358(August 1961).

31. Bier, K.; Engelhorn, H.R.; Gorenflo, D. Heat Transfer at Burnout and Leidenfrost Points for Pressures up to Critical. Heat Transfer in Boiling. Hahne, E. and Grigull, U. (editors), Hemisphere, Washington, 1977:85-97.

32. Cichelli, M.T.; Bonilla, C.F. Heat Transfer to Liquids Boiling Under Pressure. Transactions of the AIChE 41:755-787(1945).

33. Bier, K.; Gorenflo, D.; Wickenhäuser, G. Pool Boiling Heat Transfer at Saturation Pressures up to Critical. Heat Transfer in Boiling. Hahne, E. and Grigull, U. (editors), Hemisphere, Washington, 1977:137-158.

34. Huber, D.A.; Hoehne, J.C. Pool Boiling of Benzene, Diphenyl, and Benzene-Diphenyl Mixtures Under Pressure. Journal of Heat Transfer 85:215-220(August 1963).

35. Farber, E.A.; Scorah, R.L. Heat Transfer to Water Boiling Under Pressure. Transactions of the ASME 70:369-384(May 1948).

36. Hahne, E.; Feurstein, G. Heat Transfer in Pool Boiling in the Thermodynamic Critical Region: Effect of Pressure and Geometry. Heat Transfer in Boiling. Hahne, E. and Grigull, U. (editors), Hemisphere, Washington, 1977:159-206.

37. Sakurai, A.; Shiotsu, M.; Hata, K. Effect of System Pressure on Film-Boiling Heat Transfer, Minimum Heat Flux, and Minimum Temperature. Nuclear Science and Engineering 88:321-330(1984).

38. Webb, R.L. The Evolution of Enhanced Surface Geometries for Nucleate Boiling. Heat Transfer Engineering 2(3-4):46-69(January-June 1981).

39. Kajikawa, T.; Takazawa, H.; Mizuki, M. Heat Transfer Performance of Metal Fiber Sintered Surfaces. Heat Transfer Engineering 4(1):57-66(January-March 1983).

40. Young, R.K.; Hummel, R.L. Improved Nucleate Boiling Heat Transfer. Chemical Engineering Progress 60(7):53-58(July 1964).

41. Körner, W.; Photiadis, G. Pool Boiling Heat Transfer and Bubble Growth on Surfaces with Artificial Cavities for Bubble Generation. Heat Transfer in Boiling. Hahne, E. and Grigull, U. (editors), Hemisphere, Washington, 1977:159-206.

42. Judd, R.L.; Merte, H., Jr. Evaluation of Nucleate Boiling Heat Flux Predictions at Varying Levels of Subcooling and Acceleration. International Journal of Heat and Mass Transfer 15:1075-1096(1972).

43. Clements, L.D.; Colver, C. P. Natural Convection Film Boiling Heat Transfer. Industrial and Engineering Chemistry 62(9):26-46(September 1970).

44. Rohsenow, W. M. A Method of Correlating Heat-Transfer Data for Surface Boiling of Liquids. Transactions of the ASME 74:969-976(August 1952).

45. Frost, C.W.; Li, K.W. On the Rohsenow Pool-Boiling Correlation. Journal of Heat Transfer 93:232-234(May 1971).

46. Mikic, B.B.; Rohsenow, W. M. A New Correlation of Pool-Boiling Data Including the Effect of Heating Surface Characteristics. Journal of Heat Transfer 91:245-250(May 1969).

47. Stephan, K.; Abdelsalam, M. Heat-Transfer Correlations for Natural Convection Boiling. International Journal of Heat and Mass Transfer 23(1):73-87(January 1980).

48. Zuber,N. On the Stability of Boiling Heat Transfer. Transactions of the ASME 80:711-720(April, 1958).

49. Lienhard, J.H.; Dhir, V.K. Hydrodynamic Prediction of Peak Pool-Boiling Heat Fluxes from Finite Bodies. Journal of Heat Transfer 95:152-158(1973).

50. Berenson, P.J. Transition Boiling Heat Transfer from a Horizontal Surface. MIT Technical Report No. 17 (1960).

APPENDIX I

APPARATUS PREPARATION AND EXPERIMENTAL TECHNIQUES

This Appendix discusses the techniques developed to prepare the apparatuses for the respective experiments. All of the experiments performed for this thesis require the formation of a fiber bed. Therefore, the issue of making a well-dispersed fiber slurry is addressed prior to discussing specific experimental techniques. All water used in these experimental techniques is distilled and de-ionized.

DISPERSING THE CERAMIC FIBERS

Intense mechanical agitation is needed to achieve complete dispersion of the ceramic fibers. Dispersing the fibers in this manner also reduces the length, so an excessive amount of agitation must be avoided. As obtained, the 3.0 μm diameter fibers are in staple form, the 8.4 μm diameter fibers are in 3 to 7 mm lengths, and the 18.5 μm diameter fibers are in 30 cm lengths. The two smaller fiber diameters are added to the agitator as received, but the 18.5 μm diameter fibers are cut to one-inch length with a paper cutter prior to agitation.

The intensity of agitation necessary to disperse the fibers is achieved with a 5-liter Waring blender. Approximately 5 g of fiber are added to 2.5 liters of water in the blender's bucket, and the following agitation schedule yields a well-dispersed slurry having the desired fiber length of 1 to 1.5 mm:

	Fiber Diameter		
Activity	3.0 μm	8.4 μm	18.5 μm
first agitation	5 sec	5 sec	5 sec
second agitation	5 sec	5 sec	3 sec
decant	half of volume	half of volume	half of volume
third agitation	5 sec	5 sec	5 sec
decant	remainder	remainder	remainder

All agitation times are performed at the blender's HIGH setting. A number of these batches are made until the total desired weight of fiber is dispersed. After this intense agitation, dispersion is

maintained by mild agitation with a laboratory stirrer, which is not intense enough to effect further fiber length reduction.

PREPARATION OF THE BOILING CELL APPARATUS

Preparation for a boiling experiment includes formation of a fiber bed in the boiling cell, and assembly of the apparatus.

Technique for Forming a Fiber Bed in the Boiling Cell

Fiber bed formation in the boiling cell is accomplished by attaching a 8.89 cm ID, 38 cm long plexiglass formation section onto the fiber-bed-end of the boiling cell once the cell is inverted. The dispersed fiber is held in a 50 gallon mixing tank on the mezzanine above the boiling cell apparatus at a consistency of 0.1% to 0.2%. A Lightnin® mixer (model V-7) controlled with a rheostat to about 60% of full speed turns a stirring rod that has a two-inch diameter, three-blade impeller. The fiber slurry flows by gravity from the tank into the plexiglass forming section. The following bed formation technique forms a bed in approximately two hours for large diameter fibers, and four hours for small diameter fibers.

1. The forming media is positioned at the desired height in the boiling cell, and its mounting bolts are tightened. The bed compression ring is placed on the teflon guides that support the forming media.
2. The top mounting plate assembly is placed on the boiling cell. The Belleville washers and nuts are placed over the threaded support rods, and the nuts are tightened to 20 in-lb_f.
3. The boiling cell is inverted, and the 8.89 cm ID acrylic forming tube is positioned on the boiling cell, with a rubber gasket placed between the two. The mounting plate is positioned over the threaded support rods, and the nuts are tightened to 20 in-lb_f.
4. The fiber slurry supply line is mounted to feed the slurry into the center of the forming section.
5. The boiling cell is filled from the bottom with water to a level about 15 cm below the top of the forming tube.
6. The mixing tank is filled with about 30 gallons of water, and the tank agitator is turned on. An amount of fiber necessary to achieve a consistency of 0.1% to 0.2% is dispersed and added.
7. The supply header valve and the boiling cell drainage valve are opened. These valves are adjusted to maintain a constant level about 3 cm below the top of the forming tube.
8. Steps 6 and 7 are repeated until the desired bed is formed. While subsequent mixing tank batches are made up, flow through the bed is stopped, allowing the bed to relax in the pool of water in the tube.
9. The mixing tank is washed with water into the forming tube, and then the boiling cell is drained.
10. The forming tube is removed from the boiling cell and cleaned.

Assembly of the Boiling Cell Apparatus

Once the fiber bed is formed, the boiling apparatus is assembled in the following fashion. Complete assembly takes about 45 minutes. Prior to installing the heater block, any block thermocouple surface preparation is completed. Typically, the thermocouples are removed from the block, and the face is sanded to renew the junction. Two copper foil disks are inserted into the holes prior to replacing the thermocouples.

1. After the fiber bed formation tube is removed from the boiling cell, the heating block is hoisted into position, and centered on the boiling cell. The bottom mounting plate assembly is placed over the threaded support rods, a pair of Belleville washers are placed over the rods with their concave surfaces facing each other, and the nuts are tightened to 20 in-lb_f.
2. The boiling cell is rotated 180°, and the plug in the center of the top mounting plate assembly is removed.
3. The forming media mounting bolts are loosened. The fiber bed compression rod is inserted through the plug hole in the center of the top mounting plate, and is screwed onto the compression ring. The bed is compressed to the desired height, and the forming media mounting bolts are tightened. The compression rod is removed, and the plug in the top mounting plate assembly is wrapped with teflon tape and is replaced.
4. The top and bottom mounting plate assemblies are tightened to 30 in-lb_f.
5. The heater block assembly is insulated, and the guard heater is wrapped around the insulation. The guard heater thermocouple is placed between the heater and the insulation.
6. The heater block is grounded to the apparatus framework.
7. The fiber bed thermocouples are positioned within the bed.
8. The piping for the make-up water supply line, the vapor vent line, and the safety pop-off line is connected to the top mounting plate assembly. The valves in immediate proximity to the top mounting plate assembly are opened. If needed, the air pressure supply line is connected to the top mounting plate assembly piping.
9. The heater block thermocouples are connected to the data acquisition cable.
10. The pressure transducer is connected to the data acquisition cable.
11. The makeup water tank is filled with about ten gallons of water, and the water supply pump is turned on. The tank heater is turned on, and the water is heated to about 75°C.
12. The capacitive proximity switch is mounted 2.2 cm away from the perimeter of the boiling cell and is turned on.
13. The cartridge heaters are connected to the electrical supply line.
14. The boiling cell is filled with water to the desired level through 1/4 " polyethylene tubing connected to the bottom nipple. This line is then disconnected and capped.
15. The manual valve on the water re-supply line is opened.
16. The lexan shield is placed around the apparatus.
17. The pressure equalization valve on the vapor vent bypass line is closed.
21. The computer and related electronics are turned on.
22. The temperature controller is put in MANUAL mode with an output of 0%. The initial profile setpoint is set to the boiling point, and the initial profile time segment is set to CONT.
23. The computer program BOILCTL.BAT is executed. When the TBASIC prompt appears, the program BOIL.CTL is executed.
24. Prior to heating the system, the checklist illustrated in Figure 64 is completed to insure that the system is fully prepared for an experiment.

CONTROL SYSTEM																	
1. Controllers and software operable?																	
2. Low temperature controller setpoint?																	
3. Proper controller parameters?																	
HARDWARE																	
4. Piping unions tight?																	
5. Water supply valve open?																	
6. Pressure vent valve open?																	
7. Presseure equalization valve open?																	
8. Pressure gauge valves open?																	
9. Air supply valve open?																	
10. Air supply connected?																	
11. Water temperature high enough?																	
12. Water supply pump running?																	
13. Water pressure high enough?																	
14. Heating block grounded?																	
15. Cartridge heaters connected?																	
16. Proximity switch mounted?																	
17. Proximity switch turned on?																	
18. Proper water level in quartz tube?																	
19. Tube holding clamp tightened?																	
20. Heating block insulation in place?																	
21. Guard heater mounted?																	
22. Lexan shield in place?																	
INSTRUMENTATION																	
23. Block thermocouples connected?																	
23. Bed thermocouples connected?																	
22. Guard heater therm'ple connected?																	
25. Pressure transducer connected?																	

Figure 64. Checklist for assembling the boiling cell apparatus.

25. The apparatus is heated to a surface temperature about 8°C above the boiling point in MANUAL by increasing the temperature controller output. Concurrently, the system pressure is slowly approached by setting the pressure controller setpoint, and slowly opening the air pressure supply valve.
26. The temperature controller is put in AUTO, and after about 45 minutes of active boiling at this elevated temperature, the first temperature setpoint is approached. This marks the beginning of the boiling experiment.

27. The experiment progresses by collecting data once the process reaches steady-state at a given setpoint. Then, new setpoint information is downloaded to the controller, and the setpoint is approached.
28. To end the experiment, the controller is put in MANUAL mode with an output of 0%.
29. After the apparatus cools, the pressure is returned to atmospheric, and the pressure equalization valve is opened.

After the experiment is completed, the water is drained from the boiling cell, and the apparatus is disassembled. The fiber bed is removed from the cell and is dried and weighed for porosity determination.

PREPARATION OF THE CAPILLARY PRESSURE / SATURATION APPARATUS

Preparation for a capillary pressure/saturation experiment includes formation of a fiber pad in the formation tube, as illustrated in Figure 44, and assembly of the apparatus.

Technique for Forming the Fiber Pads

The following technique forms pads with porosities of 0.96-0.97 and diameters of about 4.9 cm in about 45 minutes. A constant flow of water is maintained through the forming tube during the formation process. Typically, to achieve the desired porosity, an appropriate weight of the fiber is used in the formation process. The height of the pad will vary depending on the target porosity for the compressed pad in the apparatus. The water supply tank is located eight feet above the forming media, and the water reservoir is located three feet below the forming media.

1. A laboratory agitator is mounted on the five-gallon bucket of dispersed fiber.
2. The reservoir is filled with 5 gallons of water, most of which is pumped to the supply tank.
3. A 100-mesh bronze forming wire is sandwiched between the top and bottom pieces of the forming tube, and the assembled tube is mounted on a ring stand.
4. By introducing flow through the bottom piece of the tube, the formation tube is filled about half way with water from the supply tank.
5. A 500 ml beaker of the fiber slurry is taken from the bucket and is added in small lots to the top of the tube at roughly 30 second intervals. The drainage line is opened, and a flow rate of about 500 ml/min is maintained through the tube throughout the forming process. This step is repeated until all of the fiber has been added.
6. Once the bed is formed, 1500 ml of distilled, de-ionized water that has been vacuum-treated is passed through the fiber bed to remove any air.
7. After washing, the formation tube is drained.
8. The flange bolts are removed, and the forming media and the pad are removed from the tube.

9. The pad is immediately placed in the funnel of the capillary pressure/saturation apparatus by inverting the funnel, placing the pad in the center of the fritted disk, and returning the funnel to its upright position.
10. The forming media and tube are cleaned to remove any residual fiber.

Preparing the Capillary Pressure/Saturation Apparatus

In preparing the apparatus for a test, it is important to minimize the size of the air pocket that gets trapped beneath the funnel's fritted ceramic disk while filling the liquid side of the system with water. The following procedure yields a negligibly small pocket of trapped air. Prior to connecting in-line, the proper diaphragm for the Validyne pressure transducer is installed, and it is calibrated against a CCl_4 manometer.

1. The funnel is removed from the apparatus and is cleaned.
2. The water supply flask is filled with water, and is mounted on a ring stand above the funnel.
3. All valves are opened and water flows from the water supply flask through the tubes until all air is displaced from the system tubing. The water line leading to the pressure transducer is purged of air by opening the bleed valve on the pressure transducer. The water supply valve is closed.
4. The funnel is inverted, and water is added to the cavity beneath the fritted ceramic disk. The fitting that connects the funnel assembly to the tubing is filled with water and is connected to the funnel.
5. While the funnel is inverted, the fiber bed is positioned in the center of the ceramic disk. The funnel is returned to right-side-up position, and is connected to the tubing.
6. The tubing valves are re-opened to bleed any air in the buret lines, and are closed again.
7. Three shims are positioned symmetrically about the perimeter of the pad, and the 100 μm sintered bronze disk is placed on top of the bed.
8. Two springs are placed on top of the bronze disk, and the lid is placed on top of the springs.
9. The lid nuts are tightened, which pushes the sintered bronze disk against the shims,compressing the bed in the process.
10. Water is introduced into the cavity of the funnel through a piece of small-diameter Tygon tubing that fits through the threaded hole in the funnel lid. Flow is stopped when the water level rises up to the bronze disk.
11. Once the fiber pad is saturated, the excess water is syphoned out of the funnel using the Tygon tubing. A small amount of water is left behind, but this quantity is insignificant compared to the volume of water in the bed.
12. After removing the Tygon tubing, the lid fitting is wrapped with teflon tape and is threaded into place, and the tubing from the regulator valve and the high-pressure side of the transducer is connected.
13. The position of the buret is adjusted so that the water in the buret and the funnel coincide. The buret valve is opened, and after the system equilibrates, the initial data set is taken.
14. Pressure is applied to the cavity of the funnel by opening the precision regulator valve.

System equilibration is assumed when the displaced volume changes by less that 0.1 ml per hour. After the system equilibrates, the water level in the buret is noted, and the zero suppression reading

is read from the pressure transducer amplifier. Displaced volume is determined by difference in contiguous buret readings, and the pressure difference is calculated from the zero suppression reading and full scale value of the transducer. After the test is completed, the buret valve is closed and the funnel is disconnected from the tubing. The water is drained from the funnel, the pressure is relieved, and the pad is removed from the funnel. The pad is weighed, dried, and reweighed to determine porosity and irreducible saturation.

PERFORMING A PERMEABILITY EXPERIMENT

As illustrated in Figure 45, permeability of fiber pads is measured after formation in a plexiglass tube similar to that used to form the pads for the capillary pressure/saturation experiment. Prior to connecting to the pressure tap tubing, the Validyne differential pressure transducer is calibrated against either a water manometer or a CCl_4 manometer. For pads made from 18.5 and 8.4 μm diameter fibers, a 0.2 psi diaphragm was adequate. Pads made from the 3.0 μm diameter fibers required a 1.0 psi diaphragm to maintain easily measurable flow rates. Bed formation and permeability measurement can be completed in about four hours.

1. The calibrated pressure transducer is connected to the pressure tap tubing.
2. Steps 1 through 4 from Technique for Forming the Fiber Pads are completed, with the addition that the flow diffuser is positioned in the bottom piece of the permeability-pad formation tube.
3. Air is purged from the pressure tap tubing by opening both of the bleed screws on the pressure transducer. This process is repeated until the transducer reads zero-pressure-drop.
4. Steps 5 and 6 from Technique for Forming the Fiber Pads are completed.
5. After the pad is washed, flow is stopped, and the screw jack assembly is mounted on the tube.
6. The pad is compressed to the desired height by turning the screw jack.
7. The valve on the water supply line from the pump is opened, and the flow rate is adjusted to give a mid-scale pressure reading. A data set consisting of the zero suppression reading of the transducer, the volume of water discharged to the graduated cylinder, and the time of the flow is recorded.
8. Step 7 is repeated until six data points are collected at a given bed height.
9. Step 6 through 8 are repeated until data is collected for the desired number of bed heights.

The flow rate is determined from the volume in the graduated cylinder and the time of flow, and the pressure difference is calculated from the zero suppression reading and full scale value of the transducer. After the test is completed, the water is drained from the tube, and the pad is dried and weighed to determine porosity.

APPENDIX II

THE FLUENT® MODEL OF THE COPPER HEATING BLOCK

This Appendix details the model used to design the copper heating block of the boiling cell apparatus. The main feature of the block to be determined from this model is the height necessary for one-dimensional heat flow in the region of the thermocouples, as required by the method for calculating heat flux (discussed in Appendix III). Runs with an initial crude model were based on the critical heat flux, and the heat flux at a surface temperature of 425°C, of the pool boiling curve illustrated in Figure 9. The initial model assumed that all exterior walls not engaged in boiling heat transfer were perfectly insulated. The two computational experiments to be discussed here utilized a model refined with convective heat loss data (discussed in Appendix III).

MODEL OF THE COPPER HEATING BLOCK

FLUENT, a finite-volume computational fluid dynamics code which is marketed by Creare, Inc. of Hanover, NH, is utilized in modeling the heater block. As illustrated in Figure 65, the cylindrical geometry is modeled in three dimensions with polar coordinates by considering only one-eighth of the total volume, and is discretized according to Figure 66 to yield a total of 9900 grid points [h]. In the finite-volume technique, the intersection of grid lines defines a grid point, which is the center of a cell. Cell boundaries are defined by the mid-point between adjacent cells. The spacing between axial grid lines is 0.335 cm, between radial grid lines is 0.0318 cm, and between angular grid lines is 0.0982 radians.

Because of the limitations of this version of FLUENT, the cylindrical shape of the cartridge heaters are modeled with near-rectangular shaped cells, evident as the shaded regions in Figure 66. The actual circumference of the cartridge heaters is 3.99 cm, while the modeled circumference

[h] The version of FLUENT utilized here (V. 2.8.2) has a maximum capability of 10,000 grid points.

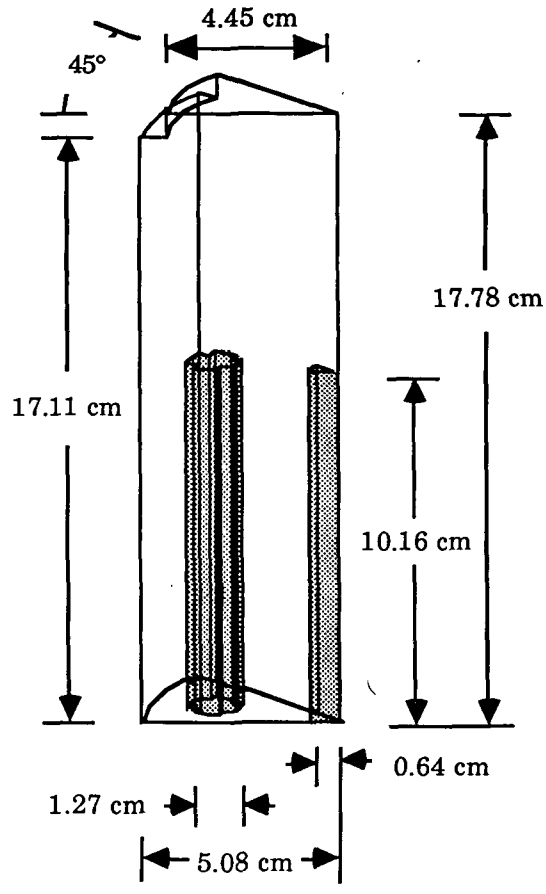

Figure 65. Schematic of the heating block domain modeled in FLUENT.

is 5.00 cm. The actual surface area of the cartridge heaters is 40.54 cm^2, while the modeled active surface area is 48.63 cm^2. The surface area differential is taken into account in determining heat flux density for the heat flux boundary condition of the cartridge heaters.

Two additional pieces of information about the model are important to communicate. First, the temperature-dependent heat capacity and thermal conductivity of the copper (discussed in Appendix III) are curve-fitted with the following cubic polynomials:

$$k_h\left[\frac{W}{m\text{-}^\circ K}\right] = 431.0 - 0.101\,T - 1.479\times10^{-4}T^2 + 2.118\times10^{-7}T^3 \quad , \tag{59}$$

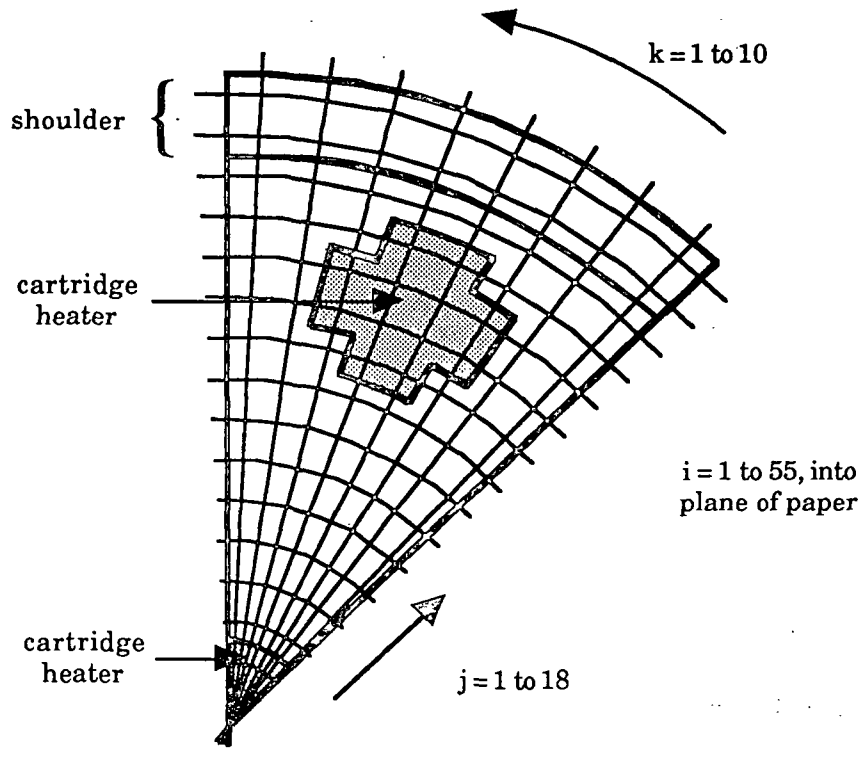

Figure 66. The grid for discretizing the heating block domain in the FLUENT model.

$$C_{p_h}\left[\frac{J}{kg\text{-}^\circ K}\right] = 183.8 - 1.186\,T - 2.087\times10^{-3}T^2 + 1.267\times10^{-6}T^3 \quad , \tag{60}$$

where temperature is in degrees Kelvin. These polynomials, and a bulk density of 888.6 kg/m^3, are used to define the physical properties of the domain in the model. Second, all solution variables except temperature and heat flux are turned off, which essentially means that the heat diffusion equation is the only conservation equation that is solved.

THE HEIGHT OF THE HEATING BLOCK

Numerical experiments with the initial model indicate that a distance of about 7 cm above the height of the cartridge heaters is needed to insure unidirectional heat flow in the region of the block thermocouples. The results of a case based on the critical pool boiling heat flux using the refined model are presented here. The boundary conditions are listed in Table 15. The boundary condition for heat supply from the cartridge heaters, and the boundary condition for the heat

transfer coefficient of the boiling surface, are based on a heat flux of 100 W/cm^2, and the corresponding wall superheat of 40°C, for a heater surface area of 8.89 cm^2. The ambient temperature for convective heat loss is assumed to be 30°C. Total heat supply is divided between boiling and convective heat transfer for heat transfer coefficient determination.

Table 17. Boundary conditions for the FLUENT model.

Surface of the Heater Block Geometry	Type of Surface Boundary Condition	Boundary Condition[a] Case 1	Case 2	
Boiling surface	heat transfer coefficient	23,360	42,961	W/(m^2-°C)
Shoulder near boiling surface	heat transfer coefficient	4599	13,983	W/(m^2-°C)
Perimeter internal to block	symmetry			
Perimeter external to block (top 15.2 cm)	heat transfer coefficient	0.36	0.36	W/(m^2°C)
Perimeter external to block (bottom 2.5 cm)	heat transfer coefficient	3.6	3.6	W/(m^2°C)
Bottom of block	heat transfer coefficient	3.6	3.6	W/(m^2°C)
External surface of cartridge heater	constant heat flux	185,236	103,000	W/m^2
Cells internal to cartridge heater	adiabatic	373	373	°K

a - Case 1 is based on the critical heat flux of the characteristic boiling curve illustrated in Figure 9, and Case 2 is based on experimental data from CBE20 for pool boiling of water at a wall superheat of 15°C.

After 3000 iterations, the normalized residual for heat flux is 1.176 x 10^{-6}. The results illustrated in Figure 67 indicate that a uniform radial temperature profile develops a short distance above the cartridge heaters. The shoulder near the boiling surface does disrupt the levelness of the profile somewhat, but the effect on the accuracy of the heat flux calculation is minimal because the three block thermocouples are located near the axis, which still exhibits undisturbed temperature profiles.

Temperature variation in the plane of the thermocouples is largely confined to the periphery of the block. For the plane of the closest (i=51), middle (i=48) and furthest (i=43) thermocouple to the boiling surface, the temperature variation is 426.3 to 427.7°K, 446.4 to 446.9°K,

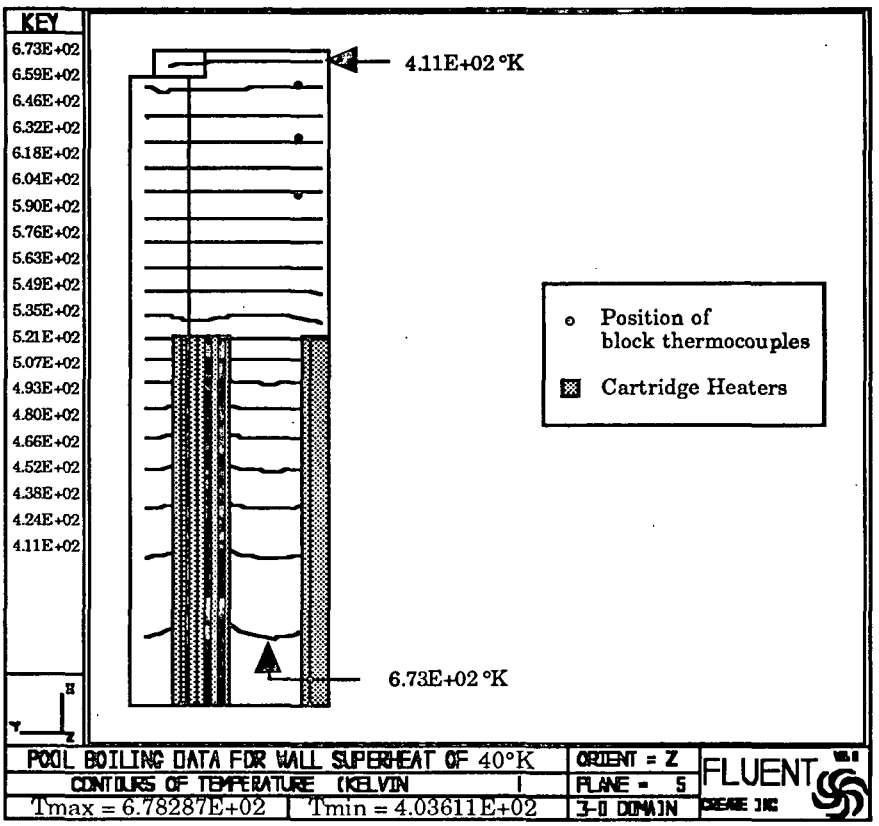

Figure 67. Axial temperature distribution in the heating block for atmospheric pool boiling of water at the critical heat flux. Boundary conditions are based on the boiling curve in Figure 9.

and 479.9 to 480.1°K, respectively. The variation is larger on the boiling surface due to the effect of the shoulder on the heat flow - 403.6 to 406.1°K. As illustrated in Figure 68 for the plane just beneath the boiling surface (this version of FLUENT can not graph profiles on a boundary), this variation is largely confined to the perimeter of the surface.

Based on results from cases similar to this, the copper heating block is designed for a total height of 17.8 cm.

MODEL COMPARISON TO EXPERIMENTAL DATA

To verify the model, a case based on experimental data collected for pool boiling with the boiling cell apparatus was run. The experimental data point, taken from data set CBE20, involves

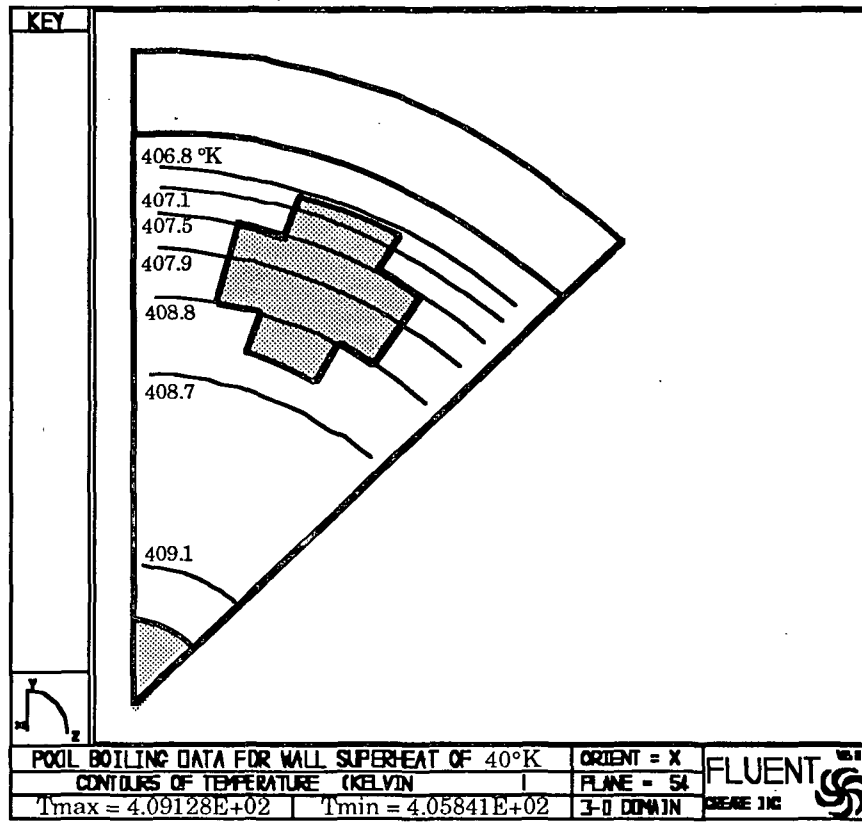

Figure 68. Radial temperature distribution for the plane just beneath the heating surface for the case of atmospheric pool boiling of water at the critical heat flux.

a heat flux of 57.9 W/cm^2 at a wall superheat of 15°C, and the appropriate boundary conditions are listed in Table 15. After 2500 iterations, the normalized residual for heat flux is 7.671 x 10^{-7}.

As illustrated in Figure 69, temperature variation proximate to the block thermocouples is small; in-plane variations for the closest, middle, and furthest thermocouple are 399.6 to 401.2°K, 414.0 to 414.6°K, and 437.8 to 437.9°K, respectively. Corresponding experimental readings are 406.2°K, 421.4°K, and 446.8°K. As illustrated in Figure 70, temperature variation in the plane just beneath the surface is confined largely to the perimeter. Computed surface temperature variation is 383.7 to 386.0°K, while the experimental value is 388.0°K. The temperature in the bottom of the block is computed to be 584.2°K, and it is measured to be 588.8°K. The model provides decent agreement with experimentally-measured temperatures, although some improvement of boundary conditions would improve accuracy.

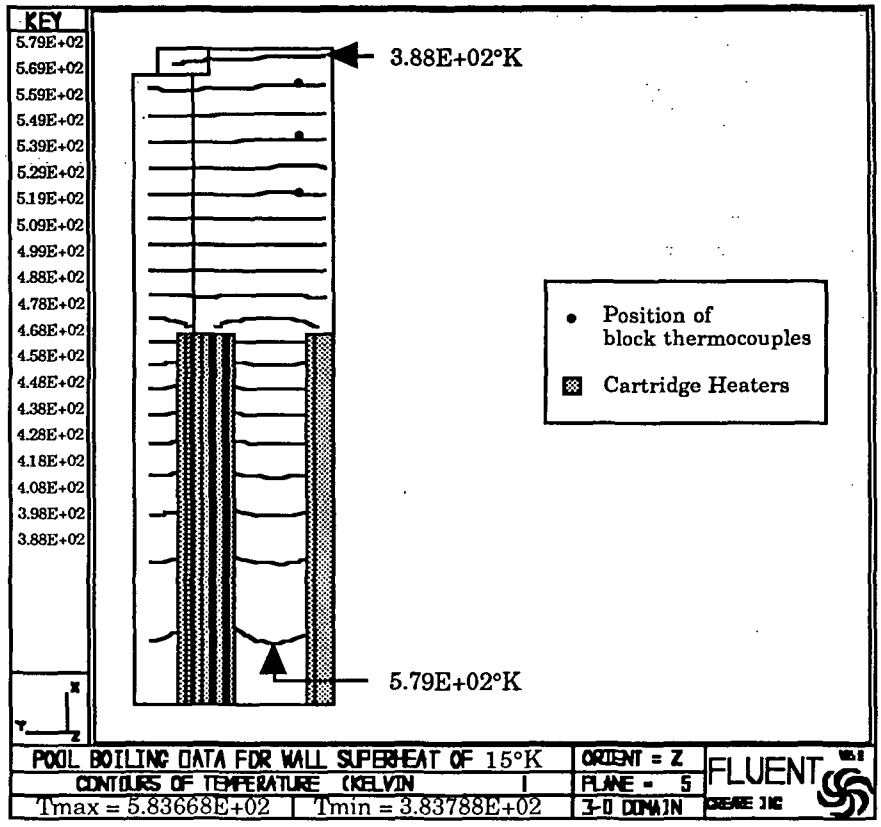

Figure 69. Axial temperature distribution in the heating block for atmospheric nucleate pool boiling of water at a wall superheat of 15°C. Boundary conditions are based on data set CBE20.

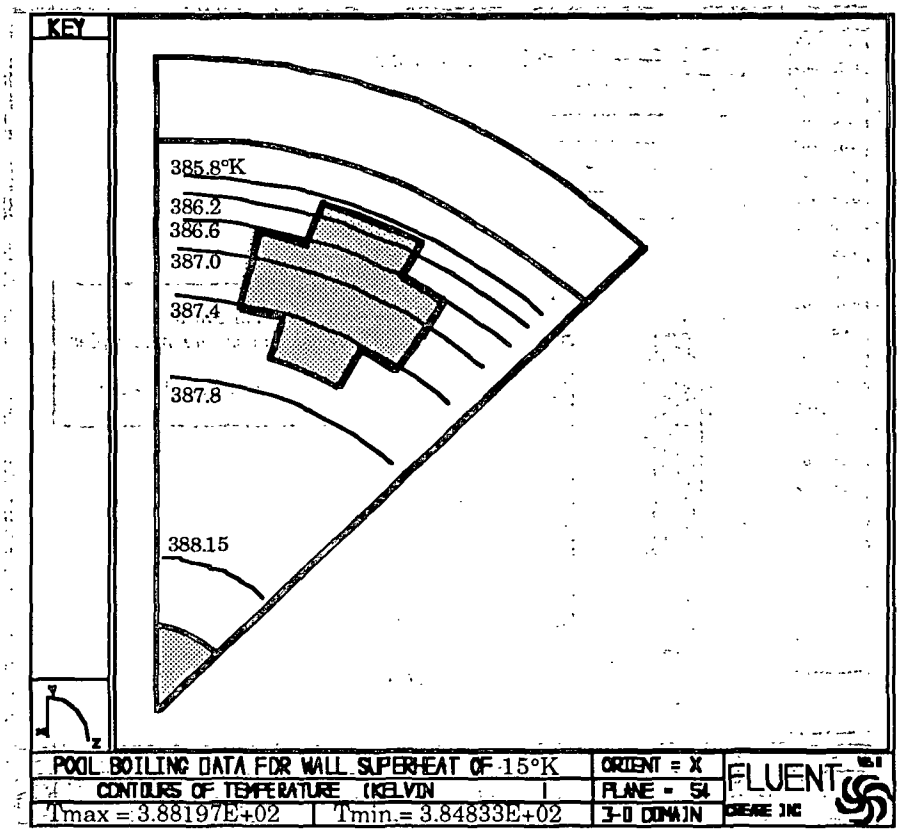

Figure 70. Radial temperature distribution for the plane just beneath the heating surface for atmospheric nucleate pool boiling of water at a wall superheat of 15°C.

APPENDIX III

THE METHOD FOR CALCULATING HEAT FLUX

The equation used to calculate heat flux based on the heating block thermocouple readings is developed in this Appendix. A few related tasks were completed to minimize inaccuracies in this calculation. First, the temperature-dependent thermal conductivity of the heating block material was determined and incorporated into the heat flux calculation. Second, a lumped-parameter heat loss test was performed to determine the scale of convective heat loss. Finally, an independent measure of system heat flux was made with a watt transducer to verify the heat flux calculation.

TEMPERATURE-DEPENDENT THERMAL CONDUCTIVITY OF THE HEATING BLOCK

The temperatures within the region of the copper block where the thermocouples are mounted reach levels as high as 400°C. Assuming a constant thermal conductivity for the heat flux calculations would severely limit the accuracy of the calculated heat flux. Consequently, a sample of the heating block material (ASTM B301) was tested to determine thermal conductivity as a function of temperature for the range of 25 to 400 °C [i]. The thermal conductivity was not measured, but was determined from the thermal diffusivity, specific heat, and density. The thermal diffusivity and specific heat were measured as functions of temperature, but the value of density at room temperature, determined from one of the samples, was used in the calculation. It is customary procedure to not correct the thermal conductivity data for thermal expansion. As calculated, the thermal conductivity is accurate to within ± 4%.

Thermal diffusivity was determined using the laser flash diffusivity method in which the temperature of the back face of a small sample disc is monitored as the front face is subjected to

---

[i] Report number PRL 786; Properties Research Lab, P.O. Box 2224, West Lafayette, IN 47906; Dr. Ray E. Taylor, Head, 317-463-1581. A copy of the report is attached at the end of this Appendix.

short laser pulses. The computer-controlled apparatus uses a Korad K2 laser, and the surface temperature is measured with either a spring-loaded thermocouple or an IR pyrometer. This technique is used in over 80% of the thermal diffusivity measurements throughout the world. Specific heat is measured with a standard Perkin-Elmer Model DSC-2 Differential Scanning Calorimeter using sapphire as the reference material.

The raw data and the calculated thermal conductivity data are listed in Table 18. The thermal conductivity data are correlated with the following cubic polynomial,

$$k_h = 3.967 - 1.345\times10^{-3} T + 2.560\times10^{-7} T^2 + 2.118\times10^{-9} T^3 \qquad (61)$$

where the temperature is expressed in degrees Celsius. The correlation coefficient for this expression is 0.987. The calculated data and the polynomial are graphically illustrated in Figure 71.

Table 18. Data for determination of the temperature-dependent thermal conductivity of the copper heating block.

Temperature (°C)	Density (g/cm^3)	Specific Heat (J/(g-°C))	Thermal Diffusivity (cm^2/sec)	Thermal Conductivity (W/(cm-°C))
23.0	8.886	0.385	1.149	3.931
100.0	8.886	0.401	1.083	3.859
150.0	8.886	0.406	1.042	3.759
200.0	8.886	0.411	1.018	3.718
250.0	8.886	0.415	1.000	3.688
300.0	8.886	0.417	0.984	3.646
400.0	8.886	0.422	0.961	3.604

DERIVATION OF THE HEAT FLUX EQUATION

Direct application of Fourier's law to calculate heat flux from the heating block thermocouple data is precluded by the temperature-dependence of the copper heating block's thermal

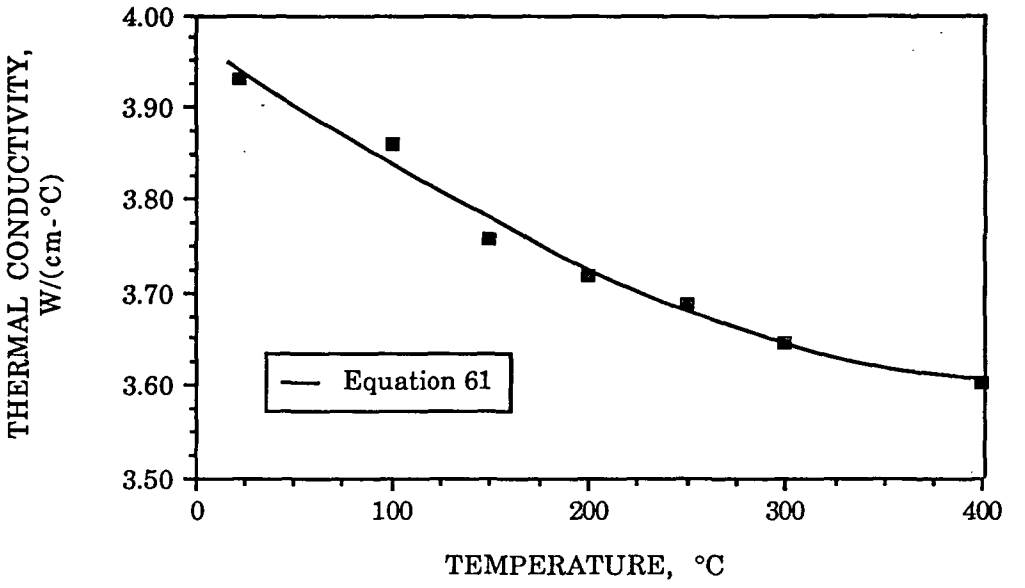

Figure 71. Temperature-dependent thermal conductivity of the copper heating block.

conductivity. For this situation, the proper expression for heat flux must be derived from the heat diffusion equation [64].

For one-dimensional flow of heat, the heat diffusion equation with temperature-dependent thermal conductivity is

$$\frac{d}{dx}\left[k(T)\frac{dT}{dx}\right] = 0 \quad . \tag{62}$$

Integrating,

$$k(T)\frac{dT}{dx} = C = q \quad . \tag{63}$$

Separating and integrating,

$$\int_{T_1}^{T_3} k(T)\,dT = \int_{x_1}^{x_3} C\,dx \quad , \tag{64}$$

where T_1 and T_3 are the temperatures at points x_1 and x_3 within the heating block, measured as the distance from the heater surface. Substituting in the cubic polynomial for thermal conductivity.

(Equation 61),

$$\int_{T_1}^{T_3} \left(3.967 - 1.345\text{x}10^{-3}\,T + 2.560\text{x}10^{-7}T^2 + 2.118\text{x}10^{-9}T^3\right)dT = \int_{x_1}^{x_3} C\,dx \quad , \qquad (65)$$

integration yields

$$3.967(T_3 - T_1) - 6.725\text{x}10^{-4}\left(T_3^2 - T_1^2\right) + 8.533\text{x}10^{-8}\left(T_3^3 - T_1^3\right) + 5.295\text{x}10^{-10}\left(T_3^4 - T_1^4\right) = C(x_3 - x_1) \quad .(66)$$

As defined in Equation 63, the constant of integration is simply equal to the heat flux, so Equation 66 is rearranged to give the equation for heat flux:

$$q = \frac{3.967(T_3 - T_1) - 6.725\text{x}10^{-4}\left(T_3^2 - T_1^2\right) + 8.533\text{x}10^{-8}\left(T_3^3 - T_1^3\right) + 5.295\text{x}10^{-10}\left(T_3^4 - T_1^4\right)}{x_3 - x_1} \quad . \qquad (67)$$

As written, this equation expresses the heat flux based on block temperatures measured closest to and furthest from the surface because uncertainty analysis identified maximum accuracy in calculated heat flux using these two block thermocouple readings.

COPPER BLOCK HEAT LOSS

The one-dimensionality of heat flow to the boiling surface can be adversely affected by convective heat loss to the ambient during a boiling experiment. The magnitude of this heat loss is estimated by determining the convective heat transfer coefficient with a lumped parameter analysis of the heating block assembly. This approach is restricted in application to systems with Biot numbers less than 0.1. The system analyzed here, illustrated in Figure 72, consists of assembly components arranged in series and parallel (as indicated by the resistance diagram), and a source of heat within the copper block. The lumped system is composed of the copper heating

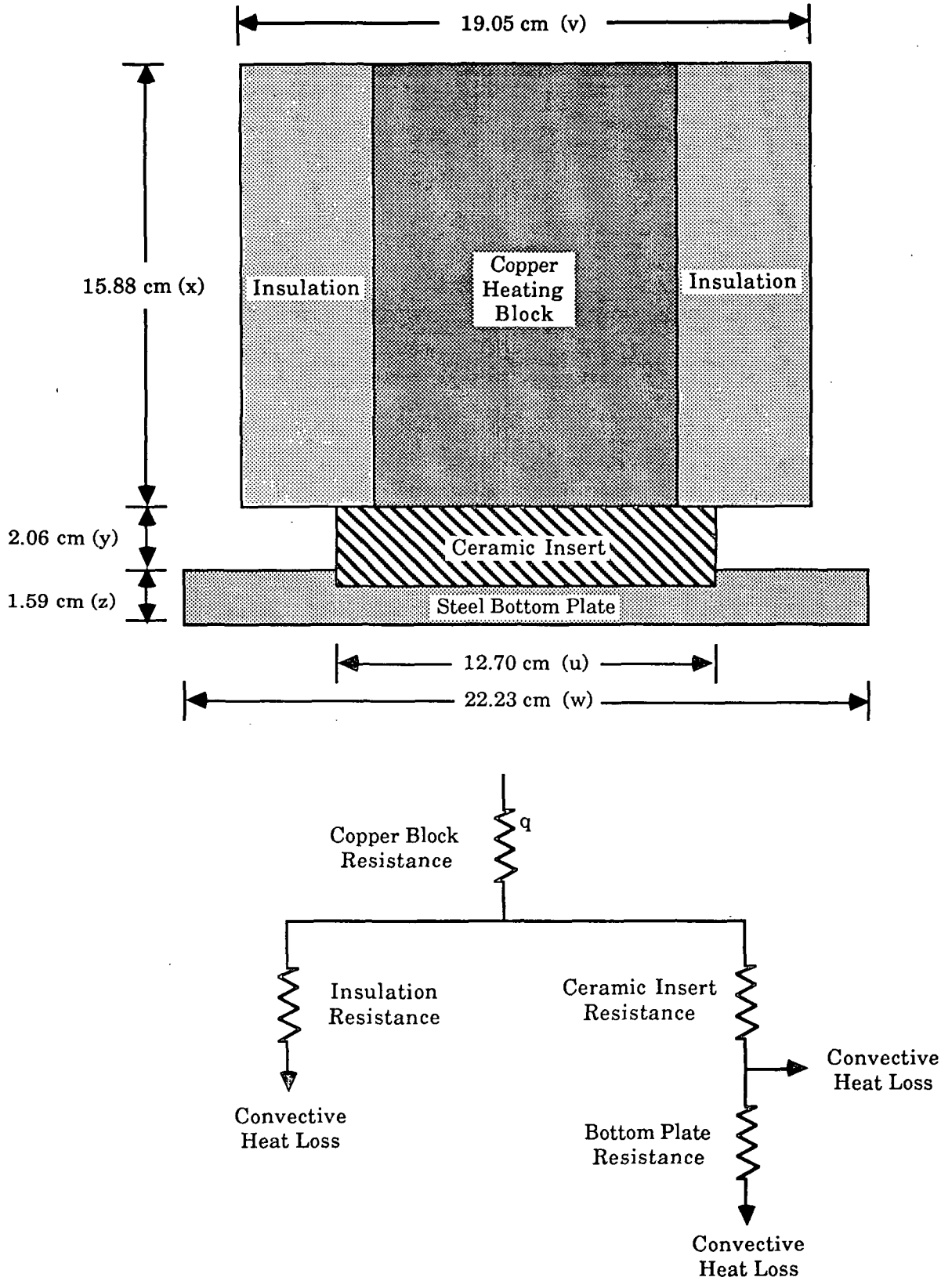

Figure 72. The model assembly of heater block components for the convective heat loss test.

block (including the thermocouples and cartridge heaters), the ceramic insulator, the steel bottom mounting plate, and the block insulation.

The lumped parameter analysis is derived from an energy balance of the system:

$$\begin{bmatrix}\text{Rate of heat loss}\\ \text{from a solid of volume V}\\ \text{through surface area A}\end{bmatrix} = \begin{bmatrix}\text{Rate of decrease}\\ \text{of internal energy}\\ \text{of the solid of volume V}\end{bmatrix} \quad . \tag{68}$$

This is mathematically expressed as

$$h_c A\left[T_\infty - T(t)\right] = \rho C_p V \frac{dT(t)}{dt} \quad . \tag{69}$$

Rearranging,

$$\rho C_p V \frac{dT(t)}{dt} + h_c A\left[T(t) - T_\infty\right] = 0 \quad , \tag{70}$$

with the initial condition

$$T(0) = T_o \quad . \tag{71}$$

Defining a dimensionless temperature,

$$\Theta(t) = \frac{T(t) - T_\infty}{T_o - T_\infty} \quad , \tag{72}$$

the differential equation representing the energy balance becomes

$$\frac{d\Theta(t)}{dt} + \frac{h_c A}{\rho C_p V}\Theta(t) = 0 \quad , \tag{73}$$

which has the solution

$$\Theta(t) = e^{-mt} \tag{74}$$

where

$$m = \frac{h_c A}{\rho C_p V} \quad . \tag{75}$$

Thus, the convective heat transfer coefficient can be determined by monitoring the temperature of the block as a function of time during a heat loss experiment. The properties required to evaluate Equation 75 are determined in Table 19.

Table 19. Definition of parameters to determine the convective heat transfer coefficient from Equation 75.

** Assembly Heat Capacity

Heater Component	Weight (g)	Weight Fraction	Component Heat Capacity (cal/(g-°C))	Weighted Heat Capacity (cal/(g-°C))
Copper Block	15,921.6	0.735	0.10	0.074
Ceramic Insert	312.1	0.014	0.22	0.003
Steel Plate	5419.6	0.251	0.12	0.030
Insulation	negligible	–	–	–
Assembly	21,655.3	1.000		C_p = 0.107

** Assembly Surface Area (refer to Figure 72)

A = exposed surface area of (insulation + ceramic + bottom plate)

$= \pi vx + \pi uy + [2w^2 + 4zw - (\pi/4)u^2]$

$= 2034.8\ cm^2$

** Assembly Volume (refer to Figure 72)

$V = (\pi/4)v^2x + (\pi/4)u^2y + w^2z$

$= 5570.3\ cm^3$

** Assembly Density

ρ = assembly weight/assembly volume

$= 21{,}655.3\ g/5570.3\ cm^3$

$= 3.89\ g/cm^3$

The heat loss test was performed to estimate of the scale of heat loss through the copper block assembly that occurs during a boiling experiment. The heater block system was assembled in normal fashion with the modification that the boiling surface was insulated to minimize convective heat loss through this surface area. After the block was heated to 340°C, the temperatures of the five block thermocouples were monitored for more than nine hours while the block cooled. Each of the five thermocouples registered nearly identical temperatures, so the data discussed below applies to all regions of the copper block. The temperature of the copper block is assumed to be representative of the entire assembly.

The data is plotted in Figures 73 and 74. Linear regression of the reduced data in Figure 74 results in the following equation:

$$\ln[\Theta(t)] = -0.0886 - 0.0046\,t \qquad r^2 = 0.998 \quad , \qquad (76)$$

where the value of the constant in the exponent of Equation 74, m, is 0.0046. From Equation 75, the convective heat transfer coefficient is determined to be 0.00036 W/(cm^2-°C). Referring to Figure 9, the heat transfer coefficient for the pool nucleate boiling regime is 1 to 2.2 W/(cm^2-°C), and for the transition regime is 0.05 to 2.2 W/(cm^2-°C). A quick calculation throughout the intended temperature range of the boiling experiments shows that the convective heat loss at elevated block temperatures is on the order of 250 W. This is negligible compared to the heat transferred during pool boiling of water. However, for boiling in the presence of a fiber bed, the convective heat loss can be as much as 50% of heat transferred to the boiling fluid at the elevated temperatures. Therefore, to minimize radial heat loss from the heating block, a guard heater is placed around the block insulation, and is controlled to the average temperature of the three upper block thermocouples at all times.

The applicability of the lumped parameter analysis is certainly questionable for this system due to the large variation in thermal conductivity of the components. Obviously, the

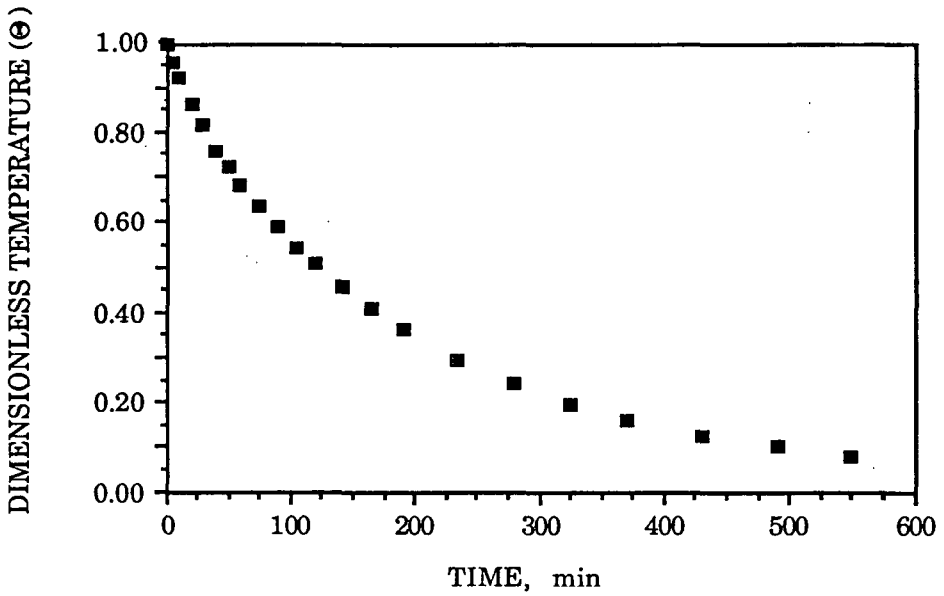

Figure 73. Raw data for transient behavior of heating block temperature during the convective heat loss test.

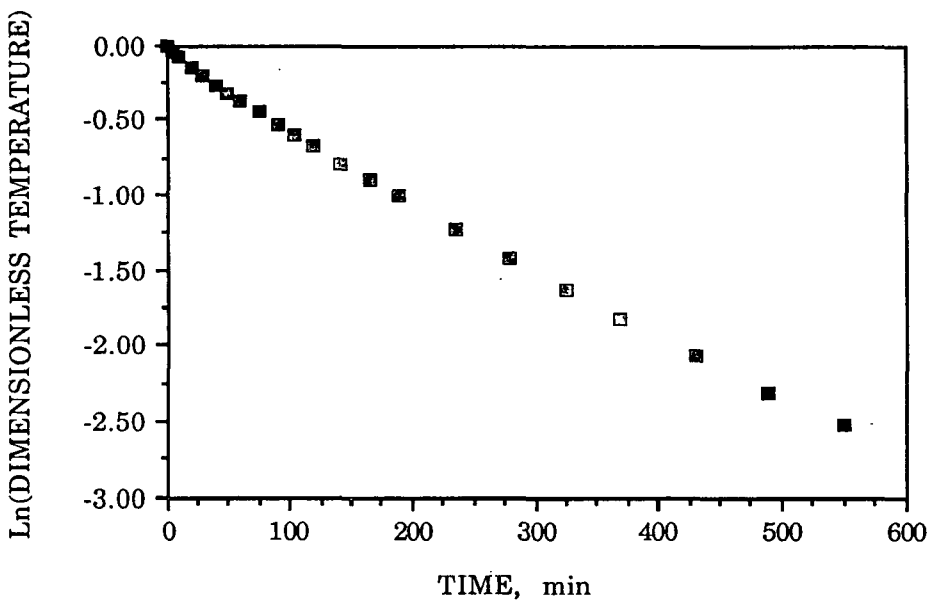

Figure 74. Reduced data for transient behavior of heating block temperature during the convective heat loss test.

requirement of uniform system temperature at any point in time is not fulfilled, which indicates that the Biot number limitation probably is not satisfied. Rather than develop a complicated expression for effective thermal conductivity based on the resistance diagram of this system, the two extremes of Biot number will be tested by treating the system as if it were composed, first, completely of copper, and second, completely of insulation. The Biot number is defined as

$$Bi = \frac{h_c\left(\frac{V}{A}\right)}{k} \qquad (77)$$

Using the thermal conductivity of copper, the Biot number is 2.38×10^{-4}, and using the thermal conductivity of the insulation, the Biot number is 10.35. Although the latter is larger than the critical Biot number, use of this analysis is acceptable because the goal is to determine the scale of convective heat transfer, and not to determine it to a high degree of accuracy.

VERIFICATION OF THE HEAT FLUX CALCULATION

Since convective heat losses are minimized through the use of a guard heater, the accuracy of the heat flux equation can be verified with an independent measure of heat flux emanating from the electrical system. Power from an electrical system can be determined either by direct measurement with a watt transducer, or, more commonly, as the product of independent measures of current and line voltage. These two techniques are straightforward for systems that have a continuous, sinusoidal a-c current waveform, but become much more complicated when dealing with a distorted waveform. A silicon-controlled rectifier (SCR), which is frequently used to proportionally control current, generates a distorted current waveform: at levels less than full power, the current output is a broken waveform consisting of a pulse of current followed by a length of time during which no current is passed. The SCR meters the relative time of current and zero current outputs in proportion to a control signal input. It is this discontinuous current waveform of the SCR that significantly complicates the task of measuring power.

Early attempts to quantify electrical power input to the boiling apparatus focused on measuring the current waveform. According to the manufacturer, an accurate measure of SCR power output can be determined as the product of line voltage and current, as measured with a true RMS ammeter. To accurately measure the RMS value of the distorted current waveform, a thermal-type true RMS ammeter was utilized. Since the ammeter was limited to a maximum reading of 1.5 A, a 20:1 current transformer configured with a proper length of copper wire (which provided the necessary resistance) was used to reduce the 40 A line current to a measurable value. This system was assembled and calibrated (up to 40 A) with a sinusoidal waveform by Keith Hardacker of the IPC. Line voltage was measured with a hand-held, true RMS multimeter. The electrical heat flux data and calculated heat flux data converged near the point of maximum power output of the SCR (where the current is a continuous, sinusoidal waveform), but differed significantly at power levels below the maximum. Observing the waveform on an oscilloscope revealed that the output current from the current transformer of the thermal ammeter circuit was appreciably distorted and did not mirror the SCR waveform at power levels less than 100%.

Because efforts to measure the current waveform were inaccurate, an analog watt transducer was inserted in the electrical system to directly measure power output of the SCR. Data collected for pool boiling of water at atmospheric pressure was used to compare heat flux calculated according to Equation 67 with the independent measure of heat flux from the watt transducer. As illustrated in Figure 75, the two techniques yield heat flux data that agree very well. The watt transducer is rated for 0.5% of rated output (4000 W) up to 20 A and 0.8% of rated output (6000 W) up to 32 A; at higher currents, the inaccuracy of the power measurement may be as much as 2% of rated output. Considering the uncertainty for calculated heat flux, this data confirms the accuracy of the technique for calculating heat flux based on the heating block thermocouple readings.

Another technique for cross-checking the heat flux calculation, and also for checking one-dimensionality of heat flow, is to compare the heat flux determined from the three possible combinations of the block thermocouples. The agreement between these three different boiling

curves, illustrated in Figure 76, provides an additional measure of confidence in the design of the heat supply system and the accuracy of the heat flux calculation technique.

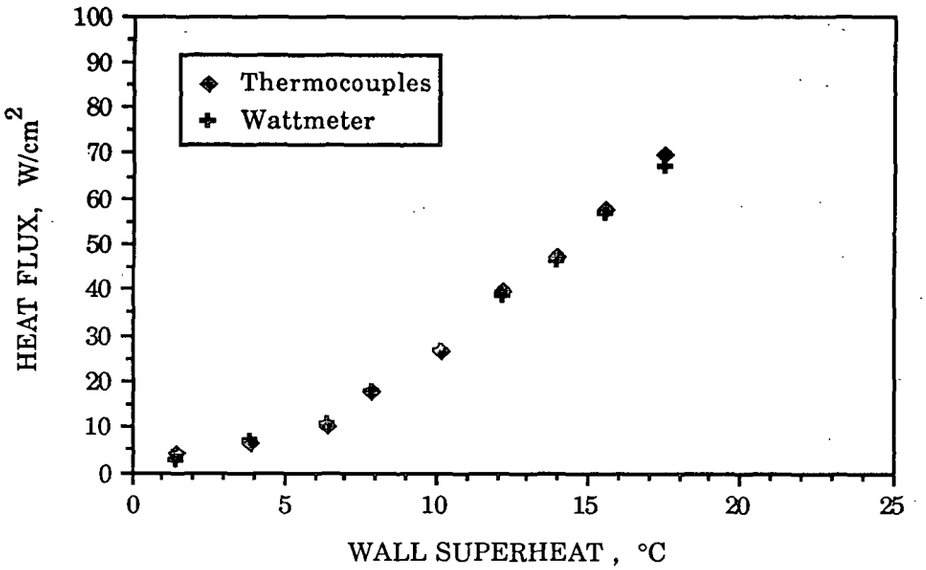

Figure 75. A comparison of the heat flux calculated from the block thermocouple readings and that measured with the wattmeter. The data are for nucleate pool boiling of water at atmospheric pressure.

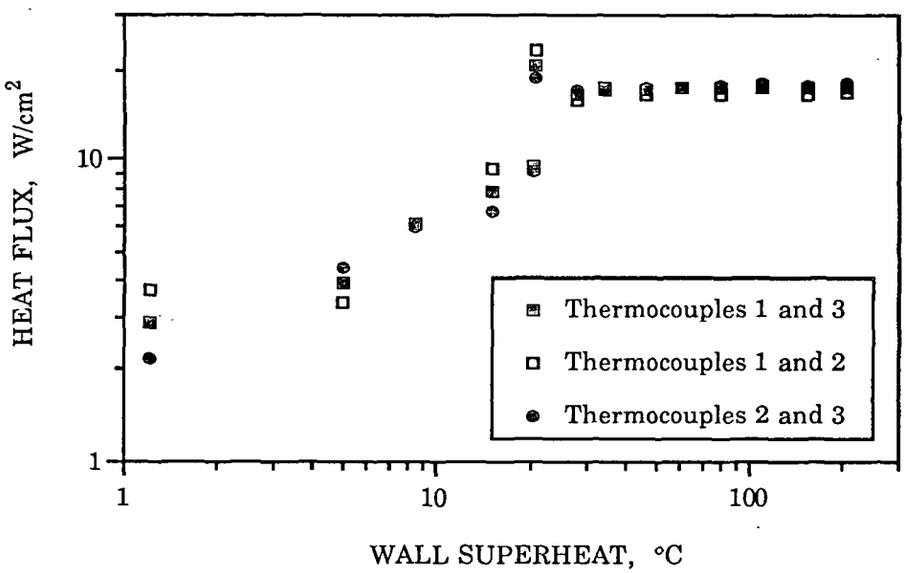

Figure 76. A comparison of heat flux calculated from the three possible combinations of temperature readings from the block thermocouples.

PRL 786

Thermal Conductivity of a Copper Alloy

A Report to the Institute of Paper Chemistry

by

R.E. Taylor, H. Groot and J. Larimore

August 1988

Properties Research Laboratory
Post Office Box 2224
West Lafayette, IN 47906

TABLE OF CONTENTS

LIST OF TABLES

LIST OF FIGURES

Thermal Conductivity of a Copper Alloy

INTRODUCTION

Samples of a copper alloy, identified as Tellurium 145 (ASTM B301) containing 99.5% copper and 0.5% Tellurium, were submitted for thermophysical property determinations.

Bulk density (d) values were calculated from the diffusivity sample's geometries and mass. Specific heat (Cp) was measured using differential scanning calorimetry. Thermal diffusivity (α) values were obtained using the laser flash technique and thermal conductivity (λ) was calculated as a product of these quantities, i.e. $\lambda = \alpha C p d$.

Specific heat was measured using a standard Perkin-Elmer Model DSC-2 Differential Scanning Calorimeter (Figure 1) using sapphire as a reference material. The standard and sample, both encapsulated in pans, were subjected to the same heat flux and the differential power required to heat the sample at the same rate was recorded using the digital data acquisition system (Figure 2). From the mass of the sapphire standard, pans, the differential power, and the known specific heat of sapphire, the specific heat of the sample is computed. The experimental data is visually displayed as the experiment progresses. All measured quantities are directly traceable to NBS standards.

Thermal diffusivity was determined using the laser flash diffusivity method. The flash method, in which the front face of a small disc-shaped sam-

ple is subjected to a short laser burst and the resulting rear face temperature rise is recorded, is used in over 80% of the present thermal diffusivity measurements throughout the world. A highly developed apparatus exists at PRL (Figure 3) and we have been involved in an extensive program to evaluate the technique and broaden its uses. The apparatus consists of a Korad K2 laser, a high vacuum system including a bell jar with windows for viewing the sample, a tantalum tube heater surrounding a sample holding assembly, a spring-loaded thermocouple or an i.r. detector, appropriate biasing circuits, amplifiers, A-D converters, crystal clocks and a minicomputer based digital data acquisition system (Figure 2) capable of accurately taking data in the 40 microsecond and longer time domain. The computer controls the experiment, collects the data, calculates the results and compares the raw data with the theoretical model.

RESULTS AND DISCUSSION

Specific heat results are given in Table 1 and are plotted in Figure 4. Thermal diffusivity results are presented in Table 2 and Figure 5. Thermal conductivity values are calculated in Table 3 and Figure 5. These values should be accurate within ±4%. The results have not been corrected for thermal expansion in line with customary procedures.

TABLE 1

Specific Heat Results

TEMP. (C)	Specific Heat ($Wsgm^{-1}K^{-1}$)
23.0	0.385
52.0	0.392
77.0	0.397
102.0	0.401
127.0	0.407
152.0	0.409
177.0	0.410
202.0	0.411
227.0	0.413
252.0	0.414
277.0	0.415
302.0	0.416
327.0	0.418
352.0	0.420
377.0	0.421
402.0	0.422

TABLE 2

Thermal Diffusivity Results

TEMP. (C)	Diffusivity ($cm^2 sec^{-1}$)
23.0	1.149
100.0	1.085
150.0	1.050
200.0	1.018
250.0	1.009
300.0	0.991
400.0	0.955

TABLE 3

Thermal Conductivity Calculations

Temp. (C)	Density ($gm\ cm^{-3}$)	Specific Heat ($W\ s\ gm^{-1}\ K^{-1}$)	Diffusivity ($cm^2\ sec^{-1}$)	Conductivity ($W\ cm^{-1}\ K^{-1}$)	Conductivity (BTU units *)	Tem (F
23.0	8.886	0.3850	1.14900	3.93086	2725.45	73.
100.0	8.886	0.4010	1.08300	3.85904	2675.65	212.
150.0	8.886	0.4060	1.04200	3.75924	2606.46	302.
200.0	8.886	0.4110	1.01800	3.71788	2577.78	392.
250.0	8.886	0.4150	1.00000	3.68769	2556.85	482.
300.0	8.886	0.4170	0.98400	3.64617	2528.06	572.
400.0	8.886	0.4220	0.96100	3.60365	2498.58	752.

* (BTU in $hr^{-1}\ ft^{-2}\ F^{-1}$)

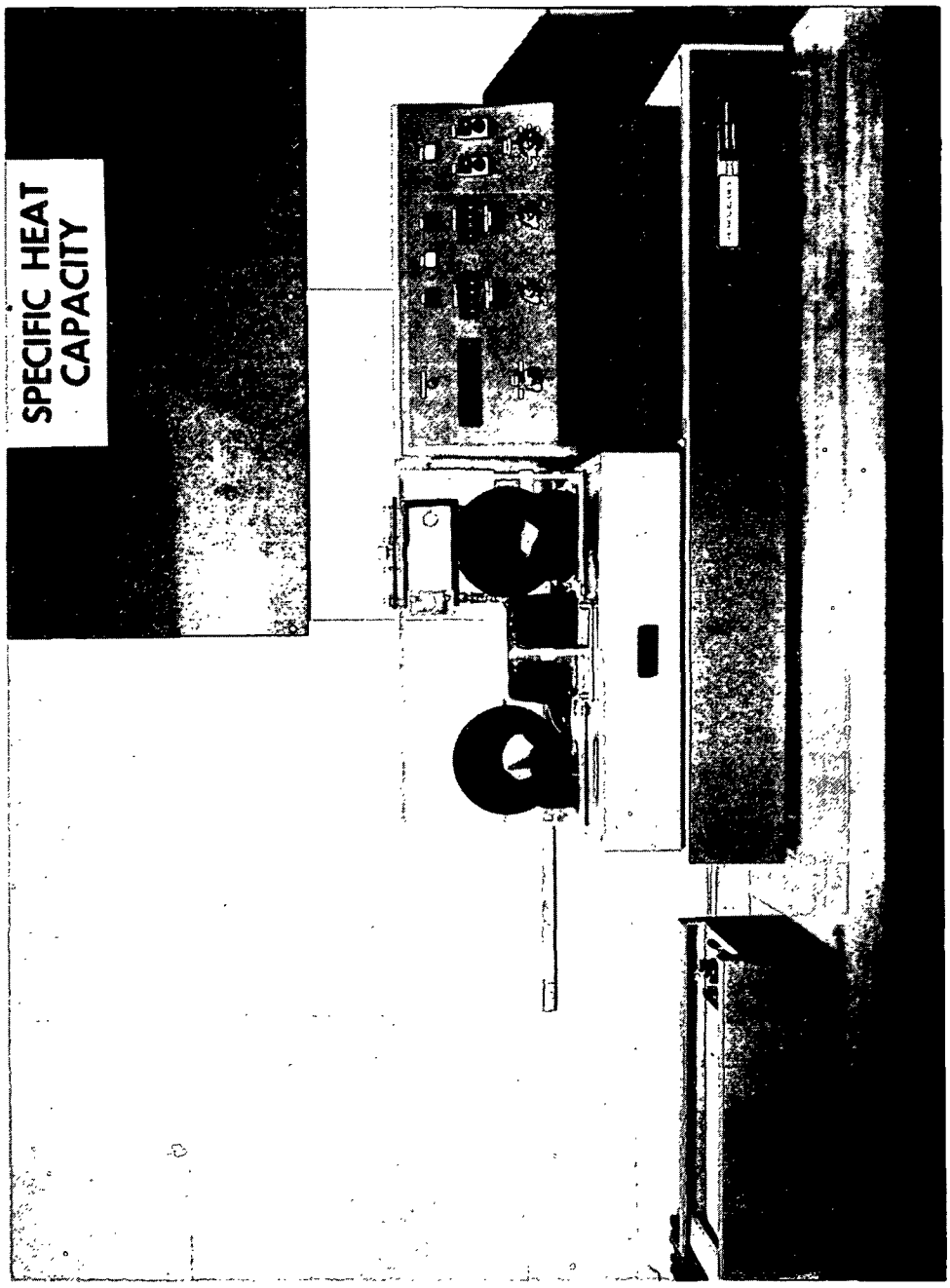

Figure 1. Differential Scanning Calorimeter

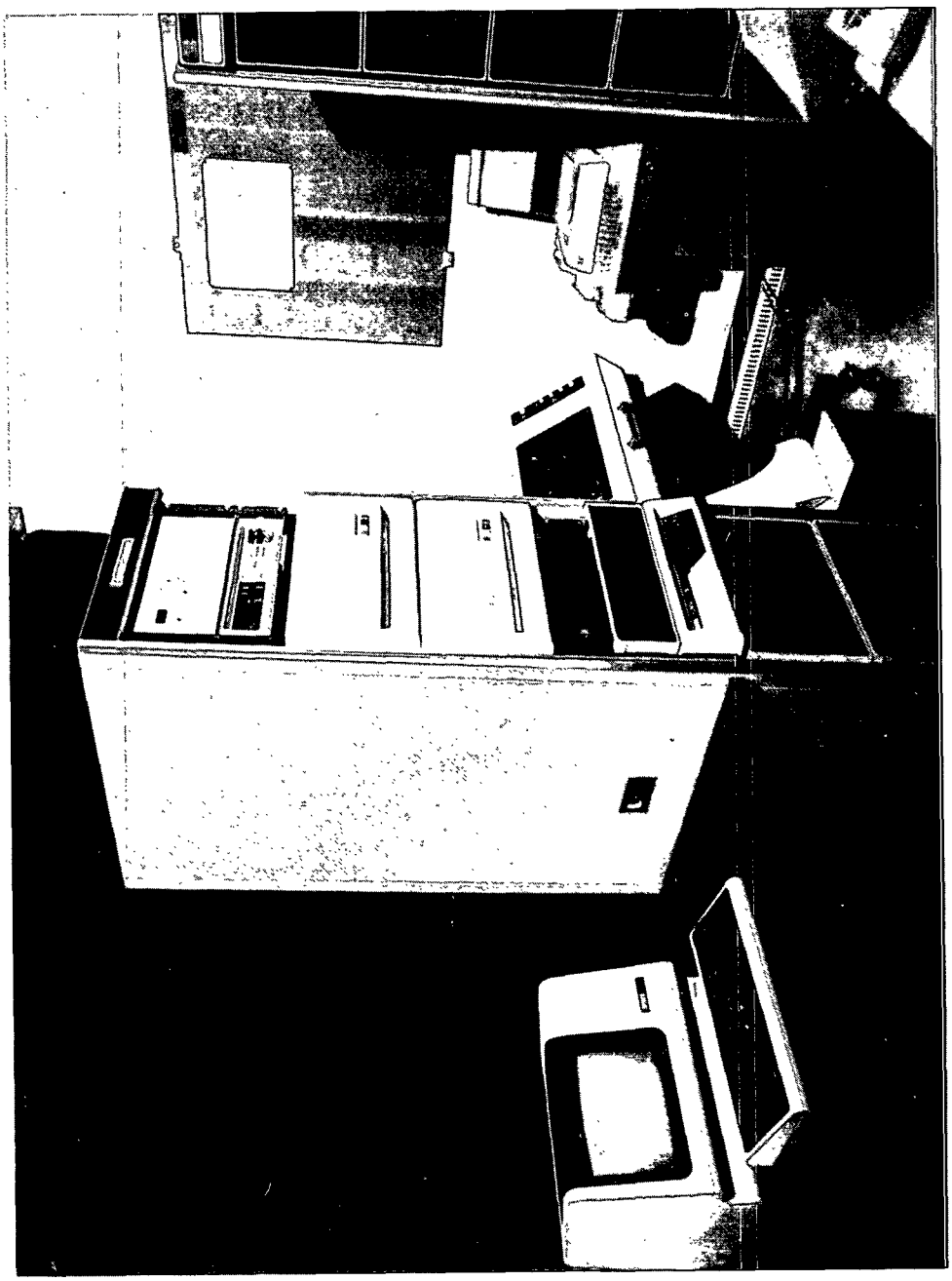

Figure 2. Digital Data Acquisition System

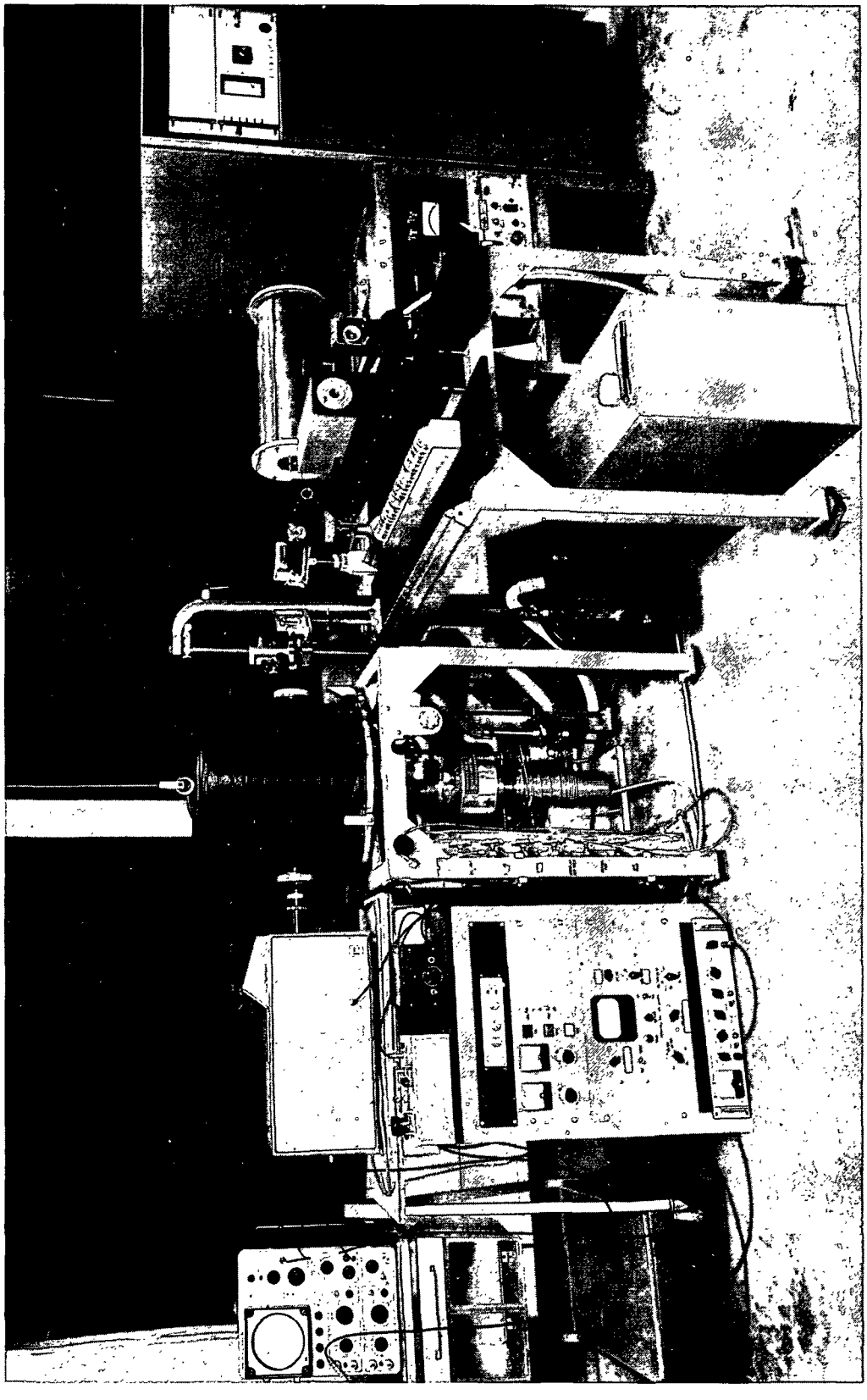

Figure 3. Flash Diffusivity Apparatus

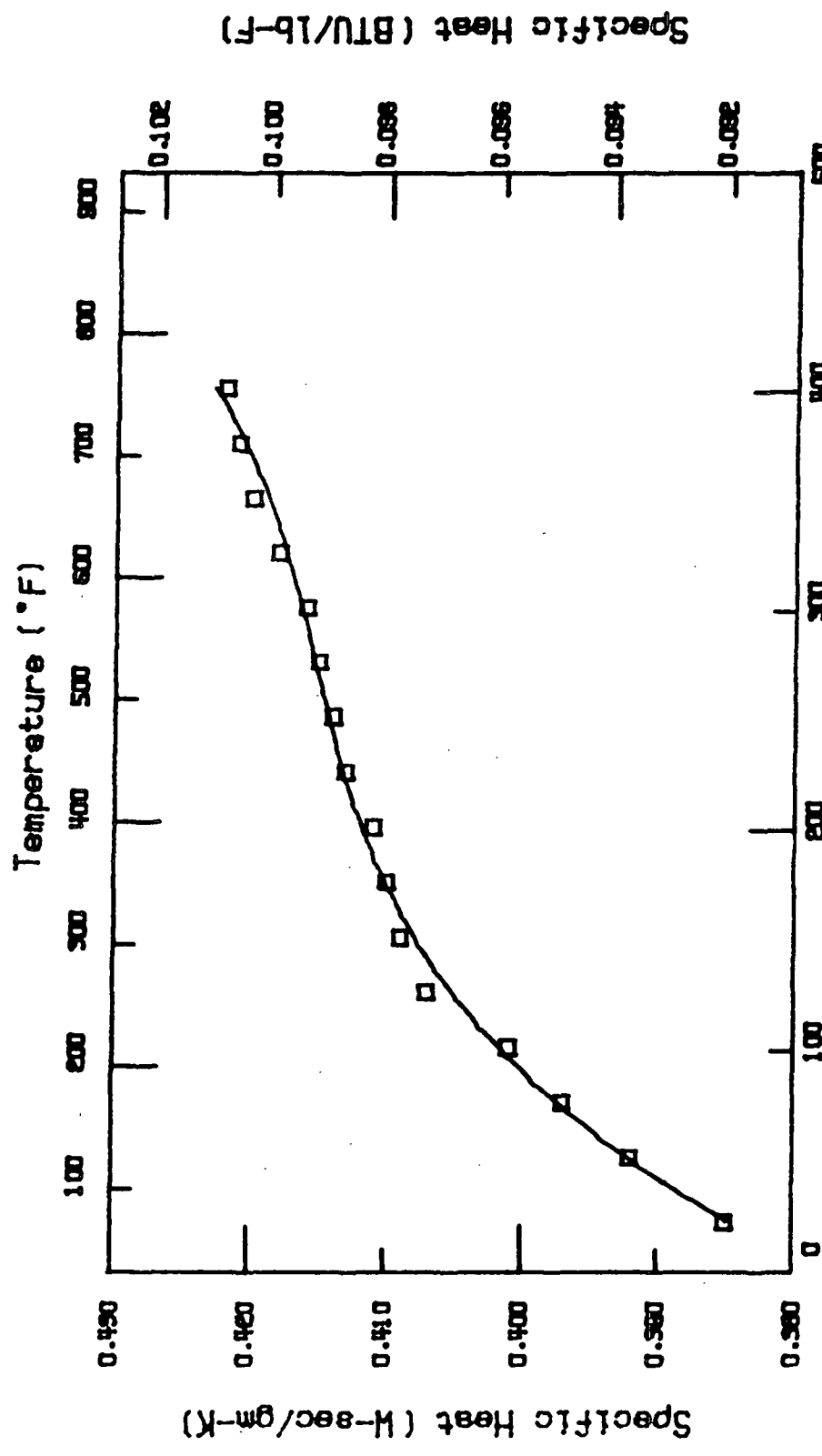

Figure 4. Specific Heat

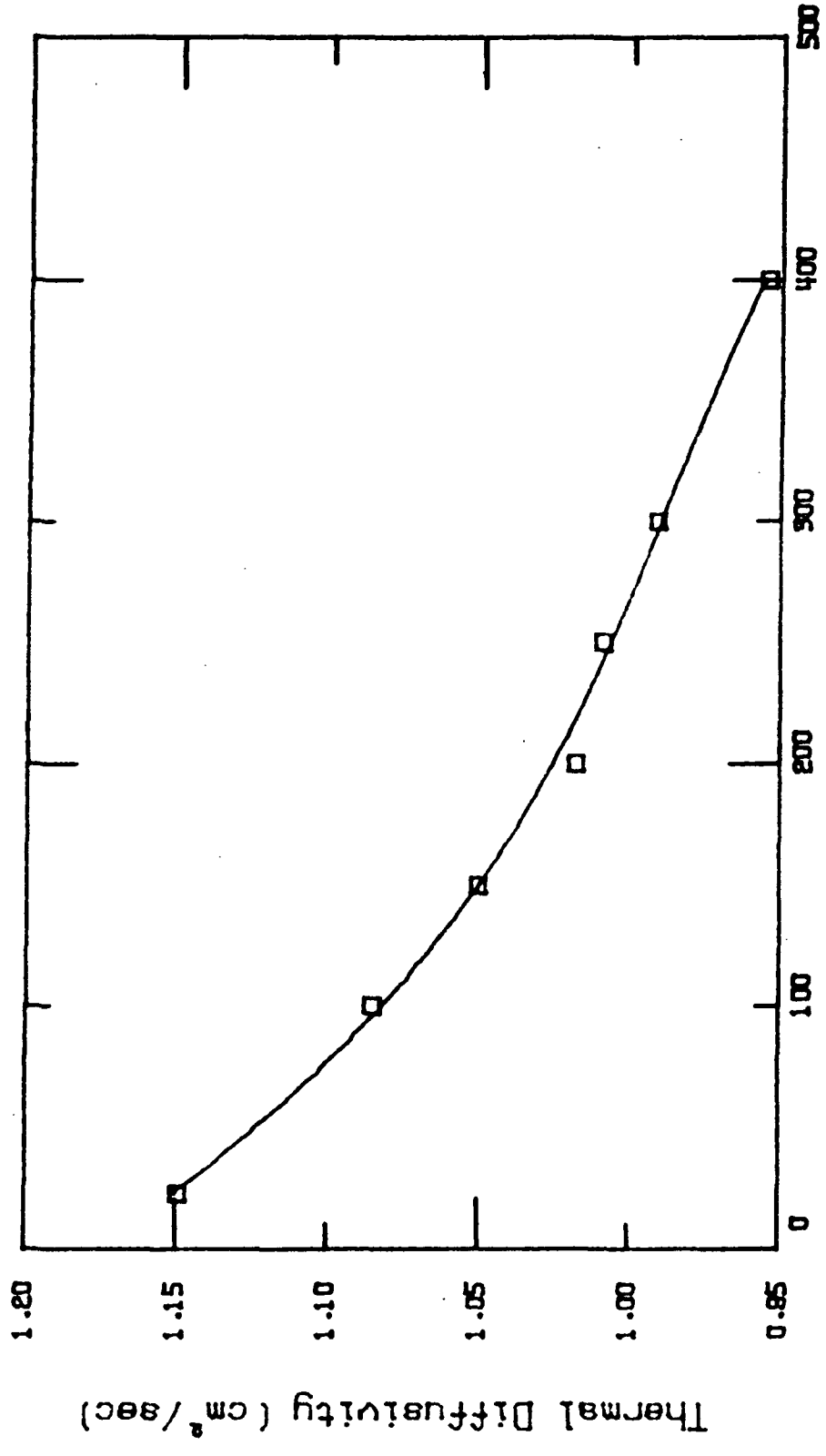

Figure 5. Thermal Diffusivity

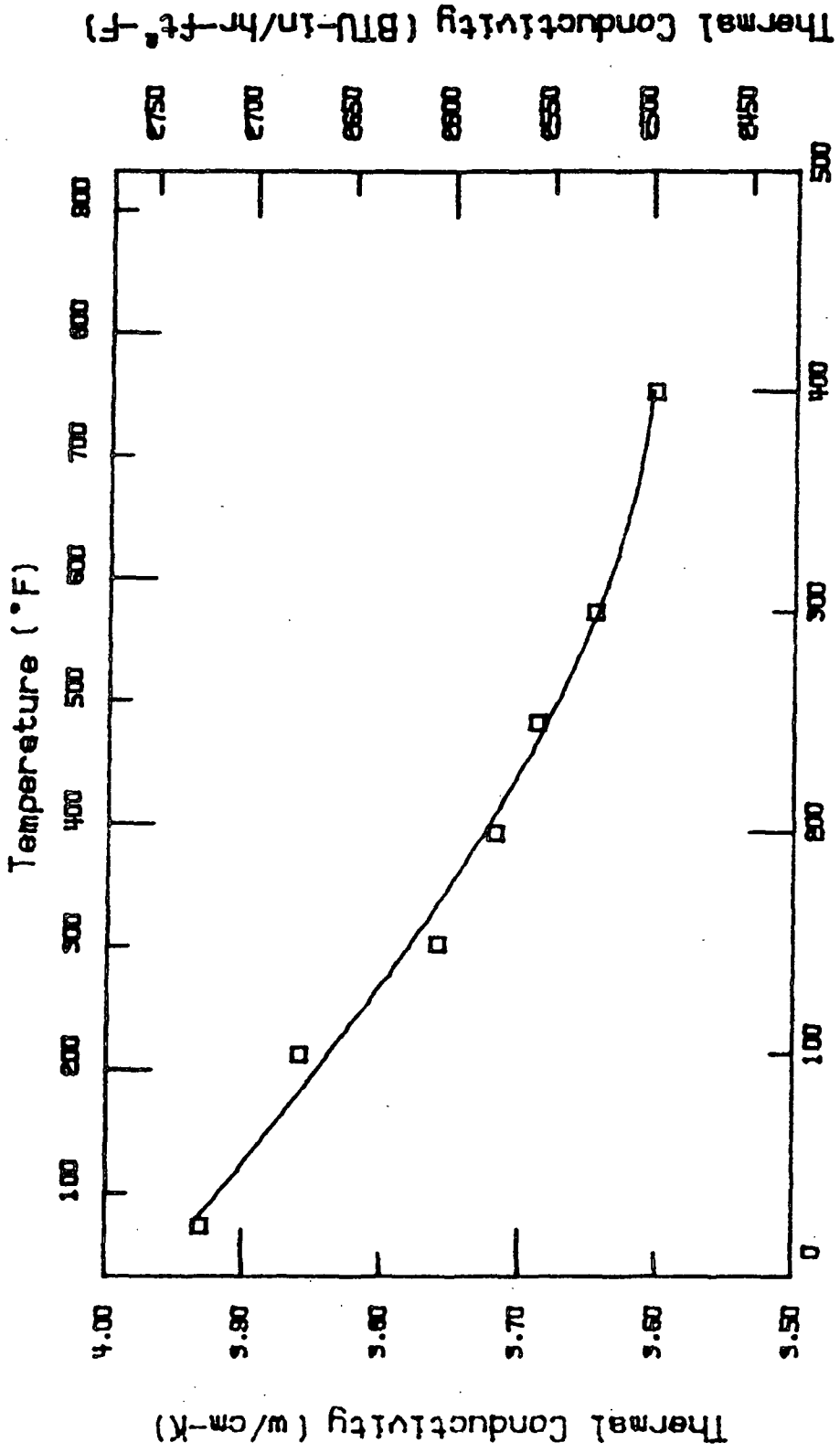

Figure 6. Theraml Conductivity

APPENDIX IV

CONTROL SOFTWARE FOR THE BOILING EXPERIMENTS

The control software written to execute the boiling experiments has been structured to perform its main function of calculating the surface temperature for input to the temperature controller while allowing user-interaction for other needed activities during the course of an experiment. The surface temperature calculation algorithm, based on Equation 37, contained within the main loop must continuously calculate a value for the controller, so excursions to subroutines have been structured to interrupt the main loop for no more than two seconds at a time. Since the structure of the software has been discussed in the EXPERIMENTAL APPARATUS section, this Appendix will address the features of the subroutines. The TBASIC source code for the software is attached after the discussion. Nomenclature is defined in the initial section of the code.

The general flowsheet of the program illustrated in Figure 41 shows a few of the activities accessed by the user. Other subroutines exist which are accessed only by the software one time during the execution of the program. Table 20 describes the functions of all of the subroutines of the control software. All variables sued in the program are globally defined.

The subroutine INKEY controls the flow of the program based on prompts from the user. A few of the letter keys have been programed to direct the software to perform special functions, but usually the user is prompted to confirm the requested action. Though the actions associated with the specific keys are briefly described in the source code (lines 32050 to 36500), a few of the keys need further explanation. After completion of an experiment, the keyboard is disabled to prevent any accidental, unwanted actions by pressing key "F". However, if further user-accessible actions are later required, the keyboard is re-activated by pressing key "A". After the user defines the temperature setpoint increment and ramp rate, the software prompts the user to acknowledge the selected values prior to downloading to the temperature controller. The user refuses these

Table 20. A description of the subroutines' functions for the boiling experiment control software.

Subroutine	Lines	Purpose
Continfo	15,250 - 21,450	To read the values of the internal scaling factors of the temperature controller to insure proper scaling of the calculated surface temperature.
Dataread	21,500 - 25,550	To read each data acquisition channel of the DAS16 and of the EXP16's.
Download	25,600 - 29,400	To download user-selected profile control segment information to the temperature controller via the RS232 serial communications link.
Endexp	29,450 - 30,500	To disable the keyboard after completion of an experiment.
Errhandlr	30,550 - 31,350	To control program flow following an execution error.
Flaghandlr	31,400 - 32,000	To control program flow following an error occurring during communication with the DAS16 driver.
Inkey	32,050 - 36,600	To control program flow according to the specially-defined input key selected by the operator.
Interpolate	36,650 - 37,550	To interpolate the surface temperature from the lookup table based upon the millivolt value determined from linear regression of the three block thermocouples.
Key{#}[a]	37,600 - 40,150	To define a new setpoint and ramp rate for the profile control segment of the temperature controller based on the function key selected by the operator.
Lookup	40,200 - 42,600	To provide the lookup table for type-K thermocouples necessary to interploate a temperature based on a known millivoltage signal.
Monsetup	42,650 - 45,800	To configure the monitor with the experimental operating faceplate.
Monupdate	45,850 - 50,200	To frequently update the monitor with recent data of selected process variables.
Udkeys	50,250 - 51,500	To define the action taken when a function key for profile control segment information of the temperature controller has been depressed.

a - {#} has a value of 1 to 20 depending on which function key is selected.

values by pressing the "N" key, after which new selections are made. During the course of an experiment, whether necessarily or accidentally, the temperature controller is sometimes taken off line. When this occurs, the controller automatically resets itself to the first control segment in the profile. To maintain correspondence between the software and the controller, the software is accordingly reset to the first profile by pressing key "T". This action downloads the most recent setpoint and ramp rate information to the first segment of the temperature controller so that the user does not have to manually re-program the first segment of the controller with this information.

All of the setpoint increment and ramp rate information to be downloaded to the temperature controller is accessed through the keyboard's function keys, which are defined in the subroutine UDKEYS (lines 50250 to 51350). The ten function keys are programmed to initiate a sequence of instructions that result in new values for the temperature setpoint increment value (in their normal position) and the ramp rate value (in their SHIFT position) for downloading to the temperature controller. "KEY1" refers to key "F1", "KEY2" refers to key "F2", etc. and "KEY11" refers to key "SHIFT-F1", "KEY12" refers to key "SHIFT-F2", etc. This subroutine is accessed only once by the software to define the action to be taken when the function keys are pressed.

```
100
OPTION LIST ALIGN
150 !  ************************************************************************
200 !*                BOIL.CTL          updated 1/24/89                        *
250 !* This TBASIC program controls the boiling experiments through the       *
300 !*  interaction of Metrabyte's DAS16 data acquisition system and an        *
350 !*  LFE Model 2012 Ramp/Soak controller to control the surface             *
400 !*  temperature of the copper heating block. The operating                 *
450 !*  parameters of the DAS16 and EXP16 boards, which are explained          *
500 !*  in the Metrabyte manuals, follow:                                      *
550 !*  DAS16: gain = 2          (variable "D16gain", line 2450)               *
600 !*           unipolar (0-5 V)     (switch on the circuit board. No software adjustment)  *
650 !*           address = 768 (&H300) (variable "Dio[1]", line 9350)          *
700 !*           interrupt = 2        (variable "Dio[2]", line 9400)           *
750 !*           DMA = 1              (variable "Dio[3]", line 9400)           *
800 !*           channels = 16        (switch on the circuit board. No software adjustment)  *
850 !*                                                                         *
900 !*  EXP16: gain = 100 (type K thermocouples)                               *
950 !*                  (variable "E16gain", line 2450)                        *
1000 !*                                                                        *
1050 !* The DAS16 channels are set up as follows:                             *
1100 !*       channel 1 = EXP16 #1                                             *
1150 !*       channel 2 = EXP16 #2                                             *
1200 !*       channel 3 = pressure transducer                                  *
1250 !*       channel 6 = cold junction compensation for the EXP16 #1          *
1300 !*       channel 7 = cold junction compensation for the EXP16 #2          *
1350 !*       D/A channel 0 = calculate surface temperature output to the      *
1400 !*                          temperature controller                        *
1450 !  ************************************************************************
1500 !
1550 !  ************************************************************************
1600 !       ***** INITIAL PROGRAM MATERIAL ****
1650 !  ************************************************************************
1700 OPTION LIST FOR 2
1750 SET KEY ON
1800 SET CASE OFF
1850 OPTION BASE 1
1900 ON ERROR GOTO Errhandlr
1950 !
2000 !
2050 !   ***** DIMENSION AND INITIALIZE VARIABLES *****
2100 DECLARE INTEGER Flags,Flagr,Timer,Md,Dio[5],Flag,Chan,Inst[3]
2150 DECLARE INTEGER Rawdata[3,16],Times,Sets,Linenum[13],Lowlim[3],Uplim[3]
2200 DECLARE INTEGER Expchan,Chcjc[2],I,Ii,J,Jj,Jjj,K,Kk,Kkk,P,Pp,L
2250 DIM Setptinc[10],Ramp$[10](4),Ddata[3,10],Update[3,5],Cjc[2]
2300 DIM Temp[3],Tempv[3],Tempmv[3],Posn[3],Posnsq[3],Posntemp[3],Store[3]
2350 !
2400 GOSUB Udkeys ! Define keys for downloading setpoint info to temp cont'ler
2450 E16gain = 100 ! D16gain = 2 ! Metrabyte board data
2500 Efactor = 5/(E16gain*2048*D16gain) ! bits-to-(Metrabyte V) conversion
2550 !                                    for data collected via the EXP16s
2600 Bell$ = CHR$(7)
2650 Chcjc[1] = 6 ! Chcjc[2] = 7 ! EXP16 cold junction compensation channels
2700 Chan = 3 ! Number of DAS16 channels to be read for data acquisition
```

```
2750 Dio2$ = "N" ! A flag for out-of-range process temperature downloaded to
2800 !                    the temperature controller
2850 Down$ = "N" ! A flag for downloading information to the temp controller
2900 Heater$ = "" ! A flag for the makeup water temperature
2950 Manual$ = "N" ! A flag for ramp-down of the experiment in MANUAL
3000 Posn[1] = 1.161 ! cm from surface of closest block thermocouple
3050 Posn[2] = 2.286 ! cm from surface of middle block thermocouple
3100 Posn[3] = 3.809 ! cm from surface of furthest block thermocouple
3150 Setnum = 0 ! Counter for sets of data collected
3200 Sets = 15 ! Number of data sets for averaging per sample time
3250 !          A set contains one reading from each data acquisition channel
3300 Sn$ = "0" ! Sn1$ = "0" ! Sn2$ = "0"
3350 Timer = 0 ! Counter for updating the monitor
3400 Times = 0 ! Counter for downloading control info to the temp controller
3450 Update$ = "N" ! A flag for updating the monitor
3500 !
3550 ! Line numbers for the Dash16 calls:
3600 Linenum[1] = 9450 ! Linenum[2] = 10600 ! Linenum[3] = 10900
3650 Linenum[4] = 11550 ! Linenum[5] = 12000 ! Linenum[6] = 12250
3700 Linenum[7] = 14050 ! Linenum[8] = 22800 ! Linenum[9] = 23150
3750 Linenum[10] = 23400 ! Linenum[11] = 4675 ! Linenum[12] = 4710
3800 Linenum[13] = 4735
3850 ! NOTE: Linenum[11] = 46750, Linenum[12] = 47100, Linenum[13] =47350
3900 !     The maximum value for an INTEGER variable is 32767.
3950 !
4000 ! Initialize setpoint info for downloading to temperature controller.
4050 !  In the temperature range of 100-400 deg C, 1 deg C = 0.041mV for
4100 !  type K thermocouples.
4150 Setptinc[1] = 0.041 ! Millivolt signal equivalent to 1 deg C
4200 Setptinc[2] = 0.082 ! Millivolt signal equivalent to 2 deg C
4250 Setptinc[3] = 0.123 ! Millivolt signal equivalent to 3 deg C
4300 Setptinc[4] = 0.164 ! Millivolt signal equivalent to 4 deg C
4350 Setptinc[5] = 0.205 ! Millivolt signal equivalent to 5 deg C
4400 Setptinc[6] = 0.287 ! Millivolt signal equivalent to 7 deg C
4450 Setptinc[7] = 0.41 ! Millivolt signal equivalent to 10 deg C
4500 Setptinc[8] = 0.615 ! Millivolt signal equivalent to 15 deg C
4550 Setptinc[9] = 0.82 ! Millivolt signal equivalent to 20 deg C
4600 Setptinc[10] = 1.025 ! Millivolt signal equivalent to 25 deg C
4650 !
4700 ! Initialize ramp rate info for downloading to temperature controller.
4750 !  First two digits are minutes, last two are seconds.
4800 Ramp$[1] = "0100" ! Ramp$[2] = "0130" ! Ramp$[3] = "0200"
4850 Ramp$[4] = "0300" ! Ramp$[5] = "0400" ! Ramp$[6] = "0500"
4900 Ramp$[7] = "0730" ! Ramp$[8] = "1000"
4950 Ramp$[9] = "1500" ! Ramp$[10] = "2000"
5000 !
5050 !
5100 !    ***** OPEN THE COMMUNICATIONS CHANNELS *****
5150 PRINT "If ""RS232"" has not been executed, exit the program and do so"
5200 PRINT "  now by running the program ""BOILCTL"" from the DOS prompt"
5250 PRINT "  ""TBASIC"". Also, be sure that the initial setpoint of the"
5300 PRINT "  temperature controller is at or below 100 degrees C." ! PRINT
5350 !
5400 ! Now, prompt for the arrangement of thermocouples on the EXP16's.
```

```
5450 INPUT PROMPT "Number of thermocouples attached to EXP16 1: ":Num1$
5000 PRINT
5550 INPUT PROMPT "Number of thermocouples attached to EXP16 2: ":Num2$
5600 PRINT
5650 Inst[1] = INT(VAL(Num1$)) ! Number of thermocouples on DAS16 channel 1
5700 Inst[2] = INT(VAL(Num2$)) ! Number of thermocouples on DAS16 channel 2
5750 Inst[3] = 1 ! One pressure transducer on DAS16 channel 3
5800 !
5850 ! Configure the temperature controller.
5900 INPUT PROMPT "Reset all temp controller profile segments to <0> ?":Rp$
5950 PRINT
6000 IF Rp$="n" THEN GOTO 6600
6050 OPEN #1:"COM1","F" ! Temp controller on serial communications port 1
6100 FOR I = 2 TO 99
6150     I$ = STR$(I) ! L = LEN(I$) ! I$ = SEG$(I$,2,L)
6200     Sp$ = "*:WS" & I$ & "/0000:" ! Ti$ = "*:WT" & I$ & "/0000:"
6250     PRINT #1:Sp$ ! INPUT #1:Trash$
6300     PRINT #1:Ti$ ! INPUT #1:Trash$
6350 NEXT I
6400 CLOSE #1
6450 !
6500 ! Get the initial value of the temperature controller setpoint
6550 !  from the controller.
6600 GOSUB Continfo
6650 !
6700 ! Create the data file for storing the experimental data.
6750 Read1: PRINT "Press the RETURN key if you do not wish to collect data."
6800 INPUT PROMPT "    Enter the data file name: ":Datafile$
6850 IF Datafile$="" THEN
6900     PRINT "No datafile is being created."
6950     GOTO 8050
7000 END IF
7050 OPEN #2:Datafile$,"R" ! Generates ERROR 102 if this file does not exist
7100 PRINT ! PRINT "This filename already exists."
7150 INPUT PROMPT "Do you want to overwrite this file? <Y/N>":Overwrite$
7200 IF Overwrite$="Y" THEN
7250     DELETE FILE Datafile$
7300     GOTO Read2
7350 END IF
7400 PRINT
7450 GOTO Read1
7500 !
7550 Read2: CLOSE #2 ! Ddate$ = DATE ! Ttime$ = TIME
7600 INPUT PROMPT "    Enter fiber diameter = ":Ans$
7650 Fiber$ = "Fiber diameter = " & Ans$ & " microns"
7700 INPUT PROMPT "    Enter system pressure = ":Ans$
7750 Pressure$ = "System pressure = " & Ans$ & " psia"
7800 OPEN #2:Datafile$,"W" ! Create data file on the hard disk
7850 IMAGE 12a,3x,10a,3x,30a,3x,28a
7900 PRINT #2 USING 7850:Ddate$,Ttime$,Fiber$,Pressure$
7950 PRINT #2:
8000 CLOSE #2
8050 PRINT
8100 PRINT "For startup in MANUAL, set the temperature controller's initial"
```

```
8150 PRINT "time segment to ""CONT"", then press return."
8200 PRINT ! INPUT KEY WAIT V$
8250 !
8300 ! Read in the thermocouple signals for temperature interpolation.
8350 GOSUB Lookup
8400 !
8450 !
8500 !    ***** FORMAT THE MONITOR *****
8550 GOSUB Monsetup
8600 !
8650 ! Begin the experiment....
8700 SET DIALOG COLOR 14
8750 PRINT AT 2,2:"Press <S> to begin the experiment."
8800 Wait1: INPUT KEY WAIT Strt$
8850 IF Strt$="S" THEN GOTO Start
8900 PRINT AT 3,2:"WRONG KEY PRESSED.  Re-enter now"
8950 GOTO  Wait1
9000 Start: PRINT AT 2,2 USING "38X": ! PRINT AT 3,2 USING "38X":
9050 PRINT AT 1,2:"Experiment in progress...          "
9100 !
9150 !
9200 !    ***** LOAD AND INSTALL THE DAS16 DRIVER *****
9250 LOAD SUB Dash16 FROM "d16tb.bin"
9300 Md = 0 ! Dash16 = 0
9350 Dio[1] = 768 ! Decimal address for the DAS16
9400 Dio[2] = 2 ! Dio[3] = 1 ! Flag = 0
9450 CALL  Dash16(Md,Dio,Flag)
9500 Dcall = 1  ! IF Flag<>0 THEN GOSUB Flaghandlr
9550 !
9600 !
9650 !   ************************************************************************
9700 !          ***** SURFACE TEMPERATURE CALCULATION LOOP *****
9750 !   ************************************************************************
9800 Calc1: CONTINUE
9850 INPUT KEY R$
9900 IF Manual$="Y" AND R$<>"A" THEN R$ = "" ! Disables the keyboard
9950 IF R$<>"" THEN GOSUB Inkey
10000 !
10050 ! Cold junction compensation for the thermocouple readings is done
10100 !  for each of the EXP16's because they vary slightly with time.
10150 !  Output of the CJC channel is scaled at 24.4 mV/deg C.  This
10200 !  corresponds to 0.1 deg C/bit.  Dividing output in bits by 10 and
10250 !  by the gain of the Das16 circuit board yields deg C.
10300 ! Lock DAS16 to CJC channel using MODE 1.
10350 FOR I = 1 TO 2
10400     Sumcjc = 0
10450     FOR Ii = 1 TO Sets
10500         Md = 1
10550         Dio[1] = Chcjc[I] ! Dio[2] = Chcjc[I]
10600         CALL  Dash16(Md,Dio,Flag)
10650         Dcall = 2 ! IF Flag<>0 THEN GOSUB Flaghandlr
10700         !
10750         ! Get the data from this channel using MODE 3.
10800         Md = 3
```

```
10850          Dio[1] = 0 ! Dash16 data returned to this variable
10900          CALL Dash16(Md,Dio,Flag)
10950          Dcall = 3 | IF Flag<>0 THEN GOSUB Flaghandlr
11000          !
11050          ! Change the digital output (bits) to voltage temperature signal.
11100          Sumcjc = Sumcjc+Dio[1]/(10*D16gain) ! Actual temperature
11150       NEXT Ii
11200       Cjc[I] = Sumcjc/Sets
11250    NEXT I
11300    !
11350    ! Now, get the block thermocouple data.  First, set the channels to
11400    !   be scanned.
11450    Md = 1
11500    Dio[1] = 1 | Dio[2] = 1 ! Block temps on EXP16 on DAS16 channel #1
11550    CALL Dash16(Md,Dio,Flag)
11600    Dcall = 4 | IF Flag<>0 THEN GOSUB Flaghandlr
11650    !
11700    ! Now, read the three block thermocouples.
11750    Store = 0 ! Reset the temporary data storage array to zero
11800    FOR I = 1 TO Sets ! Average a number of readings
11850       FOR Expchan = 1 TO 3 ! Selects the EXP16 channel
11900          Md = 13 ! This mode locks on the EXP16 sub-multiplexer channel
11950          Dio[1] = Expchan
12000          CALL Dash16(Md,Dio,Flag)
12050          Dcall = 5 | IF Flag<>0 THEN GOSUB Flaghandlr
12100          !
12150          Md = 3 ! This mode reads the channel data
12200          Dio[1] = 0 ! Dash16 data returned to this variable
12250          CALL Dash16(Md,Dio,Flag)
12300          Dcall = 6 | IF Flag<>0 THEN GOSUB Flaghandlr
12350          Store[Expchan] = Store[Expchan]+Dio[1] ! Digital temperature sum
12400       NEXT Expchan
12450    NEXT I
12500    Store = Store/Sets ! Now, calculate the average digital signals
12550    Temp[1] = Store[1] ! Temp. of thermocouple closest to the surface
12600    Temp[2] = Store[2] ! Temp. of middle block thermocouple
12650    Temp[3] = Store[3] ! Temp. of thermocouple furthest from the surface
12700    !
12750    ! Alert the operator as to the status of the makeup water heater.
12800    PRINT AT 11,2:Heater$
12850    !
12900    ! Convert the digital temperature to analog mV.
12950    FOR I = 1 TO 3
13000       Tempv[I] = Temp[I]*Efactor ! Raw V analog signal
13050       Tempmv[I] = 1000*Tempv[I]+1.0+(Cjc[1]-25)*0.0405 ! Corrected mV
13100    NEXT I !                                                    analog signal
13150    !
13200    !
13250    ! Calculate the surface temperature as the y-intercept of the linear
13300    !   regression of the three block thermocouple readings.
13350    Posntemp = Posn*Tempmv | Posnsq = Posn^2
13400    Denom = 3*SUM(Posnsq)-SUM(Posn)^2
13450    Yint = (SUM(Tempmv)*SUM(Posnsq)-SUM(Posntemp)*SUM(Posn))/Denom
13500    Tsurf = Yint ! Surface temperature in mV
```

```
13550 !
13600 ! Communicate the surface temperature to the controller.
13650 Md = 15
13700 Dio[1] = 0 ! Temperature controller on DAS16 D/A channel # 0
13750 Digtemp = (Tsurf-2.022)*248.317 ! Digital temperature
13800 Dio[2] = INT(Digtemp) ! Digital temperature
13850 IF Digtemp-Dio[2]>0.5 THEN Dio[2] = Dio[2]+1 ! Rounding up
13900 IF Dio[2]<0 THEN Dio[2] = 0 ! Puts out-of-bounds input to the temp.
13950 IF Dio[2]>4095 THEN Dio[2] = 4095 !     controller in the proper range
14000 IF Dio[2]>4095 OR Dio[2]<0 THEN Dio2$ = "Y" ! Identifies O.B. temp
14050 CALL Dash16(Md,Dio,Flag)
14100 IF Dio2$="Y" THEN Flag = 14 ! Artificially set this flag
14150 Dcall = 7 ! IF Flag<>0 THEN GOSUB Flaghandlr ! Dio2$ = "N"
14200 !
14250 ! Check timer for updating the monitor.
14300 Timer = Timer+1
14350 IF Timer>5 THEN GOSUB Monupdate
14400 !
14450 ! Blink the makeup water heater message.
14500 IF Timer=1 THEN PRINT AT 11,2 USING "38x":
14550 IF Timer=3 THEN PRINT AT 11,2 USING "38x":
14600 IF Timer=5 THEN PRINT AT 11,2 USING "38x":
14650 GOTO Calc1
14700 !
14750 !
14800 !    *****END OF EXPERIMENT*****
14850 Ending: SET DIALOG COLOR 15
14900 SET GRAPH 0 ! Clears the screen
14950 CLOSE
15000 END
15050 !
15100 !   ************************************************************************
15150 !  *************************** SUBROUTINES ****************************
15200 !   ************************************************************************
15250 Continfo:
15300 ! This subroutine communicates with the temperature controller to
15350 !  gather information required to scale the surface temperature data
15400 !  downloaded to it. The LFE controller adds a space between the colon
15450 !  and the string when responding to a request, e.g."$00: XXXX:YY".
15500 !  Proper communications syntax is discussed in the Supplemental Manual
15550 !  for the LFE controller.
15600 !
15650 OPEN  #1:"COM1","F"
15700 PRINT #1:"*:RS0:" ! Request the initial setpoint
15750 INPUT #1:Rsp$ ! Controller response
15800 Pp = POS(Rsp$,":",1)
15850 Status$ = SEG$(Rsp$,Pp-2,2)
15900 IF Status$="00" THEN GOTO Flow1
15950 PRINT "STATUS ERROR (Status = ";Status$;
16000 PRINT ") in reading the temperature setpoint"
16050 INPUT PROMPT "from the temperature controller. Continue ? <y/n>CR":A$
16100 IF A$="Y" THEN GOTO Flow1
16150 PRINT "EXPERIMENT HAS BEEN STOPPED"
16200 GOTO Ending
```

```
16250 !
16300 ! Request the low scaling value of the temperature controller.
16350 Flow1:  PRINT  #1:"*:RA6:"
16400 INPUT  #1:Ans$
16450 P = POS(Ans$,":",1)
16500 Status$ = SEG$(Ans$,P-2,2)
16550 IF Status$="00" THEN GOTO Flow2
16600 PRINT "STATUS ERROR (Status = ";Status$;
16650 PRINT ") in reading the low value "
16700 INPUT PROMPT "from the temperature controller. Continue ? <y/n>CR":A$
16750 IF A$="Y" THEN GOTO Flow2
16800 PRINT "EXPERIMENT HAS BEEN STOPPED"
16850 GOTO Ending
16900 !
16950 Flow2: Loval$ = SEG$(Ans$,P+2,4) ! Loval = VAL(Loval$)
17000 !
17050 ! Request the high scaling value of the temperature controller.
17100 PRINT  #1:"*:RA7:"
17150 INPUT  #1:Ans$
17200 P = POS(Ans$,":",1)
17250 Status$ = SEG$(Ans$,P-2,2)
17300 IF Status$="00" THEN GOTO Flow3
17350 PRINT "STATUS ERROR (Status = ";Status$;
17400 PRINT ") in reading the high value "
17450 INPUT PROMPT "from the temperature controller. Continue ? <y/n>CR":A$
17500 IF A$="Y" THEN GOTO Flow3
17550 PRINT "EXPERIMENT HAS BEEN STOPPED"
17600 GOTO Ending
17650 !
17700 Flow3: Hival$ = SEG$(Ans$,P+2,4) ! Hival = VAL(Hival$)
17750 !
17800 ! Request the display units of the temperature controller
17850 PRINT  #1:"*:RA2:"
17900 INPUT  #1:Ans$
17950 P = POS(Ans$,":",1)
18000 Status$ = SEG$(Ans$,P-2,2)
18050 IF Status$="00" THEN GOTO Flow4
18100 PRINT "STATUS ERROR (Status = ";Status$;
18150 PRINT ") in reading the display units "
18200 INPUT PROMPT "from the temperature controller. Continue ? <y/n>CR":A$
18250 IF A$="Y" THEN GOTO Flow4
18300 PRINT "EXPERIMENT HAS BEEN STOPPED"
18350 GOTO Ending
18400 !
18450 Flow4: Disp$ = SEG$(Ans$,P+2,1)
18500 SELECT CASE Disp$
18550     CASE "V" ! Temperature controller display reads volts
18600         GOTO Flow5
18650     CASE "C" ! Temperature controller display degrees C
18700         GOTO Flow6
18750     CASE ELSE
18800         PRINT "The DISPLAY UNITS of the temperature controller are neither"
18850         PRINT "  VOLTS nor DEG C.  Please correct and restart the program."
18900         GOTO Ending
```

```
18950 END SELECT
19000 !
19050 Flow5: I$ = SEG$(Rsp$,Pp+2,2) ! F$ = SEG$(Rsp$,Pp+4,2)
19100 Idotf$ = I$ & "." & F$
19150 GOTO Flow7
19200 !
19250 Flow6: Idotf$ = SEG$(Rsp$,Pp+2,4)
19300 !
19350 ! Convert the initial controller temperature setpoint to mV.
19400 Flow7: Cfactor = (Hival-Loval)/16.491 ! Scaling factor to mV
19450 Tset = (VAL(Idotf$)-50)/Cfactor+2.022
19500 ! ...The scaling factor to relate analog mV temperature signals (that
19550 !  this program handles) to the 0-5 V range of the temperature
19600 !  controller is found by equating the temperature range of 50-450 C
19650 !  (2.022-18.513 mV for type-K thermocouples; del(mV) = 16.491 mV)
19700 !  to the 0-5 V range of the controller input.  Then, the scale factor
19750 !  becomes
19800 !              5 V / 16.491 mV = 0.3032 V/mV
19850 !
19900 !  However, the D/A channel of the DAS16 converts a digital input to
19950 !  a 0-5 V output, which corresponds to the input range of the
20000 !  controller.  Thus, the mV temperature of the control software is
20050 !  first converted to bits before the call to the D/A channel is made.
20100 !  Thus, for an equivalent range of a digital signal, the conversion
20150 !  factor becomes
20200 !              4095 bits / 16.491 mV = 248.317 bits/mV
20250 !
20300 !  If the span of the temperature controller is set to a temperature
20350 !  range of 50-450 deg C {loval-hival}, the conversion factor becomes
20400 !
20450 !              400 C / 16.491 mV = 24.256 C/mV
20500 !
20550 !  The conversion equations are
20600 !          (xx.xxx mV - 2.022 mV)*0.3032 = yy.yy V
20650 !          (xx.xxx mV - 2.022 mV)*248.317 = yy.yy bits
20700 !          (xx.xxx mV - 2.022 mV)*25.256 + 50.0 = yy.yy C
20750 !
20800 ! Set the controller information for the first profile segment.
20850 PRINT #1:"*:WT1/-0001:" ! INPUT #1:Trash$
20900 SELECT CASE Disp$
20950     CASE "V" ! Temperature controller display reads volts
21000         S1$ = "*:WS1/" & I$ & F$ & ":"
21050     CASE "C" ! Temperature controller display degrees C
21100         S1$ = "*:WS1/" & Idotf$ & ":"
21150 END SELECT
21200 PRINT #1:S1$ ! INPUT #1:Trash$
21250 CLOSE #1
21300 !
21350 RETURN
21400 !
21450 !  ************************************************************************
21500 Dataread:
21550 ! This subroutine reads each data acquisition channel of the DAS16 and
21600 !  EXP16's.  An EXP16 is connected to channels 1 and 2 of the DAS16,
```

```
21650 !  and the pressure transducer is connected to channel 3.
21700 !
21750 ! Set the limits for the FOR/NEXT loop
21800 Lowlim[1] = 4 ! Uplim[1] = Inst[1] ! Thermo'cples to be read on EXP16 #1
21850 Lowlim[2] = 1 ! Uplim[2] = Inst[2] ! Therm'cples to be read on EXP16 #2
21900 Lowlim[3] = 1 ! Uplim[3] = Inst[3] ! Pressure data on DAS16 channel 3
21950 !
22000 FOR L = 2 TO 6
22050     PRINT AT L,2 USING "38x":
22100 NEXT L
22150 !
22200 Setnum = Setnum+1
22250 SET DIALOG COLOR 14
22300 PRINT Bell$,Bell$ ! PRINT AT 4,2:"Collecting data....Set # "
22350 PRINT AT 4,27 USING "2d":Setnum
22400 !
22450 Rawdata = 0 ! Ddata = 0 ! Reset data matrices to zero
22500 !
22550 ! Set up the loop to gather the data
22600 FOR J = 1 TO Sets ! Collect a number of data sets for averaging
22650     FOR Jj = 1 TO Chan
22700         Md = 1 ! Lock DAS16 to the channel using MODE 1
22750         Dio[1] = Jj ! Dio[2] = Jj
22800         CALL Dash16(Md,Dio,Flag)
22850         Dcall = 8 ! IF Flag<>0 THEN GOSUB Flaghandlr
22900         !
22950         FOR Jjj = Lowlim[Jj] TO Uplim[Jj]
23000             IF Jj=Chan THEN GOTO Pressure1
23050             Md = 13 ! Select the EXP16 channel with MODE 13
23100             Dio[1] = Jjj
23150             CALL Dash16(Md,Dio,Flag)
23200             Dcall = 9 ! IF Flag<>0 THEN GOSUB Flaghandlr
23250             !
23300             Pressure1: Md = 3 ! Read the selected channel using MODE 3
23350             Dio[1] = 0 ! Dash16 data returned to this variable
23400             CALL Dash16(Md,Dio,Flag)
23450             Dcall = 10 ! IF Flag<>0 THEN GOSUB Flaghandlr
23500             Rawdata[Jj,Jjj] = Rawdata[Jj,Jjj]+Dio[1] ! Increment the data matrix
23550         NEXT Jjj
23600     NEXT Jj
23650 NEXT J
23700 !
23750 Rawdata = Rawdata/Sets ! Average the data in the data matrix
23800 Rawdata[1,1] = Temp[1] ! Rawdata[1,2] = Temp[2] ! Rawdata[1,3] = Temp[3]
23850 !
23900 ! Now, convert the digital data to real values. Start with temperatures
23950 FOR I = 1 TO Chan-1
24000     FOR Ii = 1 TO Uplim[I]
24050         Vtemp = Rawdata[I,Ii]*Efactor ! V analog temperature
24100         Mvtemp = 1000*Vtemp+1.0+(Cjc[I]-25)*0.0405 ! Corrected mV analog
24150         GOSUB Interpolate !                                    signal
24200         Ddata[I,Ii] = Tc
24250     NEXT Ii
24300 NEXT I
```

```
24350 Mvtemp = Tsurf ! GOSUB Interpolate ! Tsurftc = Tc
24400 !
24450 ! Now, convert the pressure data
24500 Ddata[Chan,Inst[Chan]] = Rawdata[Chan,Inst[Chan]]*100.0/(2048*D16gain)
24550 !                                                          Pressure in psia
24600 !
24650 ! Now, write the data to the disk. This sequence writes the data in
24700 !  in one horizontal line in the data file.
24750 PRINT AT 5,2:"...Writing data to the disk..."
24800 OPEN #2:Datafile$,"A" ! Append to the data file
24850 PRINT #2 USING "3d.1d,s":Tsurftc;
24900 FOR I = 1 TO Chan
24950     FOR Ii = 1 TO Uplim[I]
25000         IF I=2 AND Ii=4 THEN Ii = 5 ! Don't write channel 4 on EXP16 #2
25050         PRINT #2 USING "1x,3d.1d,s":Ddata[I,Ii];
25100     NEXT Ii
25150 NEXT I
25200 PRINT #2:"" ! End of the line of data
25250 CLOSE #2
25300 !
25350 PRINT Bell$,Bell$ ! PRINT AT 6,2:"Finished collecting data!"
25400 Update$ = "Y" ! GOSUB Monupdate
25450 RETURN
25500 !
25550 !  ************************************************************************
25600 Download:
25650 ! This subroutine downloads profile segment control information to
25700 !  the temperature controller when prompted by the operator.
25750 !
25800 Setnum = 0 ! Reset the data set counter
25850 Times = Times+1 ! Number of times that info has been downloaded
25900 Segnum = Times*2-1 ! Beginning segment number for present sequence
25950 S$ = STR$(Segnum) ! L = LEN(S$) ! Sn$ = SEG$(S$,2,-L)
26000 S$ = STR$(Segnum+1) ! L = LEN(S$) ! Sn1$ = SEG$(S$,2,-L)
26050 S$ = STR$(Segnum+2) ! L = LEN(S$) ! Sn2$ = SEG$(S$,2,-L)
26100 !
26150 ! Set the download string for the new setpoint.
26200 Tnew = (Tsetnew-2.022)*Cfactor+50
26250 IF MOD(Tnew,1)>0.5 THEN Tnew = Tnew+1 ! Rounds TNEW up if applicable
26300 T$ = STR$(Tnew)
26350 Pp = POS(T$," ",1)
26400 P = POS(T$,".",1)
26450 !
26500 ! This section sets the value string for downloading.  Direct the
26550 !  flow based on the controller display units.
26600 SELECT CASE Disp$
26650     CASE "V" ! Temperature controller display reads volts
26700         GOTO Loop1
26750     CASE "C" ! Temperature controller display degrees C
26800         GOTO Loop2
26850 END SELECT
26900 !
26950 Loop1: V1$ = "0" & SEG$(T$,P-1,1) ! For 0-5 V, only 1 digit before
27000 !                    the decimal point
```

```
27050 V2$ = SEG$(T$,P+1,2)
27100 Value$ = V1$ & V2$
27150 GOTO Down1
27200 !
27250 Loop2: Value$ = SEG$(T$,Pp+1,-(P-1)) ! Whole number temperature only
27300 L = LEN(Value$)
27350 SELECT CASE L ! Make VALUE$ 4 digits long
27400     CASE 1 ! Value$ = "000" & Value$
27450     CASE 2 ! Value$ = "00" & Value$
27500     CASE 3 ! Value$ = "0" & Value$
27550 END SELECT
27600 GOTO Down1
27650 !
27700 Down1: Tnew$ = "*:WS" & Sn1$ & "/" & Value$ & ":" ! New setpoint
27750 Tnew1$ = "*:WS" & Sn2$ & "/" & Value$ & ":" ! Ending soak temperature
27800 !
27850 ! Set the ramp rate and soak time (2 minutes) strings
27900 Sotold$ = "*:WT" & Sn$ & "/0200:"
27950 Rrt$ = "*:WT" & Sn1$ & "/" & Ramp$[Flagr] & ":"
28000 Sot$ = "*:WT" & Sn2$ & "/0200:"
28050 !
28100 ! Now, download the information.
28150 OPEN  #1:"COM1","F"
28200 PRINT #1:"*:WE8/A:" ! INPUT #1:Trash$ ! Define profile "A"
28250 PRINT #1:Sotold$ ! INPUT #1:Trash$ ! Soak Time (T[i])
28300 PRINT #1:Rrt$ ! INPUT #1:Trash$ ! New ramp rate (T[i+1])
28350 PRINT #1:Tnew$ ! INPUT #1:Trash$ ! New temp set point (SP[i+1])
28400 PRINT #1:Sot$ ! INPUT #1:Trash$ ! Soak Time (T[i+2])
28450 PRINT #1:Tnew1$ ! INPUT #1:Trash$ ! Ending soak temperature (S[i+2])
28500 CLOSE #1
28550 !
28600 Told$ = "*:WS" & Sn2$ & "/" & Value$ & ":"
28650 R$ = "" ! Reset the flow control variable
28700 !
28750 ! Write this information to the monitor.
28800 SET DIALOG COLOR 14 ! yellow
28850 PRINT AT 15,74 USING "3d":Tstnew
28900 Tstnewf = Tstnew*1.8+32
28950 PRINT AT 16,74 USING "3d":Sinc
29000 Sincf = Sinc*1.8
29050 PRINT AT 17,65 USING "2a":Mi$ ! PRINT AT 17,74 USING "2a":Sec$
29100 !
29150 ! Now set the present temperature setpoint.
29200 Tset = Tsetnew
29250 !
29300 RETURN
29350 !
29400 !   ************************************************************************
29450 Endexp:
29500 ! This subroutine prompts the user to switch to manual control of the
29550 !  of the heating block temperature to ramp down the experiment once
29600 !  cessation of the experiment has been requested.  The communications
29650 !  link to the controller is maintained to provide the block surface
29700 !  temperature to the controller for the ramp down.
```

```
29750 !
29800 FOR I = 1 TO 6
29850     PRINT AT I,2 USING "38x":
29900 NEXT I
29950 !
30000 SET DIALOG COLOR 14
30050 PRINT AT 1,2:"Ending the experiment..."
30100 PRINT AT 3,2:"Put the temperature controller in"
30150 PRINT AT 4,2:"MANUAL mode, and press <F> when"
30200 PRINT AT 5,2:"ready.  Open the valve on the pressure"
30250 PRINT AT 6,2:"equalization line.  Disconnect the"
30300 PRINT AT 7,2:"cartridge heater cable."
30350 !
30400 RETURN
30450 !
30500 !   ************************************************************************
30550 Errhandlr:
30600 ! This subroutine handles all execution errors by exiting from the
30650 !   control program.
30700 !
30750 ! Look for the data file name error.
30800 IF Ern=102 THEN GOTO Read2 ! Datafile name is OK to use
30850 IF Ern=6 THEN GOTO Ending ! Control <C>
30900 !
30950 PRINT Bell$,Bell$,Bell$
31000 SET DIALOG COLOR 12
31050 PRINT AT 10,2:"EXECUTION File # or UDK = ";Erf
31100 IMAGE "Line # = ",5d,3x,"Error # = ",3d
31150 PRINT AT 11,2 USING 31100:Erl,Ern
31200 CLOSE ! close all of the open channels
31250 END
31300 !
31350 !   ************************************************************************
31400 Flaghandlr:
31450 ! This subroutine handles all errors that occur during communication
31500 !   with the DAS16.
31550 !
31600 PRINT Bell$,Bell$,Bell$
31650 SET DIALOG COLOR 12
31700 PRINT AT 10,2:"DASH16 Mode = ";Md
31750 IMAGE "Line # = ",5d,3x,"Error # = ",2d
31800 PRINT AT 11,2 USING 31750:Linenum[Dcall],Flag
31850 !
31900 RETURN
31950 !
32000 !   ************************************************************************
32050 Inkey:
32100 ! This subroutine determines the program flow based on the input key
32150 !   depressed by the operator.
32200 !
32250 ! Clear the message area on the screen.
32300 FOR L = 2 TO 7
32350     PRINT AT L,2 USING "38x":
32400 NEXT L
```

```
32450 !
32500 SET DIALOG COLOR 14
32550 SELECT CASE R$
32600     CASE "A" ! Reactivate the keyboard
32650         Manual$ = "n" ! R$ = ""
32700     CASE "C" ! Simply clear the dialog area of the screen
32750         Setnum = 0 ! Reset the data set counter
32800     CASE "D" ! Time to take a set of data?
32850         SET DIALOG COLOR 12
32900         PRINT AT 3,2:"**COMPUTER IS WAITING - NO CONTROL**"
32950         SET DIALOG COLOR 14
33000         PRINT AT 4,2:"Collect a set of data? <Y/N>" ! INPUT KEY WAIT A$
33050         IF A$="y" THEN GOSUB Dataread
33100         R$ = "C" ! IF A$="N" THEN GOTO 32300
33150         A$ = ""
33200     CASE "E" ! time to exit the experiment?
33250         SET DIALOG COLOR 12
33300         PRINT AT 3,2:"**COMPUTER IS WAITING - NO CONTROL**"
33350         SET DIALOG COLOR 14
33400         PRINT AT 4,2:"End the experiment? <Y/N>" ! INPUT KEY WAIT B$
33450         IF B$="y" THEN GOSUB Endexp ! Disables input of letters from keyboard
33500         R$ = "C" ! IF B$="n" THEN GOTO 32300
33550         B$ = ""
33600     CASE "F" ! Manual ramp down of the experiment
33650         PRINT AT 3,2:"Temperature controller in MANUAL."
33700         PRINT AT 4,2:"Keyboard is disabled."
33750         PRINT AT 5,2:"Press [cntrl<C>] to end."
33800         PRINT AT 6,2 USING "38x":
33850         Manual$ = "Y"
33900     CASE "N" ! Controller setpoint information not downloaded
33950         PRINT AT 3,2:"Reset the controller information"
34000         PRINT AT 4,2:"for downloading."
34050     CASE "T" ! Reset the profile segment index to "0"
34100         Times = 0
34150         SET DIALOG COLOR 12
34200         PRINT AT 3,2:"**COMPUTER IS WAITING - NO CONTROL**"
34250         SET DIALOG COLOR 14
34300         PRINT AT 4,2:"Reset controller segments? <Y/N>" ! INPUT KEY WAIT C$
34350         R$ = "C" ! IF C$="N" THEN GOTO 32300
34400         C$ = ""
34450         OPEN #1:"COM1","F" ! Rqst$ = "*:RS" & Sn2$ & ":"
34500         PRINT #1:Rqst$ ! Request the most recent temperature setpoint
34550         INPUT #1:Rspp$
34600         Ppp = POS(Rspp$,":",1)
34650         SELECT CASE Disp$
34700             CASE "V" ! Temperature controller display reads volts
34750                 GOTO Times1
34800             CASE "C" ! Temperature controller display degrees C
34850                 GOTO Times2
34900         END SELECT
34950         !
35000         Times1: Ii$ = SEG$(Rspp$,Ppp+2,2) ! Ff$ = SEG$(Rspp$,Pp+4,2)
35050         Iidotff$ = Ii$ & "." & Ff$
35100         Trestore$ = "*:WS0/" & Ii$ & Ff$ & ":"
```

```
35150         Trestor1$ = "*:WS1/" & Ii$ & Ff$ & ":"
35200         GOTO Times3
35250         !
35300         Times2: Iidotff$ = SEG$(Rspp$,Ppp+2,4)
35350         Trestore$ = "*:WS0/" & Iidotff$ & ":"
35400         Trestor1$ = "*:WS1/" & Iidotff$ & ":"
35450         !
35500         ! Restore current setpoint info to the controller's first profile.
35550         Times3: PRINT #1:Trestore$ ! INPUT #1:Trash$
35600         PRINT #1:"*:WT1/0100:" ! INPUT #1:Trash$
35650         PRINT #1:Trestor1$ ! INPUT #1:Trash$
35700         CLOSE #1
35750         !
35800         ! Convert the most recent controller temperature setpoint to mV.
35850         Tsett = VAL(Iidotff$)
35900         Tset = (Tsett-50)/Cfactor+2.022
35950         PRINT AT 15,74 USING "3d":Tsett
36000         PRINT AT 6,2:"Controller reset to Profile 1"
36050     CASE "Y" ! Time to download to the controller
36100         R$ = "C" ! IF Down$="N" THEN GOTO 32300
36150         GOSUB Download
36200         Down$ = "N"
36250 CASE ELSE ! PRINT AT 2,2:"UNDEFINED KEY WAS ENTERED."
36300         PRINT AT 3,2:"IT HAS BEEN IGNORED."
36350 END SELECT
36400 !
36450 R$ = "" ! Reset the flow control variable
36500 RETURN
36550 !
36600 !   ********************************************************************
36650 Interpolate:
36700 ! This subroutine, which interpolates the temperature from the type K
36750 !   thermocouple voltages, was taken from Metrabyte's program "K.BAS".
36800 !   The variable in the main program containing the millivolt
36850 !   temperature signal must be named "Mvtemp" prior to the call.
36900 !
36950 ! Find the lookup element.
37000 Ek = INT((Mvtemp-Svk)/Sik)+1 ! Add 1 to account for BASE1
37050 IF Ek<0 THEN Tc = Tk[1] ! Out of bounds, round to lower limit
37100 IF Ek<0 THEN GOTO 37350
37150 IF Ek>Nk-2 THEN Tc = Tk[Nk-1] ! Out of bounds, round to upper limit
37200 IF Ek>Nk-2 THEN GOTO 37350
37250  Do the interpolation
37300 Tc  = Tk[Ek]+(Tk[Ek+1]-Tk[Ek])*(Mvtemp-(Ek-1)*Sik-Svk)/Sik  ! Centigrade
37350 Tf = Tc*1.8+32 ! Fahrenheit
37400 !
37450 RETURN
37500 !
37550 !   ********************************************************************
37600 ! Set flags for inputting new temperature set points and ramp rates by pressing UD keys.
37650 Key1: Flags = 1 ! GOTO Targ1
37700 Key2: Flags = 2 ! GOTO Targ1
37750 Key3: Flags = 3 ! GOTO Targ1
37800 Key4: Flags = 4 ! GOTO Targ1
```

```
37850 Key5: Flags = 5 ! GOTO Targ1
37900 Key6: Flags = 6 ! GOTO Targ1
37950 Key7: Flags = 7 ! GOTO Targ1
38000 Key8: Flags = 8 ! GOTO Targ1
38050 Key9: Flags = 9 ! GOTO Targ1
38100 Key10: Flags = 10
38150 !
38200 Targ1: CONTINUE
38250 FOR L = 2 TO 7
38300     PRINT AT L,2 USING "38x":
38350 NEXT L
38400 Tsetnew = Tset+Setptinc[Flags] ! New surface temperature setpoint, mV
38450 Sinc = Setptinc[Flags]/0.041 ! Degree C value
38500 Tstnew = INT(50+(Tset-2.022)/0.041)+Sinc ! Deg. C value
38550 SET DIALOG COLOR 14
38600 PRINT AT 3,2:"Setpoint Increment = "
38650 PRINT AT 3,23 USING "2d.1d":Sinc ! PRINT AT 3,28:"C"
38700 PRINT AT 4,2:"New Setpoint = " ! PRINT AT 4,17 USING "3d.1d":Tstnew
38750 PRINT AT 4,23:"C"
38800 PRINT AT 5,2:"Now, set the ramp rate"
38850 PRINT AT 6,4:"by pressing UDK's 11-20."
38900 R$ = ""
38950 RETURN
39000 !
39050 Key11: Flagr = 1 ! GOTO Targ2
39100 Key12: Flagr = 2 ! GOTO Targ2
39150 Key13: Flagr = 3 ! GOTO Targ2
39200 Key14: Flagr = 4 ! GOTO Targ2
39250 Key15: Flagr = 5 ! GOTO Targ2
39300 Key16: Flagr = 6 ! GOTO Targ2
39350 Key17: Flagr = 7 ! GOTO Targ2
39400 Key18: Flagr = 8 ! GOTO Targ2
39450 Key19: Flagr = 9 ! GOTO Targ2
39500 Key20: Flagr = 10
39550 Targ2: Mi$ = SEG$(Ramp$[Flagr],1,2) ! Sec$ = SEG$(Ramp$[Flagr],3,2)
39600 FOR L = 5 TO 6
39650     PRINT AT L,2 USING "38x":
39700 NEXT L
39750 SET DIALOG COLOR 14
39800 IMAGE "Ramp rate = ",2a," minutes, ",2a," seconds."
39850 PRINT AT 5,2 USING 39800:Mi$,Sec$
39900 PRINT AT 6,2:"Controller info OK to download? <y/n>"
39950 Down$ = "Y" ! Set the flag for downloading
40000 R$ = ""
40050 RETURN
40100 !
40150 !   ****************************************************************
40200 Lookup:
40250 ! ---------- TABLE LOOKUP DATA FOR TYPE k THERMOCOUPLE ----------
40300 ! This subroutine was taken from Metrabyte's program "K.BAS".
40350 !  It contains the calibration data for a type K thermocouple.
40400 !  # points in table=309, mV step interval=0.2, starting mV=-6.6
40450 ! However, note that the first data point is commented out (thus, # =
40500 !  308 instead of 309). This accounts for the "BASE 1" of the TBASIC
```

```
40550 !  driver compared to the "BASE 0" of Metrabyte's BASIC driver.
40600 DATA 308,0.2,-6.4
40650 READ Nk,Sik,Svk ! Temperature at -6.4 mV, -6.2 mV, -6.0 mV, ....
40700 !
40750 ! DATA -353.5
40800 DATA -249.3,-224.0,-207.6,-194.3,-182.8,-172.3,-162.8,-153.8,-145.4
40850 DATA -137.3,-129.6,-122.3,-115.2,-108.3,-101.6,-95.1,-88.7,-82.5,-76.4
40900 DATA -70.4,-64.6,-58.8,-53.1,-47.5,-42.0,-36.6,-31.2,-25.9,-20.6
40950 DATA -15.4,-10.2,-5.1,0.0,5.0,10.1,15.1,20.0,25.0,29.9
41000 DATA 34.8,39.7,44.6,49.5,54.3,59.1,64.0,68.8,73.6,78.4
41050 DATA 83.2,88.0,92.9,97.7,102.5,107.4,112.2,117.1,122.0,126.9
41100 DATA 131.8,136.7,141.7,146.6,151.6,156.5,161.5,166.5,171.5,176.5
41150 DATA 181.6,186.6,191.6,196.6,201.6,206.6,211.6,216.6,221.5,226.5
41200 DATA 231.5,236.4,241.4,246.3,251.2,256.1,261.0,265.9,270.8,275.6
41250 DATA 280.5,285.3,290.2,295.0,299.8,304.6,309.4,314.3,319.1,323.9
41300 DATA 328.7,333.4,338.2,343.0,347.8,352.6,357.3,362.1,366.9,371.6
41350 DATA 376.4,381.1,385.9,390.6,395.4,400.1,404.8,409.6,414.3,419.0
41400 DATA 423.8,428.5,433.2,437.9,442.6,447.3,452.0,456.8,461.5,466.2
41450 DATA 470.9,475.6,480.3,485.0,489.7,494.4,499.1,503.8,508.5,513.1
41500 DATA 517.8,522.5,527.2,531.9,536.6,541.3,546.0,550.7,555.4,560.0
41550 DATA 564.7,569.4,574.1,578.8,583.5,588.2,592.9,597.6,602.3,607.0
41600 DATA 611.7,616.4,621.2,625.9,630.6,635.3,640.0,644.8,649.5,654.2
41650 DATA 658.9,663.7,668.4,673.2,677.9,682.7,687.4,692.2,696.9,701.7
41700 DATA 706.5,711.3,716.1,720.8,725.6,730.4,735.2,740.0,744.8,749.7
41750 DATA 754.5,759.3,764.1,769.0,773.8,778.7,783.5,788.4,793.3,798.1
41800 DATA 803.0,807.9,812.8,817.7,822.6,827.5,832.4,837.3,842.2,847.2
41850 DATA 852.1,857.1,862.0,867.0,872.0,876.9,881.9,886.9,891.9,896.9
41900 DATA 901.9,906.9,911.9,916.9,922.0,927.0,932.0,937.1,942.2,947.2
41950 DATA 952.3,957.4,962.5,967.6,972.7,977.8,982.9,988.0,993.1,998.2
42000 DATA 1003.4,1008.5,1013.7,1018.8,1024.0,1029.2,1034.4,1039.6,1044.8,1050.0
42050 DATA 1055.2,1060.4,1065.6,1070.8,1076.1,1081.3,1086.6,1091.9,1097.2,1102.4
42100 DATA 1107.7,1113.0,1118.3,1123.7,1129.0,1134.3,1139.7,1145.0,1150.4,1155.8
42150 DATA 1161.2,1166.6,1172.0,1177.4,1182.9,1188.3,1193.8,1199.2,1204.7,1210.2
42200 DATA 1215.7,1221.2,1226.8,1232.3,1237.9,1243.5,1249.1,1254.7,1260.3,1265.9
42250 DATA 1271.6,1277.3,1282.9,1288.6,1294.3,1300.1,1305.8,1311.5,1317.3,1323.1
42300 DATA 1328.9,1334.7,1340.5,1346.4,1352.2,1358.1,1363.9,1369.8,1375.7
42350 !
42400 DIM Tk[Nk]
42450 FOR I = 1 TO Nk ! READ Tk[I] ! NEXT I
42500 RETURN
42550 !
42600 !   ************************************************************************
42650 Monsetup:
42700 ! This subroutine configures the monitor with the operating faceplate
42750 !  to interface the operator and the software for the boiling
42800 !  experiment.
42850 !
42900 CLEAR
42950 MOVE 0,55 ! DRAW 74,55
43000 MOVE 74,52 ! DRAW 148,52
43050 MOVE 74,0 ! DRAW 74,100
43100 MOVE 0,70 ! DRAW 74,70
43150 MOVE 74,29 ! DRAW 148,29
43200 SET DIALOG COLOR 14
```

```
43250 PRINT  AT  1,2:"...Idling..."
43300 SET DIALOG COLOR 6
43350 PRINT AT 1,45:"CURRENT OPERATING INFORMATION"
43400 PRINT AT 2,45:"Surface Temperature =      C"
43450 PRINT AT 3,45:"Block Temperature 1 =      C"
43500 PRINT AT 4,45:"Block Temperature 2 =      C"
43550 PRINT AT 5,45:"Block Temperature 3 =      C"
43600 PRINT AT 6,45:"Block Temperature 4 =      C"
43650 PRINT AT 7,45:"Bottom Block Temperature =      C"
43700 PRINT AT 8,45:"Bottom Bed Temperature =      C"
43750 PRINT AT 9,45:"Top Bed Temperature =      C"
43800 PRINT AT 10,45:"Guard Heater Temperature =      C"
43850 PRINT AT 11,45:"Makeup Water Temperature =      C"
43900 PRINT AT 12,45:"Boiling Cell Pressure =      psia"
43950 SET DIALOG COLOR 12
44000 PRINT AT 9,5:"***** WARNINGS AND ERRORS *****"
44050 SET DIALOG COLOR 11
44100 PRINT AT 14,44:"CURRENT TEMPERATURE CONTROLLER INFO"
44150 PRINT AT 15,42:"Surface Temperature Setpoint =     C"
44200 PRINT AT 16,42:"Surface Temperature Increment =      C"
44250 PRINT AT 17,42:"Controller Ramp Rate =    mins,    secs"
44300 SET DIALOG COLOR 10
44350 PRINT AT 13,2:"UDK's for DOWNLOADING to CONTROLLER"
44400 PRINT AT 14,2:"Temperature" ! PRINT AT 14,20:"Ramp Rate"
44450 PRINT AT 15,2:"F1 = 1 deg C" ! PRINT AT 16,2:"F2 = 2 deg C"
44500 PRINT AT 17,2:"F3 = 3 deg C" ! PRINT AT 18,2:"F4 = 4 deg C"
44550 PRINT AT 19,2:"F5 = 5 deg C" ! PRINT AT 20,2:"F6 = 7 deg C"
44600 PRINT AT 21,2:"F7 = 10 deg C" ! PRINT AT 22,2:"F8 = 15 deg C"
44650 PRINT AT 23,2:"F9 = 20 deg C" ! PRINT AT 24,2:"F10 = 25 deg C"
44700 PRINT AT 15,20:"F11 = 1 minute" ! PRINT AT 16,20:"F12 = 1 min, 30 sec"
44750 PRINT AT 17,20:"F13 = 2 minutes" ! PRINT AT 18,20:"F14 = 3 minutes"
44800 PRINT AT 19,20:"F15 = 4 minutes" ! PRINT AT 20,20:"F16 = 5 minutes"
44850 PRINT AT 21,20:"F17 = 7 min, 30 sec" ! PRINT AT 22,20:"F18 = 10 minutes"
44900 PRINT AT 23,20:"F19 = 15 minutes" ! PRINT AT 24,20:"F20 = 20 minutes"
44950 SET DIALOG COLOR 9
45000 PRINT AT 19,44:"OTHER KEYS WITH SPECIAL FUNCTIONS"
45050 PRINT AT 20,42:"<a> - reactivate the keyboard"
45100 PRINT AT 21,42:"<c> - clear the screen message area"
45150 PRINT AT 22,42:"<d> - collect the data"
45200 PRINT AT 23,42:"<e> - end the experiment"
45250 PRINT AT 24,42:"<t> - reset controller to profile 1"
45300 SELECT CASE Disp$
45350     CASE "V" ! Temperature controller display reads volts
45400          Tinit$ = I$ & F$ ! Tinit = VAL(Tinit$)
45450     CASE "C" ! Temperature controller display degrees C
45500          Tinit = VAL(Idotf$)
45550 END SELECT
45600 SET DIALOG COLOR 14 ! PRINT AT 15,74 USING "3d":Tinit
45650 !
45700 RETURN
45750 !
45800 !   ************************************************************************
45850 Monupdate:
45900 ! This subroutine updates the monitor every 5 loops of the surface
```

```
45950 !  temperature calculation loop in the main program.
46000 !
46050 ! Set the limits for the FOR/NEXT loop.
46100 Lowlim[1] = 4 ! Uplim[1] = 5 ! Thermocouples to be read on EXP16 #1
46150 Lowlim[2] = 1 ! Uplim[2] = 4 ! Thermocouples to be read on EXP16 #2
46200 Lowlim[3] = 1 ! Uplim[3] = 1 ! Pressure data on DAS16 channel 3
46250 !
46300 SET DIALOG COLOR 14
46350 Update = 0 ! Reset the data matrix
46400 IF Update$="Y" THEN GOTO Mon1 ! Already have the data from DATAREAD
46450 !
46500 ! Read the data to be written to the screen.
46550 FOR K = 1 TO Sets ! Collect a number of data sets for averaging
46600     FOR Kk = 1 TO Chan
46650         Md = 1 ! Lock DAS16 to the channel using mode 1
46700         Dio[1] = Kk ! Dio[2] = Kk
46750         CALL Dash16(Md,Dio,Flag)
46800         Dcall = 11 ! IF Flag<>0 THEN GOSUB Flaghandlr
46850         !
46900         FOR Kkk = Lowlim[Kk] TO Uplim[Kk]
46950             IF Kk=Chan THEN GOTO Pressure2
47000             Md = 13 ! Select the EXP16 channel with MODE 13
47050             Dio[1] = Kkk
47100             CALL Dash16(Md,Dio,Flag)
47150             Dcall = 12 ! IF Flag<>0 THEN GOSUB Flaghandlr
47200             !
47250             Pressure2: Md = 3 ! Read the EXP16 channel using MODE 3
47300             Dio[1] = 0 ! Dash16 data returned to this variable
47350             CALL Dash16(Md,Dio,Flag)
47400             Dcall = 13 ! IF Flag<>0 THEN GOSUB Flaghandlr
47450             Update[Kk,Kkk] = Update[Kk,Kkk]+Dio[1] ! Increment the data matrix
47500         NEXT Kkk
47550     NEXT Kk
47600 NEXT K
47650 !
47700 Update = Update/Sets ! Average the data in the data matrix
47750 Update[1,1] = Temp[1] ! Update[1,2] = Temp[2] ! Update[1,3] = Temp[3]
47800 !
47850 ! Now, convert the digital data to real values. Start with temperatures.
47900 FOR I = 1 TO 2
47950     FOR Ii = 1 TO Uplim[I]
48000         Vtemp = Update[I,Ii]*Efactor ! V analog temperature
48050         Mvtemp = 1000*Vtemp+1.0+(Cjc[I]-25)*0.0405 ! Corrected mV analog
48100         GOSUB Interpolate !                                signal
48150         Update[I,Ii] = Tc
48200     NEXT Ii
48250 NEXT I
48300 Mvtemp = Tsurf ! GOSUB Interpolate ! Tsurftc = Tc
48350 !
48400 ! Now, convert the pressure data.
48450 Update[3,1] = Update[3,1]*100/(2048*D16gain) ! Pressure in psia
48500 GOTO Mon2
48550 !
48600 ! Print the data to the screen.
```

```
48650 Mon1: Update[1,1] = Ddata[1,1] ! Update[1,2] = Ddata[1,2]
48700 Update[1,3] = Ddata[1,3] ! Update[1,4] = Ddata[1,4]
48750 Update[1,5] = Ddata[1,5] ! Update[2,1] = Ddata[2,1]
48800 Update[2,2] = Ddata[2,2] ! Update[2,3] = Ddata[2,3]
48850 Update[2,4] = Ddata[2,4] ! Update[3,1] = Ddata[3,1]
48900 !
48950 Mon2: PRINT AT 2,67 USING "3d.1d":Tsurftc
49000 PRINT AT 3,67 USING "3d.1d":Update[1,1]
49050 PRINT AT 4,67 USING "3d.1d":Update[1,2]
49100 PRINT AT 5,67 USING "3d.1d":Update[1,3]
49150 PRINT AT 6,67 USING "3d.1d":Update[1,4]
49200 PRINT AT 7,72 USING "3d.1d":Update[1,5]
49250 PRINT AT 8,70 USING "3d.1d":Update[2,1]
49300 PRINT AT 9,67 USING "3d.1d":Update[2,2]
49350 PRINT AT 10,72 USING "3d.1d":Update[2,3]
49400 PRINT AT 11,72 USING "3d.1d":Update[2,4]
49450 PRINT AT 12,69 USING "3d.1d":Update[3,1]
49500 !
49550 IF Update[2,4]>80.0 THEN
49600     Heater$ = "Turn off the makeup water heater"
49650 END IF
49700 IF Update[2,4]<70.0 THEN
49750     Heater$ = "Turn on the makeup water heater "
49800 END IF
49850 IF Update[2,4]>70.0 AND Update[2,4]<80.0 THEN Heater$ = ""
49900 !
49950 Update$ = "N"
50000 Timer = 0 ! counter for updating the monitor
50050 !
50100 RETURN
50150 !
50200 !   ************************************************************************
50250 Udkeys:
50300 ! This subroutine initializes the user-defined keys for downloading
50350 !  profile segment information to the temperature controller.
50400 !
50450 ON KEY 1 GOSUB Key1
50500 ON KEY 2 GOSUB Key2
50550 ON KEY 3 GOSUB Key3
50600 ON KEY 4 GOSUB Key4
50650 ON KEY 5 GOSUB Key5
50700 ON KEY 6 GOSUB Key6
50750 ON KEY 7 GOSUB Key7
50800 ON KEY 8 GOSUB Key8
50850 ON KEY 9 GOSUB Key9
50900 ON KEY 10 GOSUB Key10
50950 ON KEY 11 GOSUB Key11
51000 ON KEY 12 GOSUB Key12
51050 ON KEY 13 GOSUB Key13
51100 ON KEY 14 GOSUB Key14
51150 ON KEY 15 GOSUB Key15
51200 ON KEY 16 GOSUB Key16
51250 ON KEY 17 GOSUB Key17
51300 ON KEY 18 GOSUB Key18
```

```
51350 ON KEY 19 GOSUB Key19
51400 ON KEY 20 GOSUB Key20
51450 !
51500 RETURN
```

APPENDIX V

UNCERTAINTY ANALYSIS

In this Appendix, the degree of certainty associated with the parameters derived from experimental data in all of the experiments is determined. The methods used here conform to ASME measurement uncertainty methodology [111,112]. The nomenclature used for the statistical variables in this discussion is restricted to the information contained herein, and does not necessarily conform to that defined for the remainder of the manuscript.

Since no measurement is perfectly accurate, means for describing inaccuracies are necessary. The appropriate concept for expressing inaccuracies is an "uncertainty", the value of which is determined by "uncertainty analysis". Inaccuracies are composed of a bias error component (systematic error which is considered to remain constant during a given test) and a precision error component (random error). The error in measurement is the difference between the true value and the recorded value, and uncertainty is the possible value that the error might assume in a given experiment; thus, error is a fixed number, and uncertainty is a statistical variable. In essence, the value reported for a measurement describes the central tendency (e.g. the mean), and the uncertainty describes the dispersion about the central tendency, usually in terms of a parameter associated with a stated probability level, such as the standard deviation.

THE METHOD OF DETERMINING UNCERTAINTY

The accuracy of a given number will depend on the accuracy of the data used to generate the number. For instance, the accuracy of the boiling heat flux calculated from the block thermocouple readings and their respective positions depends on the extent to which inaccuracies in these measured parameters are propagated through the calculations. To maximize accuracy of the dependent parameter, the error components of the measurements must be minimized. Bias error can be eliminated by calibration of the measuring instrument, and precision error can be minimized statistically by taking a number of measurements of the same parameter. Thus,

attention to the error components of measured data insures acceptable accuracy of the final calculated data.

Errors in measurements of various parameters (P) are propagated into a derived result (r) through the functional relationship between the result and its independent parameters,

$$r = fn(P_1, P_2, P_3, \ldots P_n) \quad . \tag{77}$$

Propagated errors of the measured parameters are combined as root-sum-squares (RSS) to determine the error components of the calculated variable. For "n" independent parameters, the bias error of a derived parameter is given by the RSS of the propagated bias errors of the independent parameters,

$$B_r = \sqrt{B_1^2 + B_2^2 + B_3^2 + \ldots + B_n^2} \quad , \tag{78}$$

and the precision error of a derived parameter is given by the RSS of the propagated precision errors of the independent parameters,

$$S_r = \sqrt{S_1^2 + S_2^2 + S_3^2 + \ldots + S_n^2} \quad . \tag{79}$$

The propagated bias error of an independent parameter is defined as

$$B_x = \left(\frac{\partial r}{\partial P_x}\right) B_{P_x} \quad , \tag{80}$$

and the propagated precision error of an independent parameter is defined as

$$S_x = \left(\frac{\partial r}{\partial P_x}\right) S_{P_x} \quad . \tag{81}$$

The partial differential terms are the sensitivity factors that are defined in terms of the functional relationship. The bias index (B_{P_x}) is fixed, but the precision index (S_{P_x}) of an independent parameter can be reduced further to the statistical expression of standard deviation (S) of a number of readings (N),

$$S_{P_x} = \frac{S}{\sqrt{N}} \quad . \tag{82}$$

The uncertainty of the derived parameter is then determined by combining its bias and precision in one of two ways: the additive method provides a measure of uncertainty with a confidence level analogous to 99%,

$$U_{r_{ADD}} = B_r + tS_r \quad , \tag{83}$$

and the root-sum-square method provides a measure of uncertainty with a confidence level analogous to 95%,

$$U_{r_{RSS}} = \sqrt{B_r^2 + (tS_r)^2} \quad , \tag{84}$$

where t represents the appropriate value from the Student's-t Table.

Table 21 lists the functional relationships used to determine the derived parameters from the raw experimental data. Also listed are the sensitivity factor equations used in Equations 80 and 81 to determine the propagated error components of the independent parameters. The need for a sensitivity factor for heating block thermal conductivity is not explicitly obvious from the

Table 21. The functional relationships and sensitivity factors used in the uncertainty analysis for the parameters derived from the experimental data.

Derived Parameter	Independent Parameters		Equations
Heat Flux	Two block thermocouples Positions of block thermocouples Block thermal conductivity	Functional Relationship	$q = \frac{3.967(T_2 - T_1) - 6.725\times10^{-4}\left(T_2^2 - T_1^2\right) + 8.533\times10^{-8}\left(T_2^3 - T_1^3\right) + 5.295\times10^{-10}\left(T_2^4 - T_1^4\right)}{x_2 - x_1}$
		Sensitivity Factors	$\frac{\partial q}{\partial T_1} = \frac{-\left(3.967 - 2*6.725\times10^{-4}*T_1 + 3*8.533\times10^{-8}*T_1^2 + 4*5.295\times10^{-10}*T_1^3\right)}{x_2 - x_1}$
			$\frac{\partial q}{\partial T_2} = \frac{3.967 - 2*6.725\times10^{-4}*T_2 + 3*8.533\times10^{-8}*T_2^2 + 4*5.295\times10^{-10}*T_2^3}{x_2 - x_1}$
			$\frac{\partial q}{\partial x_1} = \frac{3.967(T_2 - T_1) - 6.725\times10^{-4}\left(T_2^2 - T_1^2\right) + 8.533\times10^{-8}\left(T_2^3 - T_1^3\right) + 5.295\times10^{-10}\left(T_2^4 - T_1^4\right)}{(x_2 - x_1)^2}$
			$\frac{\partial q}{\partial x_2} = \frac{-\left(3.967(T_2 - T_1) - 6.725\times10^{-4}\left(T_2^2 - T_1^2\right) + 8.533\times10^{-8}\left(T_2^3 - T_1^3\right) + 5.295\times10^{-10}\left(T_2^4 - T_1^4\right)\right)}{(x_2 - x_1)^2}$
			$\frac{\partial q}{\partial k_h} = \frac{\partial T}{\partial x}$
Surface Temperature	Three block thermocouples Positions of block thermocouples	Functional Relationship	$T_s = \frac{\left(\sum_{i=1}^{3} T_i\right)\left(\sum_{i=1}^{3} x_i^2\right) - \left(\sum_{i=1}^{3} x_i\right)\left(\sum_{i=1}^{3} x_i T_i\right)}{3\left(\sum_{i=1}^{3} x_i^2\right) - \left(\sum_{i=1}^{3} x_i\right)^2}$

Table 21. (continued)

Sensitivity Factors

$$\frac{\partial T_s}{\partial T_1} = \frac{\left(\sum_{i=1}^{3} x_i^2\right) - x_1\left(\sum_{i=1}^{3} x_i\right)}{3\left(\sum_{i=1}^{3} x_i^2\right) - \left(\sum_{i=1}^{3} x_i\right)^2} \qquad \frac{\partial T_s}{\partial T_2} = \frac{\left(\sum_{i=1}^{3} x_i^2\right) - x_2\left(\sum_{i=1}^{3} x_i\right)}{3\left(\sum_{i=1}^{3} x_i^2\right) - \left(\sum_{i=1}^{3} x_i\right)^2} \qquad \frac{\partial T_s}{\partial T_3} = \frac{\left(\sum_{i=1}^{3} x_i^2\right) - x_3\left(\sum_{i=1}^{3} x_i\right)}{3\left(\sum_{i=1}^{3} x_i^2\right) - \left(\sum_{i=1}^{3} x_i\right)^2}$$

$$\frac{\partial T_s}{\partial x_1} = \frac{2x_1\left(\sum_{i=1}^{3} T_i\right) - T_1\left(x_1 + \sum_{i=1}^{3} x_i\right) - \sum_{i=2}^{3} x_i T_i}{3\left(\sum_{i=1}^{3} x_i^2\right) - \left(\sum_{i=1}^{3} x_i\right)^2} - \left[6x_1 - 2\left(\sum_{i=1}^{3} x_i\right)\right] \frac{\left(\sum_{i=1}^{3} T_i\right)\left(\sum_{i=1}^{3} x_i^2\right) - \left(\sum_{i=1}^{3} x_i\right)\left(\sum_{i=1}^{3} x_i T_i\right)}{\left[3\left(\sum_{i=1}^{3} x_i^2\right) - \left(\sum_{i=1}^{3} x_i\right)^2\right]^2}$$

$$\frac{\partial T_s}{\partial x_2} = \frac{2x_2\left(\sum_{i=1}^{3} T_i\right) - T_2\left(x_2 + \sum_{i=1}^{3} x_i\right) - x_1 T_1 - x_3 T_3}{3\left(\sum_{i=1}^{3} x_i^2\right) - \left(\sum_{i=1}^{3} x_i\right)^2} - \left[6x_2 - 2\left(\sum_{i=1}^{3} x_i\right)\right] \frac{\left(\sum_{i=1}^{3} T_i\right)\left(\sum_{i=1}^{3} x_i^2\right) - \left(\sum_{i=1}^{3} x_i\right)\left(\sum_{i=1}^{3} x_i T_i\right)}{\left[3\left(\sum_{i=1}^{3} x_i^2\right) - \left(\sum_{i=1}^{3} x_i\right)^2\right]^2}$$

$$\frac{\partial T_s}{\partial x_3} = \frac{2x_3\left(\sum_{i=1}^{3} T_i\right) - T_3\left(x_3 + \sum_{i=1}^{3} x_i\right) - \sum_{i=1}^{2} x_i T_i}{3\left(\sum_{i=1}^{3} x_i^2\right) - \left(\sum_{i=1}^{3} x_i\right)^2} - \left[6x_3 - 2\left(\sum_{i=1}^{3} x_i\right)\right] \frac{\left(\sum_{i=1}^{3} T_i\right)\left(\sum_{i=1}^{3} x_i^2\right) - \left(\sum_{i=1}^{3} x_i\right)\left(\sum_{i=1}^{3} x_i T_i\right)}{\left[3\left(\sum_{i=1}^{3} x_i^2\right) - \left(\sum_{i=1}^{3} x_i\right)^2\right]^2}$$

Average Pore Diameter

Volume change Capillary pressure

Functional Relationship

$$\overline{D} = \frac{\sum_{i=1}^{n} f_i \overline{d}_i}{\sum_{i=1}^{n} f_i} = \sigma\left(\frac{\sum_{i=1}^{n} \Delta V_i \Delta P_{c_i}}{\sum_{i=1}^{n} \Delta V_i \Delta P_{c_i}^2}\right)$$

where n = the number of local average diameters in the histogram

Sensitivity Factors

$$\frac{\partial \overline{D}}{\partial \sigma} = \frac{\sum_{i=1}^{n} \Delta V_i \Delta P_{c_i}}{\sum_{i=1}^{n} \Delta V_i \Delta P_{c_i}^2}$$

$$\frac{\partial \overline{D}}{\partial \Delta V_j} = \sigma\left[\frac{\Delta P_{c_j}}{\sum_{i=1}^{n} \Delta V_i \Delta P_{c_i}} - \Delta P_{c_j}^2\left(\frac{\sum_{i=1}^{n} \Delta V_i \Delta P_{c_i}}{\left(\sum_{i=1}^{n} \Delta V_i \Delta P_{c_i}^2\right)^2}\right)\right]$$

Table 21. (continued)

Permeability	Water volume Water viscosity Length between pressure taps Formation tube diameter Time Pressure drop	Functional Relationship	$K = \frac{V \mu L}{\frac{\pi}{4} d^2 t \Delta P}$
		Sensitivity Factors	$\frac{\partial K}{\partial V} = \frac{\mu L}{\frac{\pi}{4} d^2 t \Delta P}$ $\quad \frac{\partial K}{\partial \mu} = \frac{V L}{\frac{\pi}{4} d^2 t \Delta P}$ $\quad \frac{\partial K}{\partial L} = \frac{V \mu}{\frac{\pi}{4} d^2 t \Delta P}$
			$\frac{\partial K}{\partial d} = -\frac{V \mu L}{\frac{\pi}{4} d^3 t \Delta P}$ $\quad \frac{\partial K}{\partial t} = -\frac{V \mu L}{\frac{\pi}{4} d^2 t^2 \Delta P}$ $\quad \frac{\partial K}{\partial \Delta P} = -\frac{V \mu L}{\frac{\pi}{4} d^2 t \Delta P^2}$
Boiling Cell Porosity	Bed diameter Bed height Fiber weight	Functional Relationship	$\varepsilon = \frac{\frac{\pi}{4} H d_{bc}^2 - \frac{W_f}{\rho_f}}{\frac{\pi}{4} H d_{bc}^2} = 1 - \frac{W_f}{\frac{\pi}{4} \rho_f H d_{bc}^2}$
		Sensitivity Factors	$\frac{\partial \varepsilon}{\partial W_f} = -\frac{1}{\frac{\pi}{4} \rho_f H d_{bc}^2}$ $\quad \frac{\partial \varepsilon}{\partial H} = \frac{W_f}{\frac{\pi}{4} \rho_f H^2 d_{bc}^2}$ $\quad \frac{\partial \varepsilon}{\partial d_{bc}} = \frac{2 W_f}{\frac{\pi}{4} \rho_f H d_{bc}^3}$
Capillary Pressure/ Saturation Pad Porosity	Displaced water volume Residual water volume Fiber weight	Functional Relationship	$\varepsilon = \frac{V_R + V_D}{V_R + V_D + \frac{W_f}{\rho_f}}$
		Sensitivity Factors	$\frac{\partial \varepsilon}{\partial V_R} = \frac{1}{V_R + V_D + \frac{W_f}{\rho_f}} - \frac{V_R + V_D}{\left(V_R + V_D + \frac{W_f}{\rho_f}\right)^2}$ $\quad \frac{\partial \varepsilon}{\partial V_D} = \frac{1}{V_R + V_D + \frac{W_f}{\rho_f}} - \frac{V_R + V_D}{\left(V_R + V_D + \frac{W_f}{\rho_f}\right)^2}$
			$\frac{\partial \varepsilon}{\partial W_f} = -\frac{V_R + V_D}{\rho_f \left(V_R + V_D + \frac{W_f}{\rho_f}\right)^2}$

equation for heat flux. However, the heat flux equation is derived from the temperature-dependent thermal conductivity, and any uncertainties in the thermal conductivity data propagated to the heat flux must be accounted for. The uncertainty of the thermal conductivity data is expressed as ± 4%, which means that the product of the appropriate critical value from the Student-t distribution and the precision index of the data is 4% of the thermal conductivity. At a confidence level of 95%, the Student-t value is very nearly 2.0, which gives a precision index of 2% of the thermal conductivity,

$$S_{k_h} = 0.02\, k_h(T) \quad . \tag{85}$$

The equation for one-dimensional heat flux with a temperature-dependent thermal conductivity is recalled,

$$q = k_h(T)\frac{dT}{dx} \quad . \tag{86}$$

Differentiation with respect to thermal conductivity yields the sensitivity factor,

$$\frac{dq}{dk_h(T)} = \frac{dT}{dx} \quad . \tag{87}$$

Substituting the precision index (Equation 85) and the sensitivity factor (Equation 87) into Equation 81 gives the following expression for the propagated precision error for thermal conductivity:

$$S_{q(k_h)} = \left(\frac{dq}{dk_h(T)}\right) S_{k_h} = \left(0.02\, k_h(T)\right)\frac{dT}{dx} = 0.02\, q \quad . \tag{88}$$

Accordingly, the precision error in thermal conductivity propagated to the heat flux is simply 2% of the heat flux.

Table 22 lists the magnitude of uncertainty, and the precision and bias indices used for each independent parameter. The values of the bias indices are subjectively selected based on experience with the experiments. The bias indices for the independent parameters of the porosity in the capillary pressure/saturation experiment are relatively large to account for the error associated with graphical interpolation of the pore diameter/bed water volume curve. A precision index of zero was assigned to any independent parameter whose value is determined by only one data point; all inaccuracy is presumed to result from interpolation of the instrument reading. The precision index for the block thermocouple readings is determined from Equation 82. Ten sets consisting of fifteen thermocouple readings are used to calculate one temperature [j] ; the standard deviation is determined as the square root of the pooled variance of the ten groups. Since each group has the same number of readings (fifteen), the pooled variance is simply the average of the variances for the ten groups. For 150 degrees of freedom, the pooled standard deviation of 1.10 yields a precision index of 0.089.

[j] Experiments indicate that statistical treatment of fifteen thermocouple readings provides an acceptable value of standard deviation.

Table 22. Uncertainties for the parameters derived from the experimental data.

Derived Parameter	Independent Parameters	Value of Error Indices		Uncertainty	
		Bias (B_{P_x})	Precision (S_{P_x})	ADD	RSS
Heat Flux	Thermocouple readings	0.20 °C [a]	0.089 °C	0.9/q	0.7/q
	Thermocouple positions	0.002 cm	0		
	Block thermal conductivity	--	0.02 k_h		
Surface Temperature	Thermocouple readings	0.20 °C	0.089 °C	0.6%	0.4%
	Thermocouple positions	0.002 cm	0		
Average Pore Diameter	Volume change	0.1-0.3 ml [b]	0	2.3%	2.3%
	Capillary pressure	0 Pa [c]	0		
Permeability	Water volume	1.0 ml	0	2.9%	2.9%
	Time	0.1 sec	0		
	Distance between pressure taps	0.05 cm	0		
	Forming tube diameter	0.05 cm	0		
	Water viscosity	5E-6 Pa-sec	0		
	Pressure drop	0 Pa [c]	0		
Boiling Cell Porosity	Boiling cell diameter	0.2 cm	0	0.5%	0.5%
	Bed height	0.3 cm	0		
	Fiber weight	3.0 g	0		
Capillary Pressure/ Saturation Pad Porosity	Displaced water volume	0.2 ml	0	0.2%	0.2%
	Residual water volume	0.2 ml	0		
	Fiber weight	0.1 g	0		

a - Even though the thermocouples are calibated, a bias error of 0.20°C has been assumed.

b - The bias error is 0.1 ml for displaced water volumes less than 0.1 ml, 0.2 ml for displaced water volumes between 0.1 and 2.5 ml, and 0.3 ml for displaced water volumes larger than 2.5 ml.

c - Interpolation error for the calibrated Validyne differential pressure transducer is assumed to be negligible.

APPENDIX VI

INSPECTIONAL ANALYSIS OF TWO-PHASE FLOW AND HEAT TRANSFER IN POROUS MEDIA

The conservation equations for steady-state, two-phase flow with heat transfer through an incompressible porous medium were non-dimensionalized as an alternative to dimensional analysis to develop dimensionless groups for mathematical modeling of the data. Because these groups contain variables that are extremely difficult to quantify (v_l, v_v, ε_l, ε_v, $\dot{m}_x$, and P_v), the dimensionless groups developed from dimensional analysis are used in this thesis. However, it is instructive to present the inspectional analysis approach.

The complicated geometry within the porous medium precludes treating the fluid as a continuum on a microscopic level. The volume-averaging technique is commonly used to transform the microscopic conservation equations into a form that treats the fluid as a continuum on a macroscopic level. The terms of the microscopic equations are volume-averaged over some representative elementary volume (REV), illustrated in Figure 77, to determine the appropriate spatial average, defined as

$$\langle \Psi \rangle = \frac{1}{V} \int_V \Psi \, dV \qquad (88)$$

The intrinsic phase average defines the average value of a function (typically, a fluid property) for every point in the space occupied by a particular phase:

$$\langle \Psi \rangle' = \frac{1}{V_\alpha} \int_{V_\alpha} \Psi \, dV \quad , \qquad (89)$$

where the subscript α refers to a particular phase. The two expressions for volume-average are

related by the void volume of the phase:

$$\langle \Psi \rangle = \varepsilon_\alpha \langle \Psi \rangle^\alpha \quad . \tag{90}$$

Reference 78 gives a complete discussion of volume-averaging techniques.

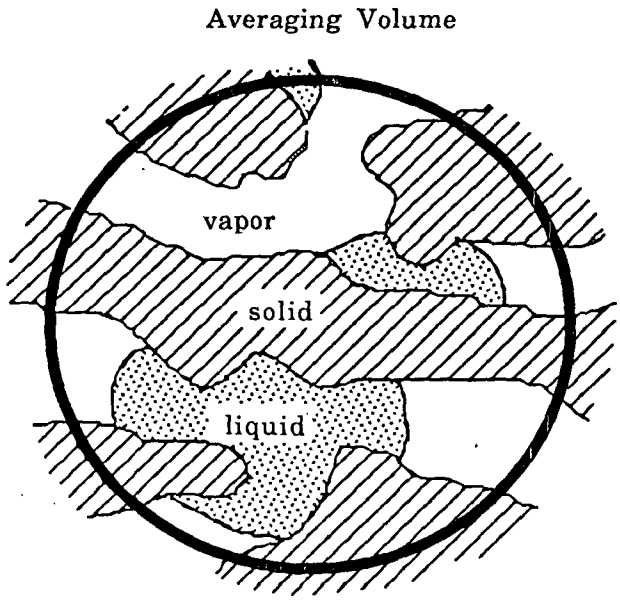

Figure 77. The relative elementary volume for the volume-averaging technique.

The physical model for one-dimensional, two-phase flow through a porous medium is illustrated in Figure 78. The appropriate set of one-dimensional, volume-averaged conservation equations used in this analysis are listed in Table 23. The continuity and energy equations are based on Reference 78, and the momentum equations are based on Reference 113. The following assumptions were used in formulating these equations:

1. Friction between the liquid water and steam phases is neglected.
2. Viscous stresses are neglected for the liquid water phase.
3. Darcy's law adequately accounts for viscous flow of both the liquid water and steam phases. Inertial effects are negligible for both phases. (This assumption introduces one piece of empiricism in the form of the medium permeability.)

4. The porous medium is incompressible, homogeneous, and isotropic.
5. The liquid water is incompressible throughout the temperature and pressure ranges.
6. The vapor phase is thermodynamically considered as an ideal gas.
7. The heat capacity and thermal conductivity of the solid and liquid phases are constant throughout the temperature and pressure ranges.
8. Transport phenomena are strictly one-dimensional.
9. The three phases are in local thermal equilibrium.

Some of these assumptions are over-simplifications, but are made in order to keep the mathematics at a workable level. This is justified because the goal of this exercise is to define appropriate dimensionless groups rather than develop a first-principles model of this system.

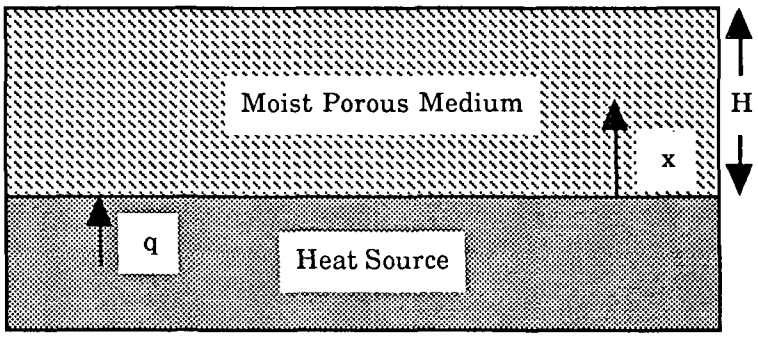

Figure 78. The model geometry for one-dimensional, two-phase flow through a porous medium.

The trade-off for using volume-averaged conservation equations is the introduction of empiricism through the medium permeability and the void volumes of the three phases in the medium, which must be measured. Recall that ε is defined as medium porosity, but in these equations, ε_f, ε_l, and ε_v are defined as the volume fractions of the respective phases. Clearly, the volume constraint is

$$\varepsilon_f + \varepsilon_l(t) + \varepsilon_v(t) = 1 \quad . \tag{91}$$

The non-dimensional forms of these equations are listed in Table 24. The scale factor for length is the depth of the porous medium (H), and for temperature is the wall superheat ($T_w - T_{sat}$).

The dimensionless groups are listed in Table 25. Only three groups are familiar to those developed from dimensional analysis -- group seven (similar to the Darcy number), group ten (similar to the geometric scale factor), and group 15 (the Nusselt number). As expected, Reynolds numbers for the two phases result from the analysis. Groups two and five represent dimensionless evaporation rates, and groups six and nine represent dimensionless pressure. Groups eight and eleven express in dimensionless form the transfer of momentum between the phases due to evaporation. Groups three and seven are dimensionless expressions of the porous medium properties. Group twelve is the dimensionless temperature. Group 13 compares conductive and convective heat transfer, and group 14 compares evaporative and convective heat transfer. Groups 15 (the Nusselt number) and 16 represent dimensionless heat transfer and evaporation at the heater surface, respectively.

Table 23. The system of steady-state, one-dimensional, volume averaged equations for two-phase flow through an incompressible porous medium with heat transfer.

Continuity of Liquid Water

$$\frac{\partial\langle v_l\rangle}{\partial x} = \frac{\langle \dot{m}_x\rangle}{\rho_l}$$

Continuity of Vapor

$$\frac{\partial\left(\langle\rho_v\rangle'\langle v_v\rangle\right)}{\partial x} = -\langle \dot{m}_x\rangle$$

Conservation of Momentum of Liquid Water

$$\frac{\rho_l\langle v_l\rangle}{\varepsilon_l^2}\frac{\partial\langle v_l\rangle}{\partial x} = -\frac{\partial\langle P_l\rangle}{\partial x} - \rho_l g - \frac{\mu_l\langle v_l\rangle}{K} + \langle \dot{m}_x\rangle\left(\langle v_l\rangle - \langle v_v\rangle\right)$$

$$= -\frac{\partial\langle P_l\rangle}{\partial x} - \frac{\mu_l\langle v_l\rangle}{K} + \langle \dot{m}_x\rangle\left(\langle v_l\rangle - \langle v_v\rangle\right)$$

Conservation of Momentum of Vapor

$$\frac{\langle\rho_v\rangle'\langle v_v\rangle}{\varepsilon_v^2}\frac{\partial\langle v_v\rangle}{\partial x} = -\frac{\partial\langle P_v\rangle}{\partial x} - \langle\rho_v\rangle' g + \frac{\mu_v}{\varepsilon_v}\frac{\partial^2\langle v_v\rangle}{\partial x^2} - \frac{\mu_v\langle v_v\rangle}{K} - \langle \dot{m}_x\rangle\left(\langle v_l\rangle - \langle v_v\rangle\right)$$

$$= -\frac{\partial\langle P_v\rangle}{\partial x} + \frac{\mu_v}{\varepsilon_v}\frac{\partial^2\langle v_v\rangle}{\partial x^2} - \frac{\mu_v\langle v_v\rangle}{K} - \langle \dot{m}_x\rangle\left(\langle v_l\rangle - \langle v_v\rangle\right)$$

Conservation of Energy

$$\left(\rho_l C_{p_l}\langle v_l\rangle + \langle\rho_v\rangle'\langle C_{p_v}\rangle'\langle v_v\rangle\right)\frac{\partial T}{\partial x} = \frac{\partial}{\partial x}\left(k_{eff}\frac{\partial T}{\partial x}\right) + \langle \dot{m}_x\rangle\Delta h_v$$

Heat Transfer Boundary Condition

$$\langle q_o\rangle = -k\frac{\partial\langle T\rangle}{\partial x} + \langle \dot{m}_o\rangle\Delta h_v$$

Table 24. The non-dimensional form of the system of steady-state, one-dimensional, volume averaged conservation equations for two-phase flow through an incompressible porous medium with heat transfer.

Continuity of Liquid Water

$$\frac{\partial\langle Re_l\rangle}{\partial x^*} = \frac{\langle \dot{m}_x\rangle H D}{\mu_l}$$

Continuity of Vapor

$$\frac{\partial\langle Re_v\rangle}{\partial x^*} = -\frac{\langle \dot{m}_x\rangle H D}{\mu_v}$$

Conservation of Momentum of Liquid Water

$$\frac{\langle Re_l\rangle}{\varepsilon_l^2}\frac{\partial\langle Re_l\rangle}{\partial x^*} = -\frac{\partial}{\partial x^*}\left(\frac{D^2\rho_l H\langle P_l\rangle}{\mu_l^2}\right) - \frac{DH}{K}\langle Re_l\rangle + \frac{D^2\rho_l H\langle \dot{m}_x\rangle}{\mu_l^2}\left(\langle v_l\rangle - \langle v_v\rangle\right)$$

Conservation of Momentum of Vapor

$$\frac{\langle Re_v\rangle}{\varepsilon_v^2}\frac{\partial\langle Re_v\rangle}{\partial x^*} = -\frac{\partial}{\partial x^*}\left(\frac{D^2\langle\rho_v\rangle' H\langle P_v\rangle}{\mu_v^2}\right) + \frac{D}{\varepsilon_v H}\frac{\partial^2\langle Re_v\rangle}{\partial x^{*2}} - \frac{DH}{K}\langle Re_v\rangle + \frac{D^2\langle\rho_v\rangle' H\langle \dot{m}_x\rangle}{\mu_v^2}\left(\langle v_l\rangle - \langle v_v\rangle\right)$$

Conservation of Energy

$$\frac{\partial\langle\Theta\rangle}{\partial x^*} = \frac{\partial}{\partial x^*}\left(\frac{D k_{eff}}{H\left(\mu_l C_{p_l}\langle Re_l\rangle + \mu_v\langle C_{p_v}\rangle'\langle Re_v\rangle\right)}\frac{\partial\langle\Theta\rangle}{\partial x^*}\right) + \frac{DH\Delta h_v\langle \dot{m}_x\rangle}{(T_w - T_{sat})\left(\mu_l C_{p_l}\langle Re_l\rangle + \mu_v\langle C_{p_v}\rangle'\langle Re_v\rangle\right)}$$

Heat Transfer Boundary Condition

$$\frac{H\langle q_o\rangle}{k(T_w - T_{sat})} = -\frac{\partial\langle\Theta\rangle}{\partial x^*} + \frac{H\langle \dot{m}_o\rangle\Delta h_v}{k(T_w - T_{sat})}$$

Table 25. The dimensionless groups resulting from inspectional analysis of the volume-averaged conservation equations.

$$\Pi_1 = \langle Re_l \rangle = \frac{D\langle v_l \rangle \rho_l}{\mu_l} \qquad \Pi_2 = \frac{\langle \dot{m}_x \rangle H D}{\mu_l} \qquad \Pi_3 = x^* = \frac{x}{H}$$

$$\Pi_4 = \langle Re_v \rangle = \frac{D\langle v_v \rangle \langle \rho_v \rangle'}{\mu_v} \qquad \Pi_5 = \frac{\langle \dot{m}_x \rangle H D}{\mu_v}$$

$$\Pi_6 = \frac{D^2 \rho_l H \langle \mathcal{P}_l \rangle}{\mu_l^2} \qquad \Pi_7 = \frac{D H}{K} \qquad \Pi_8 = \frac{D^2 \rho_l H \langle \dot{m}_x \rangle}{\mu_l^2} \left(\langle v_l \rangle - \langle v_v \rangle \right)$$

$$\Pi_9 = \frac{D^2 \langle \rho_v \rangle' H \langle \mathcal{P}_v \rangle}{\mu_v^2} \qquad \Pi_{10} = \frac{D}{H} \qquad \Pi_{11} = \frac{D^2 \langle \rho_v \rangle' H \langle \dot{m}_x \rangle}{\mu_v^2} \left(\langle v_l \rangle - \langle v_v \rangle \right)$$

$$\Pi_{12} = \Theta = \frac{T - T_{sat}}{T_o - T_{sat}} \qquad \Pi_{13} = \frac{D k_{eff}}{H \left(\mu_l C_{p_l} \langle Re_l \rangle + \mu_v \langle C_{p_v} \rangle' \langle Re_v \rangle \right)}$$

$$\Pi_{14} = \frac{D H \Delta h_v \langle \dot{m}_x \rangle}{(T_o - T_{sat}) \left(\mu_l C_{p_l} \langle Re_l \rangle + \mu_v \langle C_{p_v} \rangle' \langle Re_v \rangle \right)}$$

$$\Pi_{15} = \frac{H q_o}{k(T_o - T_{sat})} \qquad \Pi_{16} = \frac{H \Delta h_v \langle \dot{m}_o \rangle}{k(T_o - T_{sat})}$$

APPENDIX VII

CORRELATIONS FOR PHYSICAL PROPERTIES OF WATER

The dimensionless groups developed for analysis of this boiling data contain physical properties of liquid water and vapor. Property correlations for these water phases in a saturated state are developed in this Appendix for a pressure range of 0.10 to 0.44 MPa; the corresponding saturation temperature range is 100 to 147 °C. Established correlations were examined [114], but accuracy over this temperature range was limited. Consequently, data for saturated liquid and vapor [115] are fitted with cubic polynomials using multiple regression analysis. The correlations and the correlation coefficients for the polynomials are listed in Table 26, and the agreement between the physical properties and the polynomials are shown in Figures 79 through 88.

Table 26. Regression polynomials for physical properties of saturated liquid and vapor phases of water over the temperature range of 75 to 165°C. Temperature is in degrees Celsius.

Property	Regression Polynomial	r^2
Density [g/cm^3]	$\rho_l = 0.992 + 1.684\times10^{-4}T - 6.208\times10^{-6}T^2 + 1.150\times10^{-8}T^3$	0.99
	$\rho_v = -1.101\times10^{-3} + 3.845\times10^{-5}T - 4.555\times10^{-7}T^2 + 2.410\times10^{-9}T^3$	0.99
Viscosity [cP]	$\mu_l = 0.978 - 0.0123\,T + 6.613\times10^{-5}T^2 - 1.305\times10^{-7}T^3$	0.99
	$\mu_v = 7.619\times10^{-6} + 4.909\times10^{-9}T - 5.591\times10^{-11}T^2 + 5.245\times10^{-14}T^3$	0.99
Heat Capacity [J/(g-°C)]	$C_{p_l} = 4.247 - 0.00180\,T + 1.481\times10^{-5}T^2$	0.99
	$C_{p_v} = 2.014 - 0.00365\,T + 3.780\times10^{-5}T^2$	0.99
Thermal Conductivity [W/(cm-°C)]	$k_l = 5.726\times10^{-3} + 1.796\times10^{-5}T - 7.481\times10^{-8}T^2 + 3.885\times10^{-11}T^3$	0.99
	$k_v = 2.265\times10^{-4} - 6.604\times10^{-7}T + 1.093\times10^{-8}T^2 - 2.234\times10^{-11}T^3$	0.99
Surface Tension [N/cm]	$\sigma = 7.441\times10^{-4} - 1.084\times10^{-6}T - 5.564\times10^{-9}T^2 + 9.169\times10^{-12}T^3$	0.99
Latent Heat of Vaporization [kJ/kg]	$\Delta h_v = 2492.4 - 2.150\,T - 1.005\times10^{-3}T^2 - 1.010\times10^{-5}T^3$	0.99

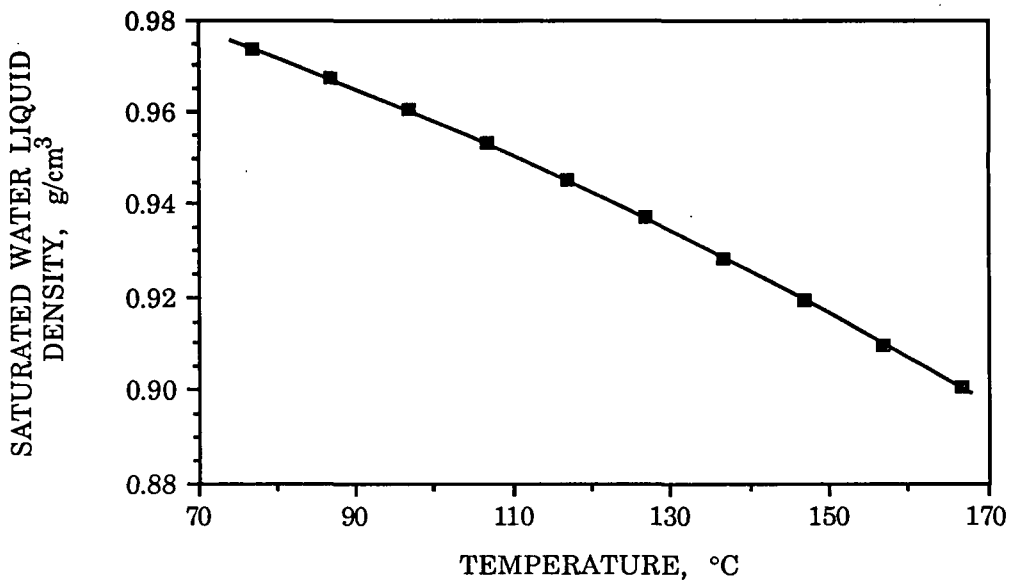

Figure 79. Density of liquid in a saturated water system.

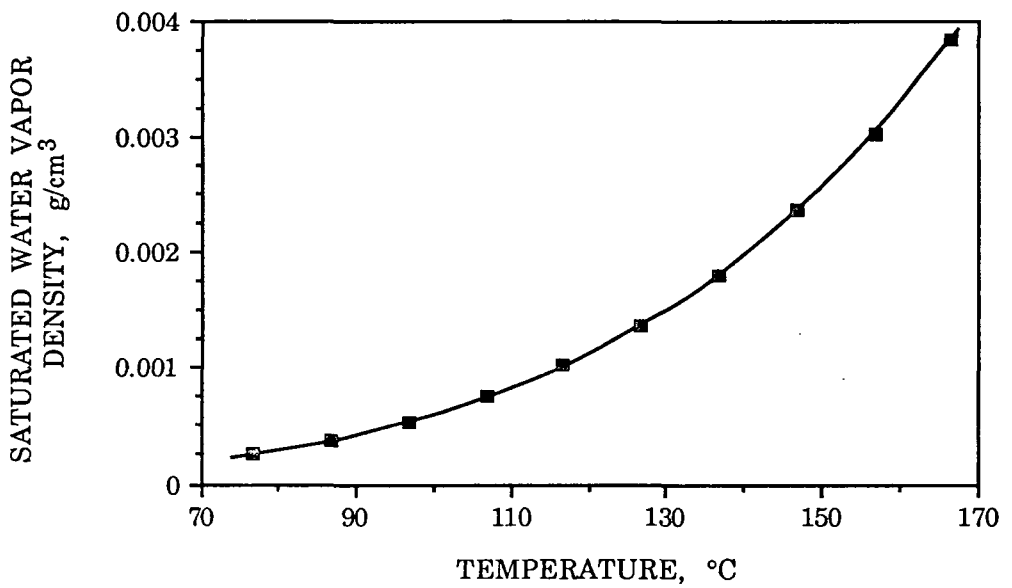

Figure 80. Density of vapor in a saturated water system.

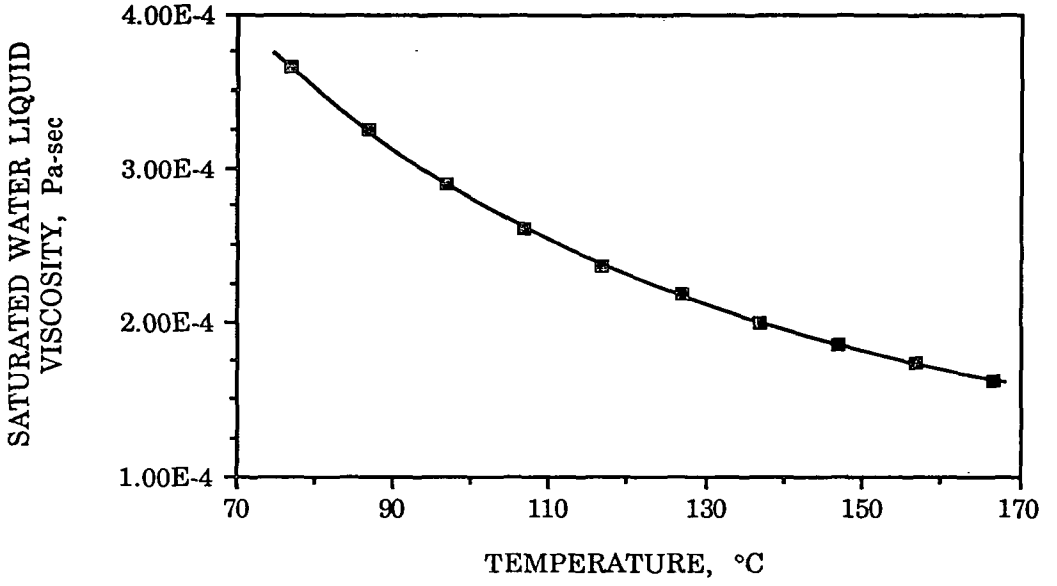

Figure 81. Viscosity of liquid in a saturated water system.

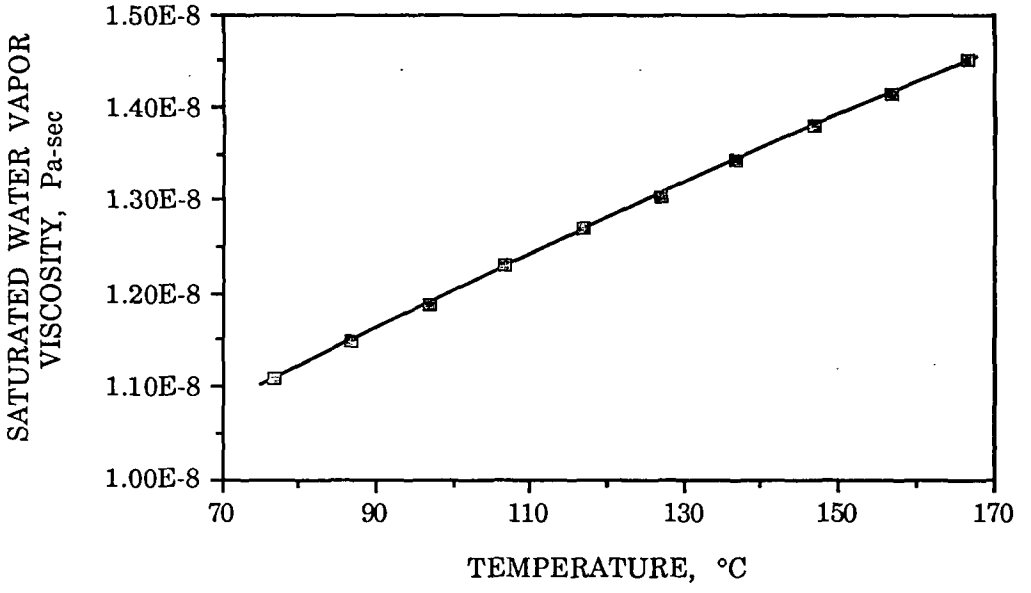

Figure 82. Viscosity of vapor in a saturated water system.

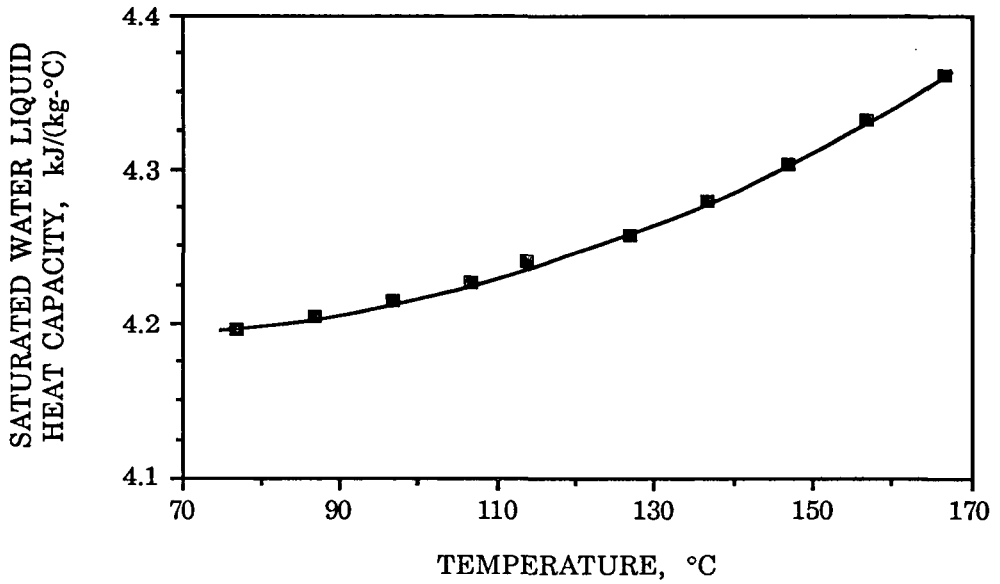

Figure 83. Heat capacity of water in a saturated water system.

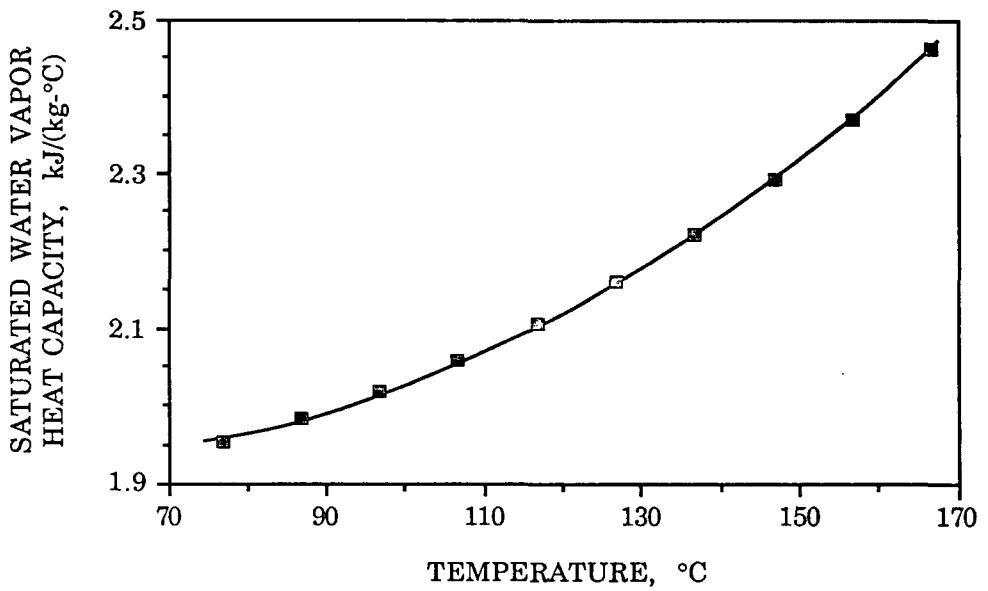

Figure 84. Heat capacity of vapor in a saturated water system.

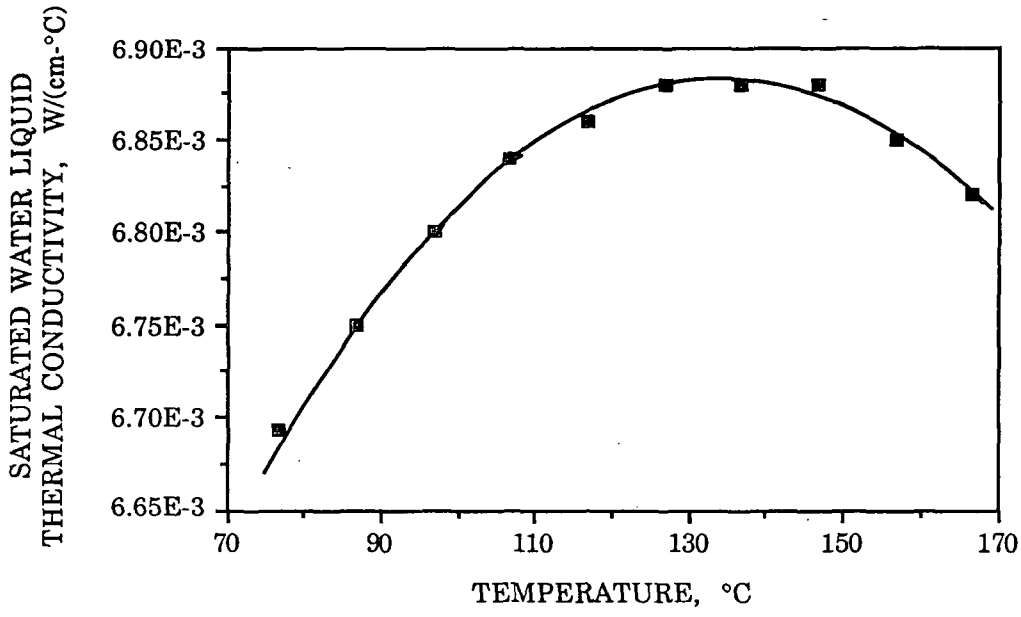

Figure 85. Thermal conductivity of liquid in a saturated water system.

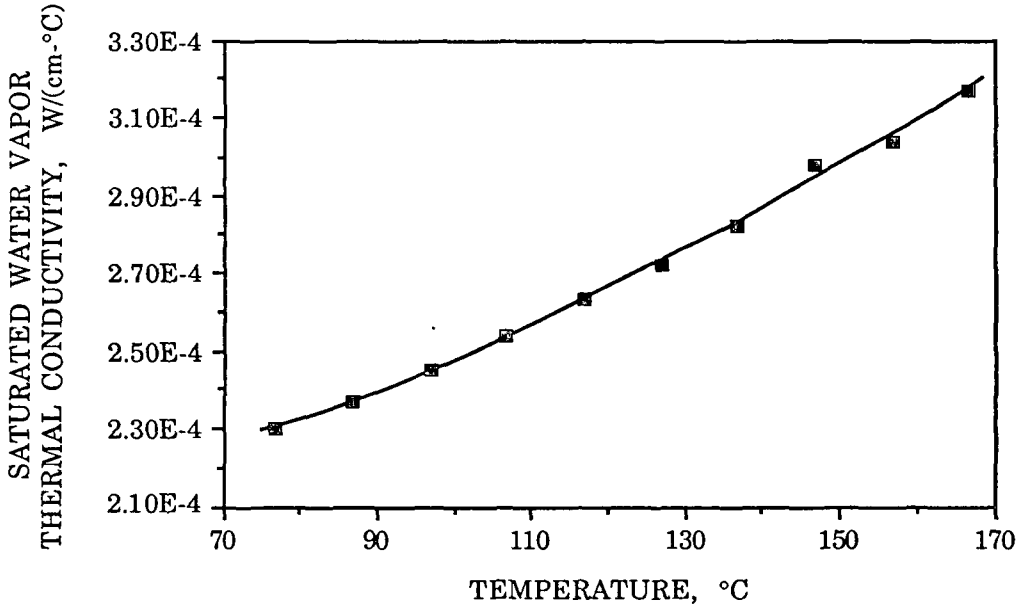

Figure 86. Thermal conductivity of vapor in a saturated water system.

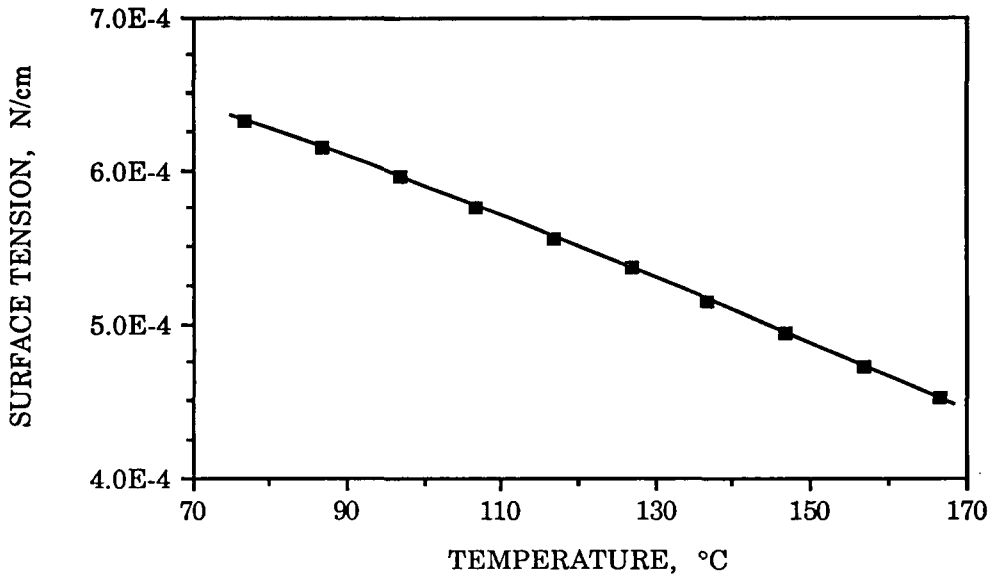

Figure 87. Surface tension a saturated water system.

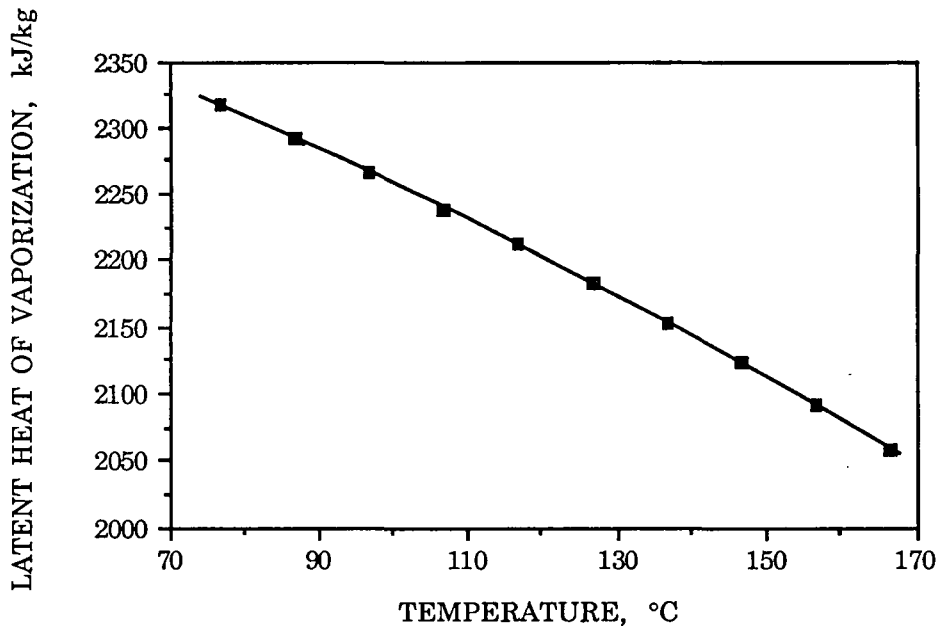

Figure 88. Latent heat of vaporization for a saturated water system.

APPENDIX VIII

EXPERIMENTAL DATA

This Appendix contains raw experimental data for the capillary pressure/saturation and permeability experiments, from which the reduced data discussed previously can be determined. The boiling curves consisting of reduced data for heat flux and wall superheat are reproduced here.

Table 27 contains the reduced data for average pore diameter and permeability that appear in Figures 49 and 52, respectively, in the RESULTS AND DISCUSSION section. Table 28 contains the raw data from the capillary pressure/saturation experiments that is used to calculate average pore diameter. Table 29 contains the raw data from the permeability experiments. Figures 89 through 111 illustrate the boiling curves for the 21 fibrous media boiling experiments and the two pool boiling experiments.

Table 27. Reduced data for average pore diameter and permeability of the fibrous pads.

	Average Pore Diameter Data				Permeability Data		
Fiber Type	Pad Number	Fiber Volume (cm^3)	Porosity	Diameter (μm)	Data Set	Porosity	Permeability (m^2)
3.0 μm diameter alumina	1	1.30	0.956	47.8	1	0.963	4.33E-11
	2	1.45	0.953	39.5	2	0.954	2.74E-11
	3	2.09	0.940	33.6	3	0.948	1.96E-11
	4	2.93	0.928	29.5	4	0.939	1.50E-11
	5	2.53	0.922	32.5	5	0.932	1.26E-11
					6	0.927	1.05E-11
8.4 μm diameter silica	1	1.22	0.959	107.0	1	0.962	2.17E-10
	2	1.44	0.956	99.4	2	0.954	1.54E-10
	3	1.73	0.945	83.5	3	0.948	1.18E-10
	4	2.18	0.933	74.0	4	0.939	9.97E-11
	5	2.75	0.913	57.3	5	0.932	8.07E-11
					6	0.926	7.83E-11
18.5 μm diameter alumina	1	1.08	0.961	358.2	1	0.962	9.11E-10
	2	1.40	0.950	274.8	2	0.954	7.44E-10
	3	1.93	0.930	123.2	3	0.948	5.72E-10
	4	2.22	0.021	140.9	4	0.940	4.41E-10
	5	2.55	0.910	176.1	5	0.933	3.67E-10
					6	0.927	2.79E-10

Table 28. Raw data for the capillary pressure/saturation experiments. Columns 1 through 5 refer to the particular fiber pad.

3.0 μm diameter alumina fiber

BED WATER VOLUME, ml				
1	2	3	4	5
27.38	29.40	33.10	38.32	30.03
25.98	28.67	31.11	35.33	28.82
25.36	28.19	31.10	34.9	28.53
25.05	28.07	30.98	34.64	28.34
24.70	27.97	30.88	34.22	27.88
23.74	27.79	30.62	30.63	23.2
20.45	27.47	30.20	27.42	19.12
16.79	26.67	29.01	25	16.45
13.30	25.47	26.27	21.81	12.59
10.28	22.87	23.09	19.26	9.39
7.37	20.07	19.40	14.63	6.72
5.19	17.47	16.42	11.08	4.67
3.21	14.55	13.31	8.92	2.91
2.10	11.75	10.30	6.95	2.41
1.04	9.39	8.19	5.39	1.49
0.69	7.03	6.15	4.25	1.18
0.64	3.80	4.50	3.47	1.09
0.64	2.79	3.36	2.91	0.98
	2.01	2.52	2.56	0.97
	1.71	1.82	2.22	
	1.45	1.41	1.91	
	1.42	1.17	1.83	
	1.40	1.02	1.83	
		0.77		
		0.72		

APPLIED PRESSURE DIFFERENCE, cm Hg				
1	2	3	4	5
0.000	0.000	0.000	0.000	0.000
0.724	0.535	0.666	0.649	0.796
1.171	1.082	1.217	1.439	1.561
1.814	1.695	1.912	2.540	2.664
2.626	2.287	2.631	4.285	4.376
3.266	2.909	3.418	5.627	5.652
3.768	3.524	4.163	6.159	6.074
4.079	4.036	4.724	6.463	6.287
4.354	4.496	5.146	6.800	6.589
4.624	4.777	5.485	7.116	6.986
4.860	4.896	5.685	7.453	7.284
5.199	5.082	5.879	7.788	7.813
5.681	5.308	6.134	8.198	8.737
6.199	5.508	6.490	8.715	9.381
6.873	5.752	6.757	9.341	10.557
7.501	6.050	7.203	10.038	11.399
8.216	6.776	7.677	10.737	12.619
8.867	7.181	8.270	11.498	14.257
	7.670	8.956	12.702	15.791
	8.389	9.769	14.274	
	9.166	10.572	15.804	
	9.469	11.318	17.828	
	9.899	12.020	20.089	
		13.382		
		15.000		

Table 28. (continued)

8.4 μm diameter silica fiber

BED WATER VOLUME, ml				
1	2	3	4	5
28.52	31.65	26.00	30.98	29.86
27.30	31.02	24.90	30.53	29.24
26.73	30.70	24.01	29.85	28.24
26.35	29.66	23.32	29.66	27.82
25.81	27.46	22.17	28.73	27.27
24.72	25.08	20.88	27.48	26.87
23.62	22.48	19.33	25.96	26.13
21.11	20.06	16.90	24.06	25.26
19.74	16.36	13.80	22.02	23.64
18.15	14.80	12.23	19.37	21.18
16.20	12.47	9.99	16.69	18.82
13.82	10.36	7.61	13.85	16.49
11.15	7.61	5.24	10.36	13.80
8.54	5.31	3.22	8.22	11.05
6.49	3.59	2.31	5.85	8.51
4.63	2.01	1.50	3.79	6.16
3.53	1.44	1.11	2.45	4.57
2.10	1.08	0.91	1.63	3.13
1.29	0.91	0.91	1.12	2.05
0.79	0.87	0.82	0.90	1.46
0.71	0.84	0.82	0.78	1.12
0.53			0.72	0.92
0.48				0.84

APPLIED PRESSURE DIFFERENCE, cm Hg				
1	2	3	4	5
0.000	0.000	0.000	0.000	0.000
0.331	0.398	0.031	0.363	0.339
0.546	0.768	0.702	0.732	0.685
0.778	1.130	1.079	1.131	1.084
1.022	1.490	1.564	1.473	1.453
1.266	1.693	1.881	1.797	1.818
1.477	1.844	2.096	2.073	2.192
1.561	1.974	2.341	2.308	2.569
1.715	2.071	2.517	2.526	2.891
1.827	2.104	2.549	2.667	3.132
1.920	2.215	2.675	2.825	3.336
2.002	2.303	2.785	2.960	3.526
2.074	2.386	2.883	3.095	3.698
2.152	2.500	2.996	3.234	3.878
2.266	2.686	3.335	3.393	4.046
2.373	2.929	3.670	3.633	4.264
2.476	3.257	4.020	3.899	4.445
2.650	3.756	4.571	4.245	4.724
3.007	4.261	5.108	4.722	5.156
3.514	4.991	5.858	5.317	5.745
4.070	5.555	6.455	5.870	6.292
4.678			6.537	6.946
5.494				7.990

Table 28. (continued)

18.5 μm diameter alumina fiber

BED WATER VOLUME, ml				
1	2	3	4	5
26.59	26.27	25.18	25.61	25.86
25.59	25.46	23.96	24.74	24.59
24.80	24.77	23.06	24.25	23.97
22.65	22.85	21.36	22.85	23.14
20.41	20.90	19.83	21.47	21.65
18.50	19.17	17.30	19.72	19.87
16.01	16.70	15.04	17.63	17.98
13.52	14.92	12.41	15.32	15.96
10.71	12.16	10.41	12.68	13.66
8.65	10.15	8.45	10.67	11.76
6.51	7.94	6.55	8.51	9.76
4.51	5.77	4.69	6.44	7.59
2.86	3.84	2.93	5.04	6.24
0.97	2.12	1.82	3.26	4.34
0.74	0.91	1.16	2.36	3.42
0.70	0.68	0.86	1.58	2.46
0.67	0.60	0.83	1.01	1.67
0.67	0.60		0.77	1.17
			0.62	0.97
			0.59	0.88

APPLIED PRESSURE DIFFERENCE, cm Hg				
1	2	3	4	5
0.000	0.000	0.000	0.000	0.000
0.135	0.180	0.436	0.428	0.379
0.316	0.372	0.622	0.695	0.645
0.377	0.474	0.712	0.896	0.925
0.415	0.542	0.831	1.030	1.055
0.450	0.589	0.921	1.136	1.146
0.493	0.624	1.005	1.234	1.273
0.531	0.661	1.083	1.297	1.362
0.532	0.671	1.174	1.358	1.463
0.575	0.723	1.239	1.446	1.569
0.634	0.767	1.337	1.528	1.662
0.716	0.832	1.460	1.623	1.777
0.822	0.896	1.652	1.723	1.878
0.951	0.982	1.940	1.902	2.045
1.297	1.238	2.213	2.070	2.204
1.632	1.542	2.499	2.285	2.384
2.204	2.094	2.738	2.671	2.776
3.105	2.947		3.155	3.330
			3.674	3.879
			4.405	4.629

Table 29. Raw data for the permeability experiments, performed at a water temperature of approximately 21.5°C.

		3.0 μm diameter alumina			8.4 μm diameter alumina			18.5 μm diameter alumina		
Data Set	Data Point	Time (sec)	Water Volume (ml)	Pressure Drop (Pa)	Time (sec)	Water Volume (ml)	Pressure Drop (Pa)	Time (sec)	Water Volume (ml)	Pressure Drop (Pa)
1	1	318	64.4	1340.1	479	163.8	157.8	481	44.4	138.0
	2	348	61.9	1531.3	470	98.8	259.2	495	83.8	74.4
	3	386	61.6	1700.0	484	82.9	314.3	482	36.0	179.3
	4	416	61.2	1876.2	485	66.1	391.6	451	26.6	237.8
	5	463	61.5	2085.0	485	50.1	519.2	486	20.2	297.7
	6	493	62.2	2193.2	481	42.8	600.7	500	108.4	61.4
2	1	245	62.2	1707.5	480	146.9	247.6	499	72.4	108.8
	2	279	63.4	1896.6	490	111.7	333.2	490	164.5	53.1
	3	299	62.5	2055.8	491	92.2	402.7	485	73.0	106.5
	4	326	62.7	2241.5	493	80.8	461.2	471	48.2	151.7
	5	345	61.6	2427.2	492	69.4	533.3	497	39.0	195.6
	6	372	61.6	2626.5	494	62.5	597.8	488	31.0	246.8
3	1	244	61.8	2387.8	491	124.7	389.1	490	26.5	293.9
	2	263	62.0	2549.7	485	110.8	438.1	491	98.9	106.4
	3	279	61.0	2761.9	477	89.1	527.9	489	152.2	68.3
	4	292	61.4	2887.8	484	81.4	587.1	492	70.7	141.4
	5	329	64.5	3087.1	485	73.6	654.6	488	55.8	179.7
	6	340	62.6	3299.3	485	65.9	731.2	479	40.8	240.1
4	1	242	62.1	3102.0	494	110.9	520.7	490	35.3	286.5
	2	253	61.7	3246.3	495	98.4	591.4	480	148.0	89.8
	3	292	65.9	3469.4	495	88.1	657.8	491	117.9	112.2
	4	299	62.4	3769.4	494	80.1	726.5	483	82.1	158.5
	5	311	62.6	3906.1	493	73.2	787.3	489	66.7	199.5
	6	329	63.4	4102.0	494	67.7	854.4	493	53.0	246.8
5	1	251	63.0	3732.7	272	61.4	642.2	490	43.5	296.9
	2	260	62.2	3912.2	371	74.2	725.2	484	175.5	91.2
	3	289	62.6	4292.5	368	66.6	802.0	487	127.9	123.4
	4	306	62.2	4612.2	379	64.4	851.8	494	100.6	159.2
	5	333	61.6	5006.8	416	63.5	941.4	490	77.4	204.1
	6	395	68.0	5412.9	440	64.1	993.7	493	65.3	243.8
6	1	282	61.3	5129.3	268	63.5	657.1	484	53.4	287.8
	2	264	61.5	4799.3	287	62.0	730.6	476	139.7	151.0
	3	310	62.9	5483.0	315	62.5	797.4	388	180.0	99.3
	4	316	61.5	5721.1	343	63.4	857.1	481	111.6	194.8
	5	333	62.0	6006.8	366	61.6	936.1	484	88.7	244.4
	6	359	63.8	6250.3	399	64.7	976.9	480	73.2	292.2

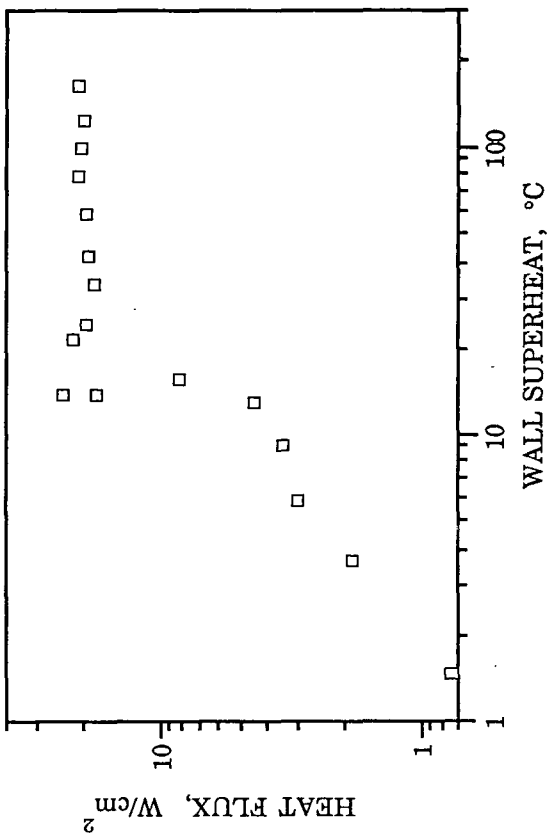

Figure 90. Boiling curve for data set CBE14.

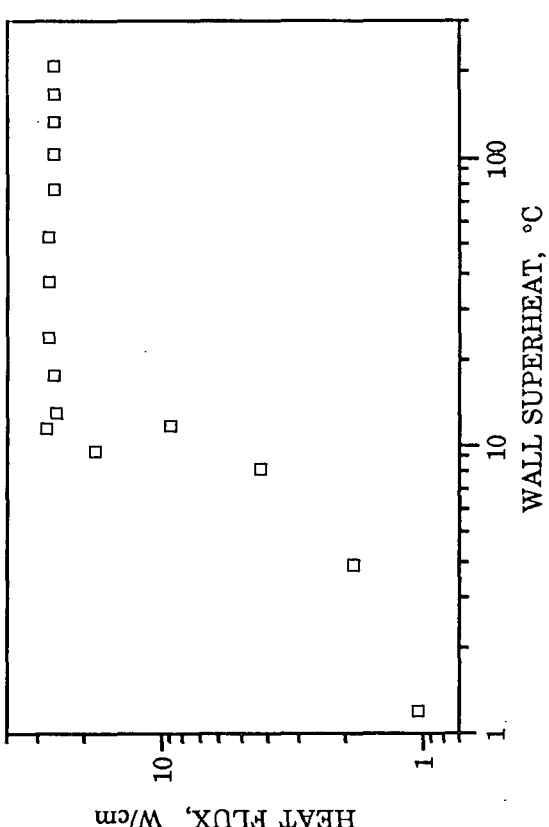

Figure 89. Boiling curve for data set CBE13.

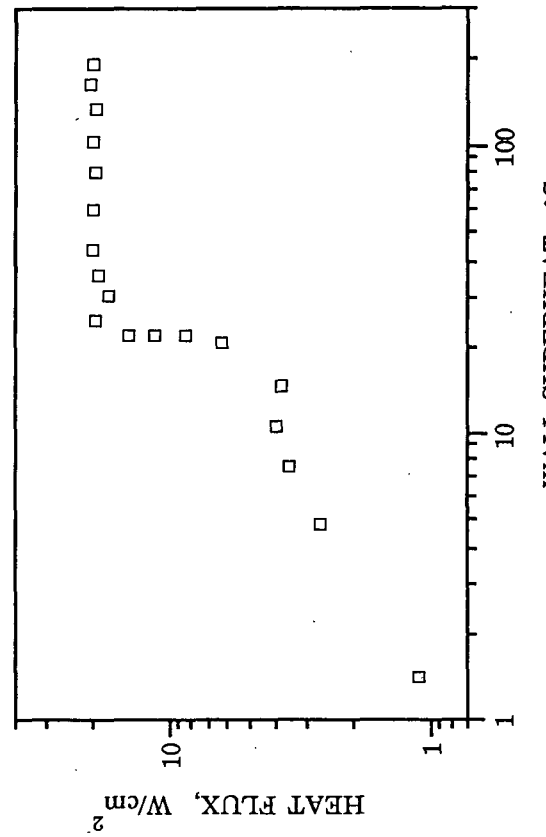

Figure 92. Boiling curve for data set CBE17.

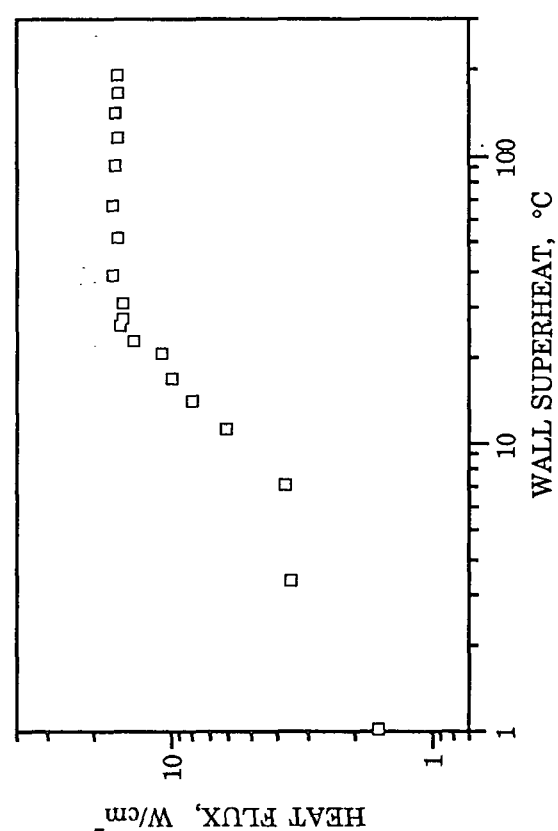

Figure 91. Boiling curve for data set CBE15.

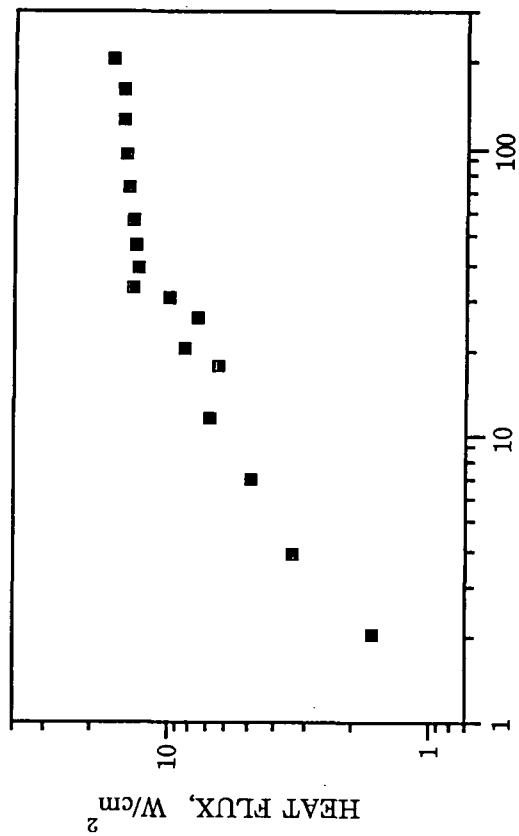

Figure 93. Boiling curve for data set CBE18.

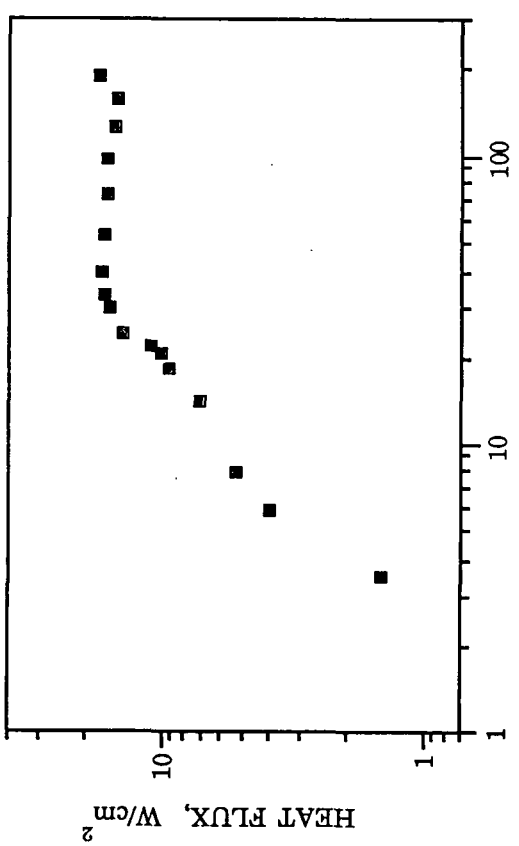

Figure 94. Boiling curve for data set CBE21.

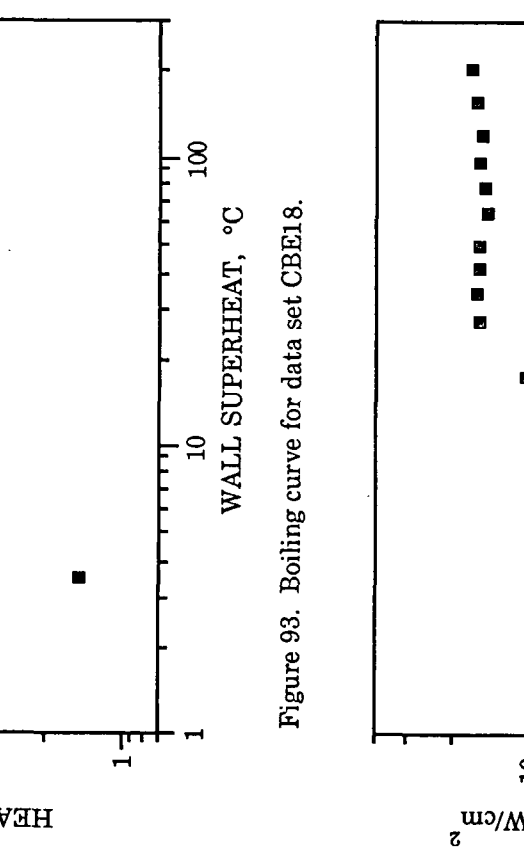

Figure 95. Boiling curve for data set CBE22.

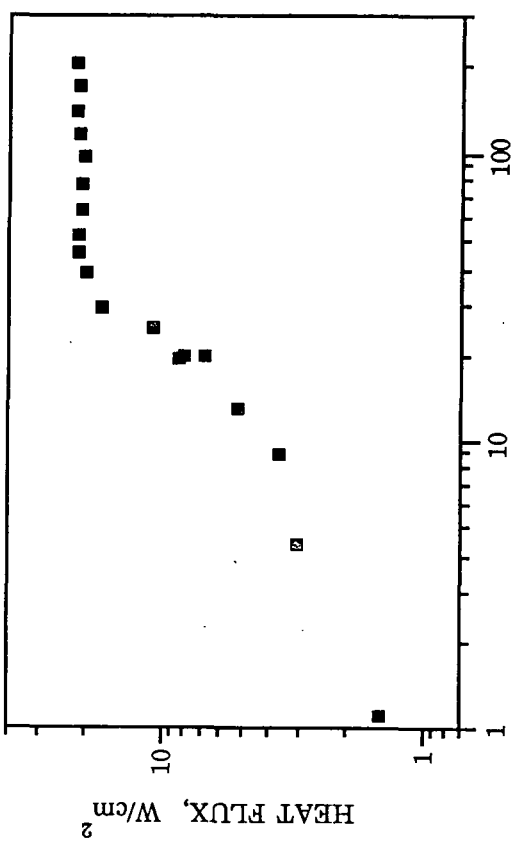

Figure 96. Boiling curve for data set CBE23.

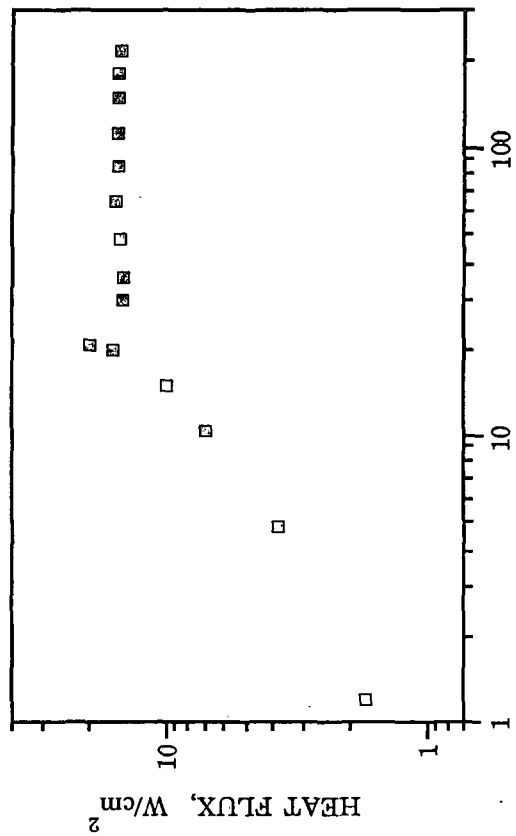

Figure 97. Boiling curve for data set CBE24. The first data point is not included on this curve.

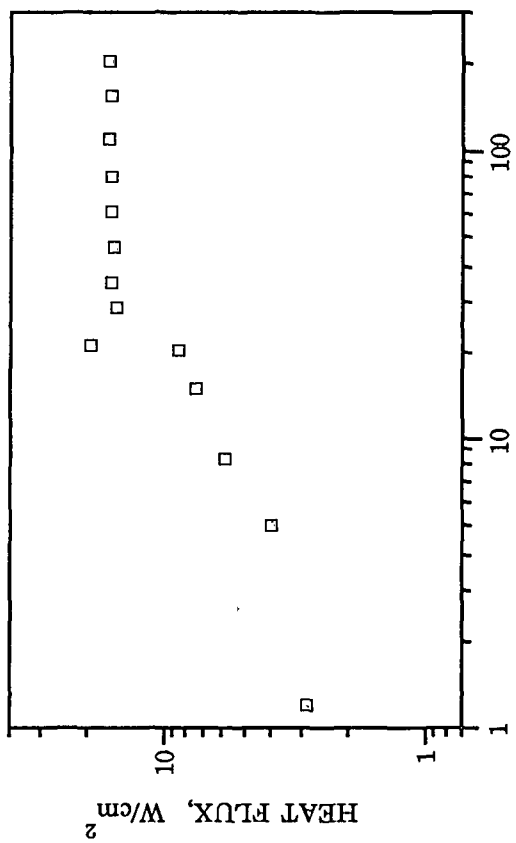

Figure 98. Boiling curve for data set CBE25.

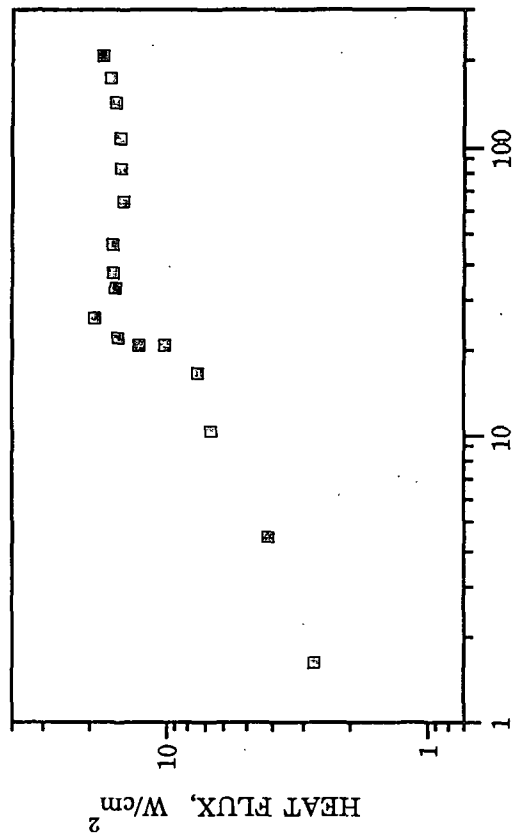

Figure 99. Boiling curve for data set CBE26.

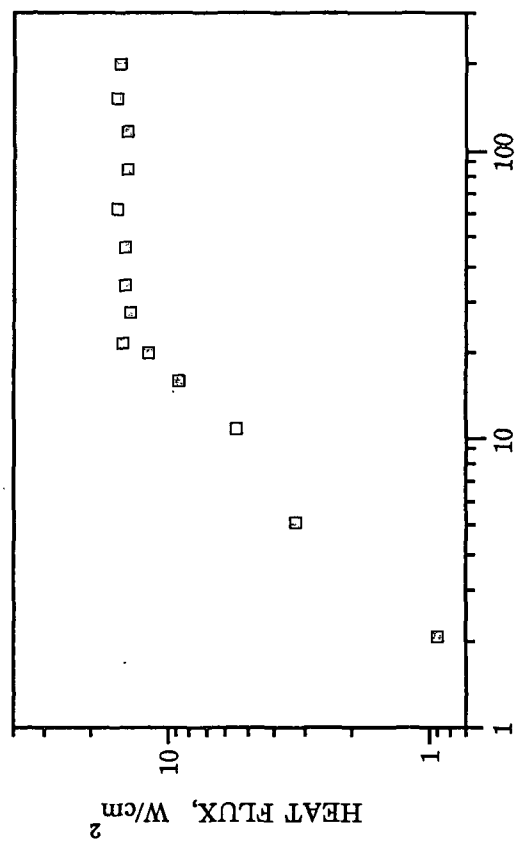

Figure 100. Boiling curve for data set CBE29.

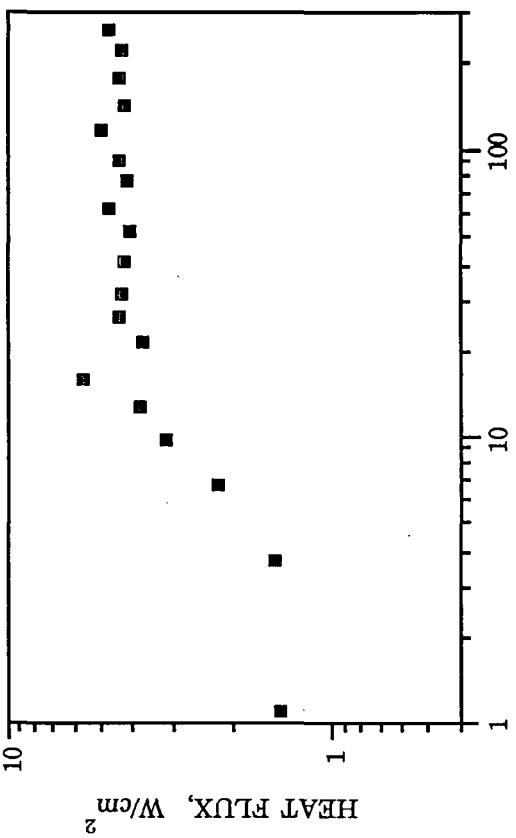

Figure 102. Boiling curve for data set CBE8.

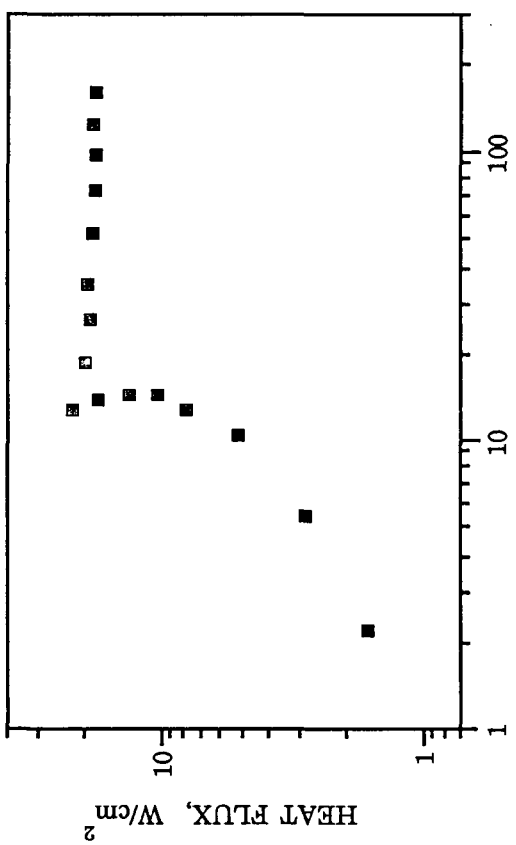

Figure 101. Boiling curve for data set CBE30.

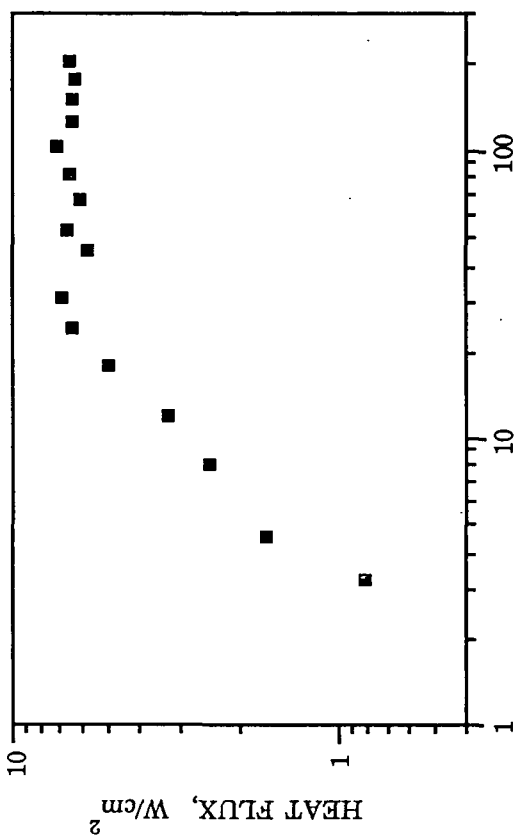

Figure 104. Boiling curve for data set CBE16.

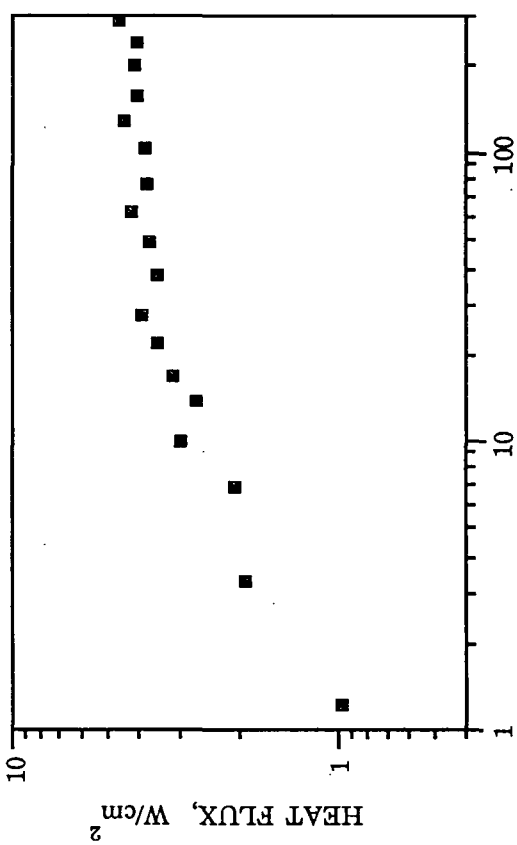

Figure 103. Boiling curve for data set CBE9.

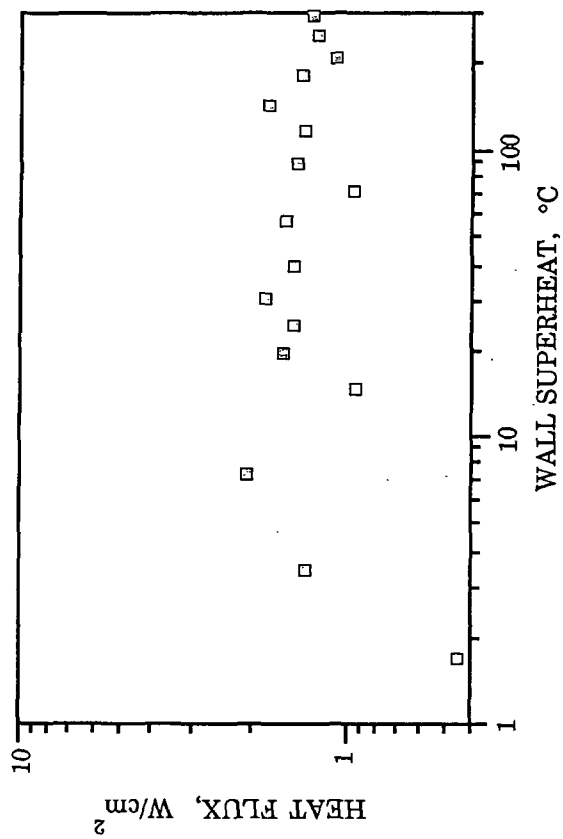

Figure 106. Boiling curve for data set CBE12.

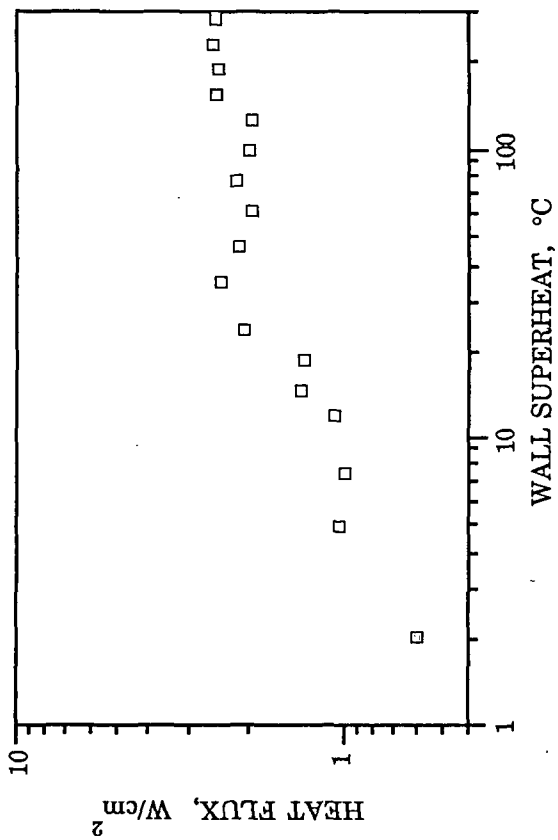

Figure 105. Boiling curve for data set CBE10.

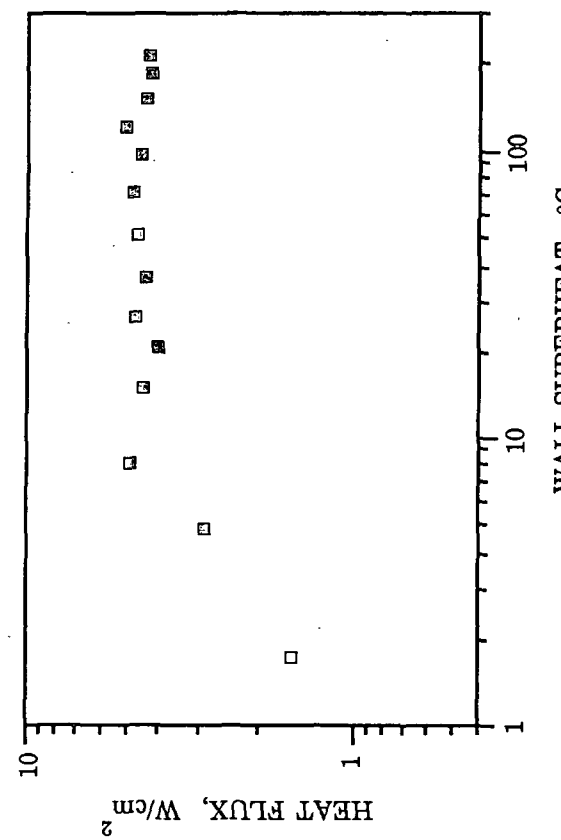

Figure 108. Boiling curve for data set CBE28.

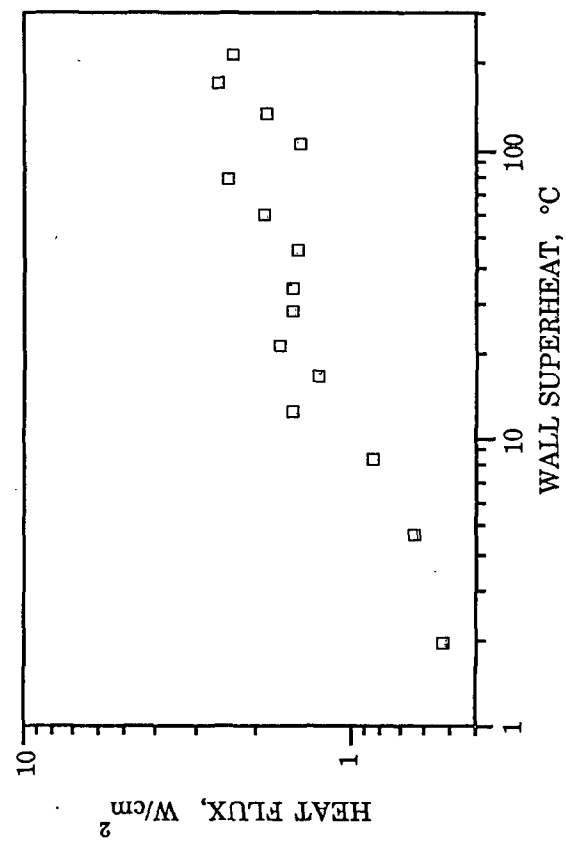

Figure 107. Boiling curve for data set CBE27.

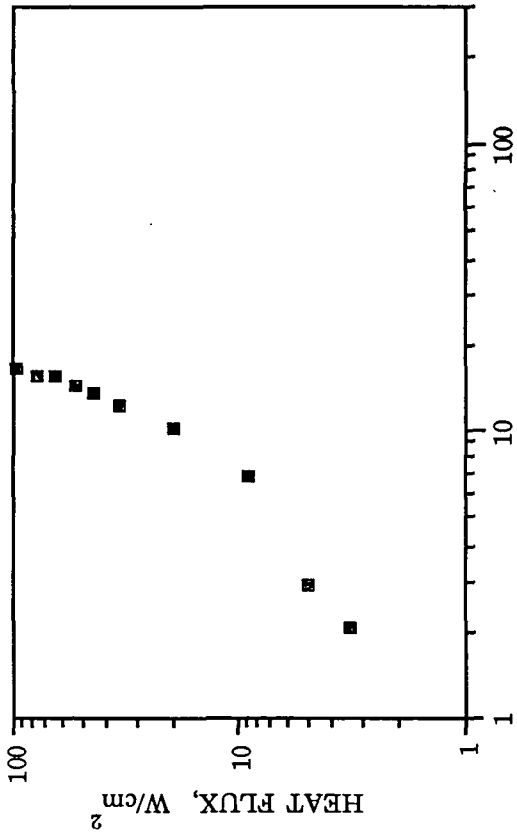

Figure 110. Boiling curve for data set CBE19.

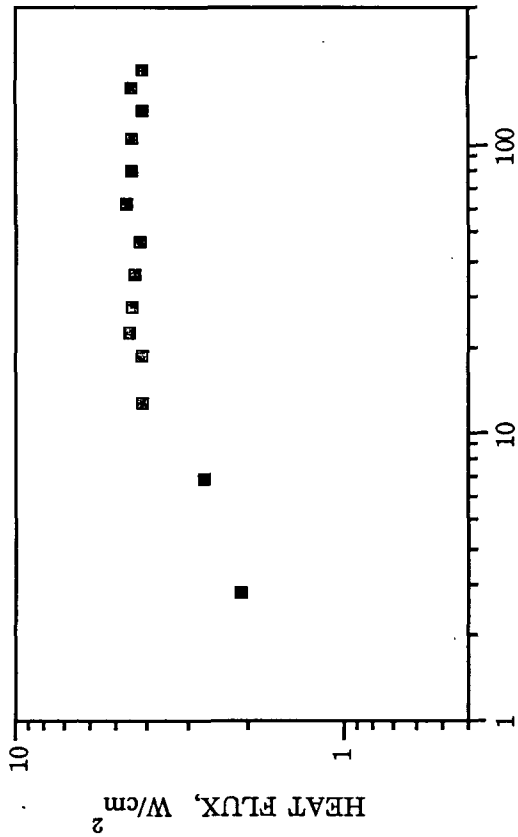

Figure 109. Boiling curve for data set CBE31.

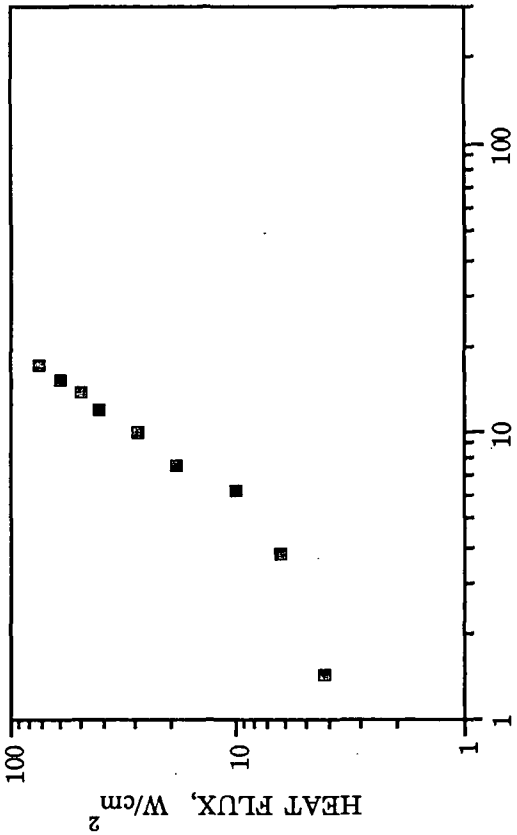

Figure 111. Boiling curve for data set CBE20.